



The Turgo impulse turbine; a CFD based approach to the design improvement with experimental validation

David Shaun Benzon

PhD Thesis

SUPERVISOR:
PROFESSOR GEORGE A. AGGIDIS

Lancaster University
in collaboration with
Gilbert Gilkes & Gordon Ltd.

Department of Engineering, Faculty of Science and Technology, Lancaster University,
Lancaster, UK

Declaration

The author declares that this thesis has not been previously submitted for award of a higher degree to this or any university, and that the contents, except where otherwise stated, are the author's own work.

Signed:



Date:

07/06/2016

Abstract

The use of Computational Fluid Dynamics (CFD) has become a well-established approach in the analysis and optimisation of impulse hydro turbines. Recent studies have shown that modern CFD tools combined with faster computing processors can be used to accurately simulate the operation of impulse turbine runners and injectors in timescales suitable for design optimisation studies and which correlate well with experimental results. This work has however focussed mainly on Pelton turbines and the use of CFD in the analysis and optimisation of Turgo turbines is still in its infancy, with no studies showing a complete simulation of a Turgo runner capturing the torque on the inside and outside blade surfaces and producing a reliable extrapolation of the torque and power at a given operating point. Although there have been some studies carried out in the past where injector geometries (similar for both Pelton and Turgo turbines) have been modified to improve their performance, there has been no thorough investigation of the basic injector design parameters and the influence they have on the injector performance.

The aim of this research is to use modern CFD tools to develop models which aid the better understanding of Turgo impulse turbine runners and injectors and facilitate the optimisation of existing designs. CFD is used to model and optimise both the injectors and the runner of a modern commercial Turgo impulse turbine and the accuracy of the models are verified by carrying out experimental tests on the original and optimised designs. The original designs together with experience in the operation of these turbines were provided by the industrial sponsors of this research *Gilbert Gilkes and Gordon Ltd*.

The research described in this thesis can be split into five main parts:

1. Development of a numerical model to analyses the flow through the Turgo runner using modern CFD tools combined with a series of assumptions to reduce the computational time while still retaining the accuracy of the model. Using this model to optimise the design of the Turgo runner provided by Gilkes.
2. Development of a similar numerical model for a simplified 2D injector design to facilitate a study of the impact of the basic design parameters on the performance over a range of operating conditions. Applying these optimisations to the existing Gilkes design and taking the numerical analysis further by including the full injector geometry as well as the branch pipe and guide vanes.
3. Manufacture and experimental testing of the original and optimised Turgo runners.
4. Manufacture and experimental testing of the original and optimised injector designs.

5. Verification of the numerical models developed in 1.) and 2.) by comparison with the experimental results.

The numerical model developed in 1.) includes several simplifying assumptions in order to reduce the computational time and produce models which could solve in reasonable timescales allowing many design variations to be analysed. As the runner simulations require a transient analysis of complex multi-phase free surface flow with a rotating frame of reference they are already computationally costly and efforts have to be made to reduce this computational cost if the models are to be effective for optimisation purposes. The runner model simplifications were the exclusion of any casing interactions by not modelling the casing and the use of a 2 blade model analysing only a single blade passage in order to reduce the size of the computational domain. Several modelling assumptions were also introduced and attempts are made to quantify the effects of these assumptions through unit tests. For discretisation of the domain two mesh sizes were used, a *coarse mesh* which slightly under predicts the efficiency but was suitable for comparing designs and a *fine mesh* which gave mesh independent results. The *fine mesh* took over 4 times longer to solve rendering it unfeasible for optimisation purposes and it was therefore used only at key points to verify the design changes made using the *coarse mesh*.

The analysis and optimisation of the injectors carried out in 2.) use similar CFD tools as the runner analysis however the geometry (excluding the branch pipe and guide vanes) could be simplified into a 2D axisymmetric case operating at steady state conditions. This drastically reduces the solve time and allows the use of a mesh independent model and the analysis of hundreds of designs and operating conditions. Once the optimisations had been carried out, the design changes were verified by extending the model to analyse the 3D case with a straight pipe upstream of the injector and a 3D full case including the branch pipe and guide vanes.

In 3.), following the optimisation of the runner in 1.), a Finite Element Analysis (FEA) of the runner was carried out to ensure the optimised runner had sufficient strength for operation at the highest heads recommended for a runner of this size. The design was strengthened based on the results of the FEA and CFD was carried out in conjunction with these changes to ensure minimal loss in hydraulic efficiency. The manufacturing process was also researched and Design for Manufacture and Assembly (DFMA) was applied to the strengthened design identifying two optimised designs (LE4 and LE1) which will be tested before and after additional dressing of the leading edges. Both optimised runner designs were manufactured and tested at the Laboratory of Hydraulic Machines, National Technical University of Athens (NTUA).

Following the injector analysis and optimisations in 2.), the optimised injectors were manufactured for experimental testing using both the Pelton and the Turgo test rig at NTUA in 4.). As the design changes made were not critical to the strength of the injectors there was no need to carry out a FEA.

The CFD model verification in Part 5.) looks initially at the full Turgo system in order to compare the absolute difference between the numerical efficiency and the experimental efficiency of the original Turgo runner at the best efficiency point. The mechanical losses of the test rig are estimated to determine the experimental hydraulic efficiency. The numerical hydraulic efficiency is then determined by calculating the losses upstream of the injector, using standard pipe flow equations and combining these with the losses through the injector, as well as the numerical efficiency of the runner by simulating the runner using the ‘real jet’ profile produced by the full injector simulations. The results showed the numerical model to be over-predicting the efficiency by 1.26%. The numerical difference in the performance of the two injectors is then compared to the experimental difference measured during testing. This is done by importing the ‘real jet’ profiles produced by the full 3D injector simulations into the LE1 runner simulation. This allows the difference in total efficiency between the injectors combined with the runner to be compared to the experimental differences which also includes the impact of the jet on the runner performance. The comparison between the injectors is less accurate as more uncertainties are introduced when combining these models and the differences are smaller however the CFD was able to predict the improvements to within 0.4%. Finally, the numerical differences between the runner designs and the experimental differences are compared showing that the runner model is able to predict differences in hydraulic efficiency to within 0.1%. This accuracy is largely down to the fact that many of the systematic experimental and modelling errors are cancelled out when comparing only the runners. The CFD model verification has shown that although the absolute performance of the Turgo system can be modelled numerically to within a good degree of accuracy, it requires combining injector and runner models as well as estimating additional losses in the pipework which can prove time consuming. However for design comparison and optimisations the CFD models have been shown to be far more accurate suggesting that this is where these numerical models are most useful.

Keywords

Renewable Energy, Hydropower, Impulse turbines, Turgo turbines, Computational Fluid Dynamics, Design Optimisation, Experimental Testing

Dedication

I would like to dedicate this research to the memory of my grandfather,

Philip Rudolf Botha

1923 -2000

From a young age he encouraged me to pursue a career in engineering. Here is a quote he often used, which I find a great source of inspiration.

*"The heights by great men reached and kept
Were not attained by sudden flight,
But they, while their companions slept,
Were toiling upward in the night."*

(From ‘The Ladder of St Augustine’ by Henry Wadsworth Longfellow)

Acknowledgements

Firstly I would like to thank my supervisor Professor George Aggidis for encouraging me to study a PhD, showing continued enthusiasm in this research and for providing support and guidance. None of this would have been possible without you.

My gratitude goes to *Gilbert Gilkes & Gordon Ltd* for sponsoring this research and supporting the experimental testing carried out in Athens. I would specifically like to thank Jonathan Martin, Alan Robinson, Dr Jo Scott and Anthony Watson for sharing their experience, providing support and giving valuable insight into this research. I would like to thank Sam Clegg, Ioannis Kassanos and Austen Wheatman for their support during the experimental testing. I would also like to thank Andy Eaton for his help in organising the presentations given at the Africa Utility Week Conference in Cape Town. Many thanks go out to other Gilkes employees who were involved in this research; it's been a great pleasure working with you all.

I would like to thank Dr Audrius Zidonis who in many ways paved the way for this research. I would also like to thank Dr Alexandros Panagiotopoulos for his assistance during the experimental testing and his help with the Greek language, ευχαριστώ πολύ! I have thoroughly enjoyed the research the three of us have carried out together and thank you for the experience you have been willing to impart. I would also like to thank Dr Ioannis Anagnostopoulos for his involvement in this research and providing invaluable guidance during this collaborative work. My thanks also go to Professor Dimitris Papantonis and the rest of the staff at the *Laboratory for Hydraulic Machines, National Technical University of Athens*.

I would like to thank Sean Petley for his help during the experimental testing in Athens and for those entertaining conversations over a Souvlaki. My thanks also go to Nilla Karlsen-Davies for her patience in helping out with and eventually taking over, the CFD Labs. I would also like to thank Scott Nash, the last member of our original office for his insight into hydrophobic polymers and much more. The working environment created by the three of you was second to none.

My thanks go to the reviewers of the academic papers published during this research whose constructive comments helped shape and improve the quality of this work.

Finally, I would like to thank my family for their unwavering love, support and guidance throughout what has been an exciting journey.

List of Journal Publications

1. Benzon, D. S., Židonis, A., Panagiotopoulos, A., Aggidis, G. A., Anagnostopoulos, J. S., Papantonis D. E. (2014). "Impulse turbine injector design improvement using Computational Fluid Dynamics." ASME J. Fluids Eng. 137(4), 041106
2. Benzon, D. S., Židonis, A., Panagiotopoulos, A., Aggidis, G. A., Anagnostopoulos, J. S., Papantonis D. E. (2015). "Numerical Investigation of the Spear Valve Configuration on the Performance of Pelton and Turgo Turbine Injectors and Runners." ASME J. Fluids Eng 137(11): 111201-111201.
3. Benzon, D. S., Aggidis, G. A., Anagnostopoulos, J. S., (2016). "Development of the Turgo Impulse turbine: Past and present." Applied Energy 166: 1-18.
4. Aggidis, G. A., and D. S. Benzon. (2013) "Operational Optimisation of a Tidal Barrage across the Mersey Estuary Using 0-D Modelling." Ocean Engineering 66, 69-81.
5. Zidonis, A., D. Benzon, Aggidis, G. A., (2015). "Development of hydro impulse turbines and new opportunities." Renewable and Sustainable Energy Reviews 51(RSER4610): 1624–1635.

List of Conference Publications

1. Benzon, D.S., Aggidis, G.A.,(2013) CFD Analysis of Turgo Impulse Turbines, Lancaster University Renewable Energy Group Seminar. 30th January 2013.
2. Benzon, D. S., G. A. Aggidis, J. Martin, J. Scott, and A. Watson., (2013) "State of the Art & Current Research on Turgo Impulse Turbines." In 13th Annual Africa Utility Week/ Clean Power Africa, edited by ESI Africa. Cape Town, 2013.
3. Benzon, D.S., Aggidis, G.A. (2013). CFD Analysis of Turgo Turbines, Lancaster University Engineering Research Review Conference. 2-3 July 2013.
4. Benzon, D.S., Aggidis, G.A., (2013) CFD Analysis and Optimisation of Nozzles for Impulse Turbines, Lancaster University Renewable Energy Group Seminar. 21 November 2013.
5. Benzon, D. S., (2014) "Using CFD in the Analysis of Impulse Turbines with a Focus on the High Capacity Turgo." In 14th Annual Africa Utility Week/ Clean Power Africa, edited by ESI Africa. Cape Town, 2014.
6. Benzon, D.S., Aggidis, G.A. (2014). CFD Analysis of Turgo Turbines, Lancaster University Engineering Research Review Conference. 1-2 July 2014.

7. Benzon, D.S., Aggidis, G.A., (2014) Turgo Impulse Turbine CFD, Lancaster University Renewable Energy Group Seminar. 17th December 2014.
8. Benzon, D.S., Aggidis, G.A. (2015). CFD Analysis of Turgo Turbines, Lancaster University Engineering Research Review Conference. 30-31 June 2015.

Contribution to knowledge

Impulse turbine injectors- The numerical optimisation of impulse turbine injectors carried out during the course of this research presents for the first time the effects that the basic injector design parameters have on the hydraulic performance for a wide range of operating conditions. Much steeper nozzle and spear angles than previous literature and design guidelines suggest are shown to be more efficient numerically and experimentally for both Pelton and Turgo turbines.

Turgo impulse turbines- Although studies have recently started to utilise CFD in the analysis and optimisation of Turgo turbines, no numerical models have been able to successfully and accurately model the flow through a single blade passage calculating the torque on both the inside and outside surfaces of the blades. This research develops such a model which is verified by experimental testing. The model is also used to investigate and present for the first time the primary design parameters of the Turgo runner and their impact on the runner performance.

Table of Contents

Declaration	i
Abstract	ii
Keywords	iv
Dedication	v
Acknowledgements	vi
List of Journal Publications.....	vii
List of Conference Publications.....	vii
Contribution to knowledge.....	viii
List of Figures	xiv
List of Tables	xxiii
Nomenclature	xxiv
Mathematical Notation.....	xxvi
List of Acronyms	xxvii
1 Introduction.....	1
1.1 Renewable Energy	1
1.2 Hydropower	1
1.3 Impulse turbines.....	2
1.4 Turgo Turbines.....	2
1.5 Computational Fluid Dynamics	5
1.6 Aims and objectives	6
1.7 Thesis Structure.....	7
2 Background	9
2.1 Invention and early development	9
2.2 Further Development	11
2.2.1 Gilkes research and development.....	11
2.2.2 Independent research and development	15
2.3 Recent development and applications.....	17
2.3.1 Pico and Micro-Turgo turbines	19

2.3.2	Small-Medium scale Turgo turbines	24
2.4	Impulse turbine injector research.....	31
2.5	Scope for even further development	35
2.5.1	Runner analysis	35
2.5.2	Injector analysis	35
3	Turgo runner analysis.....	38
3.1	CFD model assumptions	38
3.1.1	Geometric assumptions	39
3.1.2	Modelling assumptions	45
3.2	Simulation setup and analysis.....	47
3.2.1	Domain creation.....	47
3.2.2	Operating conditions	50
3.2.3	Meshing.....	50
3.2.4	Physics definition.....	53
3.2.5	Solver definition.....	59
3.2.6	Results processing.....	61
3.2.7	Simulation Sequence.....	62
3.3	Mesh refinement study.....	65
3.4	Summary of Turgo runner CFD modelling.....	68
4	Turgo runner optimisation	69
4.1	Geometry parameterisation	69
4.1.1	Parameterised Geometry Verification.....	72
4.2	Phase 1: Initial design changes	75
4.2.1	Leading edge profile and inlet angles	75
4.2.2	Jet offset and radial position DOE study (DOE1).....	84
4.2.3	Trailing edge width	89
4.2.4	Spherical blade shape.....	92
4.2.5	Blade number study	95
4.2.6	Blade thickness	97

4.3	Phase 2: Blade shape DOE study (DOE2)	100
4.3.1	DOE Study Setup.....	100
4.3.2	DOE Study Results	104
4.4	Phase 3: Additional Parameters	117
4.4.1	Outside surface exit angles.....	117
4.4.2	Jet inclination angle	121
4.5	Runner optimisation summary	122
5	Turgo runner Finite Element Analysis (FEA).....	125
5.1	$\frac{1}{4}$ Runner FEA	125
5.1.1	Mesh refinement study	125
5.1.2	Runaway speed	127
5.1.3	Jet loading	128
5.1.4	Strengthening the runner.....	130
5.2	DFMA- Leading edge width.....	133
5.2.1	1/4 Runner FEA and CFD.....	133
5.2.2	1/3 Runner FEA	134
5.2.3	Full Runner FEA.....	136
5.3	Final runner design comparison	140
6	Injector design optimisation and further analysis	141
6.1	2D generic injector optimisation using CFD	141
6.1.1	Design analysis and modelling.....	141
6.1.2	Design of Experiments (DOE) study	145
6.1.3	Further investigation	150
6.1.4	Spear tip curvature	150
6.1.5	Injector scaling.....	152
6.2	HCTI Injector design study.....	153
6.2.1	2D Straight pipe study.....	153
6.2.2	3D Straight pipe study.....	156
6.2.3	3D Full injector study	158

6.2.4	2D/3D Injector study comparison	168
7	Turgo runner experimental testing	173
7.1	Runner manufacturing.....	173
7.2	Turgo test rig.....	175
7.3	Sensors and instrumentation	177
7.4	Characteristic equations	178
7.5	Establishing the uncertainty	179
7.5.1	Systematic Uncertainty	179
7.5.2	Random and Reproducibility Uncertainty.....	179
7.5.3	Total uncertainty	181
7.6	Test plan and procedure	181
7.7	HCTI runner test results.....	182
7.8	LE4 runner test results	184
7.9	LE1 runner test results	185
7.10	Results comparison and discussion.....	186
8	Injector experimental testing.....	188
8.1	Pelton injector testing.....	188
8.1.1	Pelton test rig	189
8.1.2	Injector test plan.....	191
8.1.3	Flow curve comparison.....	192
8.1.4	Results comparison and discussion.....	193
8.2	Turgo injector testing	196
8.2.1	Injector test plan.....	196
8.2.2	Flow curve comparison.....	197
8.2.3	Results comparison and discussion	198
9	CFD model verification	205
9.1	Estimating the mechanical losses.....	205
9.1.1	Disk friction torque, M_d	206
9.1.2	Bearing friction torque, M_b	206

9.1.3	Mechanical friction torque, M_m	211
9.2	Turgo full system modelling	212
9.3	Turgo Injector modelling	216
9.3.1	Full injector and runner simulations	216
9.4	Turgo runner modelling	220
10	Conclusions.....	222
10.1	Summary	222
10.1.1	Turgo runner	222
10.1.2	Impulse turbine injectors.....	224
10.1.3	Turgo full system model verification	226
11	Recommendations for future work.....	227
11.1	Turgo runner optimisation	227
11.2	Injector optimisation	227
11.3	Casing design	227
11.4	Manufacturing methods	228
11.5	Customised designs.....	228
References.....		229
Appendices.....		234
Appendix A:	Runner mesh replay control	234
Appendix B:	CFX Command Language (CCL) for run	240

List of Figures

Fig. 1.1 Typical application range for impulse and reaction turbines (Gilbert Gilkes & Gordon Ltd. 2016).....	2
Fig. 1.2.Typical configuration of a twin jet Turgo turbine (plan view) (Gilbert Gilkes & Gordon Ltd. 2016)	3
Fig. 1.3. Design of a typical Turgo runner: front - inlet side (left); back -outlet side (right) (Gilbert Gilkes & Gordon Ltd. 2016)	3
Fig. 1.4. Typical single-jet Turgo turbine installation, with inlet pipe under the powerhouse (Gilbert Gilkes & Gordon Ltd. 2016)	4
Fig. 1.5. Turgo impulse turbine and injector research work flow chart.....	8
Fig. 2.1. Axial flow Girard turbine (Gibson 1908)	9
Fig. 2.2. Pelton and Turgo jet positioning showing inclined nature of Turgo jet (Wilson 1967)	10
Fig. 2.3. Test results from 1920 Crewdson Turgo design carried out at Afon Caletwr (Crewdson 1922).....	11
Fig. 2.4. The 1936 modified Turgo design, showing the shifted point of impact between the jet and the runner	12
Fig. 2.5. Efficiency and output for a 24in mean diameter Turgo under a head of 750ft (Wilson 1967)	13
Fig 2.6. Variations of maximum normal working and overspeed stresses with head, for all geometrically similar sized cast steel HCTI turbines, where overspeed is 1.5x normal working speed	14
Fig 2.7. Suggested strength improvement to Turgo rim (left) and comparison between theoretical stress distribution on inlet and outlet edges for both designs (right).....	15
Fig. 2.8. Experimental absolute velocities at the outlet of the Turgo runner in feet/second (Webster 1973).....	17
Fig. 2.9. Turgo turbine blades for micro hydropower (Hartvigsen Hydro 2015).....	18
Fig. 2.10. Flow simulation in Turgo runners using CFD tools: left, and right (Anagnostopoulos 2011)	18
Fig. 2.11. Indicative blades of a model Turgo turbine with optimized shape (Anagnostopoulos 2011)	19
Fig. 2.12. Turgo turbine efficiency vs. speed ratio for three radial jet positions (Cobb and Sharp 2013).....	20
Fig. 2.13. Turgo turbine laboratory tests : Model turbine set up (left), and jet-runner interaction (right – cups are marked by dotted lines) (Williamson, Stark et al. 2013)	21

Fig. 2.14. Comparison of the commercially available (black) and the redesigned (white) Turgo runner (Williamson, Stark et al. 2013).....	21
Fig. 2.15. Turgo runner picture and dimensions in the experiments of Khurana et al. (Khurana, Kumar et al. 2012; Khurana, Varun et al. 2013).....	22
Fig. 2.16. Turgo runner made of tablespoons (left) and its operation (right) (Gaiser, Erickson et al. 2016)	23
Fig. 2.17. Section view of the turbine enclosure (left), and bucket shape (right) [24].....	24
Fig. 2.18. Parametric design of Turgo runner (left) and flow modelling snapshots (right), (Anagnostopoulos and Papantonis 2007).....	25
Fig. 2.19. Indicative particle trajectories generated by the Lagrangian solver (Anagnostopoulos and Papantonis 2007).....	25
Fig. 2.20. Manufacture of the model Turgo runner (left) and installation in the Lab (right), (Koukouvinis, Anagnostopoulos et al. 2010).....	26
Fig. 2.21. Comparison between experimental and FLS numerical model results for various spear valve openings, α (Koukouvinis, Anagnostopoulos et al. 2010)	26
Fig. 2.22. Pressure coefficient distribution on the inner surface of a static blade obtained by SPH (left), and Fluent®-VOF (right) (Koukouvinis, Anagnostopoulos et al. 2010)	27
Fig. 2.23. Jet-runner set up (Koukouvinis, Anagnostopoulos et al. 2011).....	28
Fig. 2.24. Flow comparison between SPH and ANSYS® Fluent® results (Koukouvinis, Anagnostopoulos et al. 2011).....	28
Fig. 2.25. Comparison of SPH and ANSYS® Fluent® results for the Torque curve developed on a blade, zero angle refers to vertical blade position (Koukouvinis, Anagnostopoulos et al. 2011).	28
Fig. 2.26. Turgo blade and runner created by the analytic approximation method of (Correa, Andrade et al. 2012).....	29
Fig. 2.27. Flow streamlines in the Turgo runner as computed by Correa et al (Correa, Andrade et al. 2012)	30
Fig. 2.28. HPP Rabiusa-Realta: CFD simulation of the secondary flows in the jet (Staubli T., Abgottspion A. et al. 2009)	32
Fig. 2.29. Comparison of axial velocity profiles in five sections normal to the jet ideal axis x (Santolin, Cavazzini et al. 2009)	33
Fig. 2.30. Pelton turbine efficiency experimental and numerical comparisons (Jošt, Mežnar et al. 2010)	34
Fig. 2.31. Experimental (left) and numerical (right) jet shape comparison with a 90° inlet elbow (Fiereder, Riemann et al. 2010).....	34
Fig. 3.1. Periodic fluid region around a single blade	40
Fig. 3.2. Cut plane through the middle of the periodic mesh showing inflation and sizing....	40

Fig. 3.3. 7 Blade Periodicity study showing torque curves on the inside and outside of each blade.....	42
Fig. 3.4. Normalised power calculated from torque curves for each blade passage	42
Fig. 3.5. Absolute velocity contours on the axial plane in the centre of the jet for comparison between blade passages 1-2, 4-5 and 6-7	43
Fig. 3.6. Torque curve comparison for periodic blade passages 3-4, 4-5 and the 2 blade simulation.....	44
Fig. 3.7. Gilkes 7.5" HCTI runner CAD used for numerical modelling.....	48
Fig. 3.8. Runner simulation domain geometries created in Solidworks	49
Fig. 3.9. Stationary domain mesh showing structured hexahedral elements combined with tetrahedral elements	51
Fig. 3.10. Rotating domain- surface mesh detail	52
Fig. 3.11. Slice through centre of runner mesh showing mesh density regions and inflation layers	53
Fig. 3.12. Radial view of stationary and rotating domains in CFX Pre	53
Fig. 3.13. Torque curves comparison for varying timestep	59
Fig. 3.14. Torque curves comparison HCTI runner simulations with varied residual targets .	60
Fig. 3.15. Summing torques on inside and outside blade surfaces to give total torque	61
Fig. 3.16. Phase 1: Jet initialisation, showing surface of jet using an isosurface with Water Volume Fraction=0.5	63
Fig. 3.17. Phase 2: Runner rotation- showing surface of jet using an isosurface with Water Volume Fraction=0.5	64
Fig. 3.18. Mesh refinement study results: normalised efficiency against normalised grid spacing	65
Fig. 3.19. Mesh refinement study- torque curves.....	67
Fig. 4.1. HCTI Geometry provided by industrial sponsors.....	70
Fig. 4.2. Planes used to split blade into 5x6 Grid	71
Fig. 4.3. Blade surface control curves for the inside (left) and outside (right) blade surfaces.	71
Fig. 4.4. Comparison between original (red) and parameterised (grey) geometry	72
Fig. 4.5. Parameterised geometry torque curves compared to original at same operating point	73
Fig. 4.6. Pressure contours on the inside of the first blade at 60° rotation- Original (left) P000 (right)	74
Fig. 4.7. Pressure contours on the outside of the first blade at 60° rotation- Original (left) P000 (right)	74
Fig. 4.8. Peripheral flow leaving inside surface of ring	75
Fig. 4.9. Analysis of the velocity components at the inlet to a Turgo turbine	76

Fig. 4.10. Radial velocity distribution against angular position.....	78
Fig. 4.11. Relative velocity inlet angle on axial plane against angular position for all LE control points	79
Fig. 4.12. Relative velocity inlet angle on axial plane against angular position for LE control points passing through the ellipse	79
Fig. 4.13. Relative velocity inlet angle on meridional plane against angular position for all LE control points	80
Fig. 4.14. Relative velocity inlet angle on meridional plane against angular position for LE control points passing through the ellipse.....	80
Fig. 4.15. Absolute velocity distribution against angular position	81
Fig. 4.16. Relative velocity angles at jet centreline for LE control points.....	82
Fig. 4.17. LE1- LE profile modified to match blade shape.....	83
Fig. 4.18. LE profile modified to match inlet angles at peak absolute velocity with two additional control planes	83
Fig. 4.19. Phase 1: Initial design changes- LE profile and inlet angles- normalised efficiency	84
Fig. 4.20. Graph columns for initial runs.....	85
Fig. 4.21. Normalised efficiency contour for the Jet Offset against the height.....	86
Fig. 4.22. Predicted surface results against actual results	87
Fig. 4.23. Torque curve comparison for original and optimised design in Jet Offset and Radial Position DOE	88
Fig. 4.24. TE width study normalised efficiencies.....	89
Fig. 4.25. TE width study- Torque curves	90
Fig. 4.26. Flow comparison between original 7mm TE width and the optimised 11mm TE width designs at 63.81deg	91
Fig. 4.27. Pressure on the inside surface of the blades-comparison between original 7mm TE width and the optimised 11mm TE width designs at 63.81deg	91
Fig. 4.28. Flow paths and suggested circular outlet rim (Webster 1973)	92
Fig. 4.29. Circle used to modify trailing edge and create a more spherical blade	93
Fig. 4.30. Original (red) and spherical (grey) blade shapes	93
Fig. 4.31. Spherical blade study torque curves	94
Fig. 4.32. Pressure on outside of blade corresponding to negative torque region	94
Fig. 4.33. Blade number study efficiency results.....	95
Fig. 4.34. Blade number study- Normalised torque/blade number curves.....	96
Fig. 4.35. Pressure contours on outside blade surface at 83.45° 22 blades (left) and 24 blades (right)	97

Fig. 4.36. Blade thickness variation for one cross section leaving leading and trailing edges unchanged	98
Fig. 4.37. Blade thickness study- initial runs	99
Fig. 4.38. Blade thickness study- further runs	99
Fig. 4.39. DOE2 Parameters, left to right, DF, WF and EAF	100
Fig. 4.40. Variation of DOE2 parameter blade width W	101
Fig. 4.41. Variation of DOE2 parameter blade depth D	102
Fig. 4.42. Graph columns for <i>Depth Factor (DF)</i> against <i>Exit Angles Factor (EAF)</i>	103
Fig. 4.43. Graph columns for <i>Width Factor (WF)</i> against <i>Exit Angles Factor (EAF)</i>	103
Fig. 4.44. Graph columns for <i>Depth Factor (DF)</i> against <i>Width Factor (WF)</i>	104
Fig. 4.45. Torque curves for runs 3 and 2 where the DF=1.05 and WF=0.9 and the EAF is varied.....	106
Fig. 4.46. Torque curves for runs 10 and 9 where the DF=0.9 and WF=1.2 and the EAF is varied.....	106
Fig. 4.47. Torque curves for runs 2, 8 and 17 where the EAF=0.9 and WF=0.9 and the DF is varied.....	107
Fig. 4.48. Torque curves for runs 11 and 10 where the EAF=0.7 and DF=0.9 and the WF is varied.....	108
Fig. 4.49. Predicted vs. Actual DOE results	109
Fig. 4.50. Interaction between Width Factor (WF) and Exit Angles Factor (EAF)	109
Fig. 4.51. Interaction between Depth Factor (DF) and Exit Angles Factor (EAF)	110
Fig. 4.52. Interaction between Width Factor (WF) and Depth Factor (DF).....	110
Fig. 4.53. DF/EAF contours for a WF of 0.9	111
Fig. 4.54. DF/EAF contours for a WF of 1.05	111
Fig. 4.55. DF/EAF contours for a WF of 1.2	112
Fig. 4.56. WF/EAF contours for a DF of 0.90	112
Fig. 4.57. WF/EAF contours for a DF of 1.05	113
Fig. 4.58. WF/EAF contours for a DF of 1.2	113
Fig. 4.59. WF/DF contours for an EAF of 0.7	114
Fig. 4.60. . WF/DF contours for an EAF of 0.9	114
Fig. 4.61. . WF/DF contours for an EAF of 1.1	115
Fig. 4.62. Modified HCTI geometry shown in blue over original HCTI geometry in red- cut section at jet pitch circle radius.....	115
Fig. 4.63. Comparison between P036 design (optimum from TE width study) and DOE2.22 (the DOE2 study optimum design) normalised torque curves	116
Fig. 4.64. Outside surface exit angles (OEAF) study- results.....	117
Fig. 4.65. Normalised torque curves for OEAF 0.1-0.5.....	118

Fig. 4.66. Normalised torque curves for OEA0 0.5-1.2.....	119
Fig. 4.67. Jet inclination angle study results	122
Fig. 4.68. Turgo numerical runner optimisation summary showing <i>coarse mesh</i> and <i>fine mesh</i> results	123
Fig. 4.69. Normalised torque curve comparison between the original HCTI Turgo runner and the optimised Turgo runner designs using the <i>fine mesh</i>	124
Fig. 4.70. Absolute velocity contours on axial plane through centre of jet for the original HCTI Turgo runner (left) and the optimised runner (right) plotted at the peak inside torque position.....	124
Fig. 5.1. Quarter runner mesh (~130k elements), ANSYS® Mechanical, showing refinement on blade edges.....	126
Fig. 5.2. Quarter Runner FEA Setup showing cylindrical and frictionless supports	126
Fig. 5.3. 1/4 runner FEA mesh refinement study for the original 7.5" HCTI runner at 150m head runaway speed	127
Fig. 5.4. Equivalent (von-Mises) Stress plot for the original and optimised Turgo geometries at runaway speed of 4988rpm	127
Fig. 5.5. Jet loading applied to area cut out by jet diameter at maximum flow	128
Fig. 5.6. Jet loading in normal operation at 150m head and max flow (111 l/s).....	129
Fig. 5.7. Jet loading in locked operation at 150m head and max flow (111 l/s)	129
Fig. 5.8. Stress contour comparison between original HCTI runner and strengthened HCTI-opt2 runner designs for runaway speed, normal operation and locked operation.....	132
Fig. 5.9. Maximum stresses and normalised efficiencies for the original (HCTI), optimised (HCTI-opt1) and optimised and strengthened (HCTI-opt2) runners	132
Fig. 5.10. DFMA LE width study FEA (1/4 runner) and CFD results.....	134
Fig. 5.11. DFMA LE width study FEA (1/4 and 1/3 runner) and CFD results.....	135
Fig. 5.12. Full runner FEA Mesh study for the original 7.5" HCTI runner at 150m head runaway speed.....	136
Fig. 5.13. Mesh independent full runner mesh- 2.1M elements- Inlet view	137
Fig. 5.14. Mesh independent full runner mesh- 2.1M elements- Outlet view	137
Fig. 5.15. Full HCTI-Orig runner FEA at Runaway speed showing stress concentrations ...	138
Fig. 5.16. Full HCTI-Orig runner FEA under normal operation showing stress concentrations	138
Fig. 5.17. Full HCTI-Orig runner FEA under locked operation showing stress concentrations	139
Fig. 5.18. Comparison between stresses under runaway speed, normal operation and locked operation using the full runner, 1/3 runner and 1/4 runner sections for the original HCTI runner	139

Fig. 5.19. Full runner FEA design comparison	140
Fig. 6.1. 2D injector geometry showing fixed and variable operational and geometric parameters	142
Fig. 6.2. Mesh refinement study- 2D injector losses at $2D_n$	144
Fig. 6.3. Injector Losses vs. Spear Travel (Expressed as Flow Rate)-left and Injector Losses vs. Pressure Head- right	146
Fig. 6.4. Injector Losses vs. Spear Width-left and Flow Rate vs. Spear Travel-right.....	146
Fig. 6.5. Injector Loss contours for Nozzle and Spear Angles at $Q = 10 \text{ kg/s}$ (left) and 20kg/s (right).	147
Fig. 6.6. Injector Loss contours for Nozzle and Spear Angles at $Q= 30 \text{ kg/s}$ (left) and 40kg/s (right).	147
Fig. 6.7. Comparison between the initial and optimised injector geometries using CFD results at 5 different openings.....	148
Fig. 6.8. Comparison between the original 90-50 and optimised 110-70 nozzles with the same maximum flow rate	149
Fig. 6.9. Jet velocity profile comparison for original 90-50 nozzle and spear design and the optimised 110-70 design	149
Fig. 6.10. Velocity field comparison for (a) small and (b) large nozzle and spear angles	150
Fig. 6.11. Velocity magnitude contours for spear curvatures A-D	151
Fig. 6.12. Injector losses for spear curvatures A-D.....	151
Fig. 6.13. Impact of scaling on injector losses	152
Fig. 6.14. Spear travel ratio against flow rate for 2D J608 $D_n=78\text{mm}$ and $D_n=65\text{mm}$ injectors-comparison with experimental results.....	154
Fig. 6.15. Spear travel ratio [Ts]/nozzle diameter [Dn] against flow rate for the original J608 and the modified $D_n=65\text{mm}$ injectors with polynomial fit curves	154
Fig. 6.16. Flow rate against losses for the original HCTI-d78 and the modified and scaled HCTI-d78mod-scaled, $D_n=78\text{mm}$ injectors	155
Fig. 6.17. Flow rate against losses for the original HCTI-d65 and the modified and scaled HCTI-d65mod-scaled, $D_n=65\text{mm}$ injectors	155
Fig. 6.18. HCTI-d65 injector mesh	156
Fig. 6.19. HCTI-d65 injector mesh- detail view	156
Fig. 6.20. HCTI-d65 injector mesh- detail view after mesh adaption with Node Factor 2....	157
Fig. 6.21. 3D Straight pipe efficiency at planes 1D, 2D, 3D and with and without active mesh adaption (NF2)	158
Fig. 6.22. Full 3D injector domain geometry.....	159
Fig. 6.23. 3D mesh for complete HCTI-d65 injector geometry	159
Fig. 6.24. 3D mesh for complete HCTI-d65 injector geometry- spear and nozzle view	160

Fig. 6.25. 3D mesh for complete HCTI-d65 injector geometry- detailed view of restriction	160
Fig. 6.26. HCTI-d65 3D injector simulation showing the planes used in the analysis	161
Fig. 6.27. Full 3D Injector losses measured at 2 diameters from the nozzle	162
Fig. 6.28. Velocity contours on the symmetry plane for the full 3D injectors.....	163
Fig. 6.29. Pressure contours on the symmetry plane for the full 3D injectors	164
Fig. 6.30. Secondary velocities for the two injectors from P1-Outlet.....	166
Fig. 6.31. Maximum and average secondary velocities at 2D for each injector design.....	167
Fig. 6.32. HCTI-d65 and HCTI-d65mod injector losses for 2D Straight Pipe, 3D Straight Pipe and 3D Full injector studies	169
Fig. 6.33. 2D straight pipe injector study- velocity profile comparison at $2D_n$	170
Fig. 6.34. 3D straight pipe injector study- velocity profile comparison at $2D_n$	171
Fig. 6.35. 3D Full injector study- Vertical velocity profile comparison at $2D_n$	171
Fig. 6.36. 3D Full injector study- Horizontal velocity profile comparison at $2D_n$	172
Fig. 7.1. Dressed 9" HCTI design (left) and optimised LE4 design (right)- inlet side	174
Fig. 7.2. Dressed 9" HCTI design (left) and optimised LE4 design (right)- outlet side	174
Fig. 7.3. Optimised LE1 design showing dressed leading edges	175
Fig. 7.4. 3D CAD model of new 9" Turgo test rig.....	176
Fig. 7.5. New Gilkes 9" Turgo test rig, Laboratory for Hydraulic Machines, NTUA	176
Fig. 7.6. Schematic of Turgo test rig showing location of pressure, torque and speed sensors	177
Fig. 7.7. Turgo runner test plan.....	182
Fig. 7.8. 9" HCTI runner, single jet operation	183
Fig. 7.9. 9" HCTI runner, twin jet operation.....	183
Fig. 7.10. 9" LE4 runner, single jet operation.....	184
Fig. 7.11. 9" LE4 runner, twin jet operation	184
Fig. 7.12. 9" LE1 runner, single jet operation.....	185
Fig. 7.13. 9" LE1 runner, twin jet operation	185
Fig. 7.14. 9" HCTI, LE4 and LE1 runner normalised efficiency comparison for $n_{11}=42$ - single jet	187
Fig. 7.15. 9" HCTI, LE4 and LE1 runner normalised efficiency comparison for $n_{11}=42$ - twin jet	187
Fig. 8.1. Pelton spears used for experimental tests	188
Fig. 8.2. Pelton nozzles used for experimental testing.....	189
Fig. 8.3. Gilkes twin jet Pelton test rig in operation at NTUA.....	190
Fig. 8.4. Pelton injector test plan	192
Fig. 8.5. Pelton injector flow curves comparison.....	193

Fig. 8.6. Pelton normalised efficiency curves for Standard (80/55) and Novel (110/70) injectors at $n_{11}=37\text{rpm}$	194
Fig. 8.7. Pelton normalised efficiency curves for Standard (80/55) and Novel (110/70) injectors at $n_{11}=39\text{rpm}$	194
Fig. 8.8. Pelton normalised efficiency curves for Standard (80/55) and Novel (110/70) injectors at $n_{11}=41\text{rpm}$	195
Fig. 8.9. Pelton normalised efficiency curves for Standard (80/55) and Novel (110/70) injectors at $n_{11}=43\text{rpm}$	195
Fig. 8.10. Turgo injector test plan	197
Fig. 8.11. Flow curve comparison for the Standard (80/55) and Novel (110/70) injectors ...	198
Fig. 8.12. Single jet operation for $Q_{11}=0.03\text{-}0.07\text{m}^3/\text{s}$ at $n_{11}=42\text{rpm}$	199
Fig. 8.13. Single jet operation for $Q_{11}=0.11\text{-}0.25\text{m}^3/\text{s}$ at $n_{11}=42 \text{ rpm}$	200
Fig. 8.14. Single jet operation at $Q_{11}=0.03\text{m}^3/\text{s}$	201
Fig. 8.15. Twin jet operation at $Q_{11}=0.03\text{m}^3/\text{s}$	202
Fig. 8.16. Turgo injector efficiency comparison at $n_{11}=42\text{rpm}$ - single jet.....	203
Fig. 8.17. Turgo injector efficiency comparison at $n_{11}=42\text{rpm}$ - twin jet	203
Fig. 8.18. Single jet operation at $Q_{11}= 0.19 \text{ m}^3/\text{s}$	204
Fig.8.19. Twin jet operation at $Q_{11}= 0.19 \text{ m}^3/\text{s}$	204
Fig. 9.1. Torque measurements taken at $Q=0\text{m}^3/\text{s}$, with and without runner at varying speeds	206
Fig. 9.2. Turgo test rig bearing arrangement.....	207
Fig. 9.3. Bending moment diagram for showing radial loading on bearings	208
Fig. 9.4. SKF Bearing Calculator, showing input values for BEP operation at 30°C	210
Fig 9.5. Variation in Friction torque with temperature for each bearing	210
Fig. 9.6. Turgo turbine test rig, showing regions of analysis.....	212
Fig. 9.7. Loss features (1-4) and straight pipe sections ($l1-l3$) in region 1	213
Fig. 9.8. Torque curves for Turgo runner using ideal jet and real jet profiles at the inlet.....	217
Fig. 9.9. 7.5" HCTI Runner efficiencies using real jet profiles	218
Fig. 9.10. Numerical and experimental total efficiency comparison for original (d65) and optimised (d65-mod-scaled) injectors, normalised against the numerical efficiency of the 'Real jet-d65' runner simulation ($\eta r3$).	219
Fig. 9.11. Numerically obtained normalised torque curves for the original HCTI and optimised LE4 and LE1 runner designs at the BEP.....	221

List of Tables

Table 2.1 –Summary of research carried out on Turgo turbines and injectors by research area	37
*See reference number index above	37
Table 3.1- Named selections used on stationary and rotating domain boundaries	49
Table 3.2- 7.5” Turgo BEP operating conditions used in runner analysis	50
Table 3.3- ANSYS® material properties for air and water at 15°C	55
Table 3.4. Runner simulation stationary and rotating domain boundary conditions	57
Table 3.5- Average torque and efficiencies for varied timesteps.....	58
Table 3.6- Mesh refinement study results- normalised to coarsest mesh.....	65
Table 3.7- Mesh refinement study: Grid Convergence Indexes.....	66
Table 3.8- 2 bladed mesh study solve times	67
Table 3.9- Relative numerical uncertainties for the coarse and fine mesh runner simulations	68
Table 4.1- Phase 1: Initial design changes descriptions.....	83
Table 4.2- DOE initial study design details	85
Table 4.3- Jet Offset and radial position DOE results	86
Table 4.4- DOE2 initial study design details	102
Table 4.5- Blade shape and exit angles DOE study results- normalised against previous optimum	105
Table 4.6- Phase 3: Outside exit angles geometry and results table	120
Table 4.7- Jet inclination angle study results table	121
Table 5.1- DFMA LE width ¼ runner FEA results	133
Table 6.1- Boundary conditions for injector simulations.....	143
Table 7.1- details of the sensors used for the generation of the turbine hill charts	178
Table 7.2- Systematic error of each instrument	179
Table 7.3- Control points, normalised to η , used to determine standard deviation, s_η	180
Table 8.1- Systematic error of each instrument	191
Table 8.2- Pelton injectors- geometric details.....	192
Table 8.3-Turgo injector main dimensions	196
Table 9.1- Bearing forces for single and twin jet operation.....	209
Table 9.2- Bearing friction torques and losses using SKF bearing calculator	211
Table 9.3. Head loss from loss features	214

Nomenclature

a	Acceleration	[m/s ²]
A_i	Cell area cross section	[m ²]
Φ	Centre line	[$-$]
d	Jet diameter	[mm]
D	Runner pitch circle diameter	[mm]
D	Blade depth	[mm]
D_n	Nozzle opening diameter	[mm]
E_k	Kinetic energy	[J]
E_p	Potential energy	[J]
F	Force	[N]
$F_{a(Nj)}$	Axial force acting on runner	[N]
F_{Bna}	Axial force acting on bearing	[N]
F_{Bnr}	Radial force acting on bearing	[N]
\vec{F}_j	Jet loading force vector	[N]
F_m	Radial force acting on runner from runner mass	[N]
$F_{r(Nj)}$	Radial force acting on runner from jet loading	[N]
F_R	Total radial force acting on runner	[N]
g	Acceleration due to gravity	[m/s ²]
G	Injector opening diameter	[mm]
H	Pressure head	[m]
H	Blade radial height	[mm]
h_l	Individual head loss for hydraulic component	[m]
h_s	Static enthalpy	[m ² /s ²]
h_{tot}	Total enthalpy	[m ² /s ²]
H_v	Jet intersection point radial height	[mm]
k	Turbulence Kinetic Energy	[m ² /s ²]
k	Injector scaling factor	[$-$]
K	Loss factor	[$-$]
I	Turbulence intensity	[$\%$]
m	Mass	[kg]
\dot{m}	Mass flow rate	[kg/s]
m_r	Runner mass	[kg]
M	Torque	[Nm]
M_b	Bearing friction torque	[Nm]
M_d	Disk friction torque	[Nm]
M_f	Friction torque of full runner in rotation	[Nm]
M_j	Torque induced by a single jet	[Nm]
M_m	Mechanical friction torque	[Nm]
M_s	Friction torque of only shaft in rotation	[Nm]
M_t	Measured torque	[Nm]
n	Rotational speed	[rpm]
n_{11}	Unit speed	[rpm]
N	Power	[J]
N_B	Number of blades	[$-$]
N_j	Number of jets	[$-$]
p	Pressure	[Pa]

p_c	Order of convergence	[-]
p_i	Static pressure at individual mesh cell	[Pa]
P_{in}	Power in	[W]
P_{out}	Power out	[W]
Q	Flow rate	[m ³ /s]
Q'	Flow rate for reference nozzle diameter	[m ³ /s]
Q_{11}	Unit flow rate based on pitch circle diameter, D	[m ³ /s]
Q_{11k}	Unit flow rate based on bucket width, B	[m ³ /s]
r	Refinement Ratio	[-]
r	Inlet plane grid point radius	[-]
R	Residual	[-]
R_1	Jet ellipse semi axis vertical radius	[m]
R_2	Jet ellipse semi axis horizontal radius	[m]
Re	Reynold's number	[-]
s_r	Random uncertainty at 95% confidence (Student's T distribution)	[-]
s_γ	Random uncertainty standard deviation	[-]
S_e	Energy Source	[kg/m ² .s ²]
S_f	Safety Factor	[-]
S_m	Momentum Source	[kg/m ² .s ²]
t	Time for 1 revolution	[s]
t	Student's T factor	[-]
T_s	Spear travel	[mm]
\bar{u}	Ideal jet velocity	[m/s]
\vec{u}	Velocity vector	[m/s]
u_i	Velocity of fluid at individual mesh cell	[m/s]
v	Jet velocity	[m/s]
\vec{v}	Jet velocity vector	[m/s]
v_c	Absolute velocity component on tangential plane	[m/s]
v_r	Meridional absolute velocity component	[m/s]
v_{ru}	Radial absolute velocity component	[m/s]
v_u	Tangential absolute velocity component	[m/s]
v_z	Axial absolute velocity component	[m/s]
W	Work	[J]
W	Blade width	[mm]
w_u	Tangential relative velocity component	[m/s]
$Y+$	Dimensionless wall distance	[-]
α	Jet inclination angle	[deg]
α_1	Absolute velocity inlet angle on tangential plane	[deg]
γ	Inlet plane grid point angular position	[deg]
β_1	Relative velocity inlet angle on tangential plane	[deg]
β_{r1}	Relative velocity inlet angle on radial plane	[deg]
δ	Percentage error	[%]
δ_M	Torque meter systematic error	[%]
δ_n	Speed sensor systematic error	[%]
δ_p	Pressure transducer systematic error	[%]
δ_Q	Flow meter systematic error	[%]
δ_r	Total random uncertainty in efficiency η	[%]
δ_s	Total systematic uncertainty in efficiency η	[%]
δ_t	Total uncertainty in efficiency η	[%]

ε	Turbulence eddy dissipation rate	[m ² /s ³]
η	Efficiency	[%]
η_{eh}	Total experimental hydraulic efficiency	[%]
$\eta_{h=0}$	Efficiency at zero grid spacing	[%]
η_m	Mechanical efficiency	[%]
η_{nh}	Total numerical hydraulic efficiency	[%]
η_{r1}	Numerical hydraulic efficiency, region 1	[%]
η_{r2}	Numerical hydraulic efficiency, region 2	[%]
η_{r3}	Numerical hydraulic efficiency, region 3	[%]
θ	Rotated angle	[deg]
μ	Dynamic viscosity	[Pa.s]
ρ	Density	[kg/m ³]
τ	Stress	[Pa]
φ	Jet offset	[mm]
ω	Rotational frequency	[rad/s]
ω	Turbulence eddy frequency	[s ⁻¹]

Mathematical Notation

∇	Del operator
$(\cdot)^T$	Matrix transposition
δ	Identity matrix

List of Acronyms

BEP	Best Efficiency Point
CAD	Computer Aided Design
CEL	CFX Expression Language
CFD	Computational Fluid Dynamics
CPU	Central Processing Unit
DES	Detached Eddy Simulation
DF	Depth Factor
DFMA	Design for Manufacture and Assembly
DNS	Direct Numerical Simulation
DOE	Design of Experiments
DPM	Discrete Particle Model
EAF	Exit Angle Factor
FEA	Finite Element Analysis
FLS	Fast Lagrangian Simulation
GCI	Grid Convergence Index
HCTI	High Capacity Turgo Impulse
HPP	Hydro Power Plant
LE	Leading Edge
LES	Large Eddy Simulation
NTUA	National Technical University of Athens
OEAFF	Outside Exit Angle Factor
PCD	Pitch Circle Diameter
PH	Precipitation hardened
PMMA	Poly Methyl Methacrylate
RAM	Random Access Memory
RANS	Reynolds Averaged Navier Stokes Equation
RMS	Root Mean Squared
RNG	Re-normalisation Group
RSS	Root Sum Square
SPH	Smoothed Particle Hydrodynamics
SRS	Scale Resolving Simulation
SST	Shear Stress Transport
TE	Trailing Edge
URANS	Unsteady Reynolds Averaged Navier Stokes Equation
VOF	Volume of Fluid
WF	Width Factor

1 Introduction

1.1 Renewable energy

For the millennia that span our existence on this planet energy has been harnessed from renewable resources, from the burning of firewood to generate heat for warmth and cooking to the harnessing of the wind to power ships. Over the centuries, as our understanding of these resources developed we were able to take this further and we began powering mills using the wind, the flow in rivers and the ebbing and flooding of the tides.

With the industrial revolution and the increasing demand for energy, other non-renewable resources have been turned to, such as coal and oil. These came with their drawbacks, such as pollution, resource depletion and security. It is only recently, with the increased awareness of the impact the burning of these fuels is having on the environment that we have begun to focus again on these renewable resources. This has been shown by the legally binding Renewable Energy Directive (European Commission 2009) which requires the EU to source at least 20% of all its energy from renewable sources by 2020. The more recent United Nations conference on climate change (COP21 2015) in Paris highlighted a global pledge to limit the rise in global temperatures by 2°C by reducing greenhouse gas emissions. This promises to see an even greater focus on renewable energy resources in the future and significant investment into the development of these technologies.

1.2 Hydropower

With the exception of the tides, caused by the gravitational pull of the sun and the moon as they rotate around the earth, the main sources of renewable energy are produced by direct or indirect harnessing of the sun's thermal radiation. Hydropower falls under the latter category. As the sun heats the oceans, water evaporates and with the H₂O molecules having lower molecular mass than N₂ and O₂, they rise above them through buoyancy. As the altitude increases, the pressure and temperature drops, causing the molecules to condense into tiny droplets forming clouds. These clouds are moved by air currents over the land and fall as precipitation. Some of this precipitation runs across the land as surface runoff into rivers which gradually wind their way back to the ocean. It is the potential energy of this water as it flows towards the ocean which is harnessed through hydropower. The potential energy, E_p , available from this water can be expressed as:

$$E_p = mgH \quad (1.1)$$

Where m is the mass of water, g is the acceleration due to gravity and H is the pressure head. Hydropower turbines work by converting this potential energy into mechanical energy which is then converted into electrical energy using a generator.

1.3 Impulse turbines

Hydropower turbines can be split into two main categories, reaction turbines and impulse turbines. Reaction turbines, such as Francis and Kaplan turbines (including bulb turbines as used in (Aggidis and Benzon 2013)), are usually submerged completely in the fluid and utilise a rotating hydrofoil to extract the energy from the fluid by inducing a drop in pressure and velocity. Impulse turbines, such as Pelton and Turgo turbines, work by converting the potential energy E_p into kinetic energy E_k in the form of a high speed jet, the velocity of which can be described as:

$$v = \sqrt{2gH} \quad (1.2)$$

1.4 Turgo Turbines

The Turgo impulse turbine was invented and patented by Eric Crewdson, in 1919. The operating range is similar to the Pelton turbine but it is more suitable for medium heads and operates efficiently over a wide range of flow rates (Fig. 1.1).

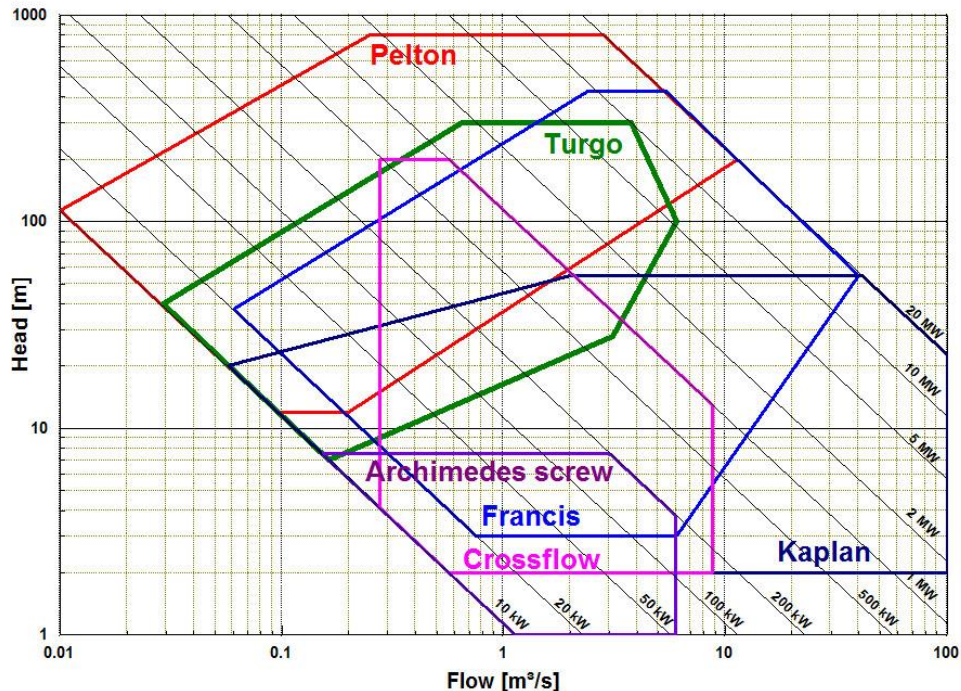


Fig. 1.1 Typical application range for impulse and reaction turbines (Gilbert Gilkes & Gordon Ltd. 2016)

Unlike in Pelton turbines, the jets of Turgo turbines are directed at an acute angle against the runner rotation plane, and the water discharges from the opposite side of the runner (Fig. 1.2.), thus minimizing the interference of the outflow with the runner and jets, which is a known problem for Pelton turbines. As the jet interacts with several blades at a time, the surface of the blades has a complex 3D shape, in order to achieve fast and complete evacuation of the water and minimise outlet energy (Fig. 1.3.).

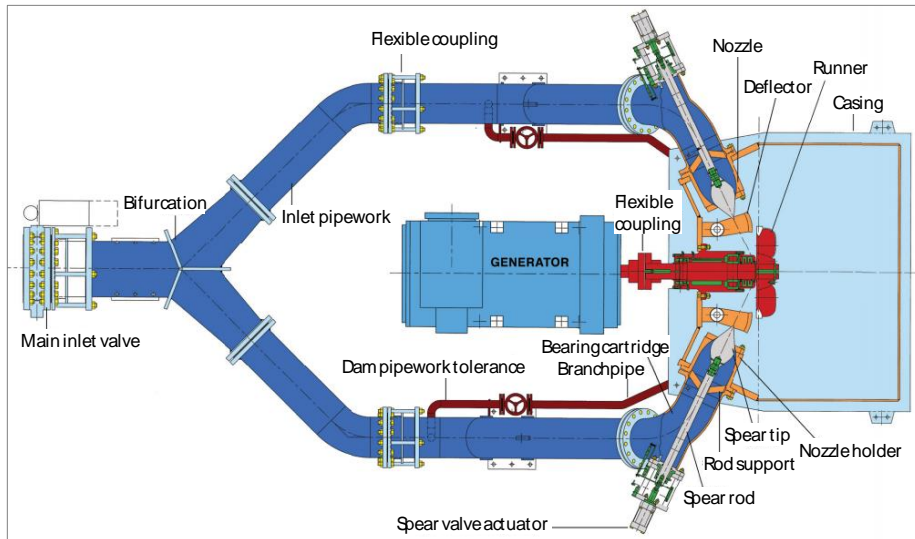


Fig. 1.2.Typical configuration of a twin jet Turgo turbine (plan view) (Gilbert Gilkes & Gordon Ltd. 2016)

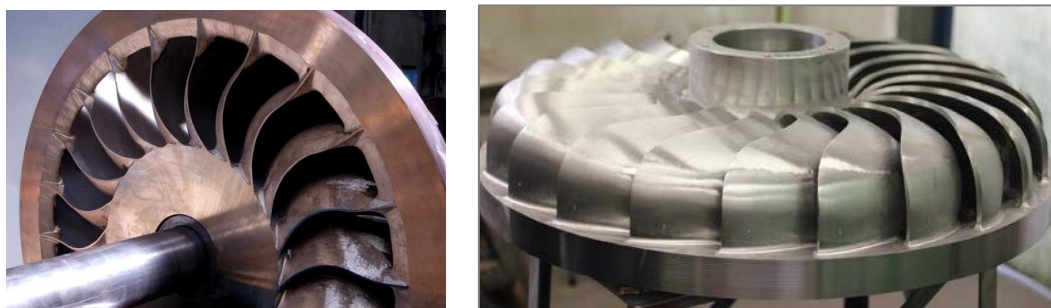


Fig. 1.3. Design of a typical Turgo runner: front - inlet side (left); back -outlet side (right) (Gilbert Gilkes & Gordon Ltd. 2016)

The Turgo runner has a high specific speed for an impulse machine, and higher ratio of jet to runner diameter than Pelton turbines. Hence, for an equivalent power the Turgo turbine usually has a smaller runner and runs at higher speeds. This makes it more feasible to directly connect the turbine shaft to the generator and therefore eliminate the need for transmission systems in medium head environments (Cobb and Sharp 2013; Gilbert Gilkes & Gordon Ltd. 2016).

Due to its simple and robust construction (Fig. 1.4), the Turgo turbine requires minimal maintenance. The bearings are usually designed to absorb the loads of the worst operating conditions, and can operate at runaway speed for a designed period of time, even though the turbine is protected from overspeed conditions using the jet deflectors, which also protect the penstock from surge pressures in a load loss event.



Fig. 1.4. Typical single-jet Turgo turbine installation, with inlet pipe under the powerhouse (Gilbert Gilkes & Gordon Ltd. 2016)

Turgo turbines are very suitable for pico-hydro off-grid installations, because they are reliable, robust and able to operate efficiently over a range of flow rates. Also, their capability of handling significantly higher water flow rates allows for efficient operation in lower head ranges than Pelton turbines and in some micro and pico scale installations studies Turgo turbines are considered for heads as low as 1m. Under the best operating conditions, pico-Turgo turbine efficiency is observed to be over 80% (Cobb and Sharp 2013).

Turgo turbines are also advantageous against the other types of turbines in cases of water containing sand, silt or glacial matter, because the effects of the erosion and abrasion wear on the efficiency are significantly less due to the nature of the design: the removal of material is small and evenly distributed across the blade surfaces (Gilbert Gilkes & Gordon Ltd. 2016)

Given the above clear advantages, the current deployment of Turgo turbines is rather restricted which could be attributed to the more difficult fabrication of its complex runner and the somewhat lower hydraulic efficiency compared to Pelton turbines. However, with the aid of modern numerical design tools and laboratory testing results, the interest for Turgo turbines of improved design and performance is expected to rise globally for their entire range of power outputs.

1.5 Computational Fluid Dynamics

Computational Fluid Dynamics (CFD) is a branch of Fluid Mechanics where numerical methods are used to solve the governing equations describing the behaviour of a viscous, heat conducting fluid.

The governing equations are based on three fundamental principles of conservation. The *continuity equation* (or conservation of mass), the *momentum equation*, obtained by applying Newton's law of motion to a fluid element, and the *energy equation* (conservation of energy) based on the 1st law of thermodynamics. The governing equations, including the Navier-Stokes equation, developed by M. Navier and G. Stokes in the first half of the 19th century, are presented in their most general form below.

Continuity equation

$$\frac{\partial \rho}{\partial t} + \nabla \cdot (\rho \vec{u}) = 0 \quad (1.3)$$

Momentum Equation

$$F = ma \quad (1.4)$$

Expressed as the Navier-Stokes Equation:

$$\frac{\partial}{\partial t}(\rho \vec{u}) + \nabla \rho \vec{u} \cdot \vec{u} = -\nabla p + \nabla \cdot \tau + S_m \quad (1.5)$$

Where the stress tensor τ is related to the strain rate by

$$\tau = \mu \left(\nabla \vec{u} + (\nabla \vec{u})^T - \frac{2}{3} \delta \nabla \vec{u} \right) \quad (1.6)$$

Energy equation

$$\frac{\partial}{\partial t}(\rho h_{tot}) - \frac{\partial \rho}{\partial t} + \nabla \cdot (\rho \vec{u} h_{tot}) = \nabla \cdot (\vec{u} \cdot \tau) + \vec{u} \cdot S_m + S_e \quad (1.7)$$

Where the total enthalpy h_{tot} is related to the static enthalpy, h_s by:

$$h_{tot} = h_s + \frac{1}{2} \vec{u} \quad (1.8)$$

As there is no analytical solution to the governing equations for complex flow geometries, discretised numerical series expansions of the partial differentials are carried out in order to approximate the solutions to these equations. This numerical technique is the underlying principle of CFD. Assumptions are usually made which allows the simplification of the

equations by removing some terms or in some cases a whole equation. These can include assuming that the fluid is isothermal, incompressible etc.

CFD methods are constantly being developed and together with improvements in computational resource capabilities, CFD has reached the stage where analysis of complex phenomena such as multiphase, free surface, highly turbulent flows is possible for a large number of design variations in a reasonable timescale (Židonis, Panagiotopoulos et al. 2014). Recent developments in CFD codes have meant that simulations of this nature show good agreement with experimental data (Perrig 2007; Jošt, Lipej et al. 2008; Klemetsen 2010) giving confidence in the reliability of the numerical results produced when simulating the complex phenomena listed above.

1.6 Aims and objectives

The aim of this research is to use modern CFD tools to aid the better understanding and facilitate the hydraulic efficiency optimisation of the Turgo impulse turbine, including the runner and the spear/valve injectors (similar for both Pelton and Turgo turbines). The aims of this research can be broken down into three distinct areas which can be applied to both the injector and runner analysis and optimisation. Success of this research is dependent on the experimental validation of parts 1. and 2. in part 3.

1. **Model selection and adaption:** This requires the selection of available numerical models which can be used to accurately model the flow through the injectors and runner and predict the performance based on variations in selected design parameters. These models must have the ability to not only accurately model the flow but do so in reasonable timescales to allow for the optimisation of the designs through the analysis of many design permutations.
2. **Design analysis and optimisation:** Using the chosen CFD models, the impact of selected injector and runner design parameters on the performance need to be investigated. Optimisations will also need to be carried out with the primary goal of improving the hydraulic efficiency.
3. **Experimental testing:** Testing of the original and optimised runner and injector designs will be carried out in order to verify whether the design changes suggested based on the numerical results show similar improvements experimentally. The experimental results will also be used to validate the CFD models used.

1.7 Thesis Structure

The work flow chart for this research is given in Fig. 1.5 showing the analysis, optimisation and experimental testing of the injectors and runners in isolation and the model verification carried out by importing the free jet profiles into the runner simulations to compare to the experimental results.

The Turgo runner is analysed numerically using a 2-blade CFD model for optimisation. As the numerical simulation of the flow within this turbine requires the analysis of several complex phenomena, such as multi-phase fluid interaction, rotating frames of reference and transient flow, the CFD model uses a series of assumptions in order to reduce the solve time and allow numerical optimisation in reasonable timescales.

The injectors were optimised using a 2D-axisymmetric simulation which was then extended to look at the 3D case including the branch pipe and guide vanes. This model was taken further by importing the jet profiles created into a runner simulation. This research resulted in two further publications (Benzon, Židonis et al. 2014; Benzon, Židonis et al. 2015) on the optimisation of injectors using a 2D CFD model and the analysis of a full 3D injector case in combination with Pelton and Turgo runner simulations respectively.

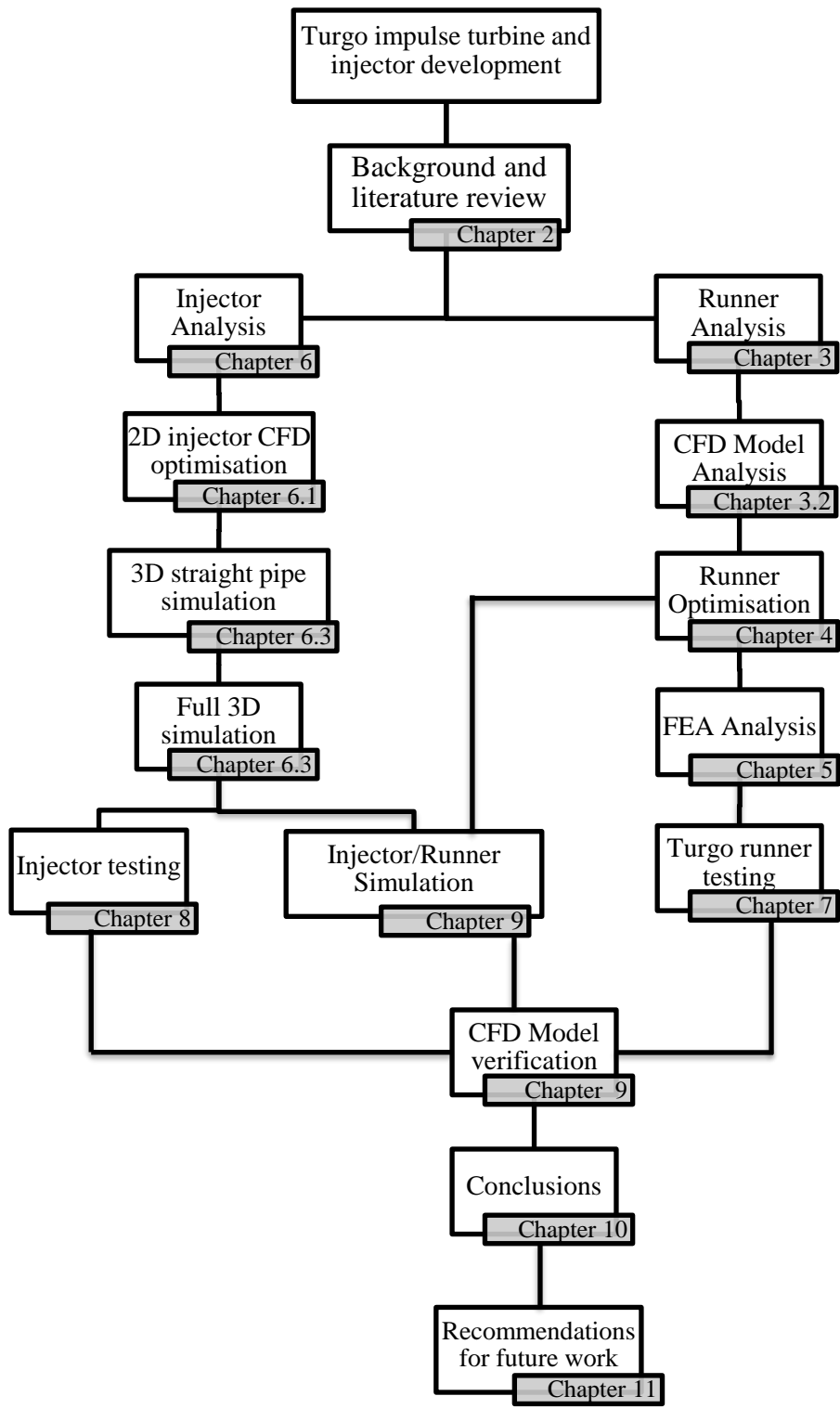


Fig. 1.5. Turgo impulse turbine and injector research work flow chart

2 Background

This section provides a background to the Turgo impulse turbine and looks at the state of the art and current development of this technology. It also gives a summary of the development work carried out to date on impulse turbine injectors, the analysis and optimisation of which also form a large part of this research. The results of this literature review were published in two journal papers looking at the development of Impulse turbines using CFD (Zidonis, Benzon et al. 2015) and the development of the Turgo impulse turbine since its invention (Benzon, Aggidis et al. 2016).

2.1 Invention and early development

In 1919, Eric Crewdson, Managing Director of Gilbert Gilkes and Gordon Ltd realised that there was a potential market for a higher specific speed version of the popular single jet Pelton turbine which existed at the time. He went about designing such a machine and came up with the first Turgo impulse turbine, described in British Patent No. 155,175 (Gilbert Gilkes & Gordon Ltd. 1920), and in the 1922 Institute of Civil Engineers conference proceedings paper Design and Performance of a New Impulse Water-Turbine (Crewdson 1922). The Turgo is described as the incorporation of a Pelton jet to an axial flow turbine runner similar to the Girard turbine (Fig. 2.1).

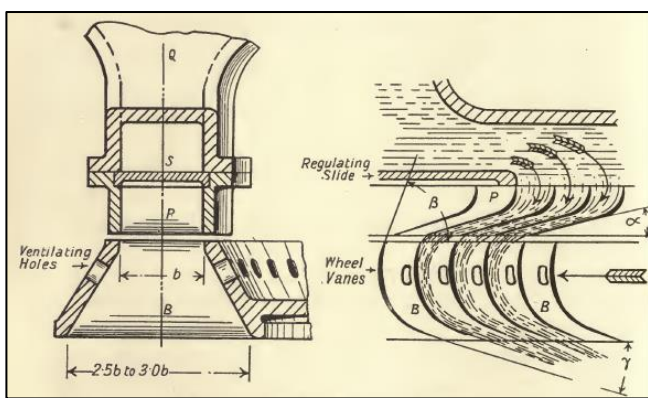


Fig. 2.1. Axial flow Girard turbine (Gibson 1908)

The motivation behind the Turgo design was to combine the relatively high capacity and efficiency of the Girard Turbine with the easy regulation of the Pelton turbine. The angle of impact of the jet and the wheel plane was fixed at 20 degrees and the inlet edge peripheral velocity was set to 0.45-0.47 of the ideal jet velocity (Crewdson 1922).

This design allowed a much larger jet diameter to be applied to a runner, a D/d ratio of 5.25:1, where D is the diameter of the Runner and d the jet diameter, compared to the Pelton wheel which was restricted to about 10:1 at the time (Wilson 1967). This is achieved with the jet entering the runner from the front side and expelling water out of the back as shown in Fig. 2.2.

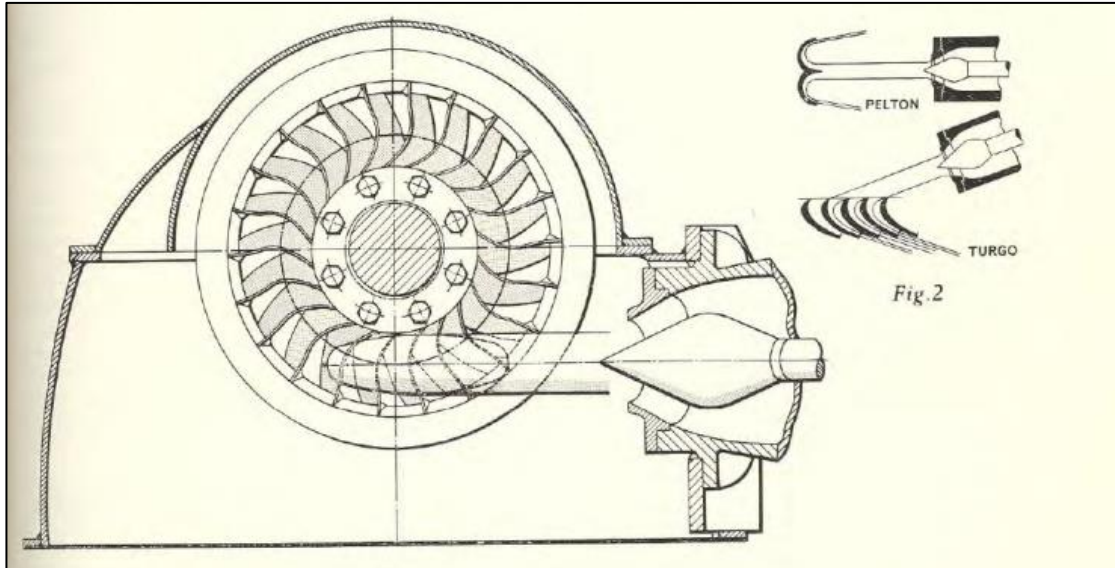


Fig. 2.2. Pelton and Turgo jet positioning showing inclined nature of Turgo jet (Wilson 1967)

The blades were designed using velocity triangles for the inlet and outlet angles combined with a series of practical assumption with regards to the nature of the flow within the runner such as: ensuring the blades are short enough to reduce frictional losses due to the relative velocity, but long enough to prevent eddy losses due to the bending of the water as it travels across the blades. It was also noted that the exit angle was the most important consideration during the design of the runner as although a smaller angle would result in higher efficiencies due to less momentum being lost at the exit, reducing the angle too much would reduce the capacity of the turbine by restricting the flow though the runner. The importance of this feature is emphasised again by further studies carried out on the Turgo (Webster 1972). A value of no more than 10-15 degrees was suggested for good results. A point is also made that the exit angles can be made considerably smaller than would appear from theory, with the experiments showing the discharge angle to be coarser than the exit angle of the blade (Crewdson 1922).

The 1920 Turgo turbine was tested independently by Dr A. H. Gibson of Manchester University showing a maximum efficiency of 83.5% under a head of 200 feet, producing 106HP, at 640rpm. The initial test results can be seen in Fig. 2.3.

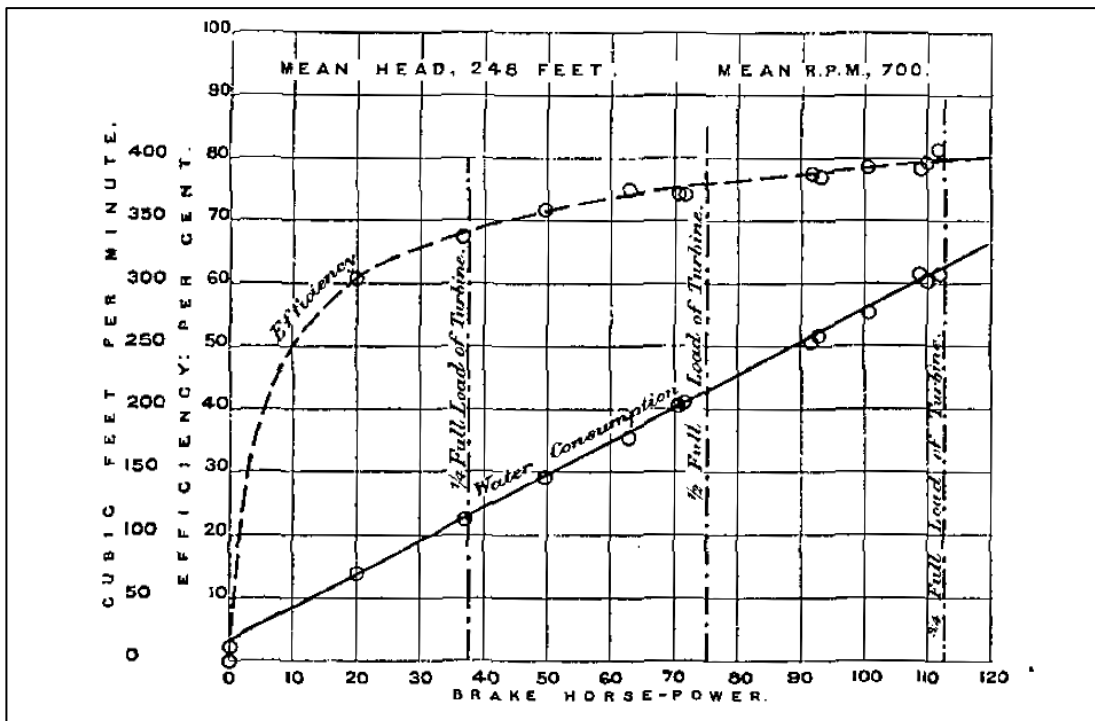


Fig. 2.3. Test results from 1920 Crewdson Turgo design carried out at Afon Calettwr (Crewdson 1922)

For many years, this Gilkes design was commissioned in locations throughout the world, with a reputation for robust, reliable design. The Turgo impulse turbine also deals particularly well with water containing particulates, making it a popular turbine for use in mining districts (Wilson 1967).

2.2 Further Development

2.2.1 Gilkes research and development

Further research was carried out on the design of the Turgo Impulse Turbine in 1936, by Gilkes' Chief Engineer, Ernest Jackson. Using the company's hydro testing facility built the previous year, Jackson was able to improve the efficiency of the turbine and reduce the D/d ratio to 4.5:1 (Wilson 1967), by moving the path of the jet so that it struck the runner ahead of the centreline as shown in Fig. 2.4. The details of this design can be found in British Patent Number 468,557 (Gilbert Gilkes & Gordon Ltd. 1937).

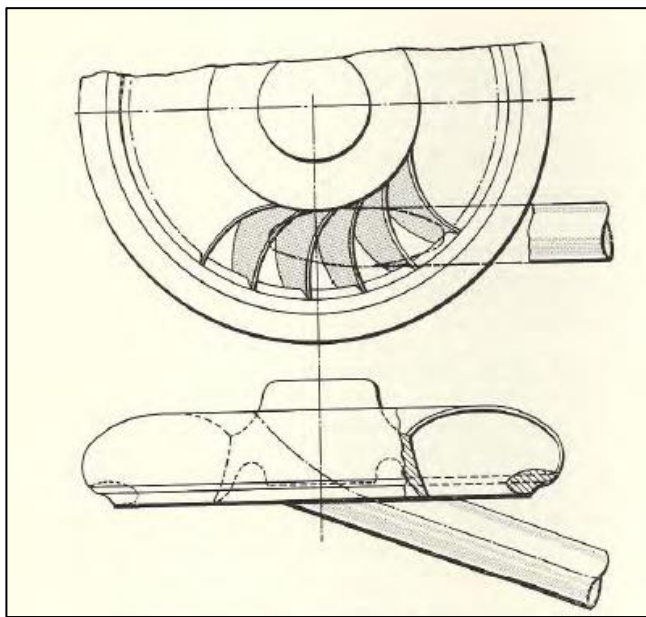


Fig. 2.4. The 1936 modified Turgo design, showing the shifted point of impact between the jet and the runner (Wilson 1967)

The further improvements made to the Turgo design were led again by Ernest Jackson in 1960. By making a wooden runner shaped as the runner would appear in the frame of reference of the jet while rotating, the profile was carved away and filled with paraffin wax and so used to improve the shape of the runner. Using this improved profile, the efficiency was greatly increased, remaining high even when the nozzle is in the fully open position (Fig. 2.5). As well as the shape of the runner, the angle of impact was also altered and the side of impact was changed to between the runner and the alternator allowing the discharge to pass freely on the opposite side to the alternator with no obstructions. These changes also facilitated an even larger jet diameter with the D/d ratio falling to 3.75:1. For the complete redesign of the runner, the British Patent Number 938 967 (Gilbert Gilkes & Gordon Ltd. 1963) was granted on 2nd May 1961 (Wilson 1967).

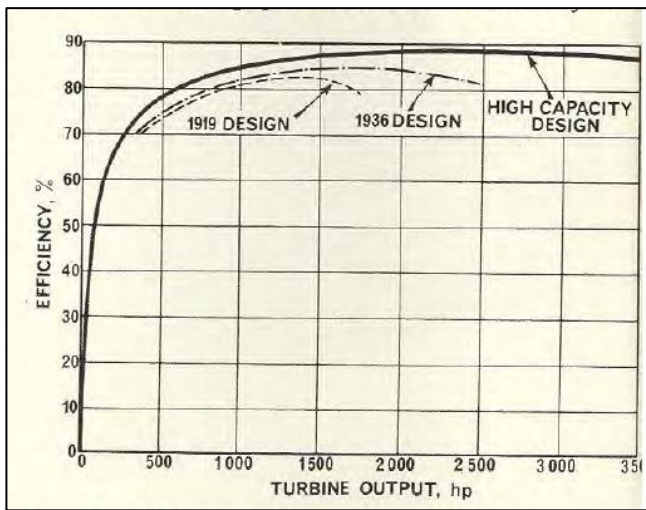


Fig. 2.5. Efficiency and output for a 24in mean diameter Turgo under a head of 750ft (Wilson 1967)

In 1964, a study on the centrifugal strains developed in a 1936 design, 6 inch nominal diameter bronze Turgo turbine was carried out at the Royal College of Science and Technology, Glasgow on behalf of Gilbert Gilkes and Gordon Ltd (MacDuff 1964). The study used electrical resistance strain gauges and a slip ring unit to determine the strains at various locations on the turbine blade leading edges and trailing edges, at speeds of 1020rpm, 1270rpm and 1575rpm.

The main objective of the study was to determine the corresponding centrifugal stresses although tests were also carried out in the reverse direction to investigate the effect of windage on the centrifugal strains.

The results showed that the effects of windage on the measured strains are virtually negligible at all the locations measured. This could be a result of the rim of the Turgo which has been shown to reduce windage losses (Shipulin 1956).

The accuracy of the measured centrifugal strains is confirmed by the proportional relationship to the angular velocity squared. At the maximum strain locations (top of runner leading edge), the measured strain corresponds to an approximate stress value of 0.3 tons/in² or 4.65MPa (MacDuff 1969). Taking the tensile strength in yield of brass to be roughly 200MPa, this corresponds to a safety factor of 43. However it is noted that the strains measured are averaged values over the length of the gauge and the peak values may be higher. The strains may also be higher at locations not measured in this study (MacDuff 1964).

MacDuff went on to complete a Thesis on the same topic titled *Stresses and deformations in impulse water turbines* (MacDuff 1969). This work covers the theoretical and experimental

analysis of the stress in a Turgo runner extensively and also looks at a Pelton wheel. The research was born out of the desire for Gilkes to use their existing high capacity design for operation at heads previously regarded as limiting. At the time, 40 years of manufacturing and servicing Turgo turbines had seen no failure due to lack of strength.

The preliminary testing carried out showed that for a medium sized runner, the centrifugal stress is almost twice the corresponding jet loading stress. For this reason, the centrifugal loading (particularly during runaway when rotational speeds are highest) is focussed on, although jet loading is also simulated in an approximate manner using mechanical methods (MacDuff 1969).

One of the most significant findings of this PhD is the relationship between stresses and nominal working head (Fig 2.6) which can be effectively used to determine whether the rated maximum head can be increased.

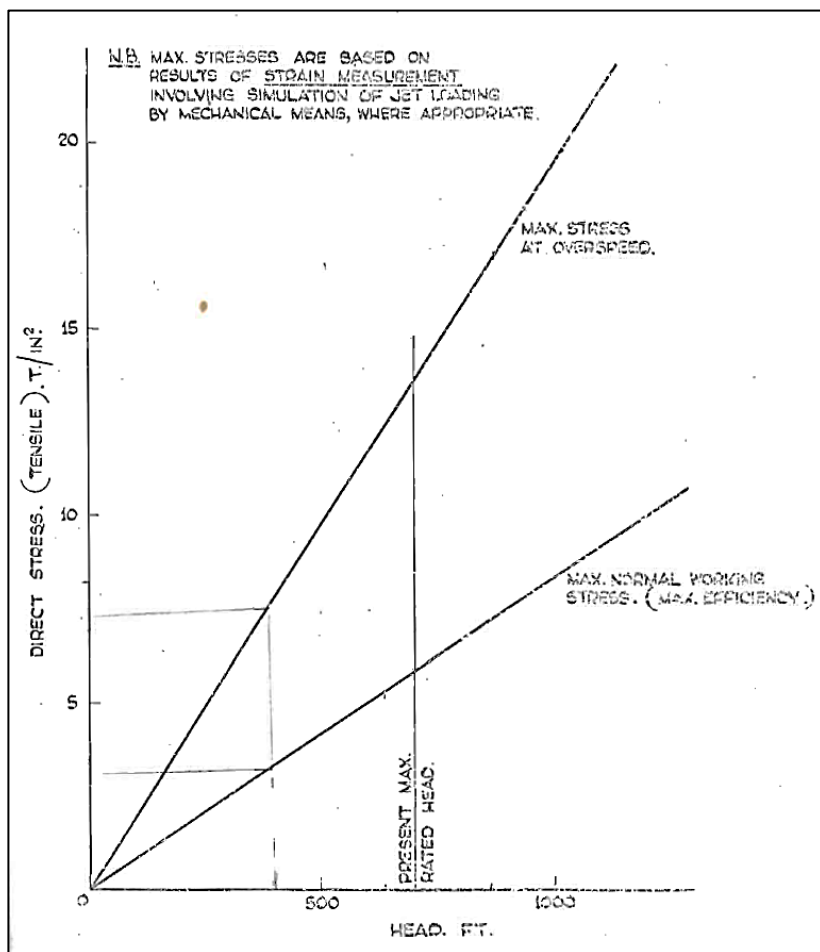


Fig 2.6. Variations of maximum normal working and overspeed stresses with head, for all geometrically similar sized cast steel HCTI turbines, where overspeed is 1.5x normal working speed (MacDuff 1969)

MacDuff goes on to suggest improvements to the design from a strength perspective such as using lighter material such as strong aluminium alloys and using more generous fillets in high stress concentration regions. MacDuff also highlights the essential part played by the rim in relation to both centrifugal and jet loading stresses. A suggested extension to the rim in the axial direction is also made which is shown theoretically to greatly reduce the stresses in both the inlet and outlet edges of the runner (Fig 2.7). The results and suggestions made provide a useful insight into the stresses experienced by the runner of an impulse machine and should be considered alongside any hydrodynamic design changes.

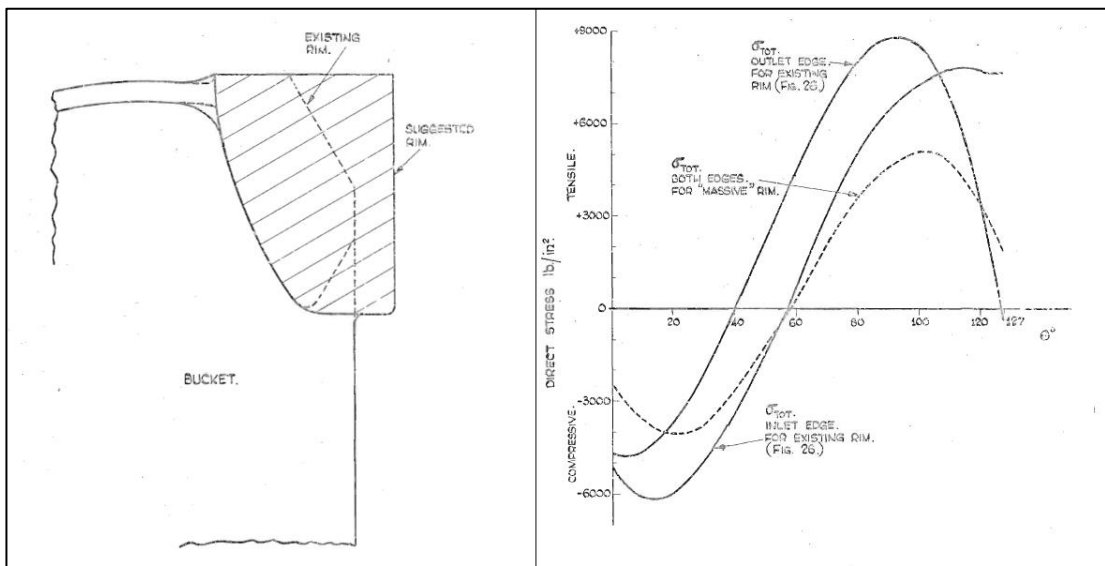


Fig 2.7. Suggested strength improvement to Turgo rim (left) and comparison between theoretical stress distribution on inlet and outlet edges for both designs (right) (MacDuff 1969)

2.2.2 Independent research and development

A one-dimensional theory was developed in 1971 to show how the difference in relative energy between the inlet and outlet of an impulse turbine runner is proportional to the jet/wheel diameter ratio and is more pronounced at relatively high specific speeds where the fall in efficiency due to mixing is greater (Webster 1971).

This theory is used to explain the relatively low efficiencies of the 'inclined jet' impulse turbine compared to tangential type turbines such as Pelton wheels. It is interesting how the perception of these two types of turbines had changed since the invention in 1919 by Crewdson, publishing higher efficiencies than Pelton turbines of the time (Crewdson 1922). The first section uses velocity triangles in one dimension combined with relative energy

equations to determine the optimum velocity triangle configurations, for both tangential and inclined jet configurations. The results show the optimum case for inclined jets where the absolute inlet velocity is equal to the relative velocity (relative energy is 0) and the speed ratio (runner tangential velocity/jet velocity) is greater than 0.5 (depending on inlet angle). The outward movement of the fluid is analysed by looking at the fluid at the inlet using a graphical analysis. Webster states that, based on this analysis, the main source of energy loss is the relative energy differential across the jet at the inlet leading to mixing and outward turning of the fluid across the blade (Webster 1971).

Further research was carried out in 1972, looking at the flow patterns relating to jet-type turbines using both graphical and experimental techniques. The paper looks at the jet cross sections cut out by Pelton and Turgo turbines and how they interact with various runners. A dimensional analysis is carried out first followed by experimental measurements of flow patterns relating to different rectangular and semi-circular cross sections (Webster 1972).

Further work was carried out in 1973 where the flow at the outlet of a Turgo runner is analysed experimentally, showing the outlet velocity and flow distributions at various locations and comparing these to theoretical conditions at the inlet. The injector is mounted vertically in this experimental setup, with the runner shaft inclined at the design angle.

Fig. 2.8 shows the distribution of absolute outlet velocities calculated by measuring the position of droplets with a stroboscope at the intersection points of a grid covering the outlet flow region. The outlet flow region is defined by taking angles from 0° - 125° , with 0° parallel to the jet axis in the plane parallel to the runner face. These angles are measured at 9 equidistant positions (1-9) from the hub to the ring along the curved rim of the bucket. This three dimensional region is plotted in two dimensions by developing the curved rim of the bucket into a straight line (Webster 1973).

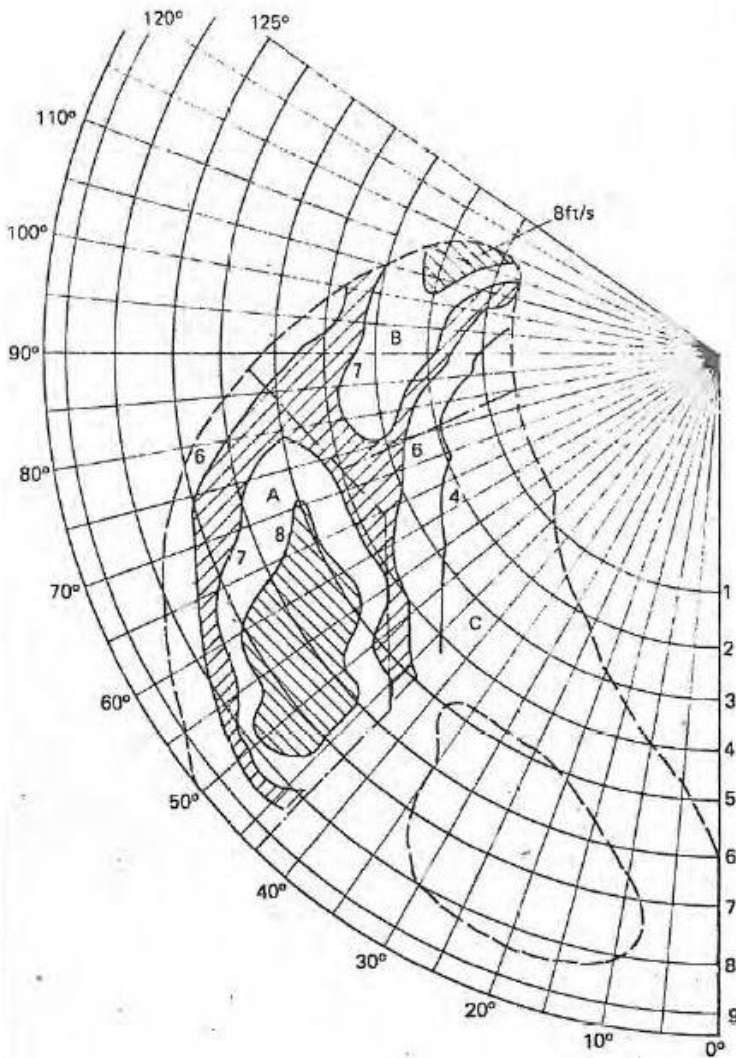


Fig. 2.8. Experimental absolute velocities at the outlet of the Turgo runner in feet/second (Webster 1973)

These experimental results show a much higher degree of lateral spreading than theory states which may be a result of viscous forces within the fluid. The author shows some improvements are possible by moving the jet radially outwards at the inlet and carried out tests showing a 4% increase in efficiency (Webster 1973).

2.3 Recent development and applications

Turgo turbine applications can be found today in two main operating regions, Micro range and Small-Medium range. Micro hydro turbines, ranging from very small power, 100-200 W (also known as pico-hydro turbines) up to about 100-300 kW (Harvey 1993), are used in remote, non-interconnected locations to provide power for small rural communities or small factories.

Low construction cost and easy maintenance are the principal desirable characteristics for these turbines, leading to relatively simplified blade designs (Fig. 2.9), that can be shaped from a half symmetric part of a Pelton bucket to a simple tablespoon. As a result, their hydrodynamic design is not optimum and the hydraulic efficiency of the runners is relatively low.



Fig. 2.9. Turgo turbine blades for micro hydropower (Hartvigsen Hydro 2015)

On the other hand, larger Turgo turbines for small to medium hydro schemes (of the order of a few hundred kW to 10-15 MW) are used mainly to produce and sell electricity to the grid, therefore high efficiency becomes the primary objective in their design. The hydraulic design is based largely on the accumulated experience of the first manufacturers, and more recently, on the implementation of modern CFD tools and their results (Fig. 2.10). As a result, the Turgo blade surfaces exhibit a more complex 3D shape with these runner designs (Fig. 2.11).

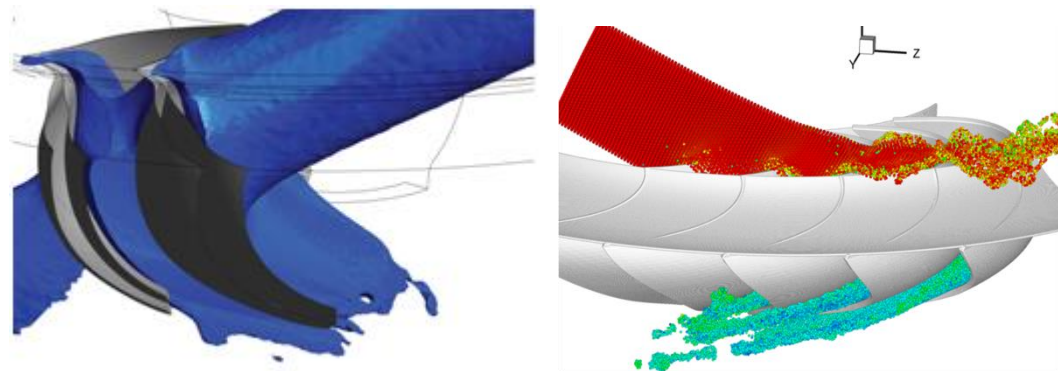


Fig. 2.10. Flow simulation in Turgo runners using CFD tools: volume fraction surface (left), and particles coloured by velocity (right) (Anagnostopoulos 2011)



Fig. 2.11. Indicative blades of a model Turgo turbine with optimized shape (Anagnostopoulos 2011)

In the following section, a review of published works on micro and pico scale Turgo turbines will be given first, followed by the presentation of recent advances in flow analysis and design of small-medium scale Turgo runners.

2.3.1 Pico and Micro-Turgo turbines

A recent experimental study was carried out by (Cobb and Sharp 2013) looking at the impact of variations in speed ratio and jet alignment on the Turgo turbine efficiency (Fig. 2.12). The tests were carried out on heads ranging from 13-28m using a Turgo runner of 169 mm pitch diameter (D) and 11.1 mm nozzle diameter (d), supplied by Hartvigsen Hydro (Hartvigsen Hydro 2015). Peak measured efficiency over 85% is reported for the 169-mm runner, for speed ratio 0.46-0.48. The latter is lower than the theoretical speed ratio for a jet inclination angle $\alpha = 20^\circ$ ($0.5/\cos\alpha = 0.53$), mainly due to the hydraulic (friction) losses in the runner that reduce the outflow velocity (the theoretical speed ratio assumes no hydraulic losses and inlet-outlet radial position of a streamline equal to the pitch radius). For this reason, the optimum speed ratio approaches 0.5 when a larger jet diameter is used and hence the percentage friction losses become smaller. Similarly, radial misalignments of the jet axis toward or away from the runner rotating axis were found to increase or reduce, respectively, the optimum speed ratio (Fig. 2.12), due to the corresponding displacement of the jet impact point at runner regions of lower or higher tangential speed. The efficiency of the Turgo turbine was also found sensitive to these small radial misalignments of the jet, and hence visual adjustments cannot be adequate for achieving the highest turbine efficiency.

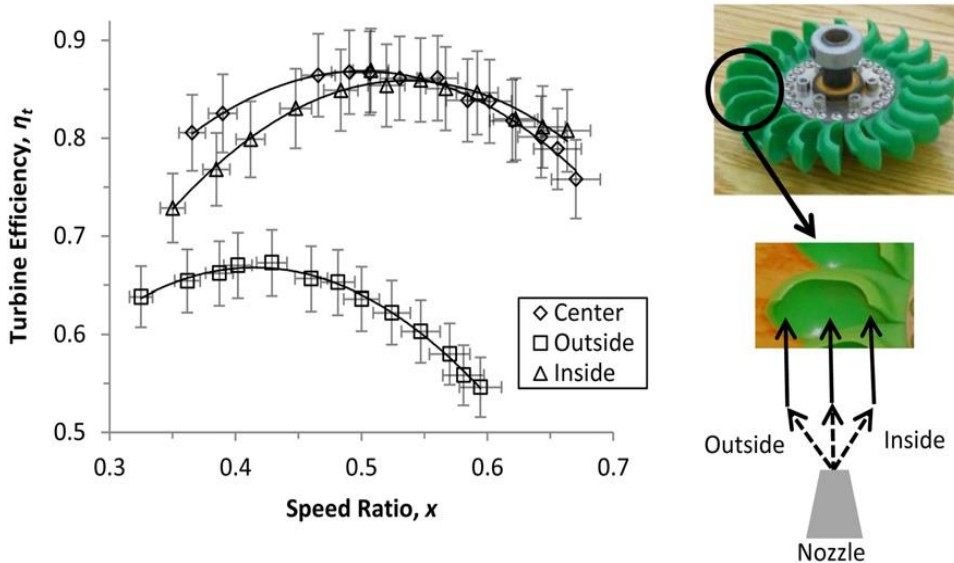


Fig. 2.12. Turgo turbine efficiency vs. speed ratio for three radial jet positions (Cobb and Sharp 2013)

A comprehensive experimental and analytical study was carried out by Williamson et al. (Williamson, Stark et al. 2012; Williamson, Stark et al. 2013) who looked at the performance characteristics of a pico-scale Turgo turbine when used for low heads, 1.0m-3.5m, which is a typical head range in remote communities. The turbine is supplied by Renewable Components Ltd, and its operating range is from 3m head- 150W to 150m head- 1900W. In this work the turbine operates at a very low head and flow rate, below $0.1 \text{ m}^3/\text{s}$, which is completely outside of its typical application domain (Fig. 1.1).

The maximum power was found to occur at quite a low speed ratio, between 0.42 and 0.44. Given the high turbine efficiency achieved, a possible explanation for this behaviour is the small number of blade-cups (9 cups) used in this runner. Because of this, the jet parcel that interacts with each cup is longer and the interaction lasts for a larger turning angle of the runner. As a result, a larger portion of the flow exits from the cup towards its outside region, where the tangential velocity of the runner is higher. Hence the rotational speed of the runner should be reduced to minimize the kinetic energy of the outflow.

A 2D quasi-steady-state simplified mathematical model was developed in this work to produce a new, improved design of the runner. However the model is not able to accurately represent the complex 3D, unsteady flow field in the runner and the interference between the rotating cups and the jet. For this reason an experimental study was carried out at the Hydraulics Laboratory of the University of Bristol (Fig. 2.13) to further examine the design parameters identified by the mathematical model, in order to improve the turbine efficiency and overall performance.

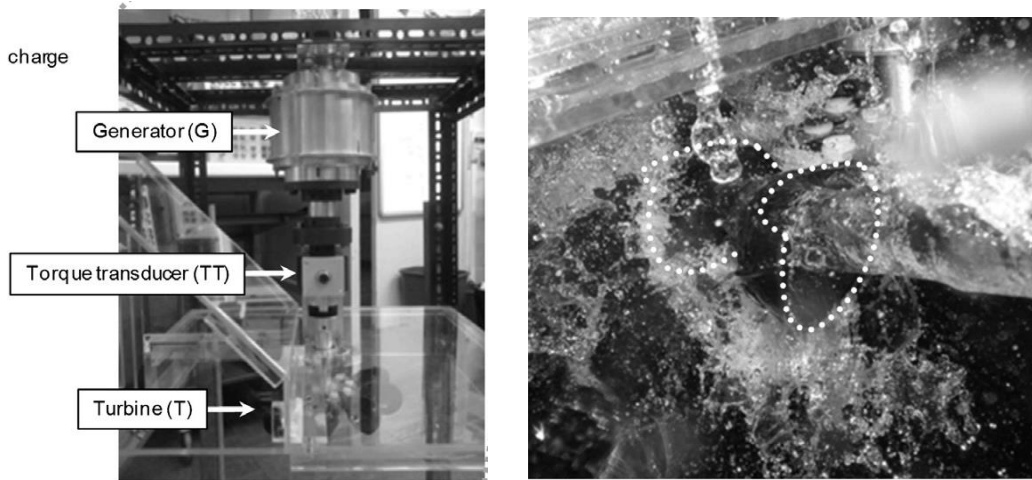


Fig. 2.13. Turgo turbine laboratory tests : Model turbine set up (left), and jet-runner interaction (right – cups are marked by dotted lines) (Williamson, Stark et al. 2013)

The new runner has larger sized cups (Fig. 2.14) and improves the turbine's performance at 3.5 m head by 5% relative to the base-line design (up to 91% peak efficiency), and even more at 1.0 m head, by 20%, to 87% peak efficiency (Williamson, Stark et al. 2013). These results indicate again that the use of a small number of cups results in less efficient interaction of the large jet parcels with each cup. This drawback can be offset by increasing the size of the cups, instead of using more cups on the runner. However, this may cause higher windage losses to arise from the rotating runner.



Fig. 2.14. Comparison of the commercially available (black) and the redesigned (white) Turgo runner (Williamson, Stark et al. 2013)

In another publication (Williamson, Stark et al. 2014), the above authors presented a method of selecting low head pico-hydro turbines through a multi-criteria quantitative and qualitative analysis. Using this method, a propeller turbine with a draft tube or a single-jet Turgo turbine was shown to be the best solution for a given low head and variable flow specification, among several other turbine types examined (Pelton/Turgo single-jet, Pelton/Turgo multiple-jet, Crossflow, Propeller turbine with or without draft tube, Radial flow turbine with or without draft tube, Archimedes screw, Overshot water wheel, Breastshot water wheel and Undershot water wheel.)

Focussing on another aspect, some studies have been carried out by (Khurana, Kumar et al. 2012; Khurana, Kumar et al. 2013; Khurana, Varun et al. 2013) and (Khurana and Goel 2014), looking at the impact of silt parameters on the erosion rate of a Turgo runner. A Turgo impulse turbine of 1.2 kW was fabricated and experimentally tested (Fig. 2.15), using clean water and water with various slit concentration and particle sizes. Moreover, the effect of some other main design and operation parameters on the erosion rate of the runner is also examined, like the jet diameter and velocity, the nozzle angle, and the operation time (Khurana, Kumar et al. 2012; Khurana, Kumar et al. 2013; Khurana, Varun et al. 2013).

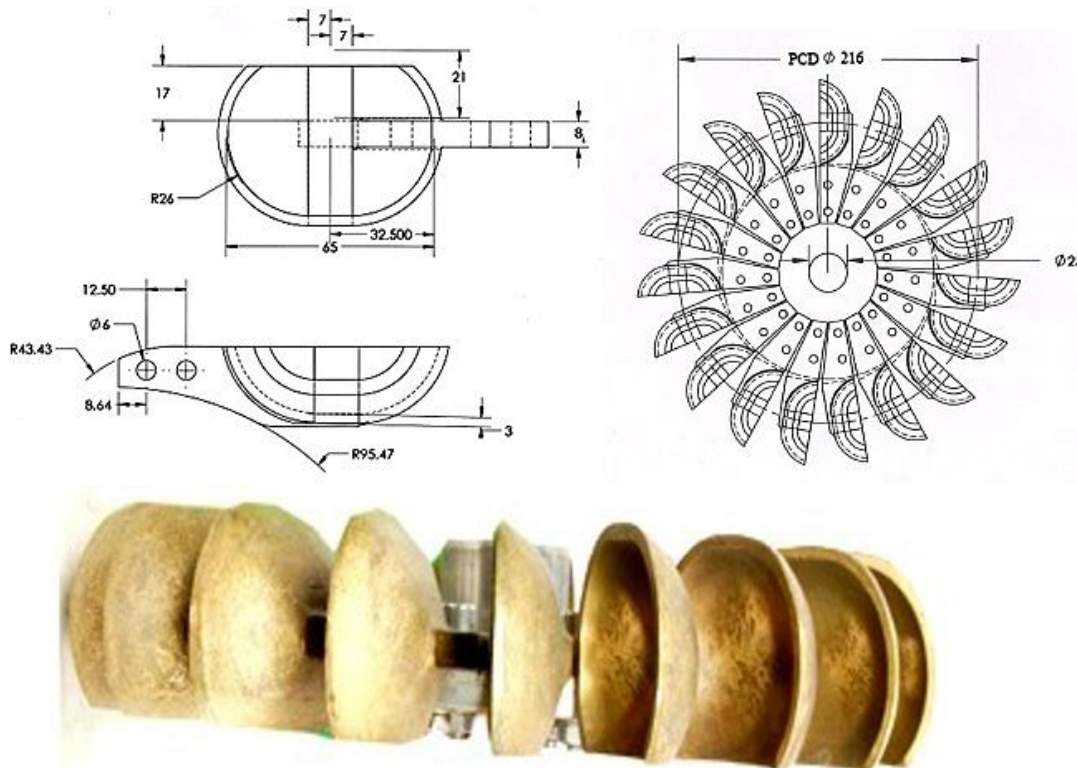


Fig. 2.15. Turgo runner picture and dimensions in the experiments of Khurana et al. (Khurana, Kumar et al. 2012; Khurana, Varun et al. 2013)

The efficiency of the turbine was also measured for both clean and silted water to estimate the efficiency losses due to erosion wear. The latter was found to be significant for the tested silt sizes and concentrations, being of the order of 0.1% to 1% for a 2-hour operation of the turbine (Khurana, Kumar et al. 2012).

The experimental results in (Khurana, Varun et al. 2013) also show that the normalised wear increases with the jet diameter, therefore the use of more jets of smaller diameter in cases of high silt concentration could reduce the erosion wear rate of the runner, without affecting the turbine output.

Gaiser et al. (Gaiser, Erickson et al. 2016) carried out an experimental investigation of design parameters for a pico-hydro turbine using a runner made of tablespoons (Fig. 2.16). According to the authors, this particular tablespoon turbine could be a more economical alternative for off-grid villages than hydroelectric turbines, because it does not require casting and pattern-made molds and the cost is considerably lower than imported commercial hydro turbines.

The authors developed a set of regression equations to describe and predict the efficiency of such low-cost Turgo turbines, as function of the jet inlet angle, number of blades, nozzle diameter, and rotational speed of the runner. The maximum efficiency of this particular runner was low, tested at about 63%, and this was attributed to the relatively large skin friction and eddy formation in the runner cups, the shape of which is very shallow compared to typical Turgo blades.



Fig. 2.16. Turgo runner made of tablespoons (left) and its operation (right) (Gaiser, Erickson et al. 2016)

Finally, a modern CFD tool (ANSYS® Fluent®) is first applied to micro-Turgo turbines in a recent study (Youssef Aaraj, Sorina Mortanda et al. 2014). A 4,5 kW, 5-jet Turgo turbine is considered to be used as a two-phase expander to generate electricity and increase the refrigeration power in a refrigeration system (Fig. 2.17).

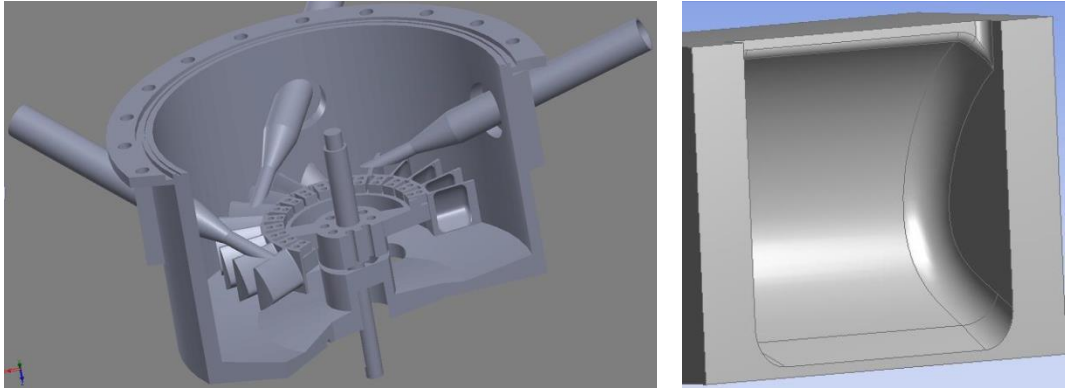


Fig. 2.17. Section view of the turbine enclosure (left), and bucket shape (right) [24]

The mechanical design of the turbine is simplified: the nozzles/expanders have fixed diameters and the runner blades are 2D shaped buckets transformed into 3D. The flow is treated as periodic and a single blade passage is modelled. The numerical simulation is used to improve the design of the runner, by optimizing the number of buckets, the pitch diameter of the runner, and the inlet-outlet angles of the bucket, while the full structure is also analysed mechanically. The attainable efficiency of the design was computed at 40%, which, although quite low due to the simplistic hydrodynamic shape of the buckets, would increase the total refrigeration power of the considered cycle by 0.8% (Youssef Aaraj, Sorina Mortanda et al. 2014).

2.3.2 Small-Medium scale Turgo turbines

The first published CFD work on Turgo turbines came in 2007 with a paper on flow modelling and runner optimisation of a Turgo turbine (Anagnostopoulos and Papantonis 2007). This work uses the main dimensions and operating conditions from a Gilkes Turgo runner installed at a small hydro power plant in Greece. A Fast Lagrangian Simulation (FLS) method is developed to analyse the free surface flow across the inner surface of the Turgo blade, which is initially shaped using a parametric design methodology based on conformal mapping and interpolation techniques. This solver works by treating the fluid as a number of particles and tracking the individual particle trajectories by integrating their motion equations across the surface of the blade, as shown in Fig. 2.18 and Fig. 2.19. (Anagnostopoulos and Papantonis 2007).

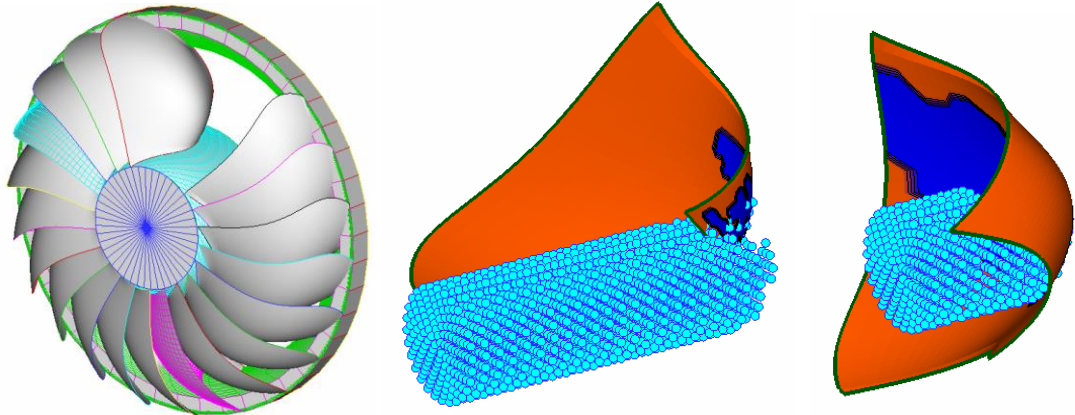


Fig. 2.18. Parametric design of Turgo runner (left) and flow modelling snapshots (right), (Anagnostopoulos and Papantonis 2007)

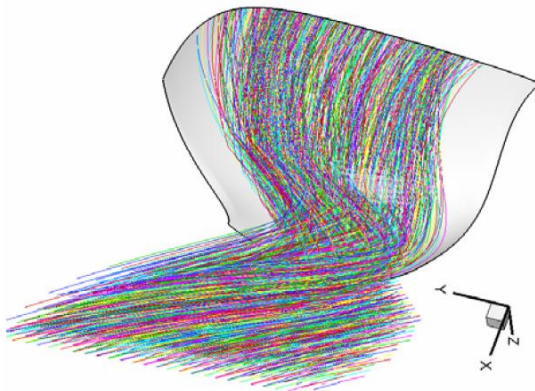


Fig. 2.19. Indicative particle trajectories generated by the Lagrangian solver, coloured to clarify individual paths (Anagnostopoulos and Papantonis 2007)

The fast simulation of the unsteady jet-runner flow, allows this FLS solver to be coupled with general optimisation software, utilising evolutionary algorithms and performing thousands of evaluations to optimise the shape of the blade surface. The results show a 6% increase in efficiency between the standard and the optimised runner, with a maximum efficiency of 85% (Anagnostopoulos and Papantonis 2007). The FLS method however is unable to simulate some secondary flow mechanisms, like the flow on the back side surface of the blades or the interaction between successive blades, as well as to accurately model hydraulic losses and spreading rate of the surface flow in the blades. For this reason, the method introduces a number of additional terms with adjustable coefficients in order to account for the above mechanisms and to reproduce more accurately the flow field and energy exchange in the runner.

In a subsequent study (Koukouvinis, Anagnostopoulos et al. 2010), the FLS tool was tuned with the aid of a more accurate CFD software and then applied for numerical design optimisation of a 70 kW Turgo model runner, which was then manufactured and tested in the laboratory (Fig. 2.20). The runner testing results showed that the best efficiency region includes the design point used in the optimisation, while the attainable efficiency was about 85%. The results also showed a relatively good correlation between the measurements and the tuned FLS model outputs (Fig. 2.21).



Fig. 2.20. Manufacture of the model Turgo runner (left) and installation in the Lab (right), (Koukouvinis, Anagnostopoulos et al. 2010)

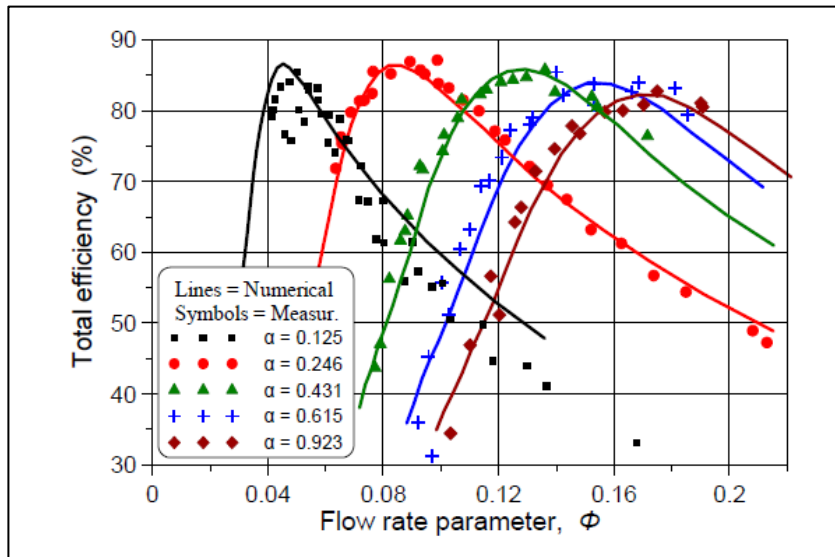


Fig. 2.21. Comparison between experimental and FLS numerical model results for various spear valve openings, α (Koukouvinis, Anagnostopoulos et al. 2010)

Another computer algorithm for the simulation of the flow in a Turgo runner was developed by Koukouvinis et al. (Koukouvinis, Anagnostopoulos et al. 2011) based again on a particulate, Lagrangian approach, and the Smoothed Particle Hydrodynamics (SPH) method.

The software is initially applied to analyse the flow across the inside surface of a static Turgo blade (Koukouvinis, Anagnostopoulos et al. 2010), and its results after fine discretization compared well with the ones obtained by the commercial Eulerian solver ANSYS® Fluent® with the Volume-of-Fluid (VOF) technique (Fig. 2.22).

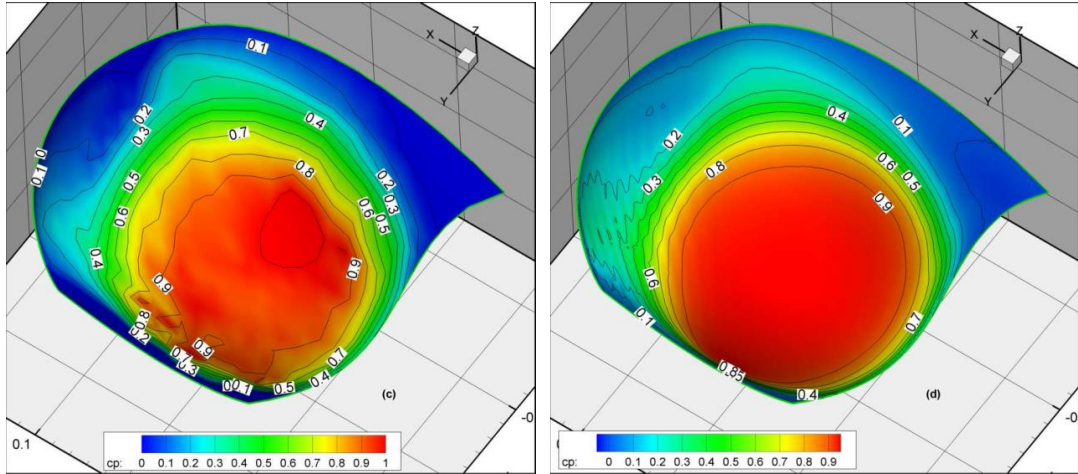


Fig. 2.22. Pressure coefficient distribution on the inner surface of a static blade obtained by SPH (left), and Fluent®-VOF (right) (Koukouvinis, Anagnostopoulos et al. 2010)

This work was expanded in 2011 (Koukouvinis, Anagnostopoulos et al. 2011) where the flow simulation results in rotating Turgo runner geometries were compared using the developed SPH code and the commercial Fluent® solver (Fig. 2.23 and Fig. 2.24). The comparison between the torque curves (Fig. 2.25) showed a good average correlation, but the SPH results were less smooth with a lot of scatter. However, the SPH with the resolution used completes the flow simulation in about one order of magnitude less CPU (Central Processing Unit) time than Fluent®.

The above works (Anagnostopoulos and Papantonis 2007; Koukouvinis, Anagnostopoulos et al. 2010; Koukouvinis, Anagnostopoulos et al. 2011; Anagnostopoulos, Koukouvinis et al. 2012) have shown the potential of Lagrangian solvers to simulate the flow in Turgo turbines in significantly smaller time scales than equivalent Eulerian solvers, making them useful tools at least in the initial design optimisation of a blade surface, with the ability to analyse many design permutations.

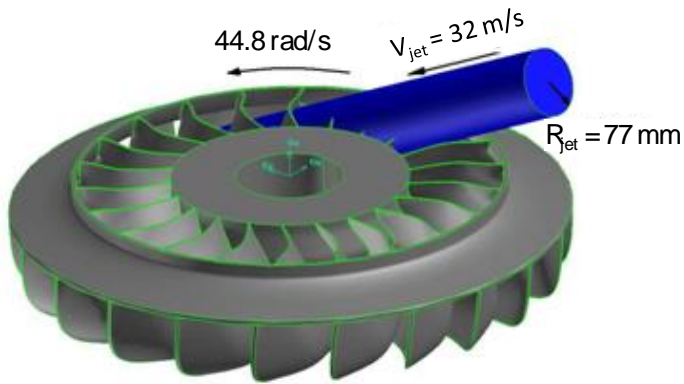


Fig. 2.23. Jet-runner set up (Koukouvinis, Anagnostopoulos et al. 2011)

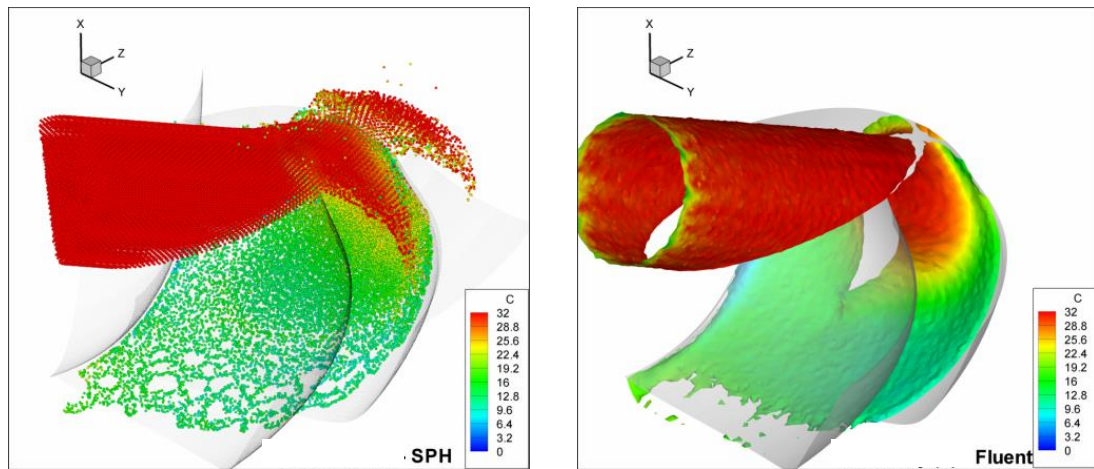


Fig. 2.24. Flow comparison between SPH and ANSYS® Fluent® results (Koukouvinis, Anagnostopoulos et al. 2011)

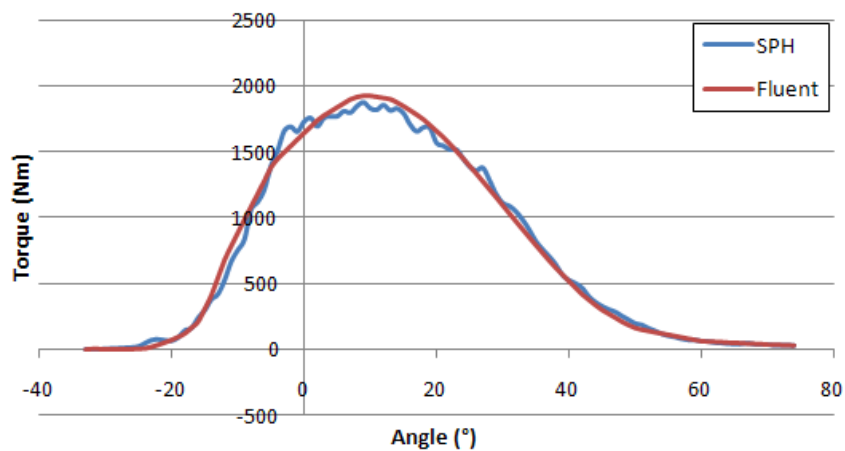


Fig. 2.25. Comparison of SPH and ANSYS® Fluent® results for the Torque curve developed on a blade, zero angle refers to vertical blade position (Koukouvinis, Anagnostopoulos et al. 2011).

(Correa, Andrade et al. 2012) developed a methodology for the design of a Turgo turbine using Rankine Ovoids, a type of three dimensional potential flow model used to develop streamlines with certain simplifying assumptions. The streamlines are then modified using various algorithms to approximate the flow passing through the Turgo blades and to define their hydraulic shape, assuming also a circular arc profile for the leading and trailing edges (Fig. 2.26). Then, the authors derived analytical expressions to estimate the energy transfer efficiency in the runner, based on hydrodynamic analysis and velocity triangles in 1D and in 3D space. It was found that the hydraulic efficiency is significantly reduced from 90% of an ideal jet-runner interaction to only 75% after considering the 3D streamlines, and the losses due to friction and due to the portion of the jet that misses the runner. Consequently, the potential flow theory does not seem capable of providing an adequate approximation of the complex jet-runner interaction flow, and hence it cannot be used for the design of runner blades in Turgo turbines.

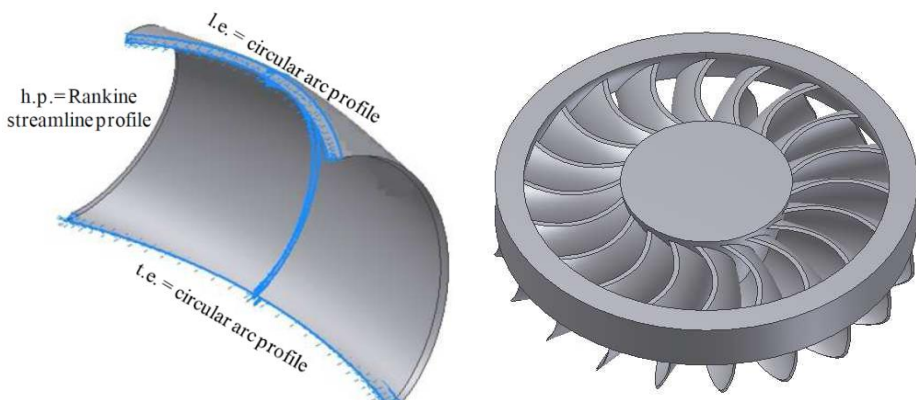


Fig. 2.26. Turgo blade and runner created by the analytic approximation method of (Correa, Andrade et al. 2012).

In an extension of this research, Correa et al. (Correa, Andrade et al. 2012) used the commercial Eulerian CFD software, ANSYS® CFX® 12.0 to simulate the performance of this Turgo turbine design. The analysis is made by a rather coarse mesh, which simulates the full runner with 20 blades as well as the casing, with just over 2 million elements, corresponding to roughly 100k elements per blade passage.

The streamlines passing through the runner as computed by the CFD simulation (Fig. 2.27) are in good agreement with the ones produced by the potential theory. However, due to the low mesh resolution, the developed torque on the shaft and the hydraulic efficiency of the runner were not studied, making it difficult to verify the effectiveness of this design methodology. The low mesh resolution also meant that the simulation struggled to capture the shape of the jet, which in Eulerian solvers requires significant refinement at the boundary

between air and water in order to accurately simulate this complex region. The conclusions of this work suggest that the next stage is a transient CFD analysis of this runner which will allow better simulation of the complex multi-phase flow, with more accurate calculations of torque and efficiency.

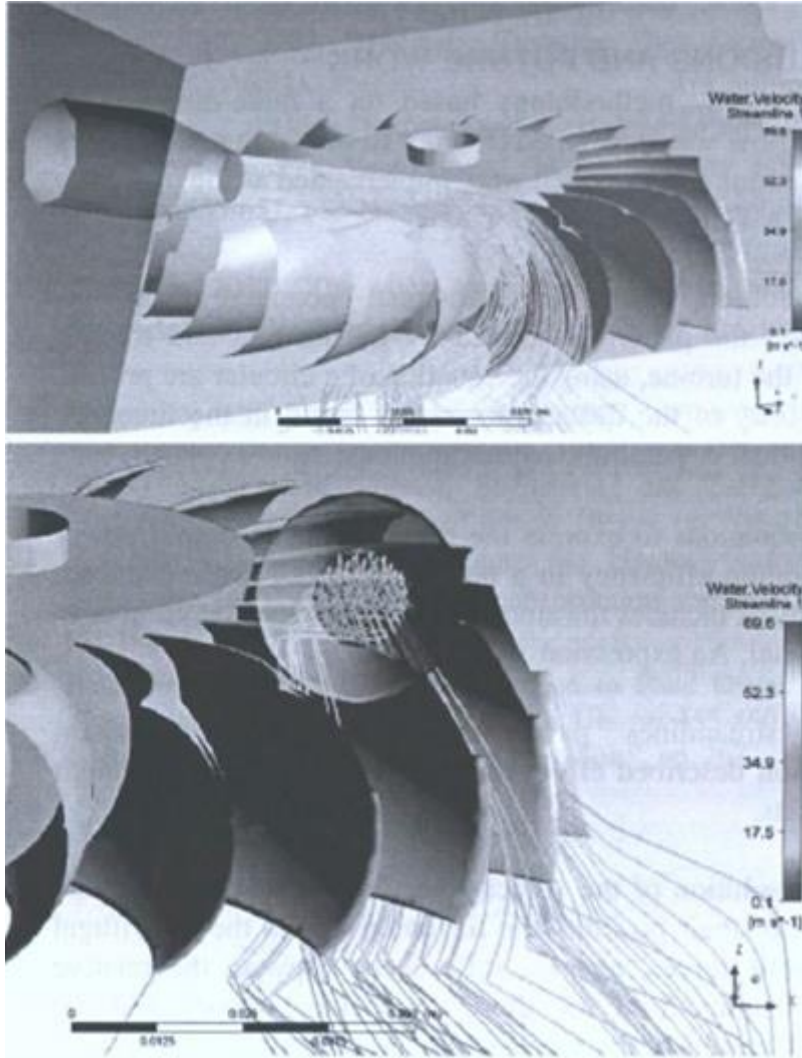


Fig. 2.27. Flow streamlines in the Turgo runner as computed by Correa et al (Correa, Andrade et al. 2012)

Finally, the possible blockage of the flow along the narrow passage between the blades is considered as an additional parameter for the design optimization of a Turgo runner (Anagnostopoulos, Aggidis et al. 2015). This study is carried out for various runners in an extended specific speed range, and showed that the attainable efficiency is higher for low to medium specific speeds, whereas it reduces drastically for high specific speed runners. For given site characteristics (water flow rate and head), such runners have relatively small pitch diameter and high rotating speed, while their blades become shorter (small wrap angle) in order to reduce the flow blockage effects, and hence they are less efficient to transfer the fluid

energy. Moreover, it was observed that in that case the axial and radial velocity components of the exit flow velocity become significant, and hence the outflow kinetic energy losses increase. For the same reason, the optimum speed ratio for high specific speed runners does not depend only on the tangential velocity components, and it may take values even above the theoretical ones (almost 0.6, compared to theoretical 0.55 for a jet inclination angle of 25 deg (Anagnostopoulos, Aggidis et al. 2015)).

2.4 Impulse turbine injector research

One of the first publications modelling the jet formed by the injector of an impulse turbine came in 2000 and compared the jet velocity profiles to measurements acquired using Laser Doppler Anemometry LDA (Muggli, Zhang et al. 2000). The turbulence model used for the simulations was $k-\epsilon$ and the multiphase model was Homogeneous. The results showed a good correlation between the numerical and experimental results.

A case study was performed to improve the injector design and increase the overall efficiency of a Pelton turbine using ANSYS® Fluent® (Veselý and Varner 2001). The chosen turbulence model was $k-\epsilon$ RNG and multiphase was modelled using Volume of Fluid method (VOF). The results showed overall improvements in efficiency however as both the runner and the injectors were modified it is difficult to distinguish where the gains were made.

A numerical study looking at the free jet formed by a Pelton turbine nozzle is carried out (Catanase, Barglazan et al. 2004) looking at the axisymmetric case in Matlab. The model is able to show the low velocity region in the center of the jet and predict the change in velocity distribution with spear position. Some experimental measurements are also carried out showing reasonable correlation between the model and experimental measurements with the differences likely to be a result of the coarse grid used, with only 50000 cells.

A more recent study looks at three different Pelton hydropower plants and includes modelling of the flow in the injector of a Pelton turbine including the branch pipe and guide vanes (Staubli T., Abgottspion A. et al. 2009). The numerical modelling was carried out with ANSYS® CFX® using the $k-\omega$ Shear Stress Transport (SST) turbulence model and a Homogeneous free-surface multiphase model. CFD was carried out on a model scale of the Rabiusa-Realta (Hydro Power Plant) HPP injectors and pipework to identify the reason for the difference between upper and lower jet operation which was attributed to the secondary velocities in the jet, shown in Fig. 2.28. Conclusions of this study suggested that there is a

relationship between the runner efficiency and the jet dispersion caused by the secondary velocities induced by the upstream bends.

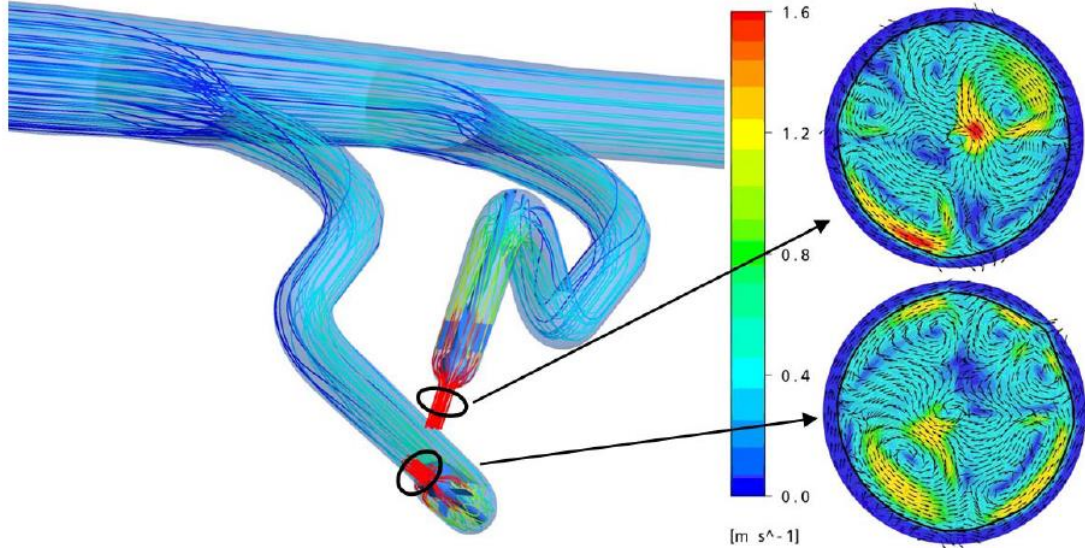


Fig. 2.28. HPP Rabiusa-Realta: CFD simulation of the secondary flows in the jet (Staubli T., Abgottsporn A. et al. 2009)

A study looking at the impact of an ideal jet and a real jet on the performance of a Pelton turbine was carried with ANSYS® CFX® -11 using the inhomogeneous multi-phase model with $k-\omega$ SST turbulence (Santolin, Cavazzini et al. 2009). The results showed a 2% reduction in efficiency using the real jet accounting for the secondary velocity within the jet. The results are also compared to experimental tests. The ideal jet (IJ) and real jet (RJ) regions are shown in Fig. 2.29 below and the development of the 2D velocity profiles of each jet from the exit of the nozzle ($0d_0$) to the runner inlet ($4d_0$) are compared. It is interesting to note how the shape and profile of the jet for both cases starts to become lost as the jet enters the larger tetrahedral elements of the rotating domain ($3d_0$ and $4d_0$) suggesting that smaller cells are required in order to better capture the jet profile in this region and its impact on the runner performance.

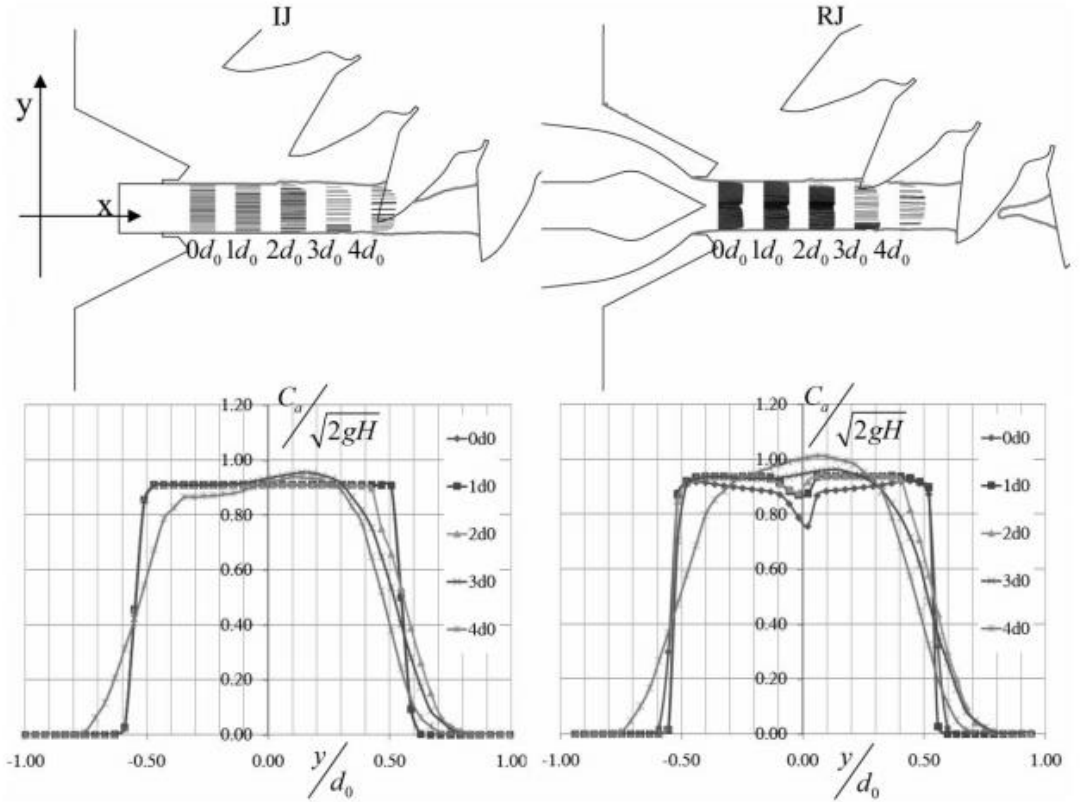


Fig. 2.29. Comparison of axial velocity profiles in five sections normal to the jet ideal axis x (Santolin, Cavazzini et al. 2009)

A very comprehensive study was carried out which modelled the flow in the injectors and upstream pipework including the branch pipes and bifurcation of a twin jet Pelton turbine (Jošt, Mežnar et al. 2010). The jet profiles obtained are combined with a full runner (using symmetry) simulation and compared to experimental tests for a range of flow rates. The results show an under prediction of the CFD model compared to the experimental tests and lower efficiencies for the theoretical jet (ideal jet) compared to the numerically obtained jets (real jet) as shown in Fig. 2.30. The under prediction in the numerical performance is attributed to insufficient grid resolution in the runner domain however there is no explanation for why the real jet results give higher efficiencies than the ideal jet which is not the case with other studies (Santolin, Cavazzini et al. 2009; Benzon, Židonis et al. 2015).

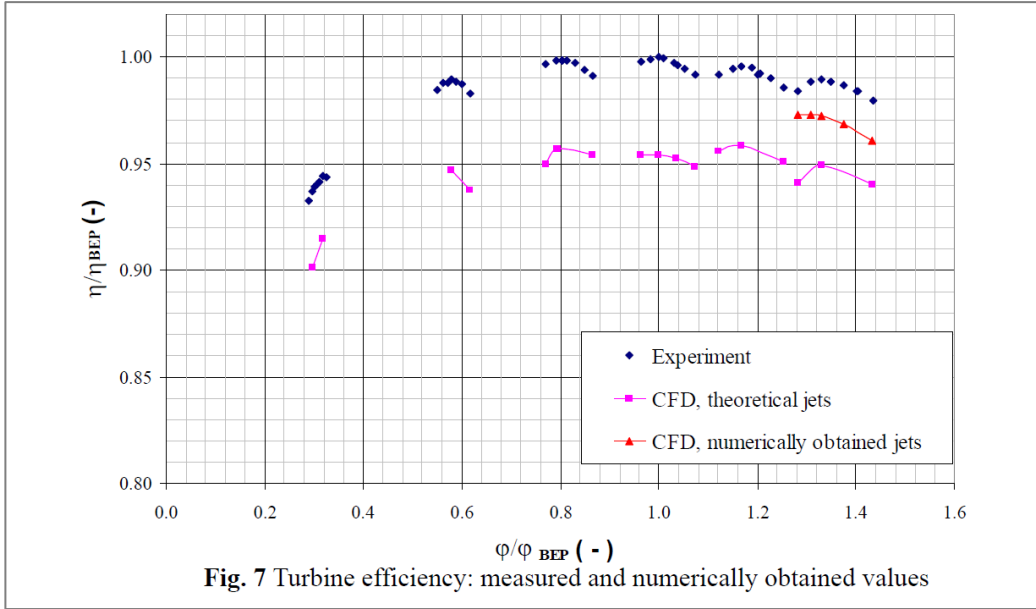


Fig. 2.30. Pelton turbine efficiency experimental and numerical comparisons (Jošt, Mežnar et al. 2010)

Another recent study uses a VOF-Model integrated into the pressure based CFD code *flow3D* with a k- ϵ turbulence model, to simulate a Pelton injector with both a straight pipe and a 90deg bend (Fiereder, Riemann et al. 2010). The results are compared to experimental measurements of the jet shape as shown in Fig. 2.31. Although the results show relatively good correlation with the experimental measurements, the reason why the bead shown in Fig. 2.31 is not completely captured is likely to be down to insufficient grid resolution at the interface between air and water which later studies have shown to be important in order to completely capture these disturbances (Benzon, Židonis et al. 2015).

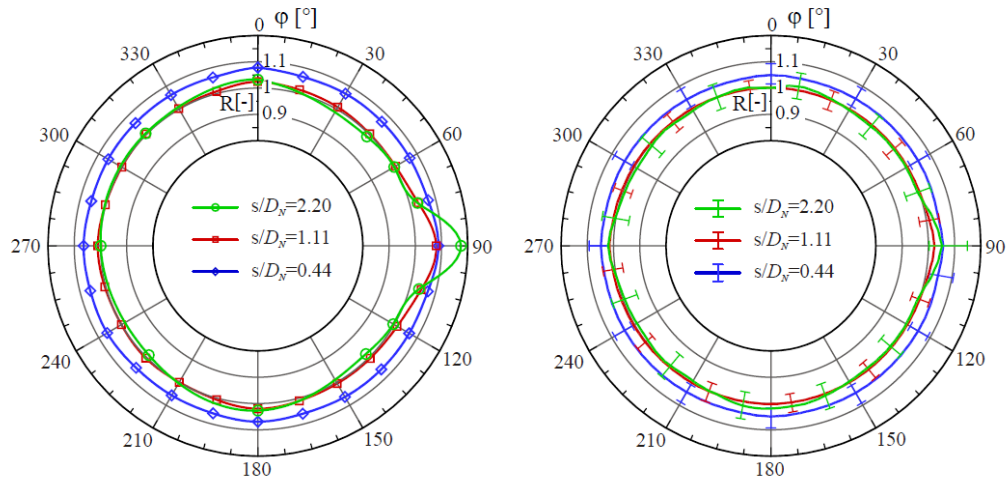


Fig. 2.31. Experimental (left) and numerical (right) jet shape comparison with a 90° inlet elbow (Fiereder, Riemann et al. 2010)

In another study, impulse injector spear erosion was modelled and compared to the abrasion field observations (Xiao, Wang et al. 2014) using Fluent®. VOF and k- ϵ RNG settings were selected for modelling. The sediment was simplified into round solid particles and the Discrete Particle Model (DPM) was employed to predict the spear abrasion characteristics.

2.5 Scope for even further development

A summary of the research carried out on the Turgo turbine and impulse turbine injectors is given in Table 2.1. The literature search has shown that the Turgo impulse turbine, although exhibiting various advantages, is the least developed amongst the other known and established hydro turbine types.

2.5.1 Runner analysis

Although some studies have started to use CFD for the analysis of this complex case, it has yet to be utilised to its full potential. A complete analysis of the Turgo turbine using CFD, capturing the high speed, highly turbulent, multiphase flow across the blades is yet to be carried out. Research on Pelton turbines have shown that using Eulerian techniques it is possible to develop a CFD model which can accurately describe the flow across the Turgo runner, calculate the torque developed and the efficiency, and capture small changes in the design in a reasonable timescale.

By combining these numerical techniques with laboratory testing, additional design improvements could be realised to improve the performance and aid the better understanding of how specific design features affect the performance of these turbines.

2.5.2 Injector analysis

There are some studies available where a selection of injector designs are modelled and compared using CFD (Vesley and Varner 2001; Peron, Parkinson et al. 2008; Patel 2010) or using a visual analysis (Gass and Water 2002; Staubli and Hauser 2004; Zhang and Casey 2009). However there is a lack of publications describing a thorough investigation of basic injector design parameters together with the importance they have on the performance of an injector.

There is also no research looking at the impact of jet quality for different injector designs, which is largely dependent on the spear/valve configuration and upstream pipework, on the on the performance of an impulse turbine runner. This leaves scope for further research on impulse turbine injectors using CFD.

Index to reference numbers in Table 2.1.

1. (Williamson, Stark et al. 2012)	2. (Williamson, Stark et al. 2013)
3. (Youssef Aaraj, Sorina Mortanda et al. 2014)	4. (Gaiser, Erickson et al. 2016)
5. (Khurana, Kumar et al. 2012)	6. (Khurana, Kumar et al. 2013)
7. (Khurana, Varun et al. 2013)	8. (Khurana and Goel 2014)
9. (Fraenkel, Paish et al. 1991)	10. (Williamson, Stark et al. 2011)
11. (Cobb and Sharp 2013)	12. (Gilbert Gilkes & Gordon Ltd. 1920)
13. (Crewdson 1922)	14. (Gilbert Gilkes & Gordon Ltd. 1937)
15. (Gilbert Gilkes & Gordon Ltd. 1963)	16. (Webster 1971)
17. (Webster 1972)	18. (Webster 1973)
19. (Anagnostopoulos and Papantonis 2007)	20. (Koukouvinis, Anagnostopoulos et al. 2010)
21. (Koukouvinis, Anagnostopoulos et al. 2011)	22. (Correa, Andrade et al. 2012)
23. (Correa, Andrade et al. 2012)	24. (Gilbert, Gilkes & Gordon Ltd. 2012)
25. (Benzon, Aggidis et al. 2013)	26. (Benzon 2014)
27. (Anagnostopoulos, Aggidis et al. 2015)	28. Muggli, Zhang et al. 2000
29. (Veselý and Varner 2001)	30. (Gass and Water 2002)
31. (Peron, Parkinson et al. 2008)	32. (Catanase, Barglazan et al. 2004)
33. (Jošt, Mežnar et al. 2010 Matthias and Promper 2004)	34. (Santolin, Cavazzini et al. 2009)
35. (Staubli T. 2009)	36. (Zhang and Casey 2009)
37. (Fiereder, Riemann et al. 2010)	38. (Patel 2010)
39. (Xiao, Wang et al. 2014)	40. (Benzon, Židonis et al. 2014)
41. (Benzon, Židonis et al. 2015)	42. (Wilson 1967)

		Nature of research (Number of Publications)						Comments	
		Research Area	Theoretical	Numerical		Scope for further development	Reference number*	Most Recent Publication	Comments
			Eulerian	Lagrangian	Experimental				
Pico Hydro (100W-100kW)	Runner Design	2	1		2	High	[1-4]	2016	<ul style="list-style-type: none"> Experimental optimisations show good efficiencies. More research can be done using CFD.
	Injector Design	1			3	Medium	[5-8]	2014	<ul style="list-style-type: none"> Little has been done with optimisations of the injectors for improved hydraulic performance.
	Operation	3	1		3	High	[1,3,4, 9-11]	2016	<ul style="list-style-type: none"> Some experimental studies have been carried out over a limited operating range. Very little CFD available.
Small- Medium Hydro (100kW-10MW)	Runner Design	6	5	5	3	High	[12-27]	2014	<ul style="list-style-type: none"> Several theoretical studies are available. Some work has been done using CFD but there is scope for more accurate simulations and further optimisations.
	Injector Design		5		3	Medium	[28-41]	2015	<ul style="list-style-type: none"> Some CFD and flow visualisation carried out. Not used for parametric design optimisation or multiple injector/runner simulations until (Benzon, Židonis et al. 2014; Benzon, Židonis et al. 2015)
	Operation	2	3	2	1	High	[11,12, 14- 16,18, 19,21, 25,26, 42]	2014	<ul style="list-style-type: none"> Limited experimental studies available Several CFD studies using Lagrangian solvers Little CFD using Eulerian solvers

Table 2.1 –Summary of research carried out on Turgo turbines and injectors by research area

*See reference number index above

3 Turgo runner analysis

In this chapter, the Gilkes HCTI (High Capacity Turgo Impulse) runner is modelled using the commercial CFD tool, ANSYS® CFX® at the best efficiency point (BEP). The fluid domain around the runner is created using a series of assumptions in order to reduce the computational time for the purpose of design optimisation.

Although the background research showed that the use of CFD to model the Turgo turbine is still in its infancy, there have been several studies carried out where a Pelton runner has been modelled using CFD as shown in the detailed review carried out on the development of hydro impulse turbines, including Pelton and Turgo (Zidonis, Benzon et al. 2015). Many of the challenges faced when modelling a Pelton runner are similar for the Turgo. These include high turbulence, multi-phase fluid interaction and rotating geometry. For this reason, the state of the art in Pelton modelling can be used to decide on an appropriate CFD model to use for the Turgo runner analysis.

The majority of the studies carried out on Pelton runners, simulating a jet interacting with a rotating runner have been carried out using the commercial Eulerian solver ANSYS® CFX®. The most recent studies use the homogeneous multiphase model combined with the k- ω SST turbulence model (Zidonis 2015; Zidonis, Benzon et al. 2015).

3.1 CFD model assumptions

This section details the creation, development and initial validation of the numerical model used in the optimisation of the Turgo runner. The model focusses on the turbine Best Efficiency Point (BEP) conditions in order to compare the simulation results to available test data. In this manner the CFD analysis method can be analysed, adapted and improved for increased accuracy and reduced computational cost creating an efficient platform for the optimisation phase.

There are several assumptions which have to be made in order to produce a CFD model which can accurately simulate the flow within the runner but do so in timescales which make optimisation studies feasible. These assumptions are listed below and detailed in the following chapters.

3.1.1 Geometric assumptions

Simulation of the full Turgo runner and casing using both single and twin jet operation requires a significant amount of computational resource making it unfeasible for optimisation of the runner geometry. For this reason several simplifying assumptions are made in order to reduce the size of the computational domain and the simulation time.

3.1.1.1 Casing interaction

Modelling of the runner and the casing requires a significantly larger computational domain with a higher mesh density in order to capture the formation of water droplets and the interaction of these droplets with the casing walls. Due to the axially inclined nature of the Turgo jets, entering the runner at the inlet side and expelling water at the outlet, the interaction between the casing and the rotating runner is relatively simple compared to Pelton turbines (Shipulin 1956; Wilson 1967; Benzon, Aggidis et al. 2016). For this reason and with the assumption that the casing interaction is not required for numerical comparisons between different runner designs, the casing is not modelled.

3.1.1.2 Periodicity

It is assumed that in steady conditions, the torque acting on each individual blade is periodic in nature and a single blade passage can be used to calculate the total torque acting on the runner using this periodicity. In order to investigate the periodic nature of the torque on each consecutive blade and determine the number of blades required for an accurate prediction of the runner performance, a periodicity study was carried out.

The rotating domain for the periodicity study was created by taking a periodic fluid region around a single blade from the full HCTI runner CAD (Computer Aided Design) geometry. This was done by cutting the fluid region around a single blade using a periodic surface as shown in Fig. 3.1.

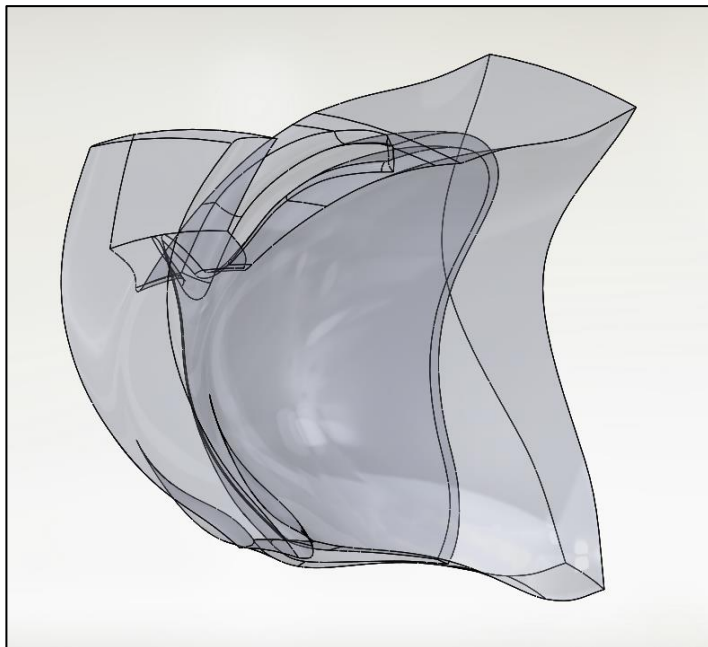


Fig. 3.1. Periodic fluid region around a single blade

The periodic fluid region was meshed with identical surface elements on the periodic faces (Fig. 3.2) and patterned 7 times around the rotational axis in the simulation setup.

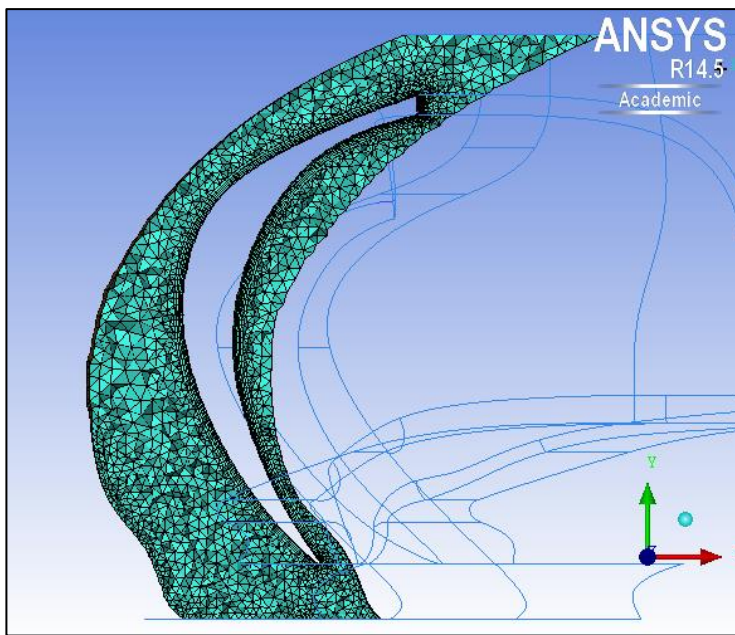


Fig. 3.2. Cut plane through the middle of the periodic mesh showing inflation and sizing

The total torque curves for the 6 blade passages, excluding the outside of the first blade and the inside of the seventh blade, can be seen in Fig. 3.3. The corresponding normalised power resulting from the torque for each blade passage as well as the power for an equivalent 2 bladed simulation is given in Fig. 3.4.

The torque curves are overall periodic however the torque for the first blade passage is higher than consecutive blade passages. When looking at the normalised power for each blade passage (normalised against the power from blade passage 1-2), blade passage 1-2 shows a much greater power than all consecutive blade passages. There is also a small oscillation in the power being captured by each consecutive blade passage.

In order to investigate the cause of these differences, the superficial velocity contours along the axial plane in the centre of the jet were compared for blade passages 1-2, 4-5 and 6-7 at 62.18° periodic rotation where the largest difference in torque on each blade is measured (Fig. 3.5). These contours show an overall very similar flow pattern at the centre of the jet for each blade passage.

The only slight visual difference in the flow for each three blade passages is the amount of flow traversing the back of the previous blade passage which can cause some slight interference along the trailing edge. For blade passage 1-2, the flow is minimal as there are no previous blades adding to this sheet of water traversing the back of the blades. For blade passage 4-5, this increases slightly as more flow is being added to this sheet of water and blade passage 6-7 sees the accumulation of all the flow leaving the previous blades which could explain the slight dip seen in the peak torque.

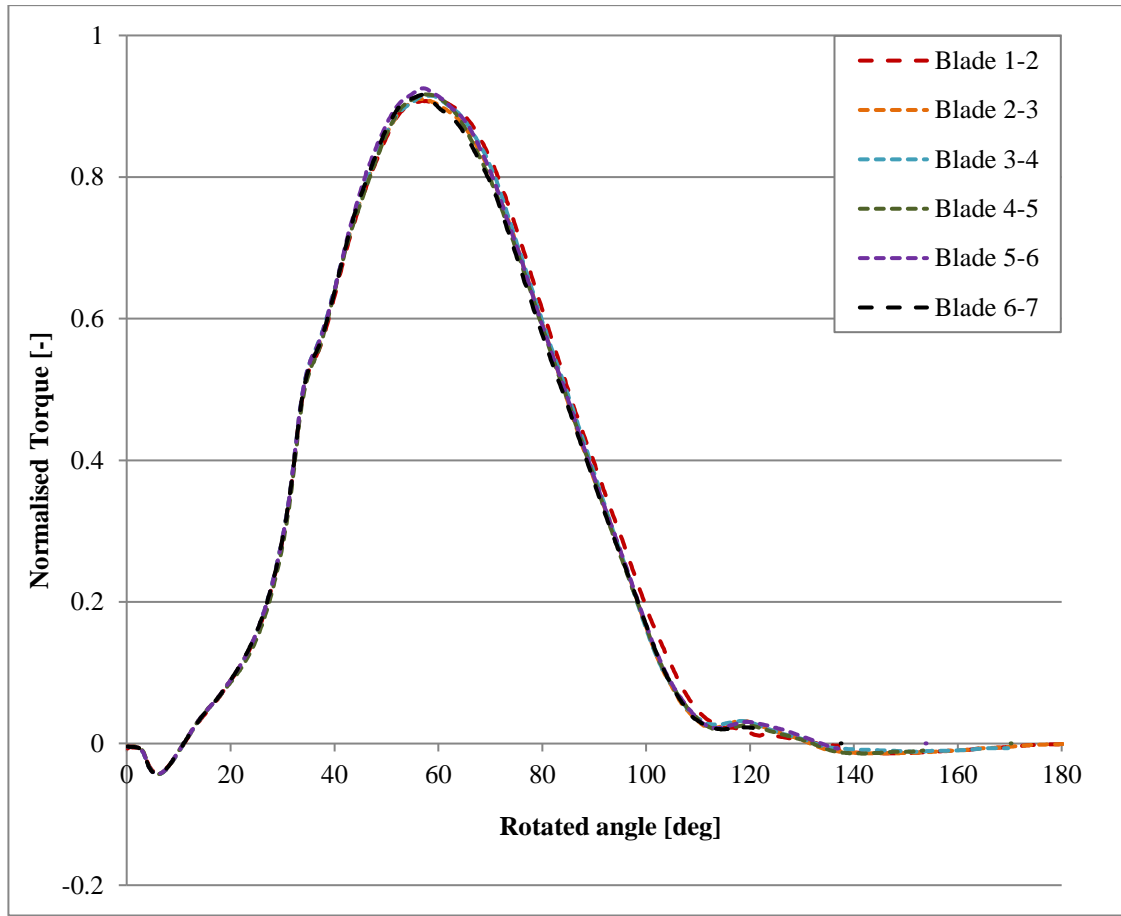


Fig. 3.3. 7 Blade Periodicity study showing torque curves on the inside and outside of each blade

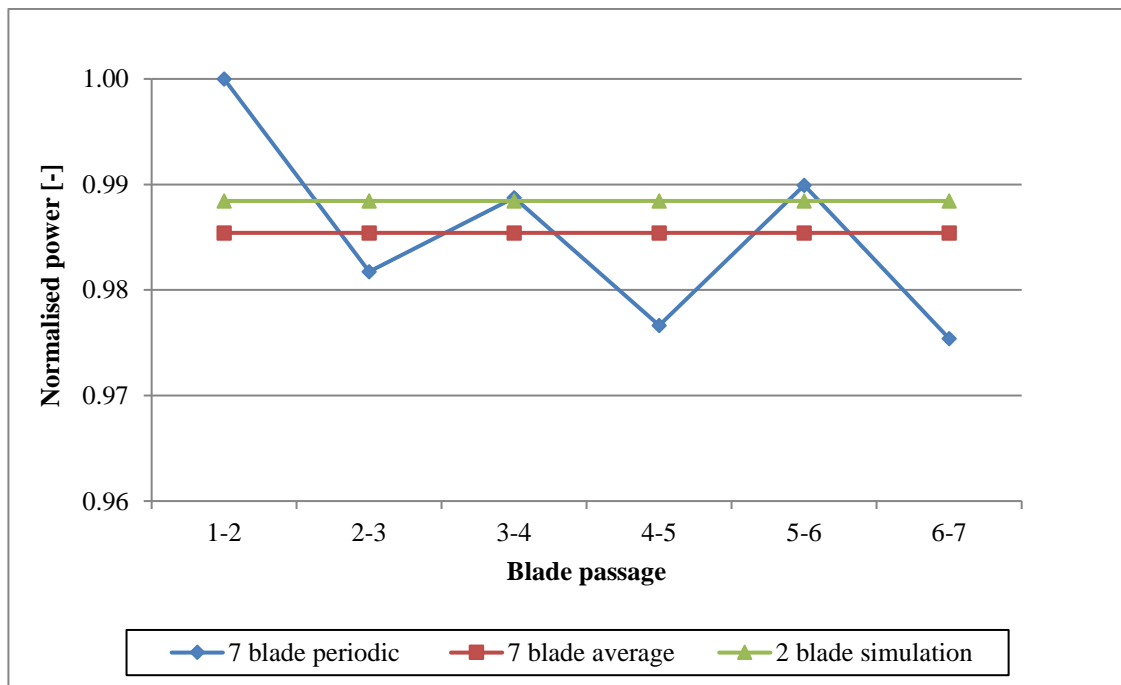


Fig. 3.4. Normalised power calculated from torque curves for each blade passage

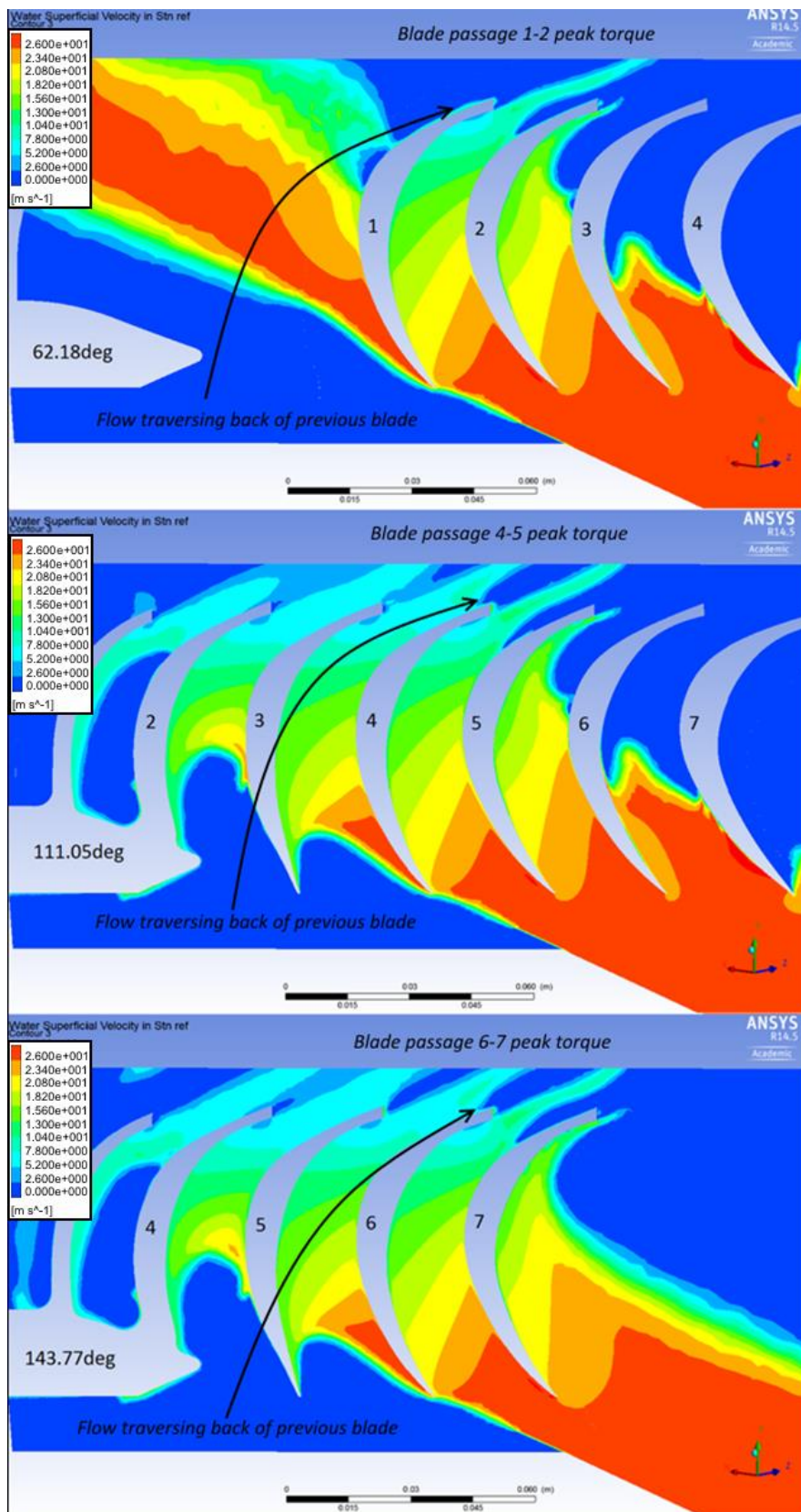


Fig. 3.5. Absolute velocity contours on the axial plane in the centre of the jet for comparison between blade passages 1-2, 4-5 and 6-7

The torque curves for blade passages 3-4 and 4-5 are compared to the 2 blade (1 blade passage) simulation in Fig. 3.6. The results show a very similar overall shape with the main differences seen at the peak torque and the torque between 90° and 160° rotation, where the interference of the flow leaving the blades takes place.

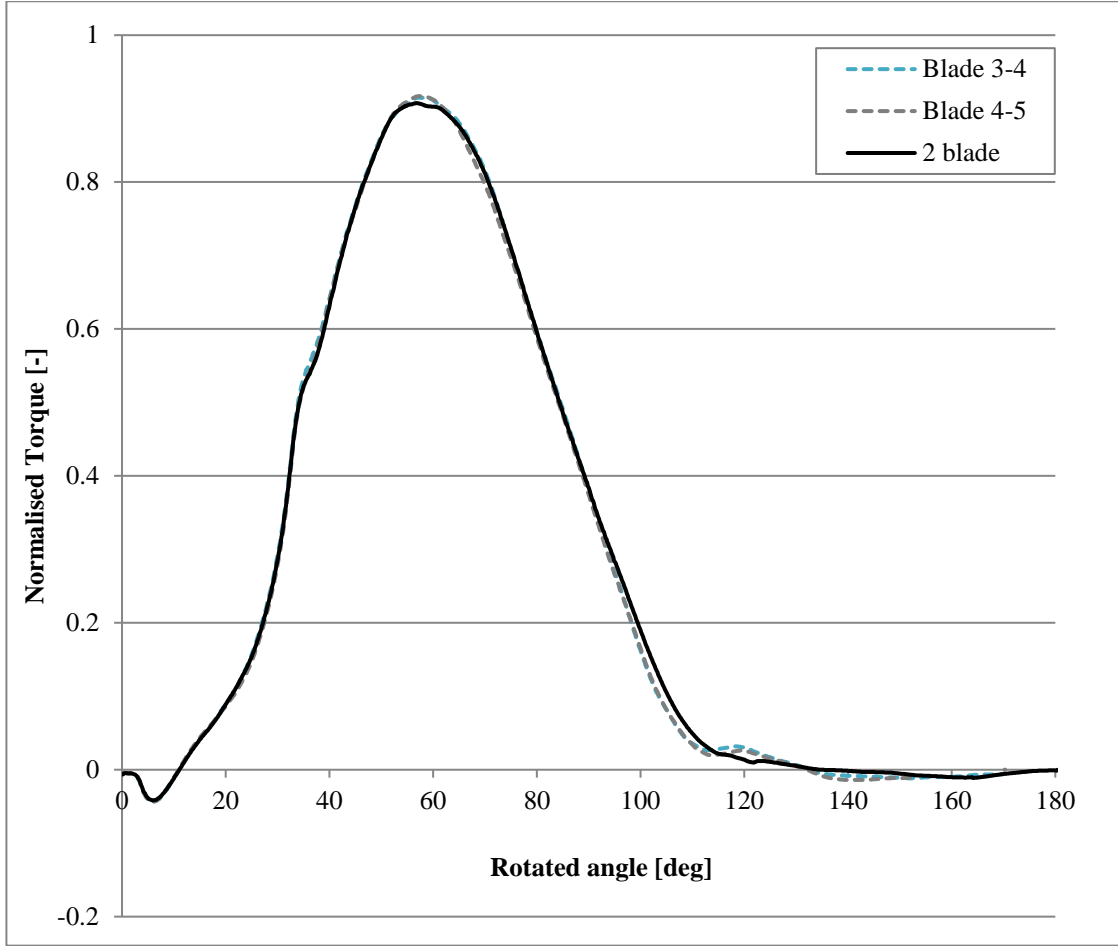


Fig. 3.6. Torque curve comparison for periodic blade passages 3-4, 4-5 and the 2 blade simulation

The results of the periodicity study have shown that the behaviour of the flow through each blade passage is not entirely periodic as there is a small fluctuation in the power captured by each blade. It is unclear whether this fluctuation is real for a full runner in operation or whether it is induced by the difference in the flow traversing the back of the first blade having a cascade effect on the consecutive blades. A simulation using more blades or a full runner would need to be carried out in order to verify this.

For the purpose of this research, it was decided that only a single blade passage (2 blade simulation) will be modelled which although it gives a slightly higher power than the 7 blade average (0.41% normalised power) it should still be able to capture incremental changes in the geometry for the purpose of optimisation.

3.1.1.3 Jet profile

Previous studies have shown that the jet profile, with a lower velocity in the centre of the jet developed as the water flows through the spear/nozzle valve, as well as the secondary velocities created by the upstream pipework and spear holding vanes can have a significant impact on the performance of impulse turbine runners (Peron, Parkinson et al. 2008; Staubli T., Abgottspion A. et al. 2009; Jošt, Mežnar et al. 2010; Benzon, Židonis et al. 2015). For the purpose of optimising the runner geometry however, an ideal jet is used with a uniform velocity profile across the jet. This is based on the assumption that any changes to the runner geometry will be captured using the ideal jet and the impact of the real jet on the runner will be systematic.

3.1.2 Modelling assumptions

As well as the geometric assumptions made in the creation of the modelling domain, a series of assumptions on the definition of the physics used to define the problem as well as the numerical techniques chosen to analyse the problem are made. These modelling assumptions are detailed in this section.

3.1.2.1 Multiphase model

ANSYS® CFX® has the option to use either a homogeneous multiphase model (which is similar to the Volume of Fluid (VOF) model in ANSYS® Fluent®) where all fluids share both pressure and velocity fields as well as other fields which are relevant such as turbulence, temperature etc. and the inhomogeneous model where only the pressure field is shared. Previous studies have shown the homogeneous multiphase model with free surface fluid interaction (where the fluid phases are separated by a distinct interface and defined by their volume fraction) or VOF models to be used predominantly in the numerical analysis of impulse turbines (Zidonis, Benzon et al. 2015). Studies have also shown the homogeneous multiphase model with free surface fluid interaction to give good agreement with experimental results (Zoppe, Pellone et al. 2006; Fiereder, Riemann et al. 2010; Jošt, Mežnar et al. 2010; Zidonis, Benzon et al. 2015).

In addition, by not modelling the casing interaction, which is the only region where violent free surface flow effects such as wave breaking, sloshing and vapour entrapment should be seen, means that the use of the homogeneous multiphase model with free surface fluid interaction can be justified.

3.1.2.2 *Turbulence model*

Turbulent flows are characterised by unsteady, aperiodic motion in which transported quantities such as mass and momentum fluctuate in space and time. Turbulent flows usually contain a wide range of eddy sizes with large eddies often carrying smaller eddies. Instantaneous fluctuations are random and unpredictable in both space and time however statistical averaging of these fluctuations can be used to predict the effect turbulence has on the transport mechanisms.

In most cases, the eddy length scale is smaller than the edge length of the grid being used which is why Direct Numerical Simulation (DNS) of turbulence, which resolves all the turbulence scales, requires incredibly large computational resources. Other Scale Resolving Simulation (SRS) options are available which resolve the larger eddy scales and model the smaller eddy scales which are smaller than the mesh. In ANSYS® CFX®, the SRS options are Large Eddy Simulation (LES) and Detached Eddy Simulation (DES). Although SRS is more accurate when the resolution of the large eddies is important it requires a very fine grid with very small timesteps in order to capture the eddy formation. This results in simulations which are very computationally costly and use up large amounts of data.

Although the flow is unsteady for a single flow passage, the interest in this study is in the periodic nature of the flow which for an infinite number of revolutions is treated as steady. For this reason, the URANS (Unsteady Reynolds Averaged Navier Stokes) turbulence equations can be used, which model all turbulence eddies as opposed to resolving them. All the current studies using CFD to model impulse turbines use URANS turbulence models as the focus is not on the turbulence fluctuations but on the impact the turbulence has on the mean flow. The vast majority of these studies use the two equation $k-\omega$ SST turbulence model (Zidonis, Benzon et al. 2015). Based on this previous work, which showed good comparison with experimental studies, the $k-\omega$ SST turbulence model was used for the runner simulations. Although the results may differ from a more accurate, direct turbulence model it is assumed that this difference will be systematic and cancel out when comparing different designs.

3.1.2.3 *Buoyancy*

As the turbine was modelled with no casing, the water leaving the runner was free to exit the domain without causing any interference with the runner. For this reason, and due to the relatively high velocity of the jet, the effects of gravity on the water velocity are negligible. For example, the distance from the stationary domain inlet to the runner PCD (Pitch Circle

Diameter) D is 196mm. At the ideal jet velocity of 25.4m/s, the jet deviation due to gravity is 0.314mm or 0.091° , which is negligible.

3.1.2.4 Surface tension

The free surface, interface control option was chosen without surface tension as it was assumed that the effects would be negligible. This was validated by carrying out a computational unit test where surface tension was modelled. The surface tension coefficient for water in contact with air at 15°C was taken as 0.0735N/m which gave a reduction in efficiency of 0.02%.

3.1.2.5 Precision

Although it is advised that double precision should be used with simulations containing multiphase flow (ANSYS 2013a), it requires significantly more computational resources. In order to try and reduce the computational cost, single precision was used which when compared to double precision in a unit test showed no measureable difference.

3.2 Simulation setup and analysis

This section details the setup of the runner simulation based on the geometric and modelling assumptions discussed in *3.1 CFD model assumptions*. It also covers the post-processing analysis of the numerical results in order to determine the performance of the runner.

3.2.1 Domain creation

The rotating domain used for the initial numerical analysis of the runner and development of the numerical model was created using the CAD geometry for the 7.5" HCTI Turgo runner provided by the industrial sponsors Gilbert Gilkes & Gordon Ltd (Fig. 3.7).

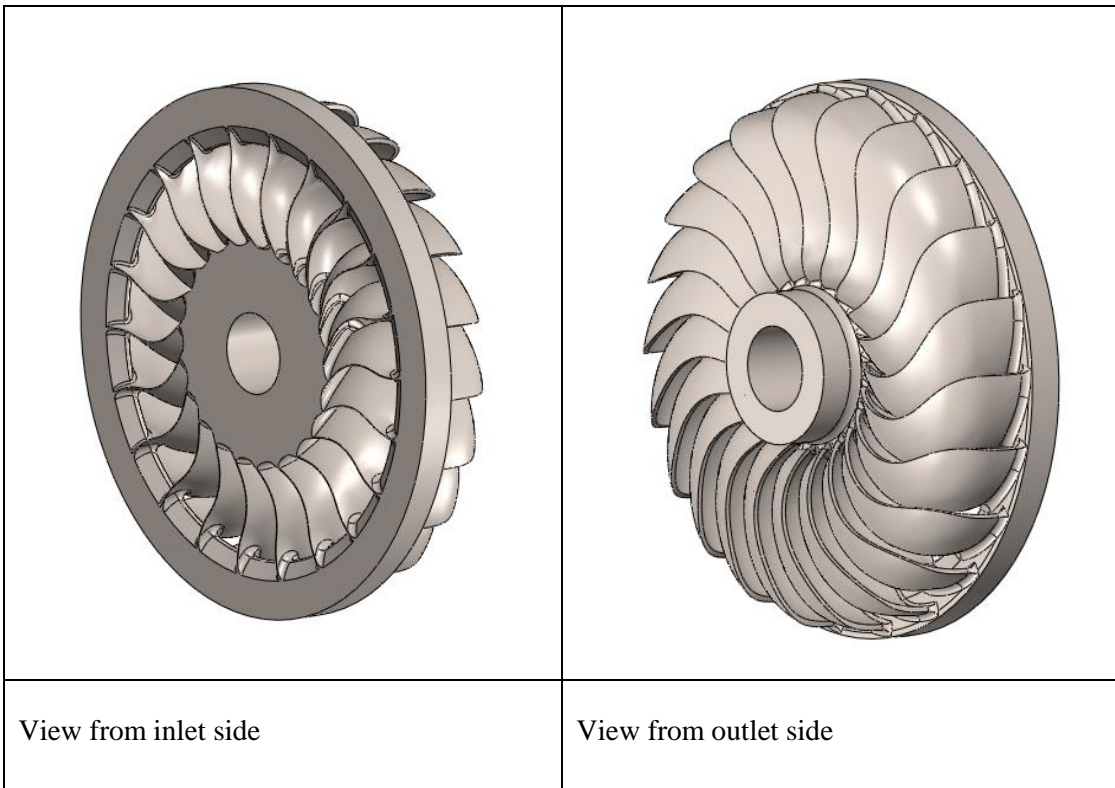


Fig. 3.7. Gilkes 7.5" HCTI runner CAD used for numerical modelling

The runner simulation fluid domains were created using the CAD software Solidworks (Fig. 3.8). The rotating domain, containing the runner blades from the 7.5" HCTI runner CAD, was created by taking the fluid region around a two blade section of the runner, including the ring and hub. For all the runner simulations in this chapter, an ideal jet of uniform velocity was used as mentioned in *3.1.1.3 Jet profile*. The stationary domain was created using the BEP flow conditions from the 7.5" HCTI Turgo Hill chart to determine the diameter of the cylinder containing the jet in the stationary domain which enters the rotating domain at the pitch circle diameter of the runner.

In order to streamline the meshing and simulation setup, named selections were defined in Solidworks using the ANSYS® add-in tool. This allowed naming to be applied to all the faces in each domain which could then be used once the geometry was imported into the meshing software, to apply mesh controls, and to set up the solver physics in CFX® Pre. The named selections used for the stationary and rotating domains are shown in Table 3.1, below.

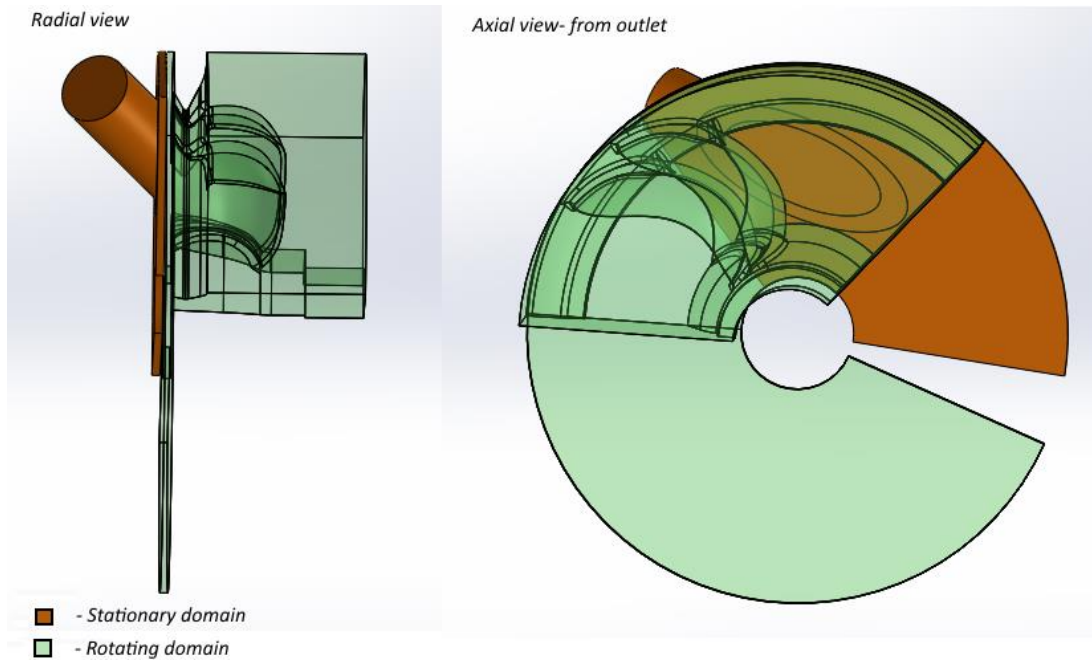


Fig. 3.8. Runner simulation domain geometries created in Solidworks

	Selection Name	Description
Stationary Domain	S_jet_inlet	Jet inlet face
	S_jet_wall	Cylindrical face perpendicular to S_jet_inlet
	S_cyl_if1	Cylindrical face between larger cylinder and shroud
	S_cyl_if2	Cylindrical face between larger cylinder and shroud
	S_interface	Interface surface between stationary and rotating domains
	S_opening	All remaining external faces in stationary domain
Rotating Domain	R_blade1_in	Inside surface of first blade
	R_blade1_le	Leading edge of first blade
	R_blade1_out	Outside surface of first blade
	R_blade1_radsin	Radii on inside surface of 1st blade where meets the ring and hub
	R_blade1_radsout	Radii on outside surface of 1st blade where meets the ring and hub
	R_blade1_te	Trailing edge of first blade
	R_blade2_in	Inside surface of second blade
	R_blade2_le	Leading edge of second blade
	R_blade2_out	Outside surface of second blade
	R_blade2_radsin	Radii on inside surface of 2nd blade where meets the ring and hub
	R_blade2_radsout	Radii on outside surface of 2nd blade where meets the ring and hub
	R_blade2_te	Trailing edge of second blade
	R_interface	Interface surface between rotating and stationary domains
	R_hub	Hub surfaces
	R_shaft	Cylindrical shaft surfaces
	R_ring	Ring surfaces
	R_opening	All remaining external surfaces in rotating domain

Table 3.1- Named selections used on stationary and rotating domain boundaries

3.2.2 Operating conditions

The jet velocity at the inlet to the stationary domain was calculated from the test head and the rotational speed of the rotating domain was taken from the hill chart at the BEP. The operating conditions used to calculate the jet diameter used in the stationary domain and provide the conditions for the runner simulation are provided in Table 3.2.

		7.5" Turgo BEP
PCD	[mm]	190.5
Rotational Speed	[rpm]	1249
Rotational Speed	[rps]	20.81667
ω	[rad/s]	130.795
Velocity@PCD	[m/s]	12.45822
Head	[m]	30.5
Ideal Jet velocity	[m/s]	24.46791
Peripheral jet velocity	[m/s]	22.17545
Flow Rate	[l/s]	37.50524
Q	m^3/s	0.037505
Jet Area	m^2	0.001533
Jet Radius	m	0.022089
Jet Diameter	m	0.044178

Table 3.2- 7.5" Turgo BEP operating conditions used in runner analysis

3.2.3 Meshing

The software used to generate the meshes used in this analysis was ICEM® CFD. The reason why ICEM® was chosen is due to the flexibility it provides with regards to mesh control, such as allowing manual control of vertex positioning around complex features in order to improve mesh quality, an area where more automated solvers often fall short. The methodology used for the meshing of the stationary and rotating domains is detailed in this section.

3.2.3.1 Stationary domain

In order to mesh the stationary domain as efficiently as possible, the domain was split up into a cylinder representing the jet encircled by another cylinder as it enters the shroud region. The two cylindrical regions, shown in blue and amber in Fig. 3.9, could be meshed using structured hexahedral elements. A tetrahedral mesh was created for the shroud region with pyramid elements at the interface to the outer cylinder. The element faces could then be matched at this region while still retaining the mesh

The mesh was improved further by adding an O-grid to the inside of the cylinder so that the inflation layers are on either side of the interface between air and water as the jet enters the

shroud. The size of the elements were also reduced inside the cylinder to better represent the cross-sectional area. The stationary domain mesh had a total of 183k elements or 0.183M elements.

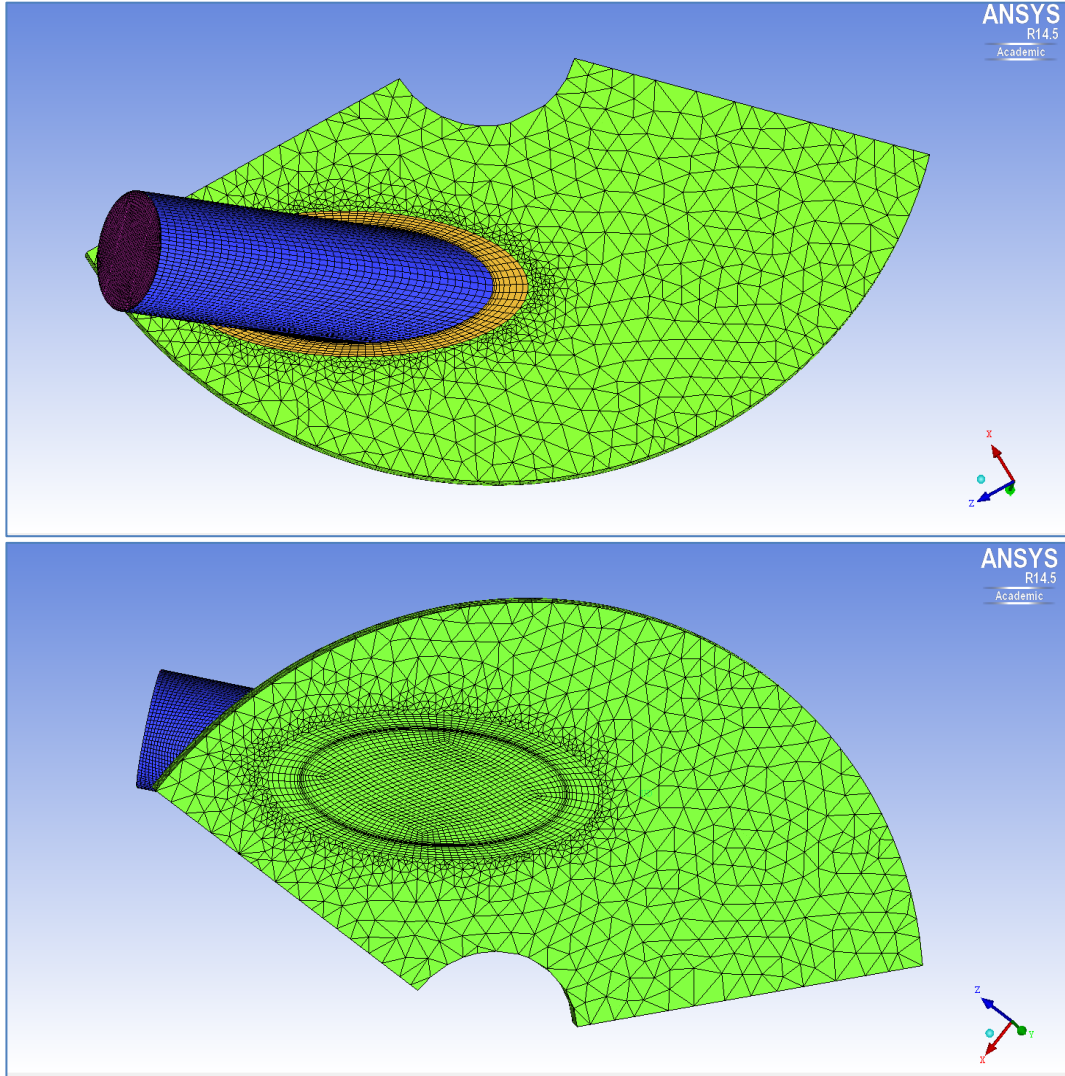


Fig. 3.9. Stationary domain mesh showing structured hexahedral elements combined with tetrahedral elements

3.2.3.2 *Rotating Domain*

The rotating domain was meshed as an unstructured tetrahedral mesh with 5 inflation layers on the wall boundaries. The rotating domain was meshed in four stages.

1. Octree mesh generation

An Octree mesh is generated for the entire domain with the specified mesh sizing parameters. Mesh density regions are added to the leading and trailing edge regions to

better capture the nature of the flow as it enters and leaves the runner. Inflation layers and mesh sizing is specified on the blade surfaces where the torque is being measured.

2. Delaunay mesh generation with smoothing

Once the Octree mesh is generated it is converted into a Delaunay mesh to which some initial smoothing is applied to elements with an orthogonal quality below 0.4.

3. Prism generation

Once the Delaunay mesh has been created, the surface mesh is manually edited in order to remove any bad quality elements and re-smoothed with the same smoothing criteria as step 2. When the orthogonal quality of all the elements is above 0.4, the prism layers are added to the blade surfaces.

4. Final Smoothing

Once the Delaunay mesh is generated along with the prism layers, the unstructured mesh, ignoring the prism layers, is smoothed to remove further any bad quality elements. The orthogonal quality was maintained above 0.2 for all the rotating domain meshes.

Element sizing was applied to the blade surfaces where the torque is measured as well as the leading and trailing edges in order to capture the flow field accurately in this region. This sizing is depicted in the surface mesh shown in Fig. 3.10 and the inflation layers and mesh density regions are shown in Fig. 3.11. The rotating domain mesh for the original runner had a total of 3.10M elements.

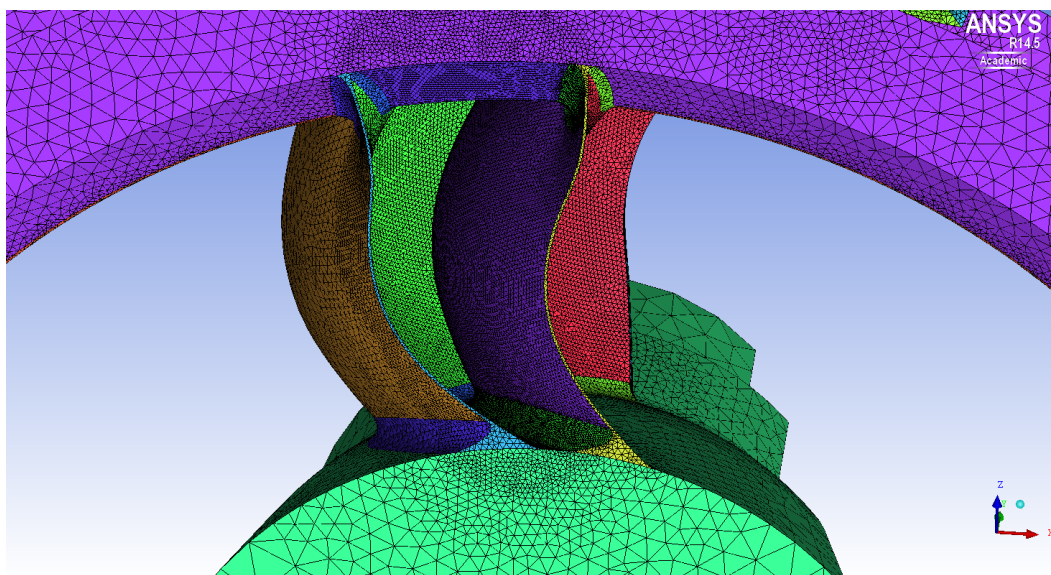


Fig. 3.10. Rotating domain- surface mesh detail

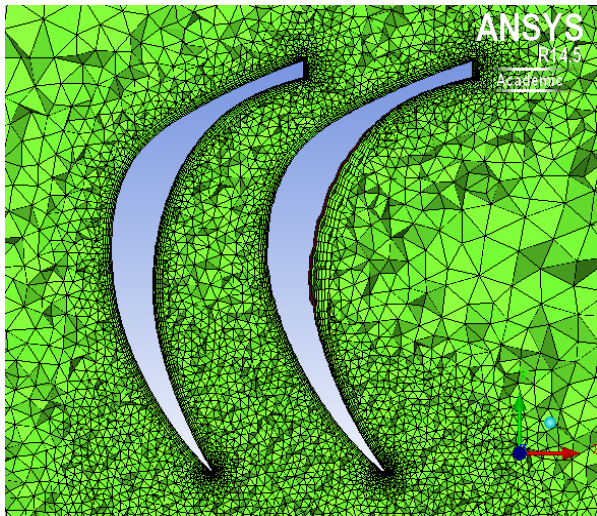


Fig. 3.11. Slice through centre of runner mesh showing mesh density regions and inflation layers

By maintaining the same naming convention for the named selections, shown in Table 3.1, throughout the runner optimisation, the mesh sizing and stages 1 and 2 could be automated using *Replay Control* which records any meshing operations, in a similar way to journal files, allow them to be replayed for future meshes.

3.2.4 Physics definition

The definition of the simulation physics was carried out in CFX-Pre, a pre-processor for ANSYS® CFX®, where the meshes are imported and the simulation is setup (Fig. 3.12). The named selections defined in Solidworks (3.2.1- *Domain creation*) were carried through ICEM® CFD from Solidworks to CFX-Pre and used to define the boundary conditions.

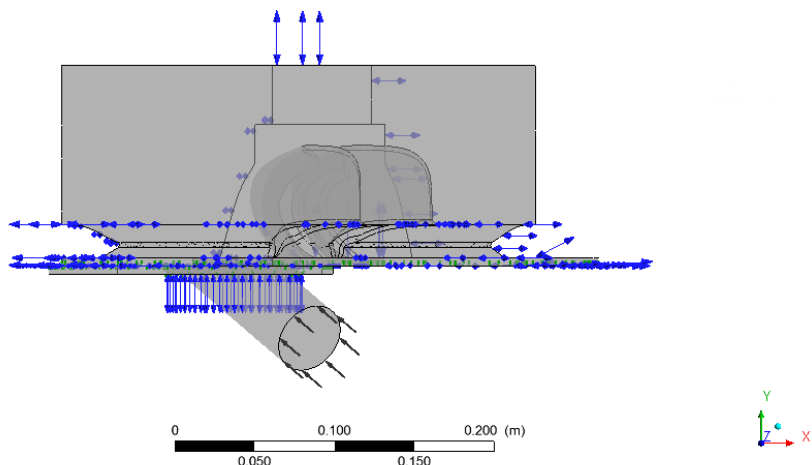


Fig. 3.12. Radial view of stationary and rotating domains in CFX Pre

3.2.4.1 User defined CEL Expressions

ANSYS® CFX® facilitates the creation of user defined expressions which can be used to control the simulation as well as calculate output parameters. The expressions used in the runner simulations to facilitate the automation of the optimisation procedure are given below.

EXPRESSIONS:

Degperstep = 360/2200

Defines the angle to rotate in each timestep.

Rotational Speed = 1249

Defines the rotational speed of the runner at the BEP.

Degpersec = (Rotational Speed*360)/60

Calculates the angular speed in deg/s.

timestat = 0.008[s]

Period of time before runner starts rotating to allow jet to form.

stepstat = 0.00005

Larger time step to be used while jet is being formed.

tstep = Degperstep/Degpersec

Smaller timestep to be used for rest of simulation.

Timestep = (step((timestat-t)/1[s])*stepstat +step \ ((t-timestat)/1[s])*tstep)[s]

Controls timestep size variation during simulation

Total time = timestat+200[s]/Degpersec

Defines the total simulation time in terms of rotated angle (200° in this case).

rpm = (-Rotational Speed*step((t-timestat)/1[s]))[rev min^-1]

Controls the variation in the rotational speed of the runner.

jetvel = 24.46790551 [m s^-1]

Defines the jet velocity at the inlet (ideal jet velocity).

jetvfair = step(((t-165[s]/Degpersec))/1[s])*1

Controls the gradual variation of the air volume fraction at the jet inlet.

jetvfwater = step(((165[s]/Degpersec)-t)/1[s])*1

Controls the gradual variation of the water volume fraction at the jet inlet.

$\text{Torque1b} = -\text{torque_y}() @ R_{\text{blade1_out}}$

Calculates torque on outside of first blade

$\text{Torque1f} = -\text{torque_y}() @ R_{\text{blade1_in}}$

Calculates torque on inside of first blade

$\text{Torque2b} = -\text{torque_y}() @ R_{\text{blade2_out}}$

Calculates torque on outside of first blade

$\text{Torque2f} = -\text{torque_y}() @ R_{\text{blade2_in}}$

Calculates torque on inside of first blade

$\text{massflowin} = \text{Water.massFlow}() @ S_{\text{JET_INLET}}$

Calculates the mass flow rate entering the stationary domain.

$\text{massflowout} = -\text{massFlow}() @ R_{\text{OPENING}}$

Calculates the mass flow rate leaving the rotating domain.

3.2.4.2 Materials

The simulation contained two fluids which were defined under isothermal conditions and constant fluid properties. The fluids were air and water at 15°C which were chosen with a ‘continuous’ morphology option. The material options for each fluid are given in Table 3.3 below.

Fluid name	Density ρ	Dynamic viscosity μ
	[kg/m ³]	[Pa .s]
Water	998.78	1.108*10 ⁻³
Air	1.2257	1.797*10 ⁻⁵

Table 3.3- ANSYS® material properties for air and water at 15°C

3.2.4.3 Domain interfaces

Stationary domain cylinder interface:

The static interface between the structured and unstructured meshes in the stationary domain (Stat_cyl_if1 and Stat_cyl_if2) was a Fluid-Fluid interface with a General Connection.

Stationary and rotating domain interface:

The dynamic interface between the stationary and rotating domains was also a Fluid-Fluid interface with a General Connection however for Pitch Change option, Specified Pitch Angles was chosen with pitch angles of 360° as the rotating domain is simply an arbitrary section of the runner rather than a periodic section.

3.2.4.4 Boundary conditions

In order to solve the differential form of the governing equations, they have to be closed by specifying boundary conditions. The boundary conditions used in the runner simulations are detailed in Table 3.4 below.

	Boundary name	Location	Type	Boundary details	Fluid values
Stationary Domain	S_jet_inlet	S_jet_inlet	Inlet	Flow regime: Subsonic Mass and momentum: Normal speed Value: jetvel Turbulence: Medium (Intensity=5%)	Air Volume Fraction: Value: jetvfair, Water Volume Fraction: Value: jetvfwater
	S_jet_wall	S_jet_wall	Wall	Mass and momentum: Free slip wall	n/a
	S_interface Side 1	S_cyl_if1	Interface	Mass and momentum: Conservative interface flux Turbulence: Conservative interface flux	n/a
	S_interface Side 2	S_cyl_if2	Interface	Mass and momentum: Conservative interface flux Turbulence: Conservative interface flux	n/a
	Fluid Interface Side 1	S_interface	Interface	Mass and momentum: Conservative interface flux Turbulence: Conservative interface flux	n/a
	S_opening	S_opening	Opening	Flow regime: Subsonic Mass and momentum: Entrainment Relative Pressure: Value: 0Pa Turbulence: Zero gradient	n/a

Rotating Domain	R_blade1_in	R_blade1_in R_blade1_radsin R_blade1_le R_blade1_te	Wall	Frame type: Rotating Mass and momentum: No slip wall Roughness: Smooth wall	n/a
	R_blade1_out	R_blade1_out R_blade1_radsout	Wall	Frame type: Rotating Mass and momentum: No slip wall Roughness: Smooth wall	n/a
	R_blade2_in	R_blade2_in R_blade2_radsin R_blade2_le R_blade2_te	Wall	Frame type: Rotating Mass and momentum: No slip wall Roughness: Smooth wall	n/a
	R_blade2_out	R_blade2_out R_blade2_radsout	Wall	Frame type: Rotating Mass and momentum: No slip wall Roughness: Smooth wall	n/a
	R_ring	R_ring	Wall	Frame type: Rotating Mass and momentum: No slip wall Roughness: smooth wall	n/a
	R_hub	R_hub R_shaft	Wall	Frame type: Rotating Mass and momentum: No slip wall Roughness: Smooth wall	n/a
	R_opening	R_opening	Opening	Frame type: Rotating Flow regime: Subsonic Mass and momentum: Entrainment Relative Pressure: Value: 0Pa Turbulence: Zero gradient	Air Volume Fraction: Value: 1 Water Volume Fraction: Value: 0
	Fluid Interface Side 1	R_interface	Interface	Mass and momentum: Conservative interface flux, Turbulence: Conservative interface flux	n/a

Table 3.4. Runner simulation stationary and rotating domain boundary conditions

3.2.4.5 Initialisation

The initial conditions in both the stationary and rotating domains for the runner simulations are the whole domain filled with air (Air Volume Fraction=1 and Water Volume Fraction=0) at a velocity of 0m/s.

3.2.4.6 Timestep

The timestep is a critical parameter in any transient simulation. It is advised that the optimum timestep for transient simulations maintain a Courant number below 1, where for a one dimensional grid:

$$\text{Courant number} = \frac{udt}{dx} \quad (3.1)$$

The Courant number is calculated in CFX® for each timestep as a multidimensional generalisation of equation (3.1). Maintaining a value below 1 helps to ensure that the flow doesn't move across more than one cell during a single timestep. This means that the Courant number is highest when the flow is travelling through the densest regions of the mesh, with the highest velocity which in this case is when the jet enters the rotating runner blades. It is for this portion of the simulations that the Courant number is monitored. The timestep in these simulations is controlled by the angle rotated in each timestep given by *Degperstep* in the CEL expressions. A very conservative timestep of 1.46×10^{-5} s was initially chosen to maintain a RMS Courant number below 0.5, however a timestep study was also carried out in order to try and reduce the simulations time by using as large a timestep as possible without affecting the results.

Table 3.5 shows the differences in the normalised efficiencies for the 5 time step variations and the torque curves for these simulations are shown in Fig. 3.13. Although the torque curves show very similar results, the difference in the normalised efficiencies for each timestep is more pronounced, showing quite a substantial drop (1.75%) between the original timestep of 1.46×10^{-5} s and the largest timestep of 5.46×10^{-5} s. Based on these results, a timestep of 2.18×10^{-5} s was chosen as the difference in normalised efficiency is only 0.3% compared to the original timestep but the solve time is nearly 10 hours shorter.

		Timestep= 1.46e-5s	Timestep= 2.18e-5s	Timestep= 4.37e-5s	Timestep= 5.46e-5s
Mean Velocity	[m/s]	24.46	24.46	24.46	24.46
Mass Flow rate	[kg/s]	37.34	37.34	37.34	37.34
Omega	[rad/s]	130.79	130.79	130.79	130.79
Normalised efficiency	[%]	100.00%	99.70%	98.83%	98.25%
Solve Time	hrs, min	38hrs 45min	28hrs 55min	18hrs 1min	17hrs 7min

Table 3.5- Average torque and efficiencies for varied timesteps

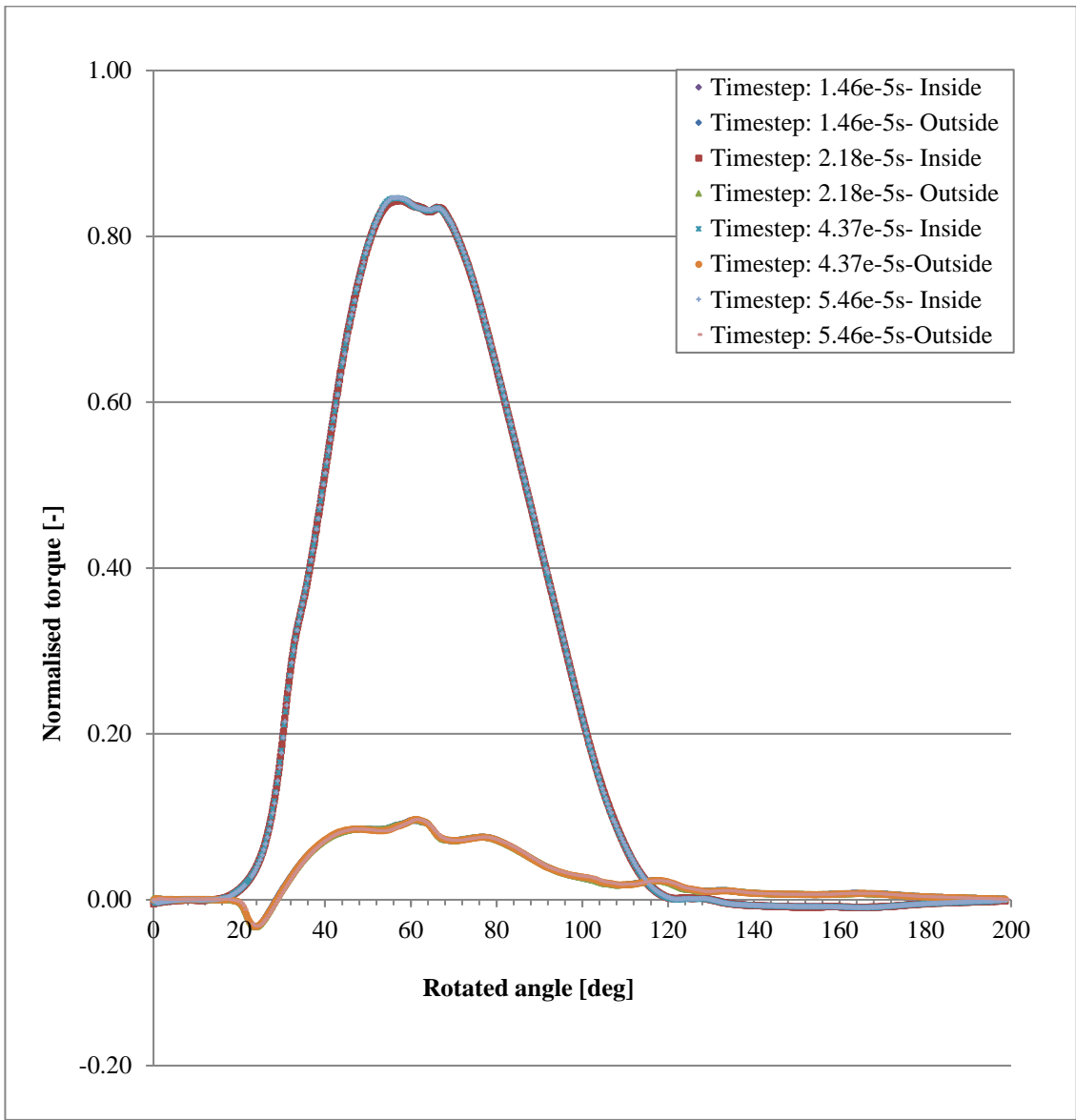


Fig. 3.13. Torque curves comparison for varying timestep

3.2.5 Solver definition

3.2.5.1 Solver control

The High Resolution advection scheme was chosen which uses a Fourth Order numerical model and blends to Second Order near pressure extrema. This is recommended by the ANSYS® *Solver Modelling Guide* as it gives a good balance between robustness and accuracy (ANSYS 2013a). For the transient scheme, the Second Order Backward Euler option was chosen which is generally recommended for transient runs in CFX®.

3.2.5.2 Residual target

ANSYS® describes a residual target of 1e-4 as being sufficient for most engineering applications (ANSYS 2013a). In order to investigate this, two simulations were run with a residual target of 1e-6 and 1e-4. The timestep was fixed at a conservative 1.46e-5s giving an average courant number of around 0.2. Fig. 3.14 shows that the torque curves for the two simulations are almost identical and the calculated efficiency differed by only 0.02%. The simulation with the residual target of 1e-4 took 38hrs and 45mins to solve compared to 97hrs and 10mins for the 1e-6 residual target simulation.

It was decided that the residual target will be set at 1e-4, giving a 250% reduction in simulation time compared to using 1e-6.

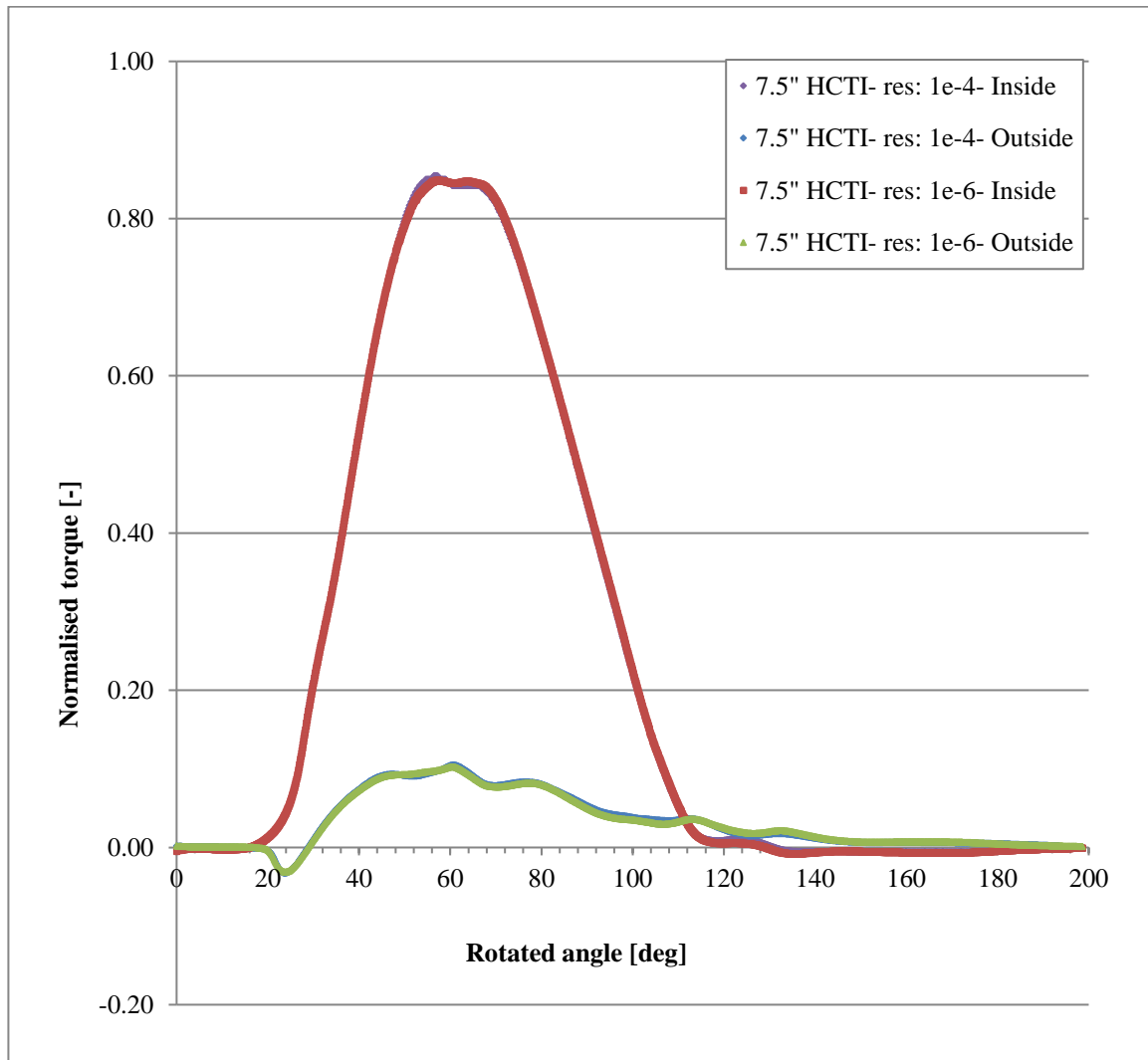


Fig. 3.14. Torque curves comparison HCTI runner simulations with varied residual targets

3.2.5.3 Solver settings

A unit test was carried out which found that single precision produces almost identical results to double precision while significantly reducing the simulation time and memory requirements. Therefore, single precision was chosen for the runner simulations. The chosen run mode was Platform MPI Local Parallel with 4 partitions. All the simulations were carried out using a quad core 3.4GHz Intel Xeon processor with 32GB of RAM.

3.2.6 Results processing

Once the simulation has solved, the results are processed accordingly. Although detailed plots are often carried out showing the velocity profiles, pressure contours and jet interaction, the primary output from these simulations is the runner hydraulic efficiency which is calculated as follows.

The torque is calculated and plotted for the inside of the first blade and the outside of the second blade for each timestep using the expressions given in 3.2.4.1 *User defined CEL Expressions*. These two torques are then summed together to give the total torque for a single blade passage as shown in Fig. 3.15.

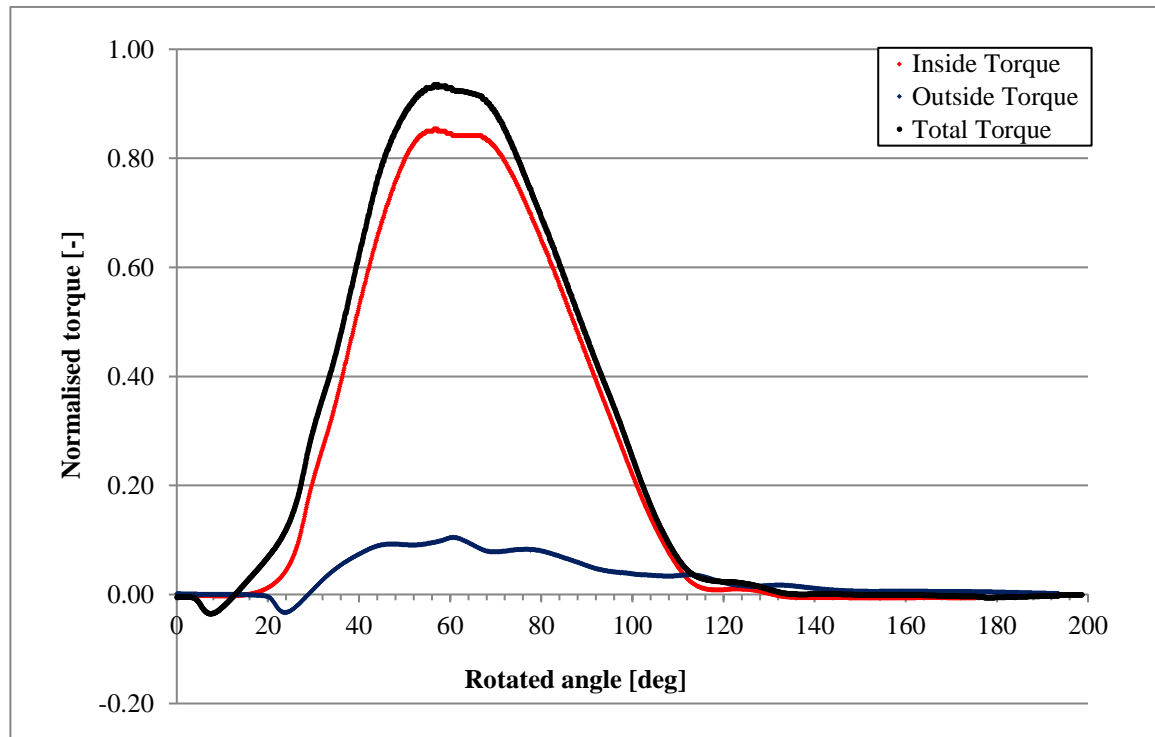


Fig. 3.15. Summing torques on inside and outside blade surfaces to give total torque

The torque is then numerically integrated using the Trapezium rule to give the area under the total torque curve or the Work done by a single blade.

$$W = \int_b^a M(\theta) d\theta = \frac{1}{2} \sum_{i=1}^n (M(\theta_{i+1}) + M(\theta_i))(\theta_{i+1} - \theta_i) \quad (3.2)$$

The time for a single revolution can be calculated as:

$$t = \frac{2\pi}{\omega} \quad (3.3)$$

Using equations (3.2) and (3.3), the Power produced by the full runner, where N_B is the number of blades, can be calculated as:

$$P_{out} = \frac{N_B W}{t} \quad (3.4)$$

In order to calculate the runner efficiency, the power input P_{in} is required, which for an ideal jet, as used in the runner simulations, is given by:

$$P_{in} = \frac{\dot{m} \bar{u}^2}{2} \quad (3.5)$$

Using equations (3.4) and (3.5), the runner efficiency can be calculated as:

$$\eta = \frac{P_{out}}{P_{in}} \quad (3.6)$$

3.2.7 Simulation Sequence

In order to calculate the full torque acting on the runner, assuming periodic behaviour, the development of a complete single torque curve is needed as shown in Fig. 3.15. This requires sufficient time for the flow to enter and completely evacuate the single blade passage being simulated. It was found through observation of the flow that 200 degrees of rotation, over a period of 34.6ms is sufficient. This runner simulation is split into two phases as described below.

3.2.7.1 Phase 1: Jet initialisation

Before the runner begins rotation, the jet is initialised behind the runner blades for a time period *timestat*, given in 3.2.4.1 *User defined CEL Expressions*. A larger timestep (*stepstat*) is also used for this phase in order to speed up the overall simulation. The initialisation of the jet before the runner starts rotating is shown in Fig. 3.16.

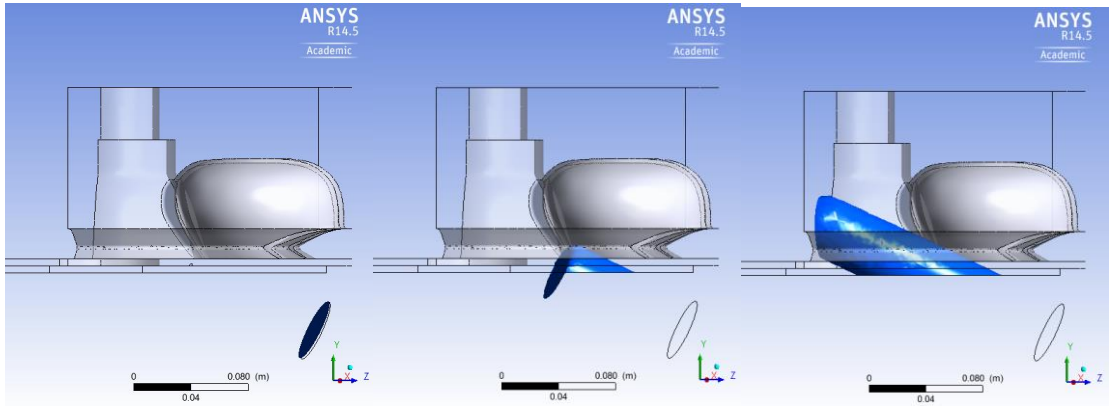
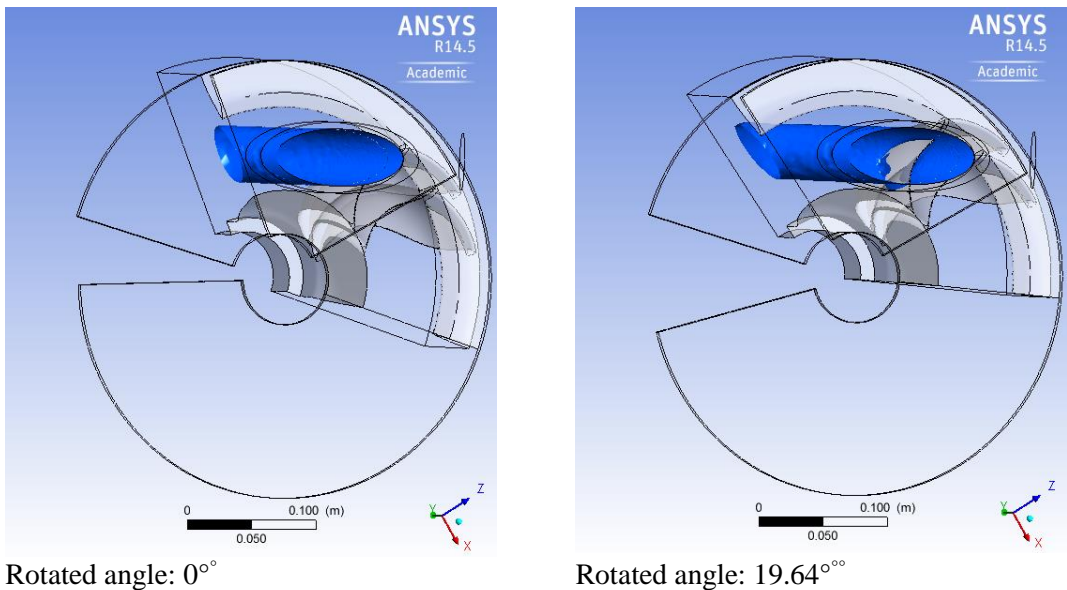


Fig. 3.16. Phase 1: Jet initialisation, showing surface of jet using an isosurface with Water Volume Fraction=0.5

3.2.7.2 Phase 2: Runner rotation

Once the jet has been fully formed and Phase 1 is complete, Phase 2, the rotation of the runner begins. During Phase 2, a smaller timestep is used given by *tstep* in 3.2.4.1 *User defined CEL Expressions*. The runner is rotated by a total of 200° as shown in Fig. 3.17, until the water has completed evacuated both the inside of the first blade and the outside of the second blade and the torque measured on both blade surface is ~ 0 .



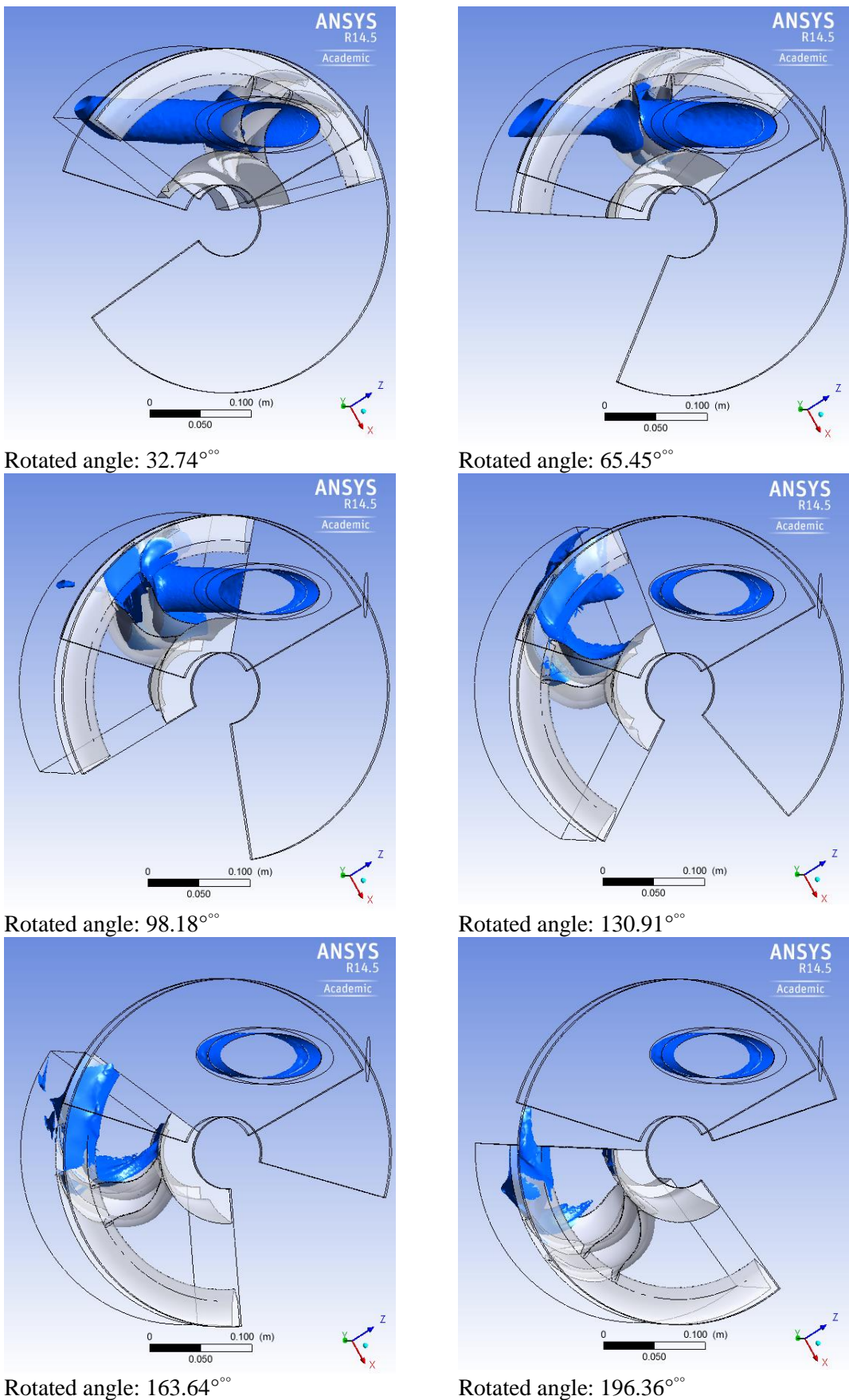


Fig. 3.17. Phase 2: Runner rotation- showing surface of jet using an isosurface with Water Volume Fraction=0.5

3.3 Mesh refinement study

A mesh refinement study was carried out using the 3.10M element runner mesh described in 3.2.3 *Meshing* in order to investigate the discretisation error. The Grid Convergence Index (GCI) for the uniform reporting of grid refinement studies suggested by (Roache 1994) was used. Three meshes were created using a refinement ratio $r = 1.6$ with the coarsest mesh containing 3.10M elements and the finest mesh containing 10.65M elements. The results of the three meshes, normalised to the coarsest mesh result are shown in Table 3.6 below. The results are also plotted in Fig. 3.18.

Mesh # []	Normalised grid spacing []	Number of elements [Millions]	Normalised efficiency [%]
1	1.00	3.10	100.00%
2	0.56	7.6	100.63%
3	0.31	10.95	100.98%

Table 3.6- Mesh refinement study results- normalised to coarsest mesh

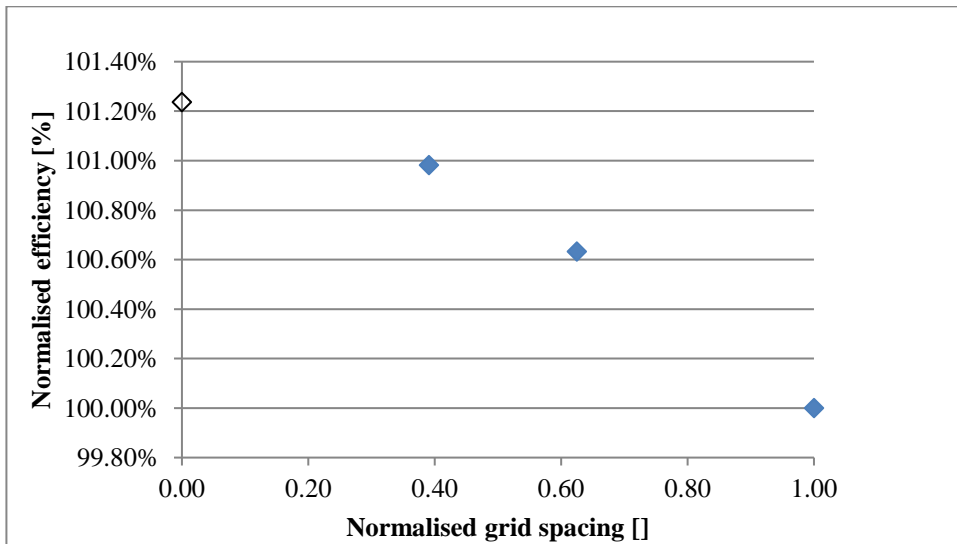


Fig. 3.18. Mesh refinement study results: normalised efficiency against normalised grid spacing

As the grid spacing is reduced, the efficiency approaches the asymptotic zero grid spacing value. The order of convergence, p_c , can be calculated using equation (3.7) below.

$$p_c = \frac{\ln\left(\frac{\eta_1 - \eta_2}{\eta_2 - \eta_3}\right)}{\ln(r)} \quad (3.7)$$

Where η_n is the efficiency for each mesh and n is the mesh number.

Using the order of convergence obtained, the efficiency at zero grid spacing, $\eta_{h=0}$, can be determined using a Richardson extrapolation of the two finest meshes.

$$\eta_{h=0} = \eta_3 + \frac{\eta_3 - \eta_2}{2^{p_c} - 1} \quad (3.8)$$

This gives a zero grid spacing efficiency of 101.24% which is also plotted in Fig. 3.18.

The order of convergence can also be used to calculate the GCI using a safety factor S_f of 1.25 as suggested by (Roache 1994) for grid convergence studies using three or more grids. The GCI for Mesh 3 & 2 and Mesh 3 & 1 can be calculated as:

$$GCI_{32} = \frac{F_s(\eta_3 - \eta_2)/\eta_3}{r^{p_c} - 1} \quad (3.9)$$

$$GCI_{31} = \frac{F_s(\eta_3 - 1)/\eta_3}{r^{p_c} - 1} \quad (3.10)$$

The grid convergence indexes are given in Table 3.7 below.

Refinement ratio	r	1.6
Order of convergence	p_c	1.0025
Safety factor	F_s	1.25
GCI for meshes 3 and 2	GCI_{32}	0.54%
GCI for meshes 2 and 1	GCI_{21}	0.98%
GCI for meshes 3 and 1	GCI_{31}	1.52%

Table 3.7- Mesh refinement study: Grid Convergence Indexes

Equation (3.11) can be used to check if the solutions are within the asymptotic range.

$$\frac{GCI_{21}}{r^{p_c} \cdot GCI_{32}} = 1.003 \quad (3.11)$$

The result is very close to 1 which indicates that the solutions are well within the asymptotic range.

Fig. 3.19 shows the normalised torque curves on the inside of the first blade and the outside of the second blade for each mesh used in the mesh refinement study. The timestep was fixed for each simulation at 2.18e-5s which was shown to produce accurate results in 3.2.4.6 *Timestep*. The results show a systematic difference in the peak torque on both the inside and the outside of each blade. It is important to note that although the magnitude of the torque differs as the number of elements increases, the general shape of the torque curve is still captured with the coarser mesh (Mesh 1).

Table 3.8 shows the time taken for each simulation in the mesh refinement study to run using a quad core 3.4GHz Intel Xeon processor with 32GB of RAM. The results of this mesh

refinement study have shown that Mesh 1 (*Coarse mesh*) would be suitable for the optimisation studies as the absolute error (given in Table 3.7) is only 1.52% and it is assumed that this error will cancel out when comparing different runner designs. The computational time is also low enough (at just over 2 days) to allow many model variations to be run for the purposes of optimisation. Mesh 3 (*Fine mesh*) will also be used periodically to verify the optimisations made using Mesh 1.

	Mesh 1	Mesh 2	Mesh 3
No. Elements (M)	3.15	7.59	10.95
Timestep	2.18E-05	2.18E-05	2.18E-05
Solve Time	2days, 1hr	5 days, 20 hrs	8days 14hrs

Table 3.8- 2 bladed mesh study solve times

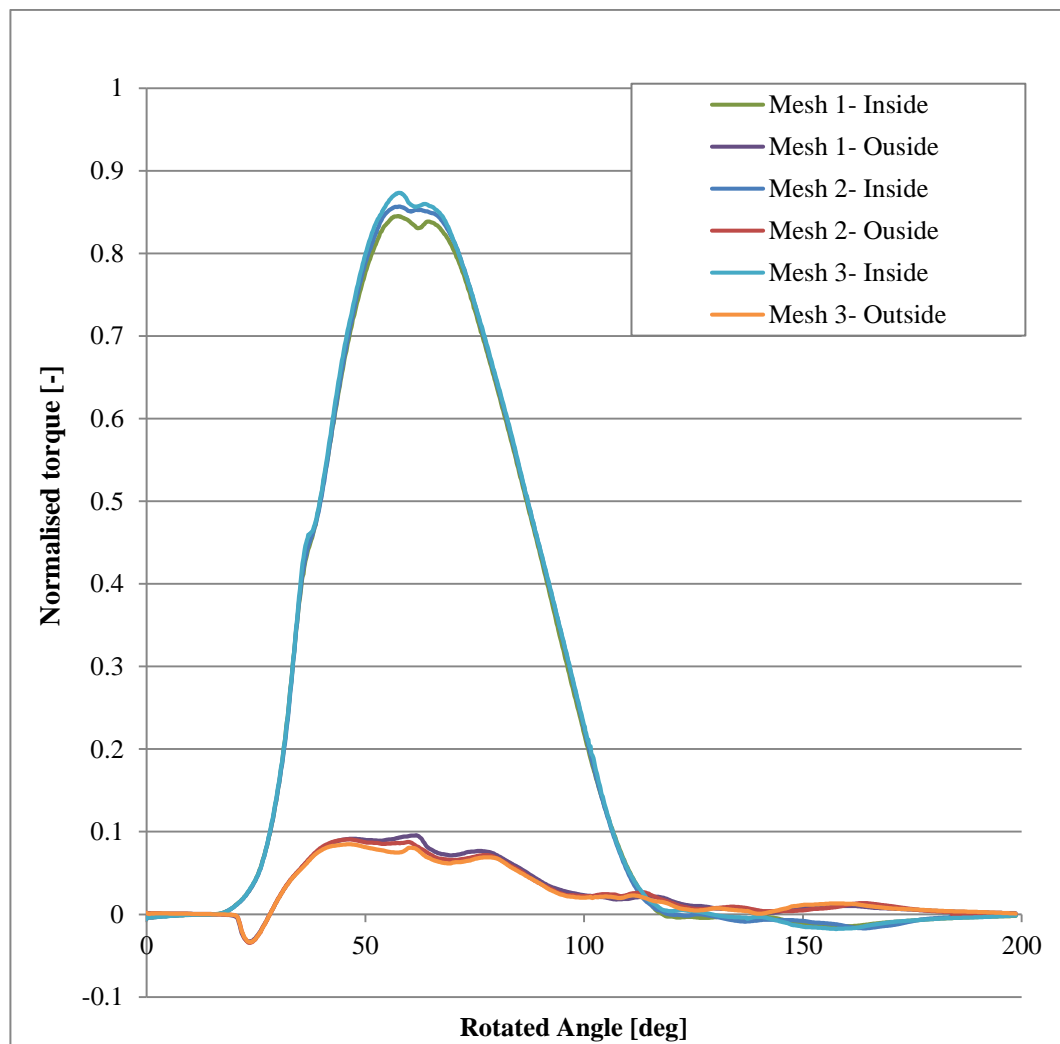


Fig. 3.19. Mesh refinement study- torque curves

3.4 Summary of Turgo runner CFD modelling

This chapter has presented the general principles behind the CFD model used to analyse the Turgo runner and discussed, justified and attempted where possible to quantify the assumptions introduced. The creation of the modelling domains, meshes, definition of the solver physics and general setup of the simulation as well as the post-processing of the results has also been discussed in detail. The relative numerical errors based on the assumptions discussed in this chapter are given in Table 3.9 below. The total numerical error is calculated using the root-sum-square (RSS) method. It should be noted that although most of the geometric sources of error in the runner numerical model have been accounted for there could be further sources of error not included, such as the casing effects. There could also be additional errors arising from the turbulence model used which was not compared to a SRS model which would be more accurate albeit with a higher computational cost. The error as a result of the jet profile, using an ideal jet and not a real jet is purposefully not included in this table as its effects are investigated in more detail in chapter 9 *CFD model verification*. Further sources of error not included in this table could arise from the turbulence modelling, boundary layer resolution or multiphase model and would require further analysis in order to determine their effects.

Source of error	<i>Coarse mesh-</i> Numerical error δ [%]	<i>Fine mesh-</i> Numerical error δ [%]
Periodicity	0.12	0.12
Buoyancy	0.00	0.00
Surface tension	0.02	0.02
Single precision	0.00	0.00
Timestep	0.30	0.30
Discretisation error	1.52	0.54
Total (RSS)	1.55	0.62

Table 3.9- Relative numerical uncertainties for the coarse and fine mesh runner simulations

4 Turgo runner optimisation

The hydraulic efficiency optimisation process used for the Turgo runner is described in this chapter using the CFD model developed in *3 Turgo runner analysis*. The parametric investigation leading to the optimisation of the runner is carried out in three phases:

1. Phase 1: Initial design changes
2. Phase 2: Blade shape Design of Experiments (DOE) study
3. Phase 3: Additional parameters

All the simulations are run using the *coarse mesh* described in *3.3 Mesh refinement study*. The design changes made at the end of each phase are then verified using the *fine mesh*. A full FEA (Finite Element Analysis) is then carried out on the optimised runner design in *5 Turgo runner Finite Element Analysis (FEA)*, where the design is strengthened and two optimised designs are chosen for manufacturing and testing (LE4 and LE1).

4.1 Geometry parameterisation

Before beginning the parametric investigation leading to the optimisation of the Turgo, the geometry had to be parameterised into a series of guide curves and surfaces which could be easily manipulated to vary the design parameters being investigated. Although a parameterised version was provided by Gilkes (Fig. 4.1), it was built around the existing ring design, making it difficult to vary the design of the ring or adjust the size and maintain the same blade shape.

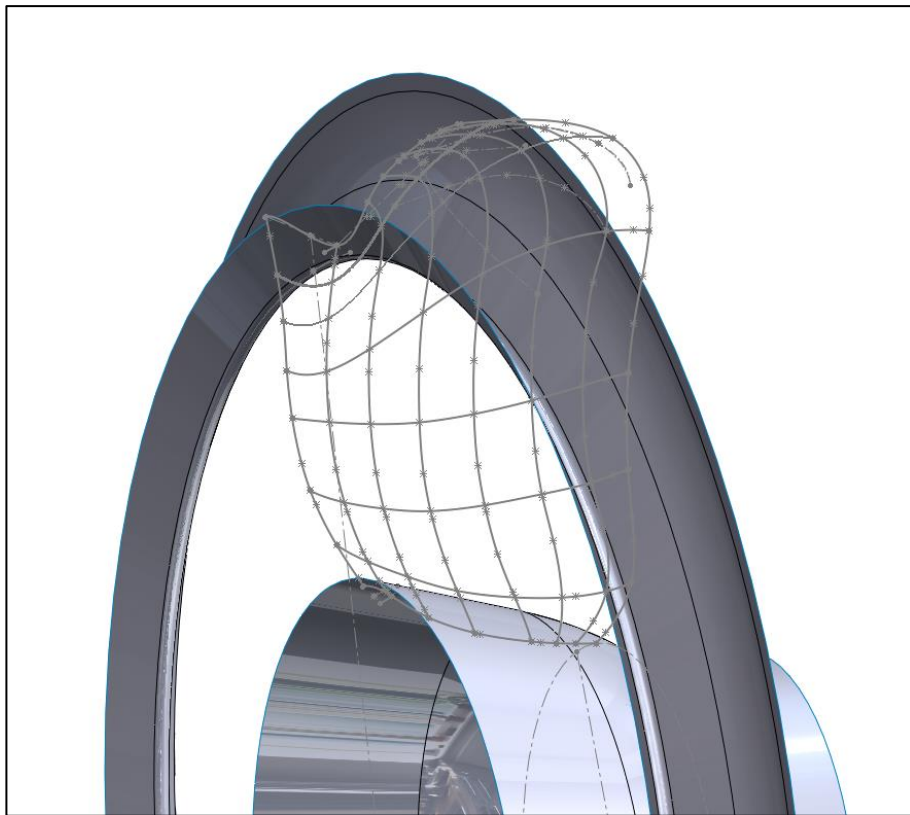


Fig. 4.1. HCTI Geometry provided by industrial sponsors

To facilitate the optimisation process, the blade geometry was reconstructed into a more structured series of guide curves making it easier to vary the design of the ring, blade surfaces and inlet and exit angles during the optimisation process.

It was found through a series of trials that that shape of the HCTI blade could be captured sufficiently using curves on the 8 planes shown in Fig. 4.2 as well as the leading and trailing edge curves. A split line was created at each intersection between the planes and the original geometry and a spline curve drawn over this to create the curves for the new geometry. The spline control points could then be adjusted to match the spline curves to the original geometry curves. Using this method, the geometry could be altered and compared to the original curves during the design variation.

The three dimensional boundary curves were projected onto 2D surfaces allowing parametric changes to be made to these curves in 2D.

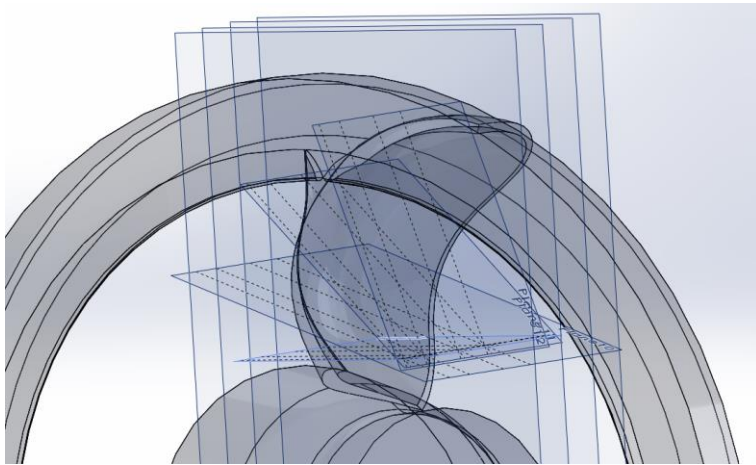


Fig. 4.2. Planes used to split blade into 5x6 Grid

The control curves used to generate each blade surface are shown in Fig. 4.3, below.

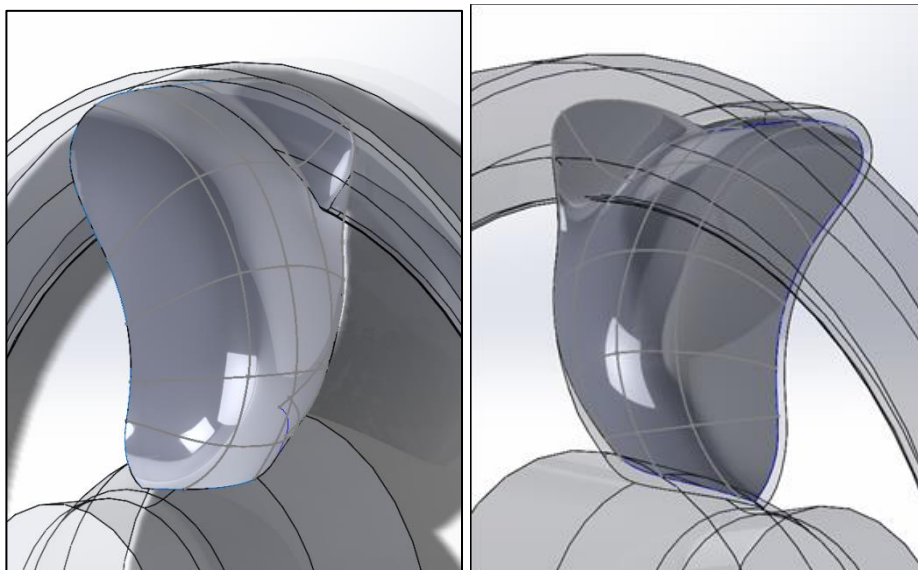


Fig. 4.3. Blade surface control curves for the inside (left) and outside (right) blade surfaces

Using these control curves, the blades could be re-drawn independent of the ring profile allowing the blade and ring geometries to be varied independently. Fig. 4.4 below shows the original geometry in red overlaid by the parameterised geometry in grey. The cut sections show how well the geometry has been captured by the new control curves.

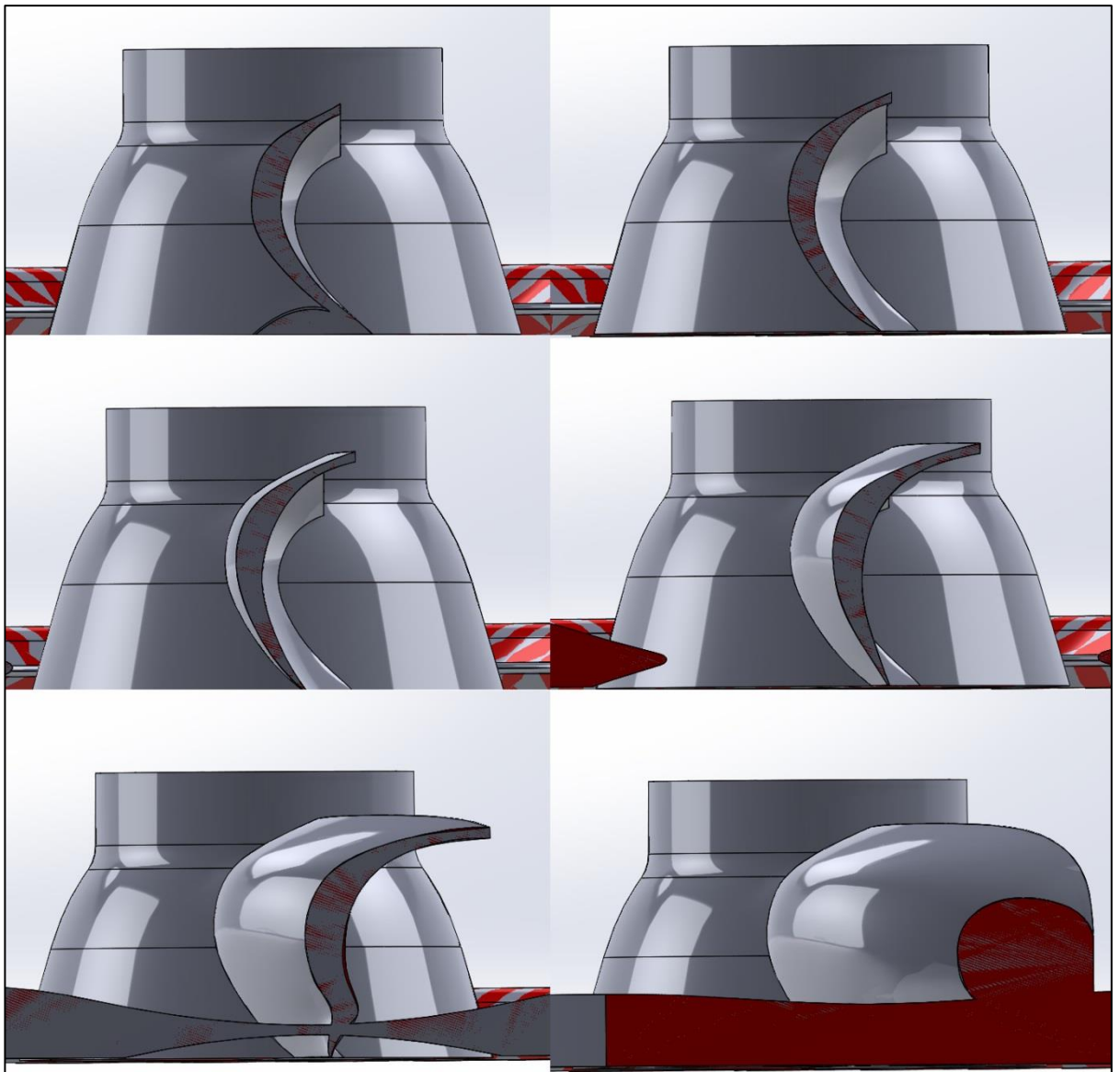


Fig. 4.4. Comparison between original (red) and parameterised (grey) geometry

4.1.1 Parameterised Geometry Verification

In order to verify that the parameterised geometry (P000) has captured the geometry and resultant performance of the HCTI Runner a comparative simulation was run. The resultant torque curves can be seen in Fig. 4.5. Although there are some small differences in the shape of the curves at around 60° rotation, the difference in normalised efficiency is only 0.4%.

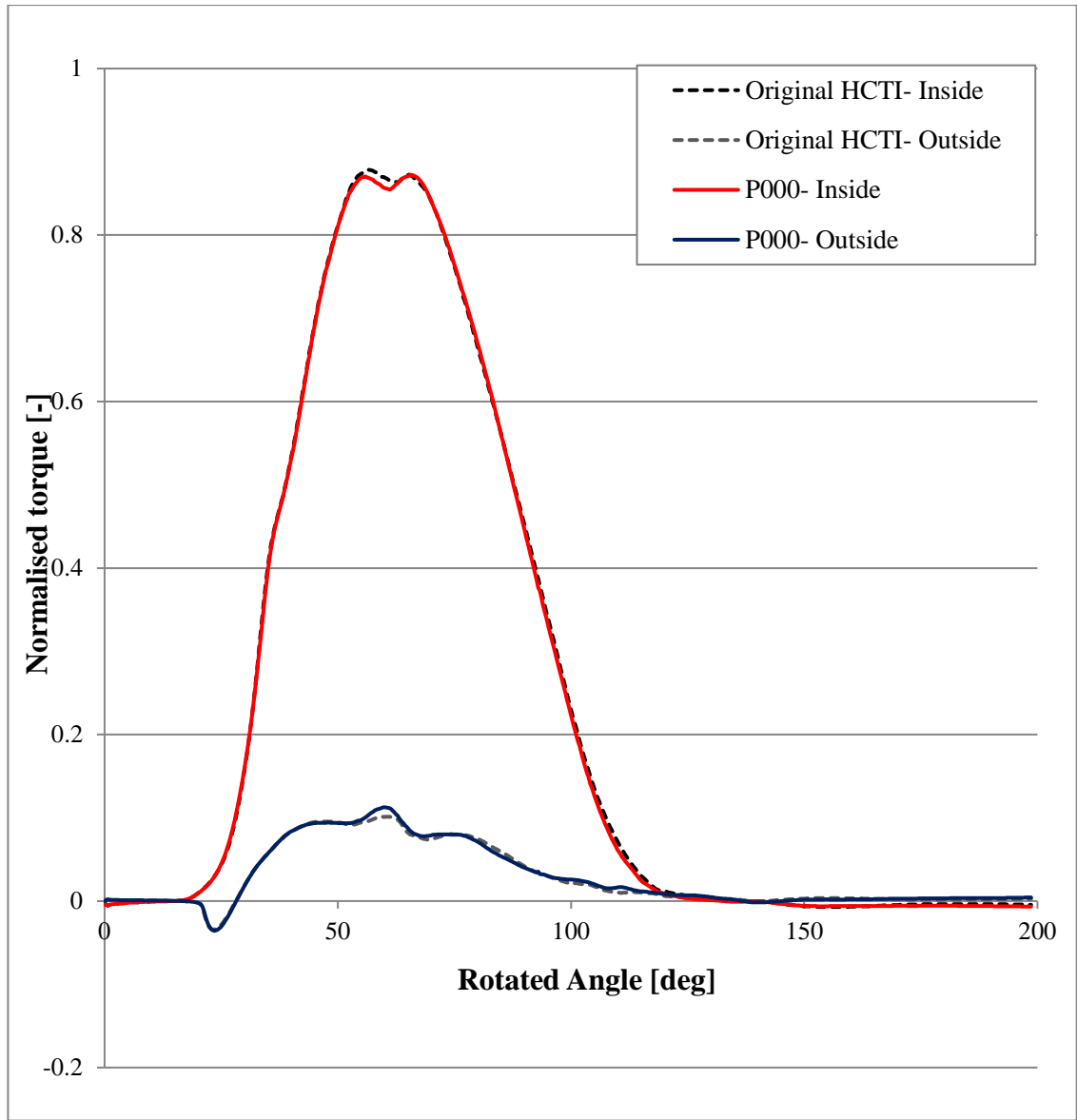


Fig. 4.5. Parameterised geometry torque curves compared to original at same operating point

The pressure contours on the inside and outside surfaces of the first and second blade are compared for the original HCTI and P000 runners in Fig. 4.6 and Fig. 4.7 at 60° rotation respectively. The results showed very little difference in the pressure contours on the inside and outside of each blade and therefore, although the torque curves and efficiencies differed slightly, as an initial design the P000 was acceptable.

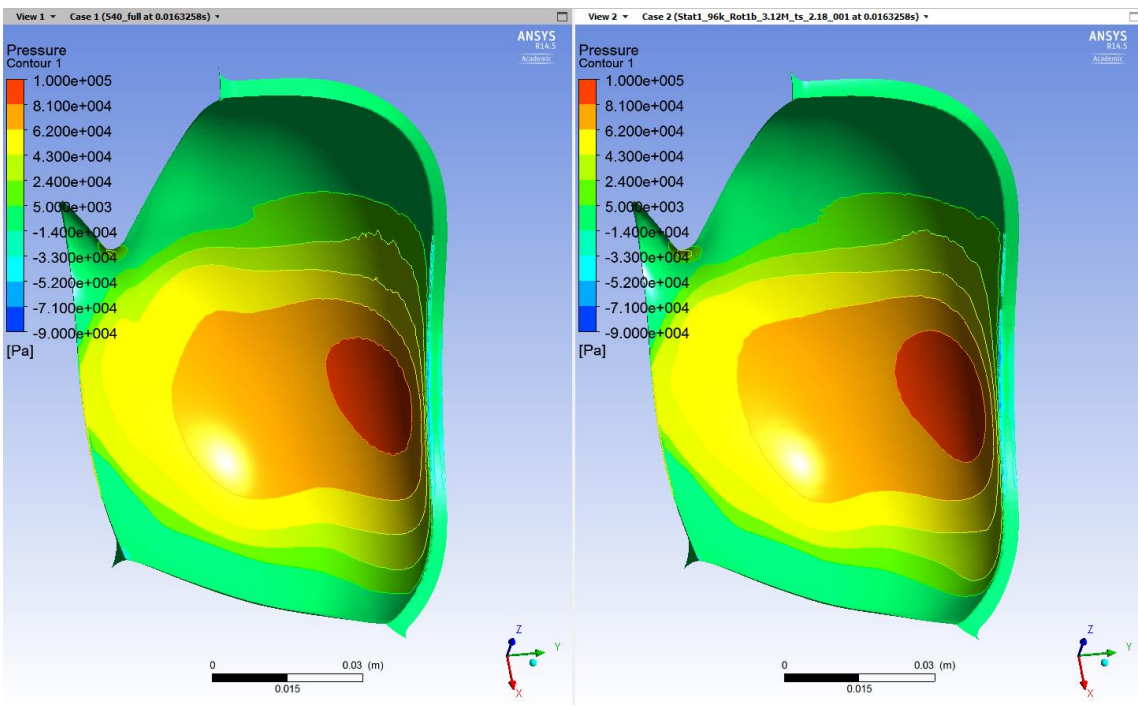


Fig. 4.6. Pressure contours on the inside of the first blade at 60° rotation- Original (left) P000 (right)

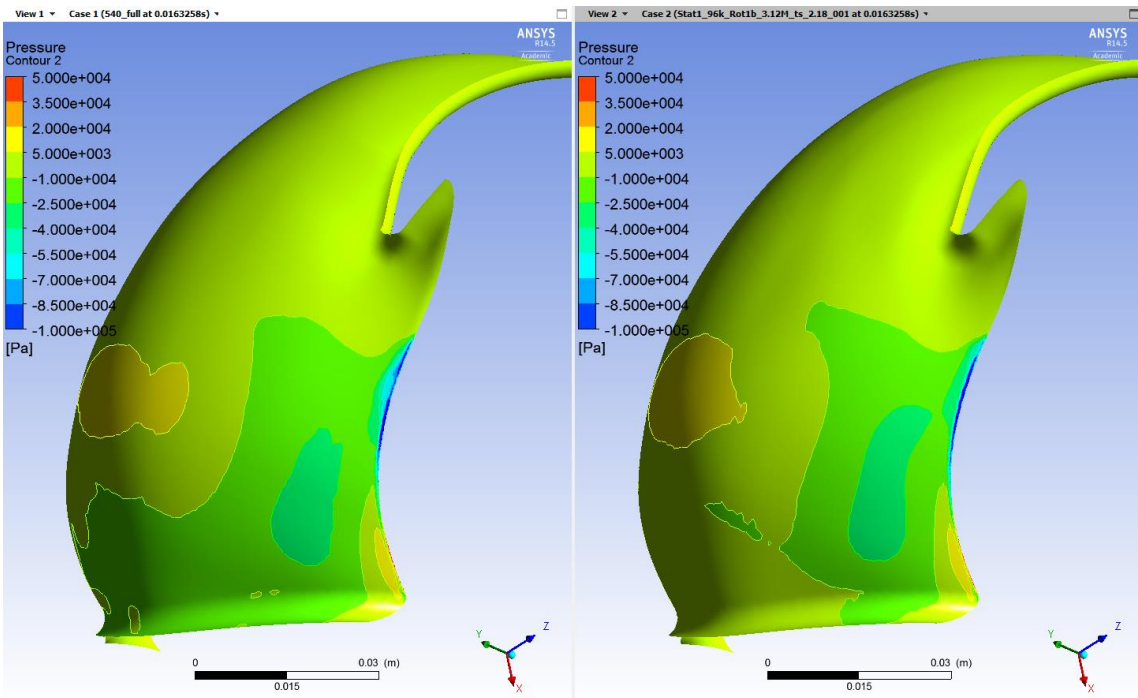


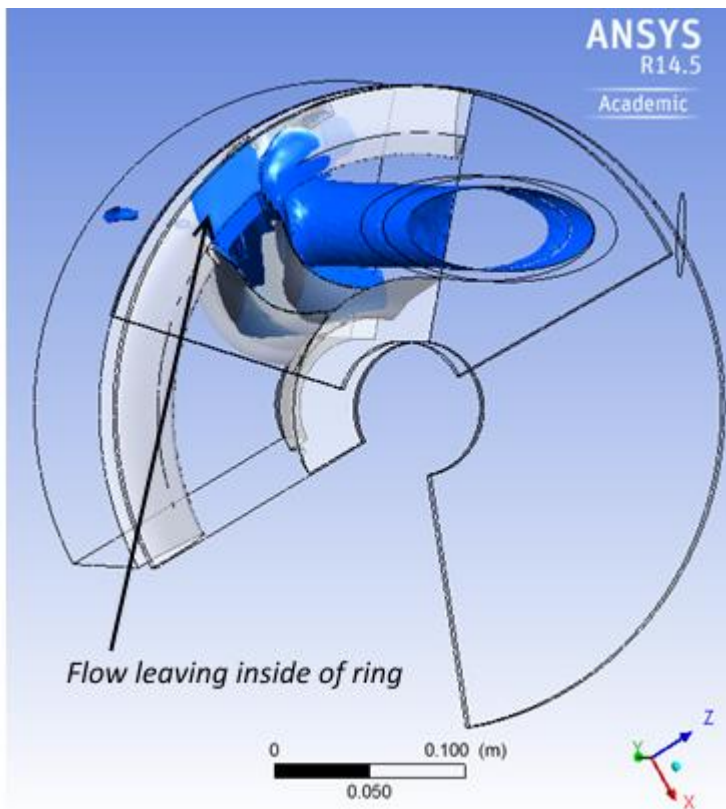
Fig. 4.7. Pressure contours on the outside of the first blade at 60° rotation- Original (left) P000 (right)

4.2 Phase 1: Initial design changes

This chapter describes the initial design changes made to the Turgo runner based on observations of the flow from the initial runner simulations, suggestions from some of the literature and discussions with engineers from Gilkes who have carried out development work on the Turgo runner in the past.

4.2.1 Leading edge profile and inlet angles

The first design changes made to the Turgo runner involved adjusting the leading edge (LE) profile and inlet angles in order to try and reduce the amount of flow leaving peripherally along the leading edge side of the ring as shown in Fig. 4.8.



Rotated angle: 98.18°

Fig. 4.8. Peripheral flow leaving inside surface of ring

Before adjusting the LE profile, a program was written in MatLab to calculate the relative velocity magnitudes and angles within the ellipse created by the jet at the inlet to the runner. This program can also be used to calculate the relative flow angles at the control points used along the leading edge to create the geometry. This means that for any leading edge profile design, the angles at the control points can be set to match the flow angles.

4.2.1.1 Calculating the inlet flow angles

As the jet strikes the runner at an inclination angle, α , an ellipse is created at the inlet as shown in Fig. 4.9, below.

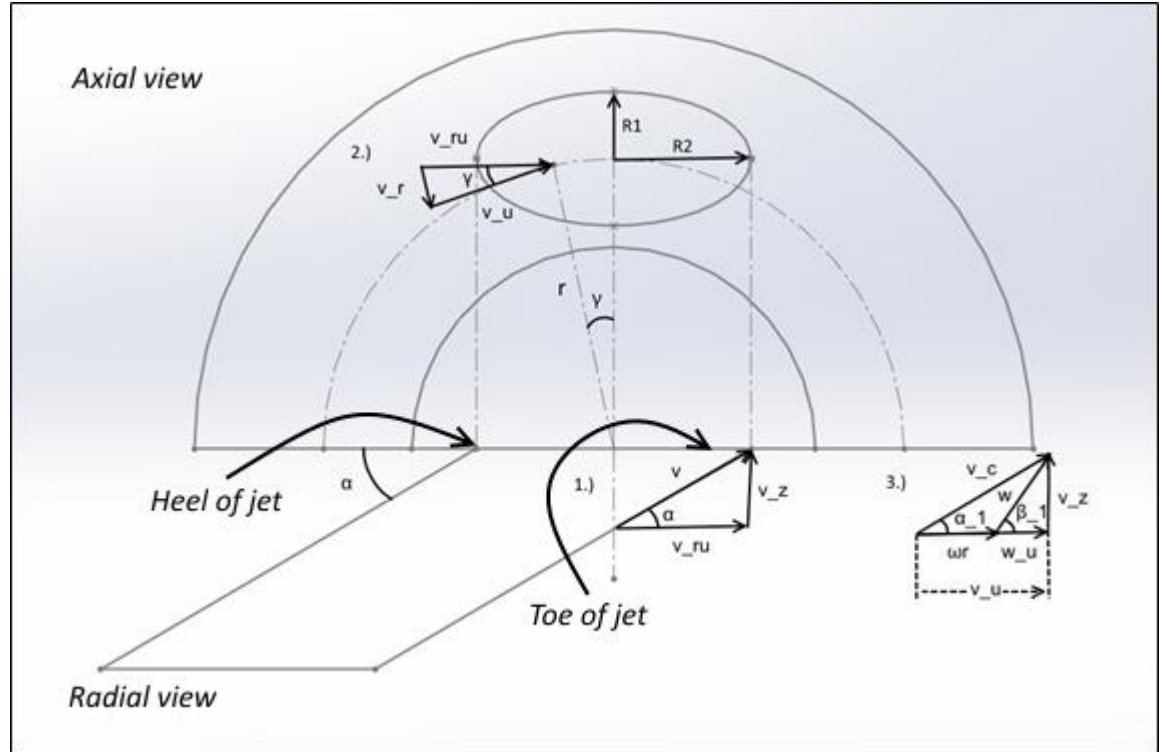


Fig. 4.9. Analysis of the velocity components at the inlet to a Turgo turbine

The semi axes of the ellipse are given by:

$$R_1 = \frac{d}{2} \quad (4.1)$$

$$R_2 = \frac{d}{2\sin(\alpha)} \quad (4.2)$$

The region within the ellipse created by the jet at the inlet can be described as:

$$\frac{(x - x_0)^2}{R_1^2} + \frac{(y - y_0)^2}{R_2^2} \leq 1 \quad (4.3)$$

By treating the inlet plane as a grid made up of points described by their radius (r) and their angular position (γ), the relative velocity (w) and relative velocity angles (β_1 and β_{r1}) can be calculated for each point as follows.

$$v_z = v \sin(\alpha) \quad (4.4)$$

$$v_{ru} = v \cos(\alpha) \quad (4.5)$$

$$v_r = v_{ru} \sin(\gamma) \quad (4.6)$$

$$w_u = v_u - \omega r \quad (4.7)$$

The absolute velocity component (v_c) which produces the angular momentum and therefore the power in the turbine can be described as:

$$v_c = v_z^2 + v_u^2 \quad (4.8)$$

The relative velocity angles in the axial plane, β_1 and the meridional plane, β_{r1} can be calculated as:

$$\beta_1 = \tan^{-1} \frac{v_z}{w_u} \quad (4.9)$$

$$\beta_{r1} = \tan^{-1} \frac{v_r}{w_u} \quad (4.10)$$

Using these equations, a program was written which calculates the velocity components at the inlet to the Turgo for any range of radii and angular positions for either the entire inlet domain or only the region within the ellipse, defined by equation (4.3).

Using the control points for the leading edge of runner P000 as the radial positions and using a range of angles from -45° to 30° in 0.5° increments, the velocity components for these points could be calculated as they pass through the jet ellipse.

Fig. 4.10 below shows how the radial velocity component changes across the ellipse, varying by as much as 25m/s from the one end of the ellipse to the next. This phenomenon is largely responsible for the mixing of the flow across the blades and the associated losses as described by (Webster 1973).

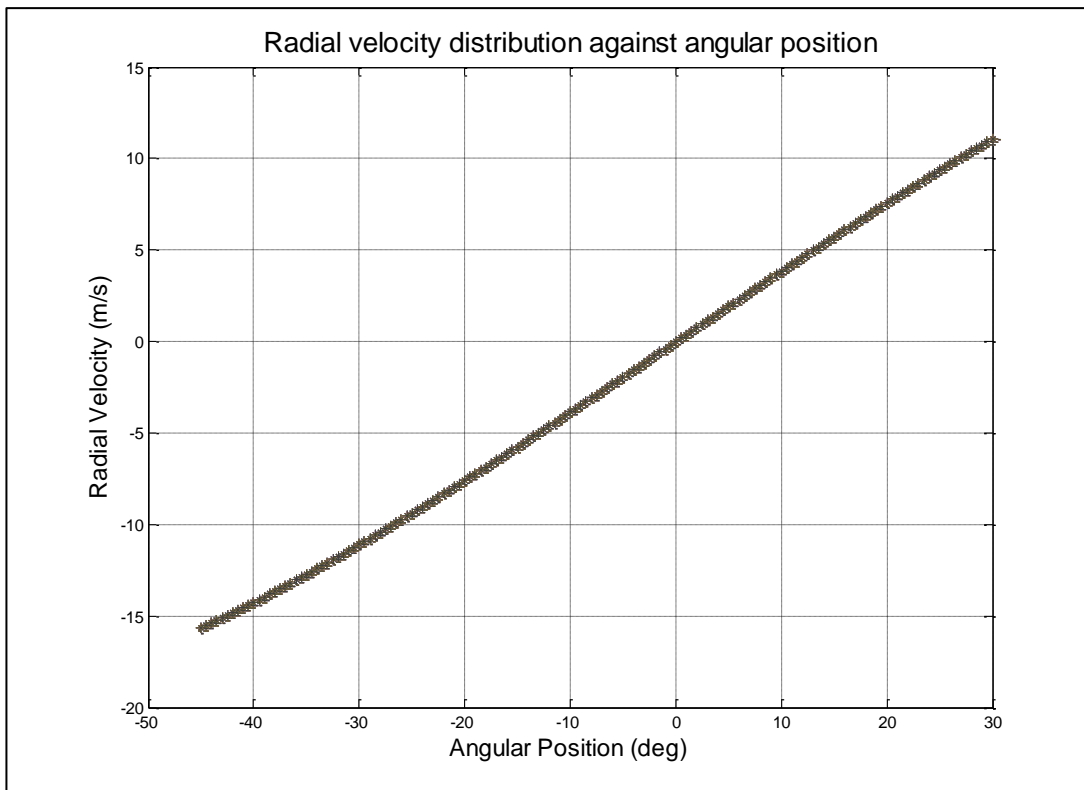


Fig. 4.10. Radial velocity distribution against angular position

Fig. 4.11 and Fig. 4.12 show the relative velocity angles on the axial plane for all the LE control points and the LE control points which pass directly through the ellipse. This shows that the relative velocity can shift by as much as 30 degrees for a single point on the LE as it passes through the jet ellipse making it difficult to match the flow angles to the inlet angles.

Fig. 4.13 and Fig. 4.14 show the relative velocity angles on the meridional plane for all the LE control points and the LE control points which pass directly through the ellipse. This also shows a large variation in relative velocity angles, from -80deg to 60deg across the jet ellipse.

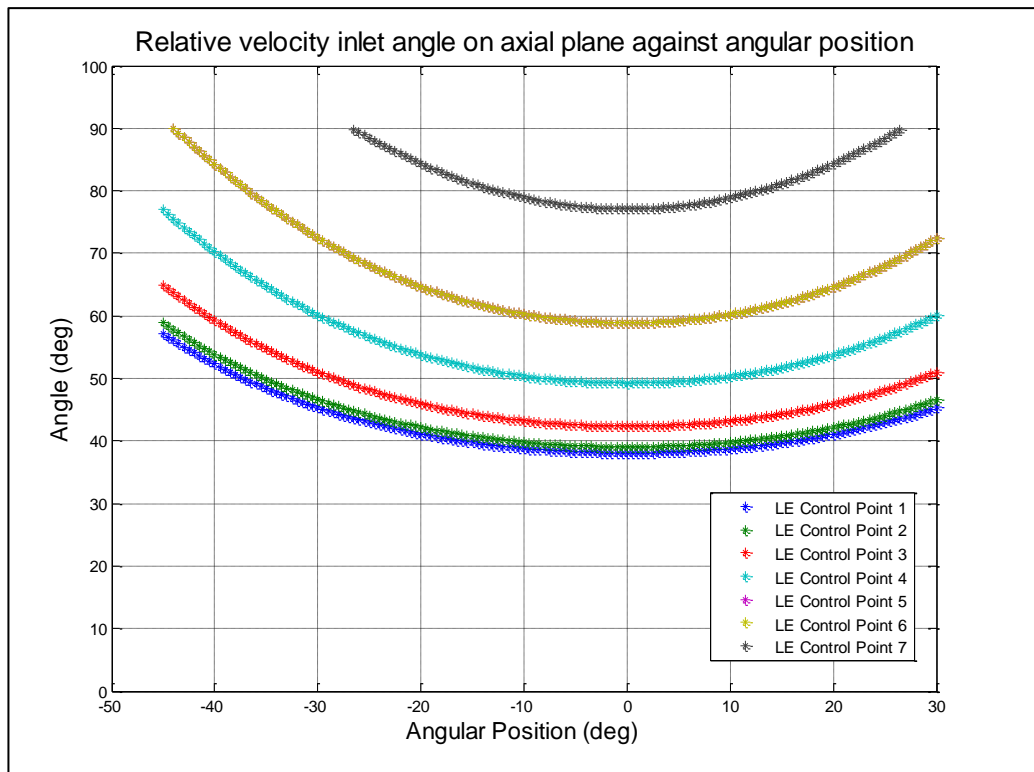


Fig. 4.11. Relative velocity inlet angle on axial plane against angular position for all LE control points

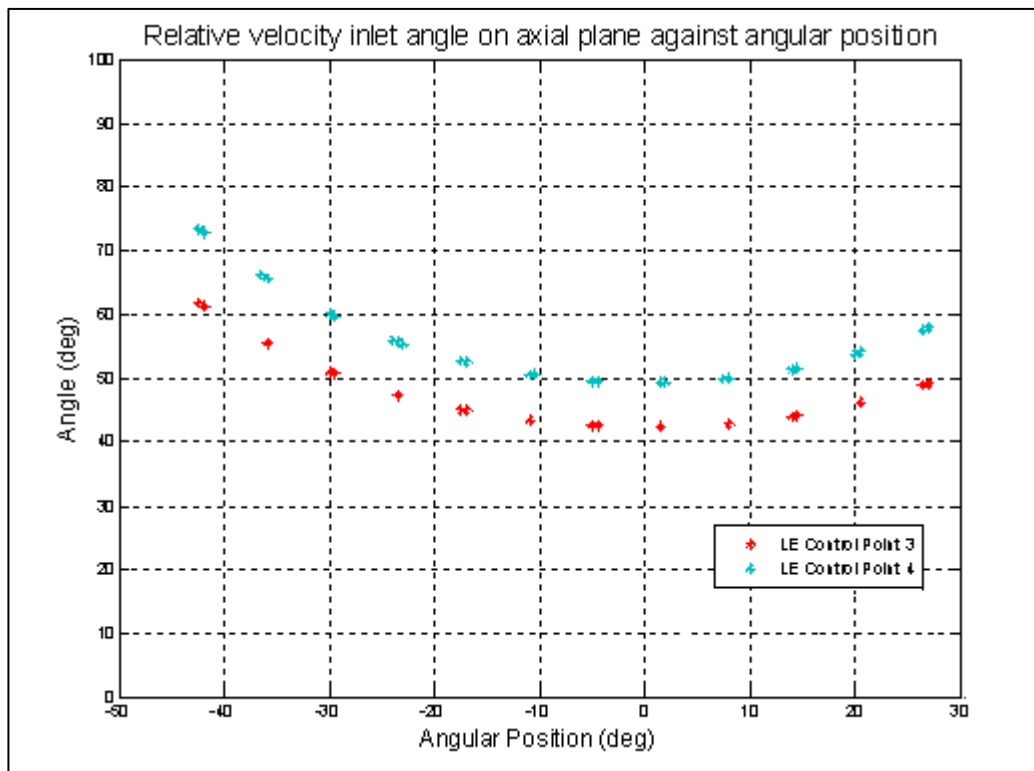


Fig. 4.12. Relative velocity inlet angle on axial plane against angular position for LE control points passing through the ellipse

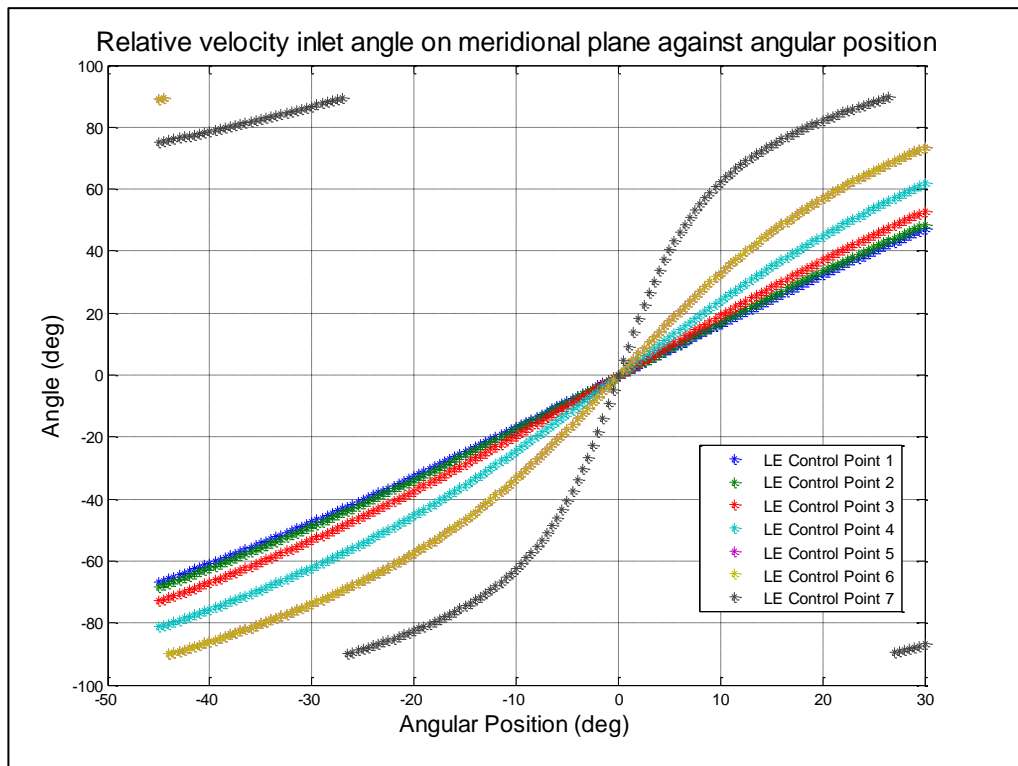


Fig. 4.13. Relative velocity inlet angle on meridional plane against angular position for all LE control points

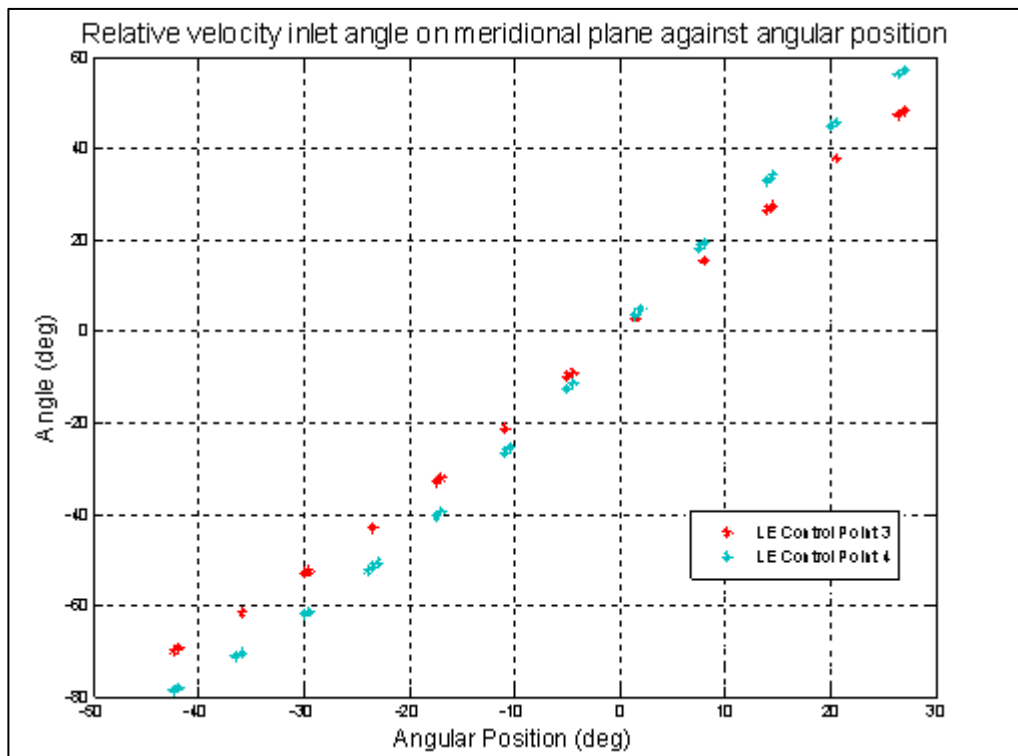


Fig. 4.14. Relative velocity inlet angle on meridional plane against angular position for LE control points passing through the ellipse

Fig. 4.15 shows how the absolute velocity component varies across the jet inlet, with the largest distribution of high values around the centre of the ellipse and towards the toe of the jet.

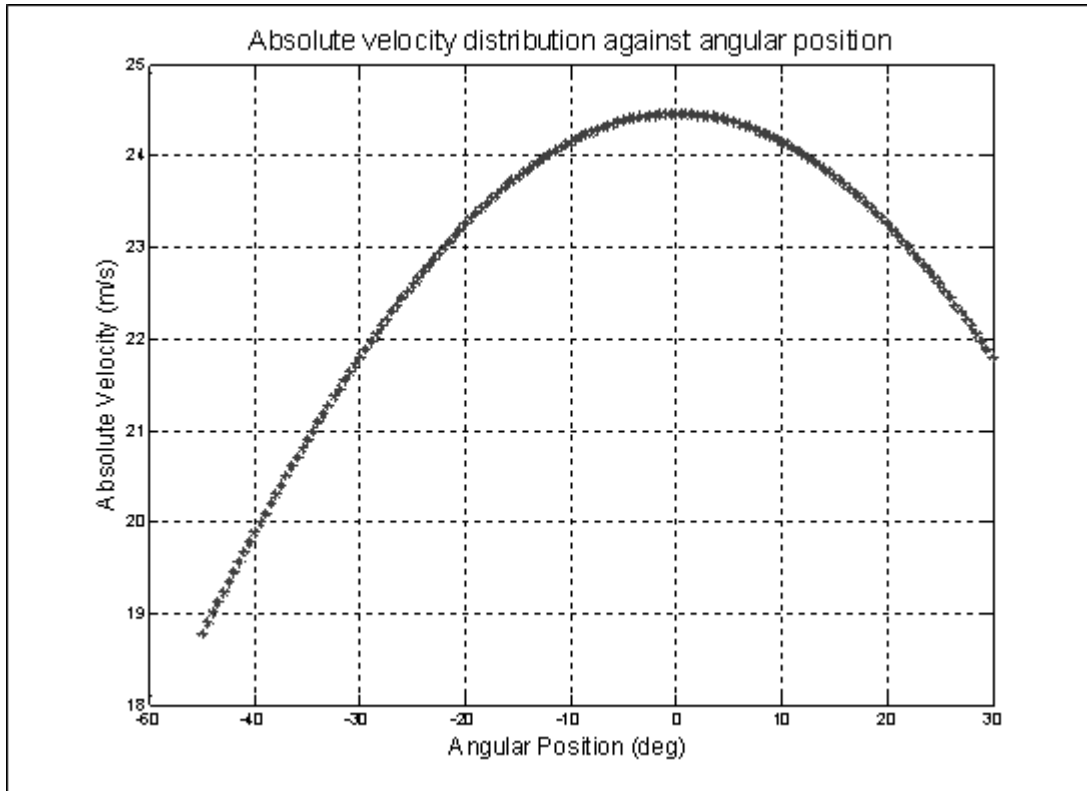


Fig. 4.15. Absolute velocity distribution against angular position

The model can also be used to calculate the relative velocity angles at set positions within the jet ellipse to try and match the inlet angles of the turbine to the flow angles with more accuracy. Fig. 4.16 shows the calculated relative velocity angles on the axial plane at the jet centreline and peak absolute velocity compared to the current P000 design inlet angles. The results show that the relative velocity angles at the peak absolute velocity and the jet centreline are almost identical and either can be used to adjust the inlet angles of the runner at each control point along the leading edge.

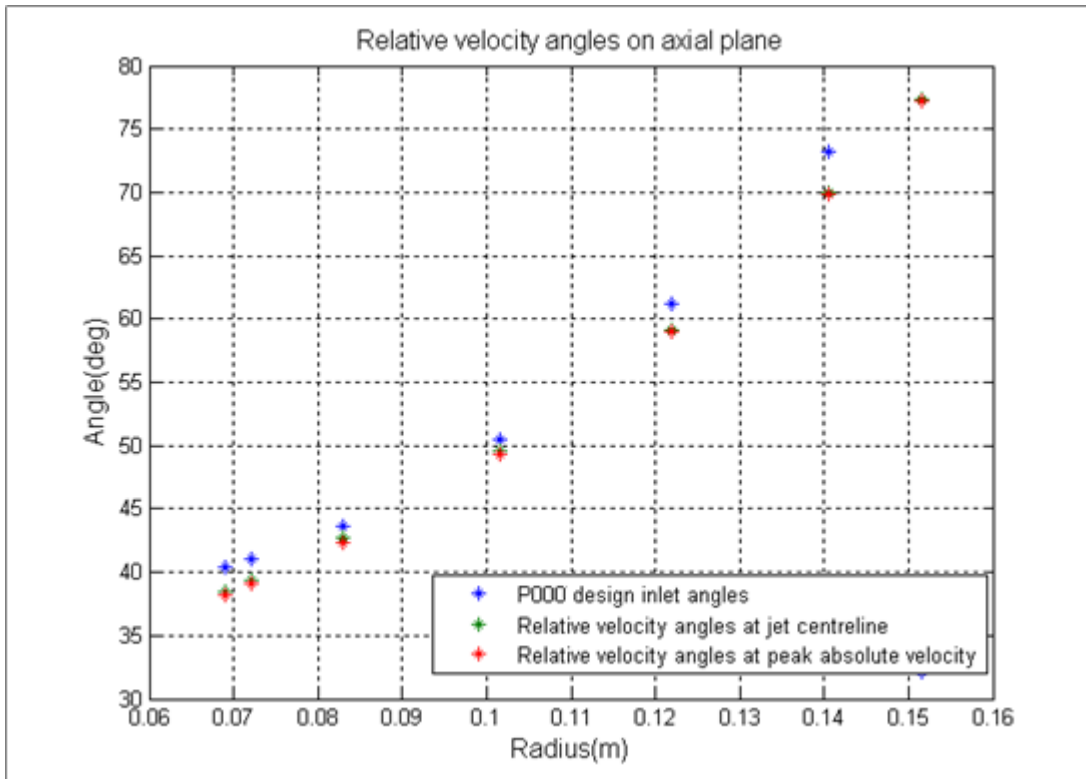


Fig. 4.16. Relative velocity angles at jet centreline for LE control points

4.2.1.2 *Initial LE and inlet angle adjustments*

Based on the identified mismatch of the relative velocity angles taken at the jet centreline and peak absolute velocity and the inlet angles of the P000 design, some modifications were made to the LE profile and angles. Two leading edge profiles were made (LE1 and LE2) as shown in Fig. 4.17 and Fig. 4.18. LE1 was created by manually adjusting the LE profile to better match the overall blade shape (ignoring the ring) and LE2 was created by modifying the LE to follow the relative velocity inlet angles at the peak absolute velocity.

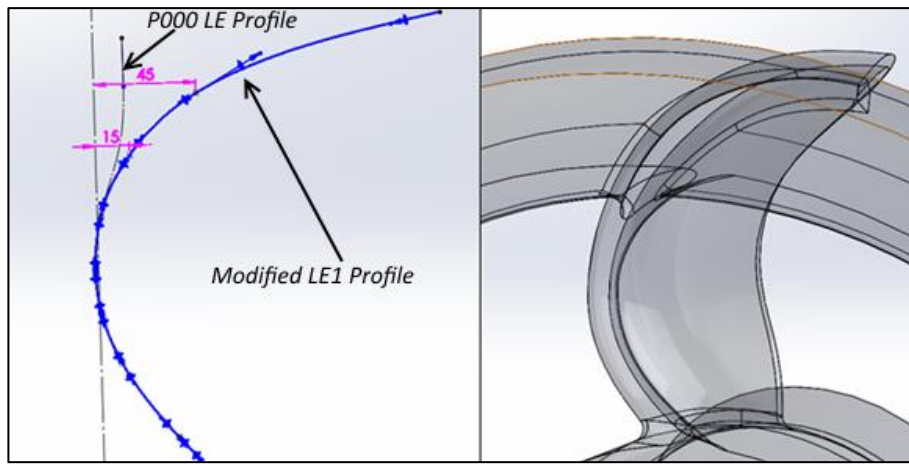


Fig. 4.17. LE1- LE profile modified to match blade shape

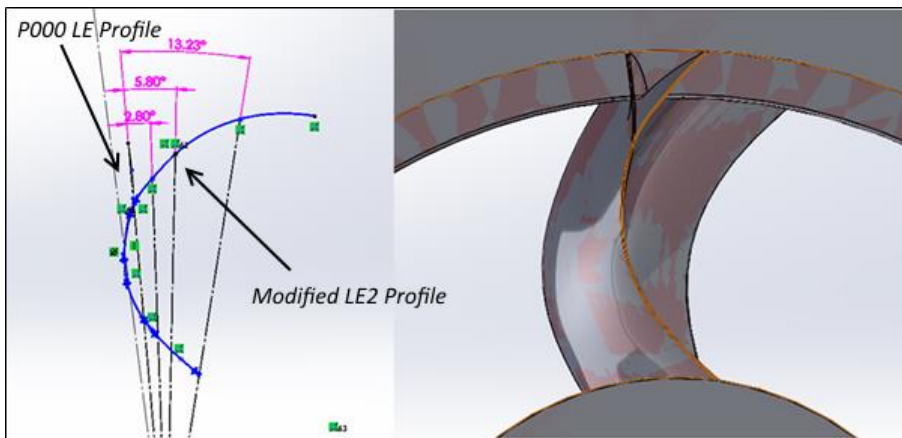


Fig. 4.18. LE profile modified to match inlet angles at peak absolute velocity with two additional control planes

Table 4.1 shows the initial design changes which were carried out and Fig. 4.19 shows the normalised efficiencies for each runner design.

Design #	Design modifications
P000	Parameterised Geometry
P001	P000 Inlet Angles modified to match relative velocity angles at jet Φ
P002	LE1- LE profile moved to match shape of blade without ring to try and prevent flow leaving blade at outside of LE.
P003	P001 inlet angles modified to match relative velocity angles at jet Φ
P004	LE2 Profile and inlet angles modified to match relative velocity angles at jet Φ
P005	LE2 Profile and inlet angles modified. Two additional planes added to improve shape

Table 4.1- Phase 1: Initial design changes descriptions

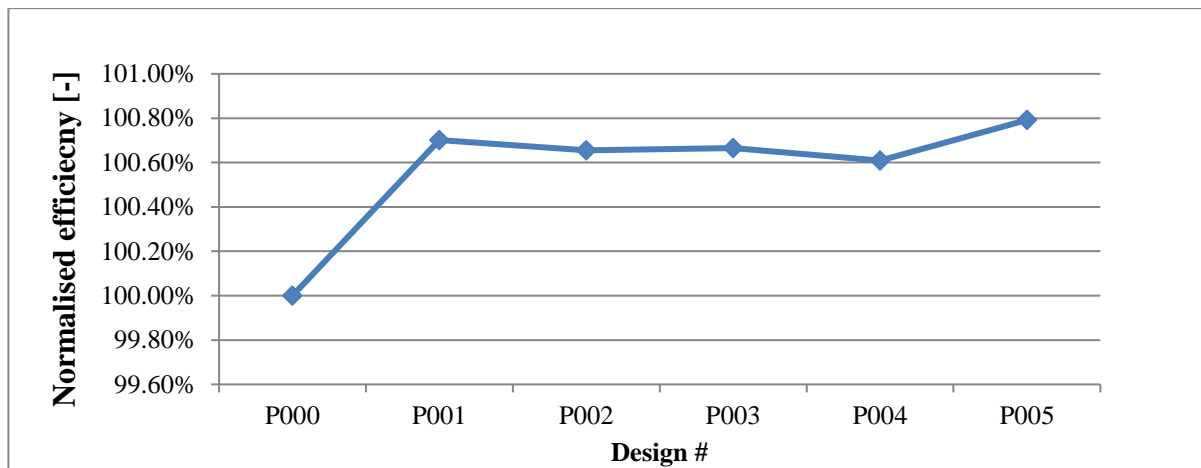


Fig. 4.19. Phase 1: Initial design changes- LE profile and inlet angles- normalised efficiency

The results show that in every case where the inlet angles are adjusted to match the relative flow angles at the jet centreline the efficiencies are increased with the largest increase for the P000 design where the mismatch is greatest. The LE1 profile showed almost no change in efficiency compared to the P001 design, with the original LE profile however the LE2 profile showed a slight increase when two additional control curves were introduced to give better control over the blade shape.

In summary this initial study has shown that the inlet angles of the Turgo runner do have a slight impact on efficiency (~0.6% for the original design) and matching the inlet angles to the relative flow angles does improve the performance. The LE profile seems less critical although matching the LE profile to the relative flow inlet angles does show improvements (P005). This study could be taken further by independently varying the inlet angles at each control point as a DOE study although this will require a large computational resource.

4.2.2 Jet offset and radial position DOE study (DOE1)

During his experimental testing of the Turgo runner in 1973, Webster showed an increase in efficiency can be achieved by adjusting the radial position of the jet at the inlet (Webster 1973). Previous tests have also shown that improvements in performance can be achieved by changing the jet offset.

A DOE study was set up using the Design Experts (Stat-Ease®. 2013) software to look at the relationship between these two parameters and how they affect the turbine performance. The details of the initial experiment design are given in Table 4.2, below.

Study Type	Response Surface	Runs	11
Design Type	Central Composite	Simulation Time	16.5 Days
Design Model	Quadratic		

Table 4.2- DOE initial study design details

The range of jet offsets [ϕ] were set as 0mm-14mm and the range of vertical heights [H_v] from the axis from 92mm to 105mm. In addition to the 9 suggested runs for the central composite model, shown in Fig. 4.20. An additional run was included at the current design height of 93.57mm and an offset of 8.3mm.

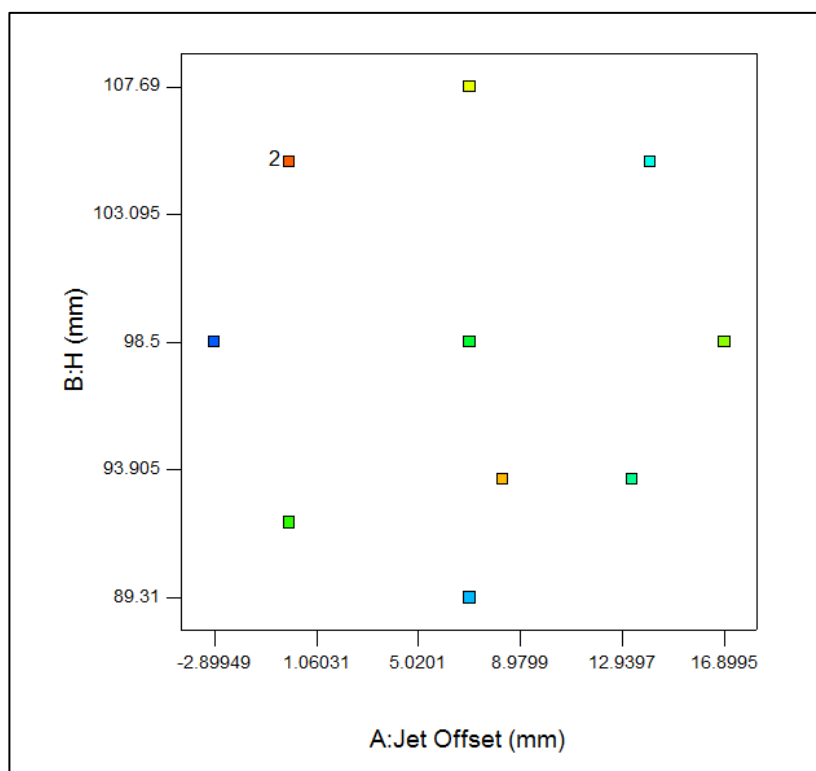


Fig. 4.20. Graph columns for initial runs

The results for these initial runs are given in Table 4.3 below. The efficiencies are normalised against the original offset and radial height of 8.3mm and 93.57mm respectively.

Run	ϕ	H_v	Efficiency
#	[mm]	[mm]	[%]
1	0	105	99.11%
2	-2.90	98.5	100.14%
3	7	89.31	97.89%
4	14	105	96.04%
5	13.3	93.57	98.46%
6	7	98.5	99.71%
7	0	92	100.14%
8	16.90	98.5	95.75%
9	7	107.69	97.44%
10	8.3	93.57	100.00%
1	0	105	99.11%

Table 4.3- Jet Offset and radial position DOE results

The results for these initial runs gave a reasonable quadratic response surface fit to the data points, with an R^2 of 0.8923. Fig. 4.21 shows the contour plot for the efficiency against the jet offset and the vertical height of the jet. The surface predicts an optimum efficiency at a jet offset of 2.1mm and a radial position of 97.5mm. The predicted normalised efficiency is 100.73% at this point.

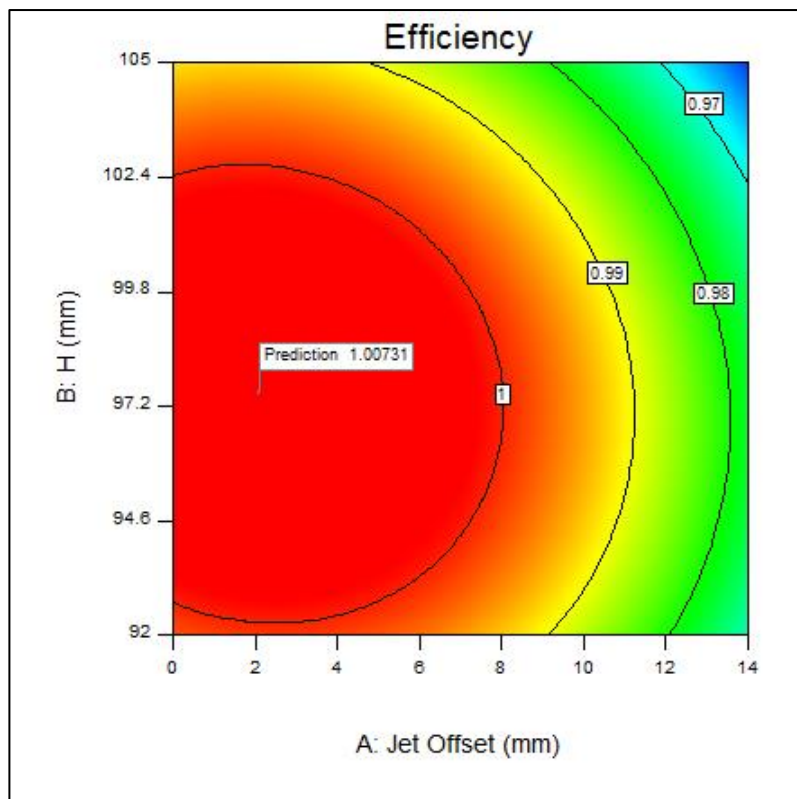


Fig. 4.21. Normalised efficiency contour for the Jet Offset against the height.

Based on these results, an additional run was carried out at the suggested optimum of a 2.1mm offset and a 97.6 mm radial height. This produced a normalised efficiency of 100.76% which is very close to the predicted efficiency of 100.73%.

This additional run was included in the DOE study which changed the R^2 value to 0.8957. The predicted values against the actual data points are plotted in Fig. 4.22 and show fairly good correlation.

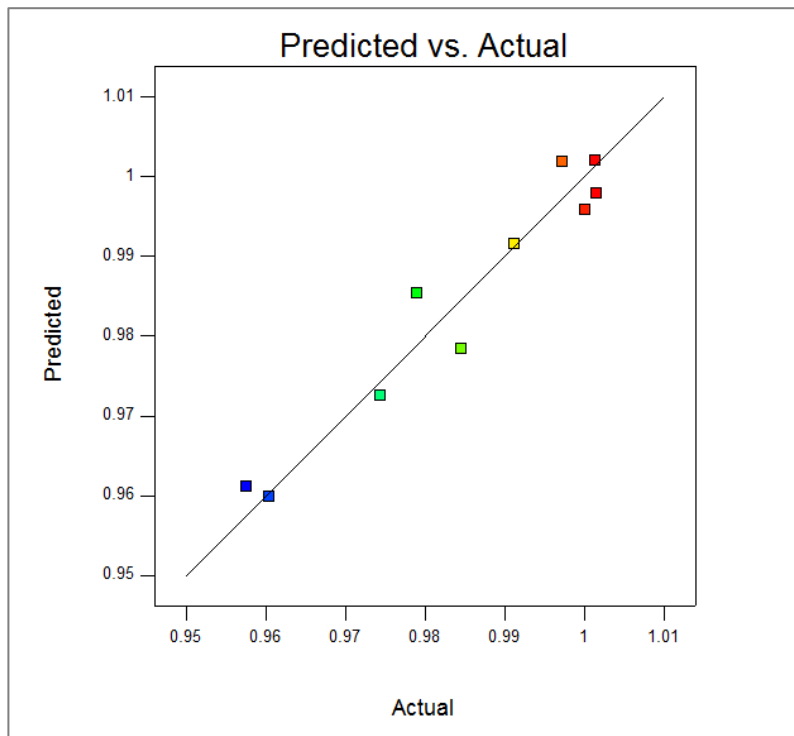


Fig. 4.22. Predicted surface results against actual results

The updated contour plot showing the efficiency for the range of radial positions and jet offsets now points towards an optimum with an offset of 2.2mm and a radial height of 97.5mm which has hardly changed from the previous optimum showing that the response surface is accurate in predicting the correct offset and radial height.

The normalised torque curves for the original and the optimised jet offset and radial position are compared in Fig. 4.23 below. As the jet offset is reduced and the radial position is increased, the negative torque on the outside of the blades decreases, and the peak torque on the inside of the blades increases. The double peak visible in the original larger offset design, caused by a wave created in the jet as a result of flow/inlet angle mismatch, is also eliminated when the offset is reduced.

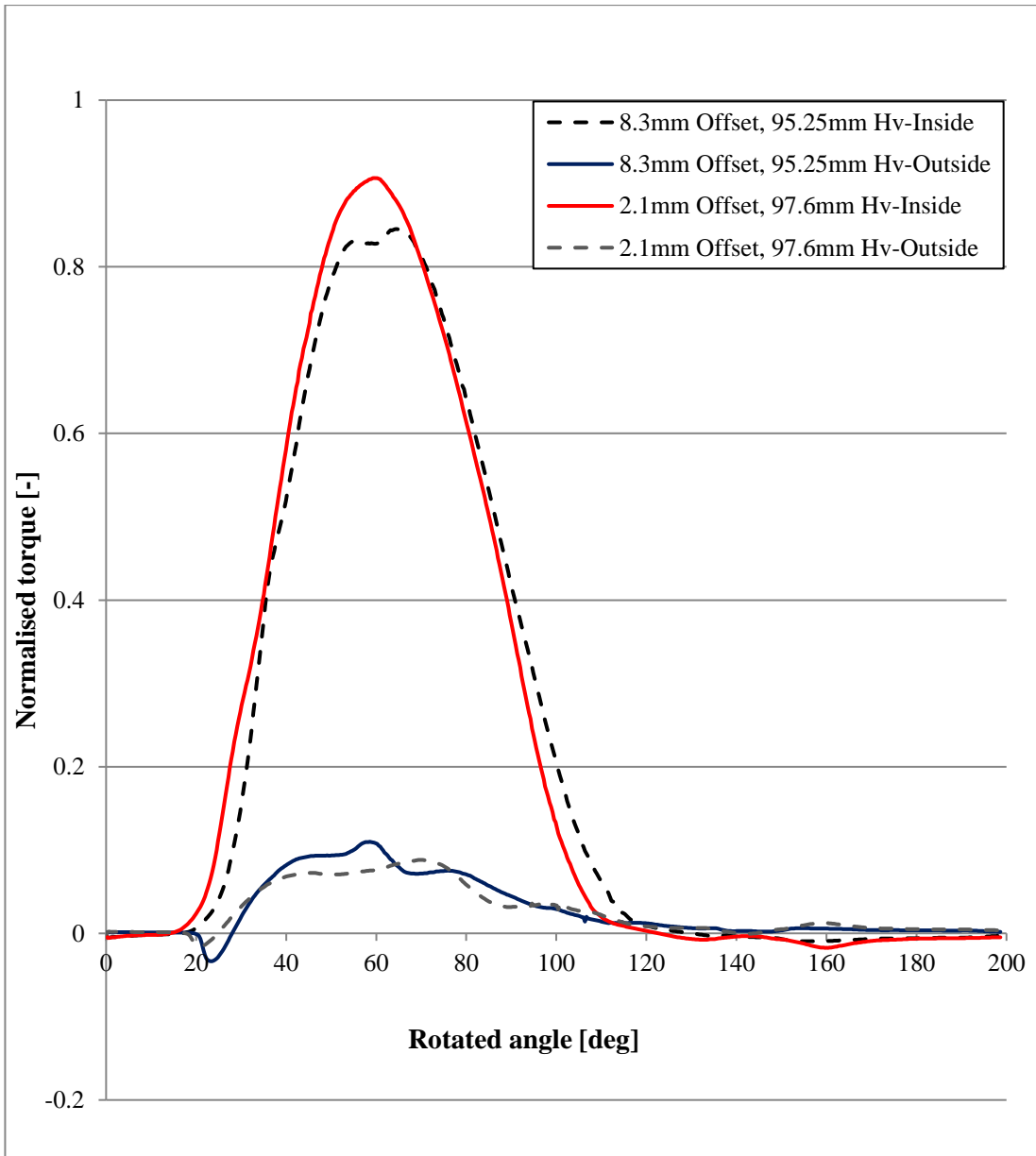


Fig. 4.23. Torque curve comparison for original and optimised design in Jet Offset and Radial Position DOE

Shipulin's work (Shipulin 1956) showed that the optimum offset ratio (offset distance: runner diameter) is $40/250 = 0.16$ which translates to an offset of 12.63mm on a 7.5" machine. This is a much higher offset than the optimum found in this study; however Shipulin uses a much narrower jet, with a d/D ratio at the BEP of 1:5.81, compared to Gilkes at 1:3.66. Shipulin also uses an inlet angle of 22.5 degrees compared to 25 degrees. Gilkes found by experiment that anything lower than 25 degrees caused the relatively large jet to foul the rim (Hancock 1982).

The results agree to an extent to Webster's experimental work, which showed that increasing the radial height of the jet at the inlet (by $\frac{1}{4}$ " or 6.35mm) increased the efficiency by around

4% (Webster 1973), however the DOE study showed the optimum to be an increase in radial height of 4mm and a reduction in the offset of 6.2mm resulting in only a 0.76% increase in normalised efficiency compared to the original.

The differences between the results of this study and Webster's experimental work could be due to several factors. Webster used a much lower head ($6 \frac{1}{2}'$ as opposed to $100'$) which is likely to have a considerable impact on the results. It may also be found that changing the offset and radial position experimentally, where other effects not included in the numerical model, such as casing effects, are included, gives different results.

4.2.3 Trailing edge width

During the jet offset and radial position DOE study, another study was also carried out looking at the width of the trailing edge (TE) using the original 8.3mm offset and 93.6mm radial height. The width of the original 7.5" HCTI Turgo runner TE is around 7mm shown in black in Fig. 4.24.

By changing only the outside surface of the blades, the TE width was reduced to 5mm and 3mm. These simulations actually showed the efficiency decreasing with a reduction in the TE width and three further designs were created with 9mm, 11mm and 13mm TE widths to see whether increasing the TE width is beneficial. Fig. 4.24 shows the results of the TE study. It was found that increasing the TE width improves the performance of the runner up to a certain point after which the efficiency drops. The optimum in this case is 11mm, which gave a 0.55% increase in normalised efficiency compared to the original.

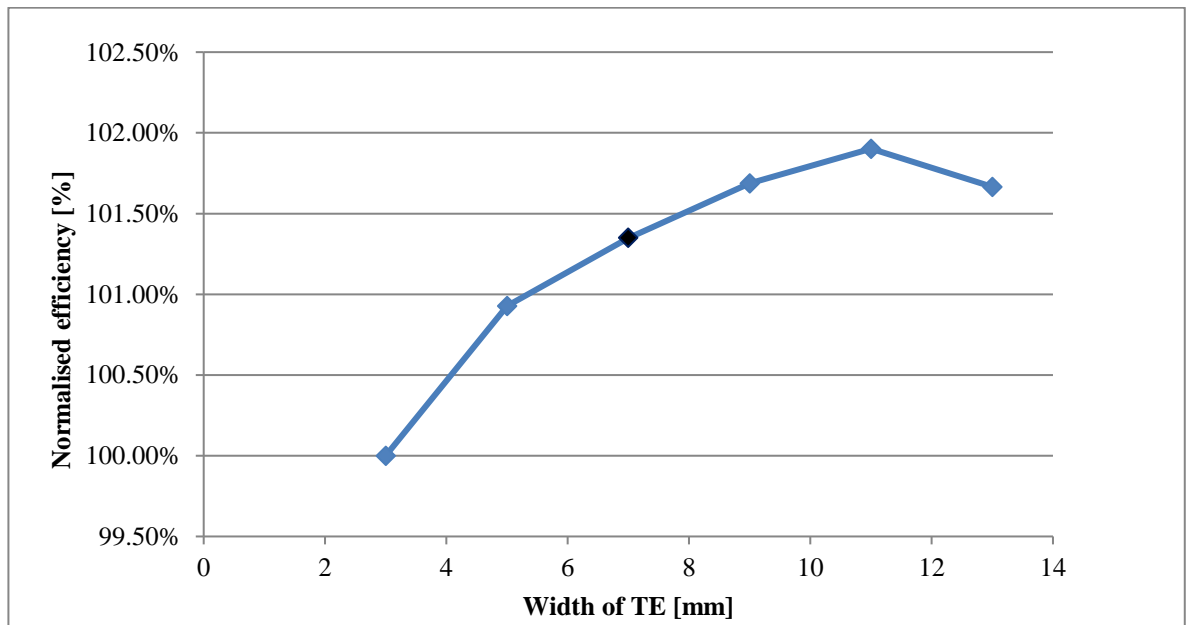


Fig. 4.24. TE width study normalised efficiencies

The normalised torque curves in Fig. 4.25 show that when the TE width is increased, the torque on the inside of the blades is increased and the outside of the blades is reduced. For TE widths 9mm-11mm the overall increase in the inside torque is greater than the decrease in the outside torque (compared to the original TE width) however in the case of the 13mm TE width, although there is an increase in the inside torque compared to the 7mm design, the decrease in the outside torque outweighs this and the overall efficiency is less than the original 7mm design.

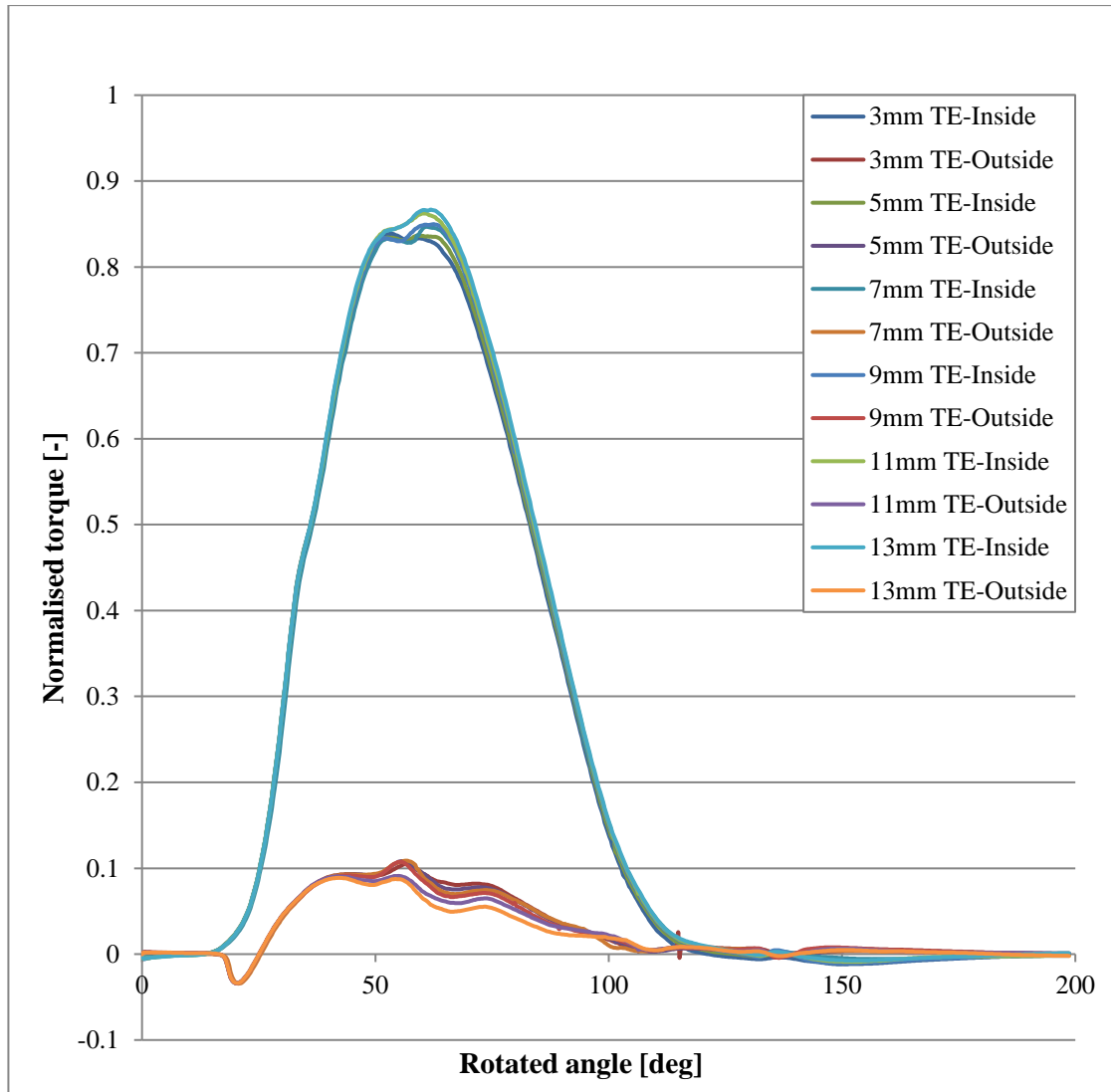


Fig. 4.25. TE width study- Torque curves

Fig. 4.26 shows a comparison between the flows for the original 7mm TE width design and the optimised 11mm TE width design. An isosurface is plotted at a water volume fraction of 0.5, which is coloured by the water velocity in the stationary domain. It can be seen from this comparison, at a rotated angle of 63.81deg that the wider trailing edge helps to separate the flow leaving the inside and the outside of the blades. This reduces the interference and

negative pressure visible on the trailing edge of the blades shown by the blue pressure contours in Fig. 4.27 and results in a higher total torque on the inside of the blades.

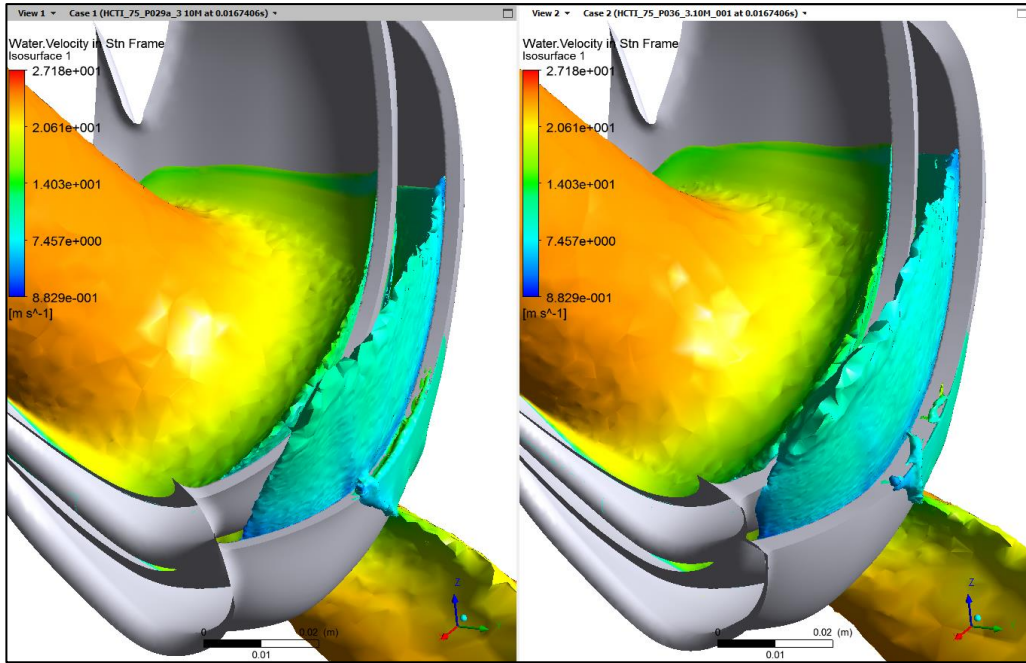


Fig. 4.26. Flow comparison between original 7mm TE width and the optimised 11mm TE width designs at 63.81deg

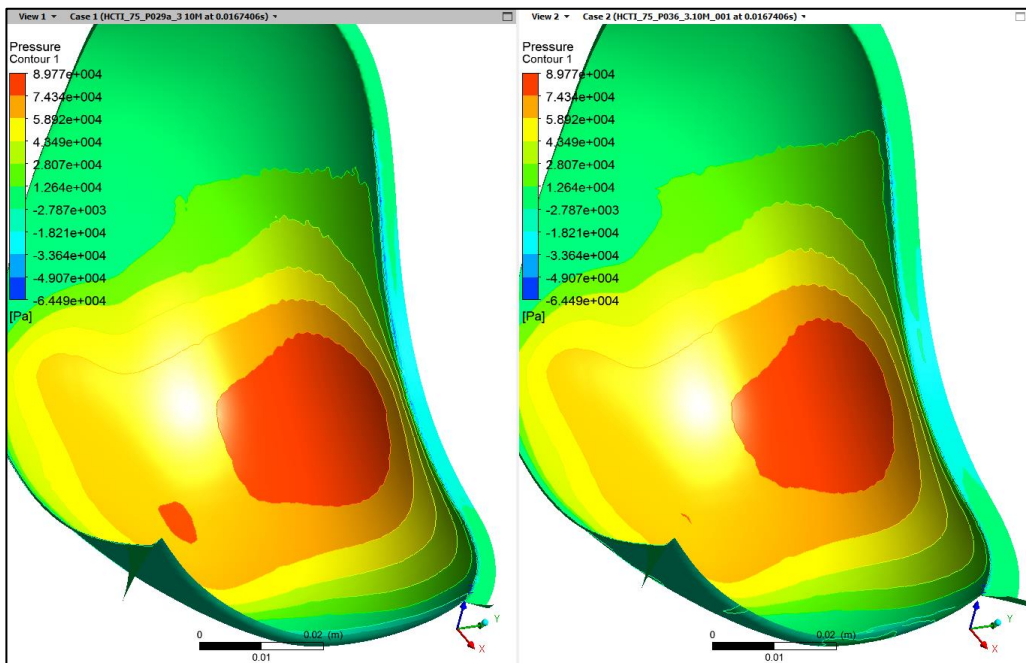


Fig. 4.27. Pressure on the inside surface of the blades-comparison between original 7mm TE width and the optimised 11mm TE width designs at 63.81deg

The optimised TE width design was then simulated at the optimum jet offset and radial position from the DOE study. The performance showed the sum of the improvements seen by both studies, showing that the two studies are mutually exclusive.

4.2.4 Spherical blade shape

It was suggested by Webster in his 1973 paper in *Water Power* that changing the shape of the blades to a more spherical shape (Fig. 4.28) could harness more of the energy at the outlet by reducing the spread (Webster 1973). This concept was tested by creating a more spherical blade shape while attempting to alter little else regarding the blade design as possible. The way in which this was done was by adjusting the trailing edge profile of the blade in the same plane as shown in Fig. 4.28 while maintaining the same exit angles at each control curve. Fig. 4.29 shows the circle used to modify the trailing edge shape and Fig. 4.30 shows the new spherical blade compared to the previous design.

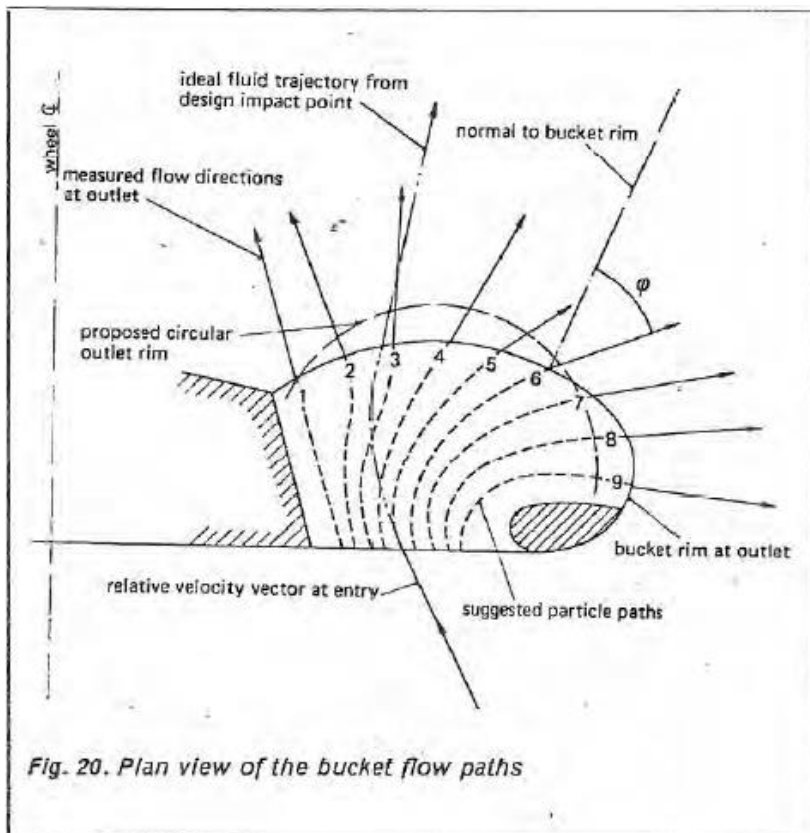


Fig. 4.28. Flow paths and suggested circular outlet rim (Webster 1973)

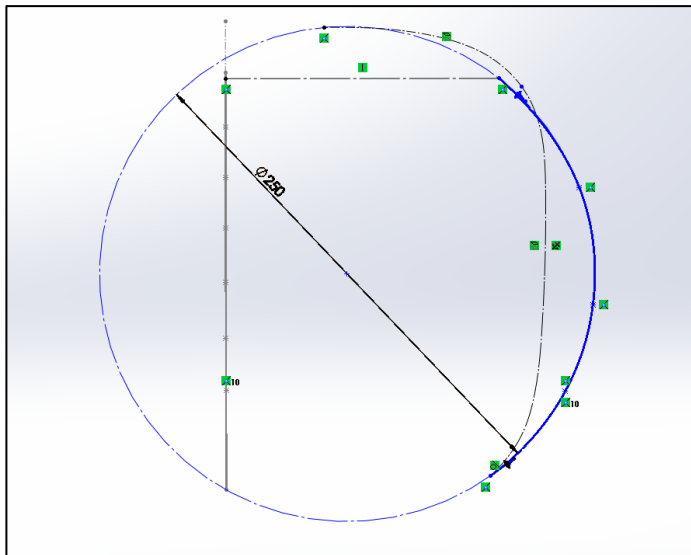


Fig. 4.29. Circle used to modify trailing edge and create a more spherical blade

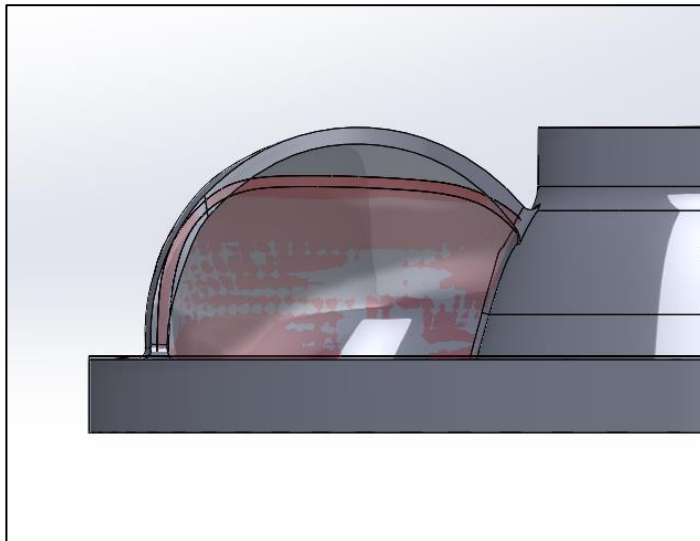


Fig. 4.30. Original (red) and spherical (grey) blade shapes

The results showed a reduction in efficiency of over 2% between the previous optimised design (P036) and the spherical blade design (P037) which is largely due to the flow leaving the inside of the first blade impinging on the outside of the second blade. This phenomenon causes the large negative torque on the outside blade between 80° and 100° rotation as shown in Fig. 4.31. The pressure contours on the outside blade are also shown for this region of the torque curve (Fig. 4.32) and it can be seen clearly here where the flow is impinging on the outside of the blade and inducing a negative torque.

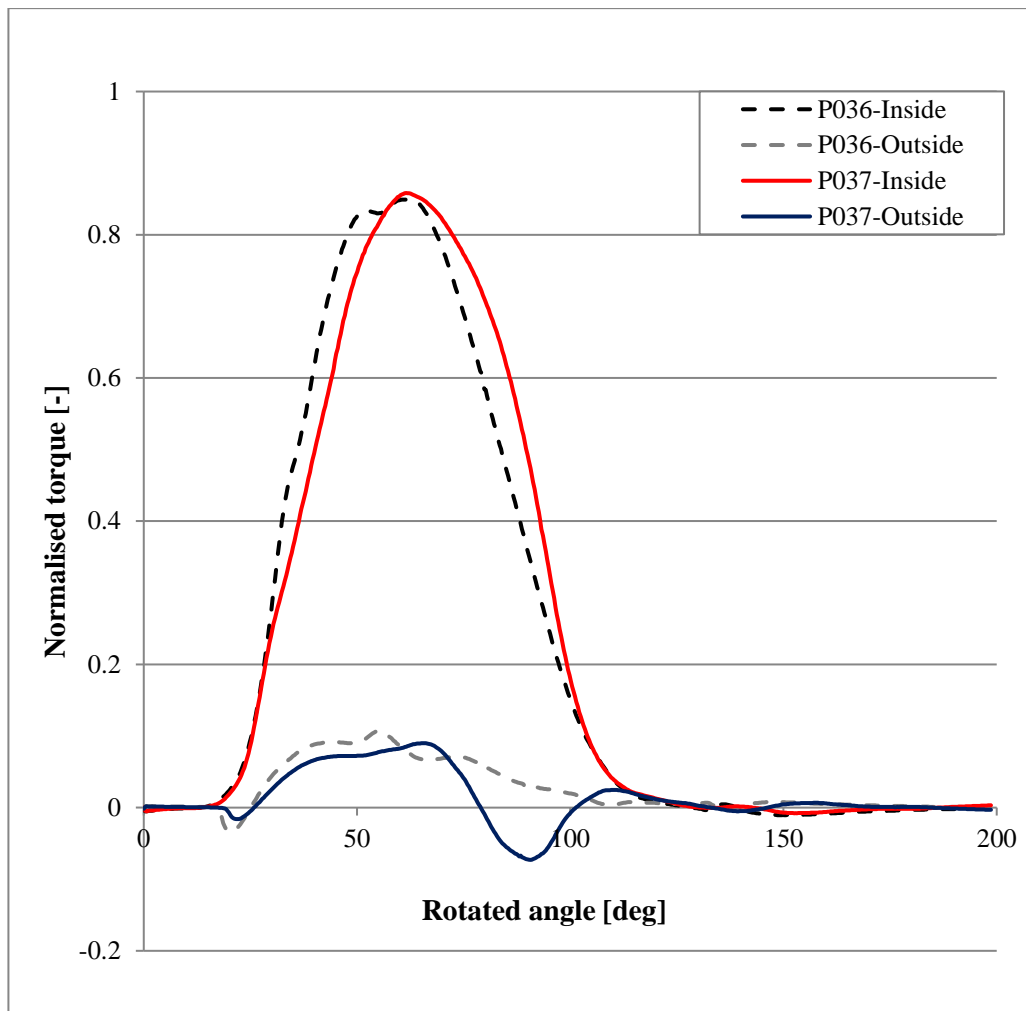


Fig. 4.31. Spherical blade study torque curves

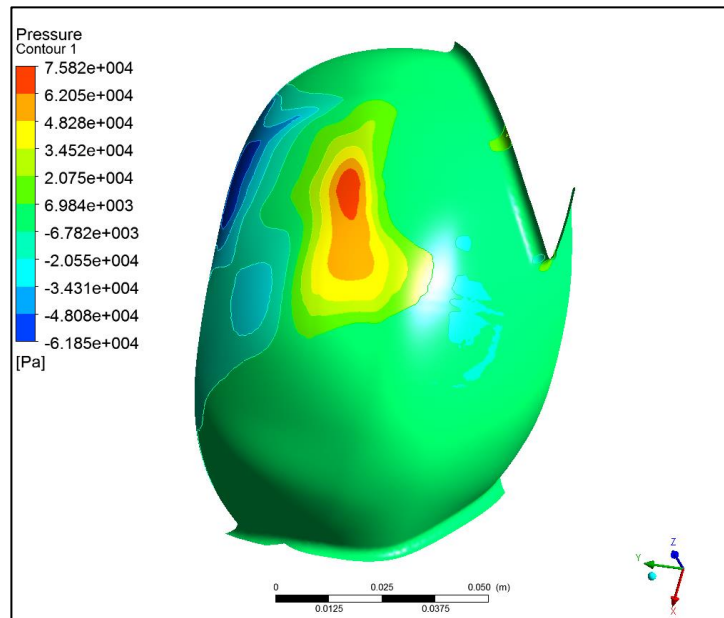


Fig. 4.32. Pressure on outside of blade corresponding to negative torque region

This shows that although in theory a more spherical blade could be beneficial, the thickness and shape of the blades would need to be altered accordingly and would require a more in depth study than there is scope for in this research.

4.2.5 Blade number study

Using the improved HCTI design, P036, with the optimised radial position and jet offset, the number of blades was varied from 19 to 25. The efficiencies for these designs are given in Fig. 4.33. The results show that the current design, with 22 blades, performs almost as well as the optimal 23 blade design (0.09% lower) and reducing the number of blades from 22 to 19 will result in an efficiency drop of around 1.51% based on the numerical model.

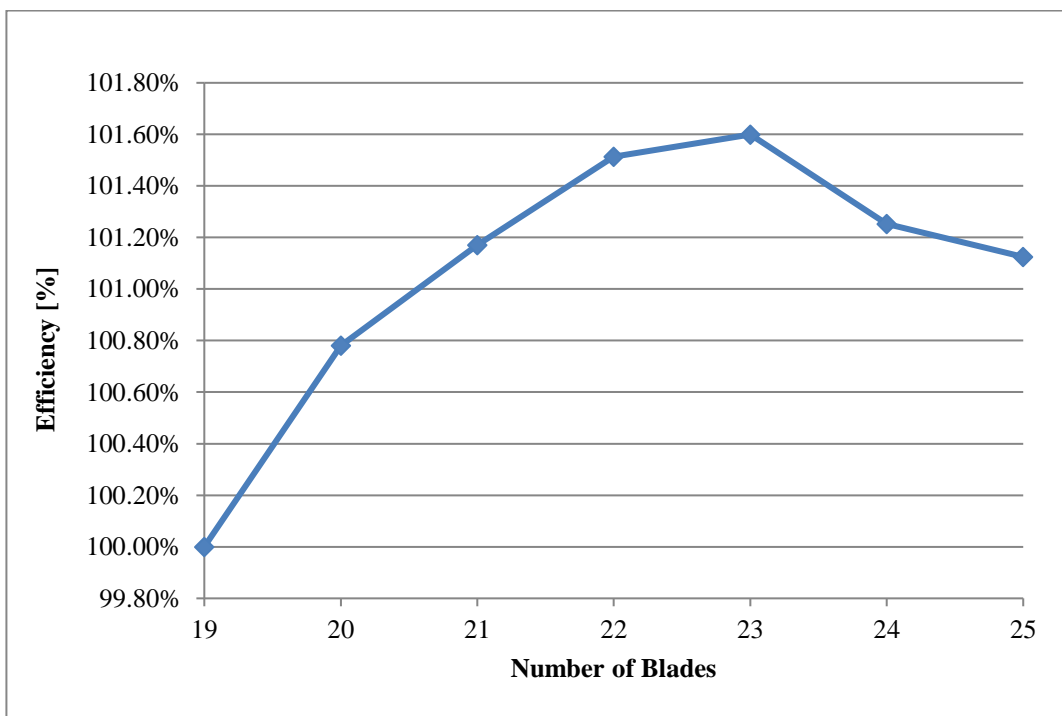


Fig. 4.33. Blade number study efficiency results

The reason for the drop in efficiency from 22- 23 blades to 24-25 blades is explored further by comparing the torque curves for each design. Fig. 4.34 shows the normalised torque curves, also normalised against the blade number, which compares the average torque curves for each runner. It can be seen that as the number of blades is increased, the normalised torque on the inside blade surface is increased however for 23 to 25 blades, there is a large drop in the torque on the outside blade surface (even producing a negative torque at around 80deg rotation). The 19 blade design has a considerably lower normalised torque on the inside of the blades however the torque on the outside of the blades is higher in comparison to the other designs which accounts for the linearity of this part of the curve in Fig. 4.33.

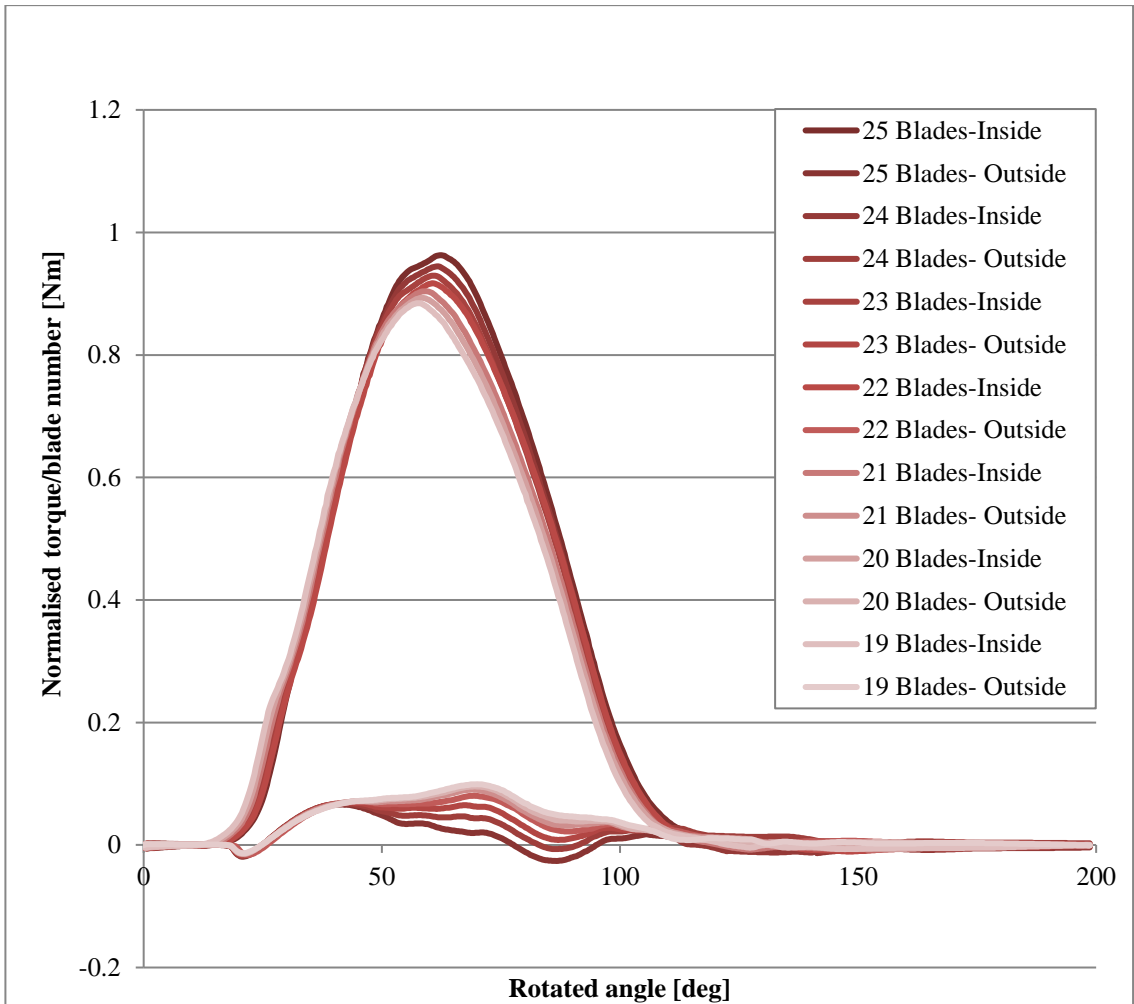


Fig. 4.34. Blade number study- Normalised torque/blade number curves

The pressure contours on the outside blade surface are compared for the 22 and 24 blade designs at a rotated angle of 83.45deg to try and identify the reason for the lower torque measured in the 24 blade design (Fig. 4.35).

The profiles show that for both designs, there is a region in the centre of the blade where an undesirable positive pressure is measured. This is likely to be due to the flow leaving the inside of the first blade impinging on the outside of the second blade, a phenomena which is more profound with more blades and a narrower blade passage. The 22 blade design also shows a larger desirable negative torque on the right of the positive torque which is beneficial to the performance of the turbine.

These results show that increasing the number of blades up to 23 is beneficial with regards to performance however more than 23 blades results in a drop in efficiency which is likely to be due to obstruction of the flow passage. In order to realise the benefits of using more than 23 blades, the thickness and shape of the blades would also need to be altered in conjunction with

the number of blades to prevent flow blockage. It may also be found that changing the number of blades also affects the optimum radial position and offset of the jet.

As the gain in efficiency from 22 to 23 blades is very small it is not worth modifying this design to 23 blades which is closer to the drop in efficiency as a result of choking and is more likely to cause problems when using higher flow rates.

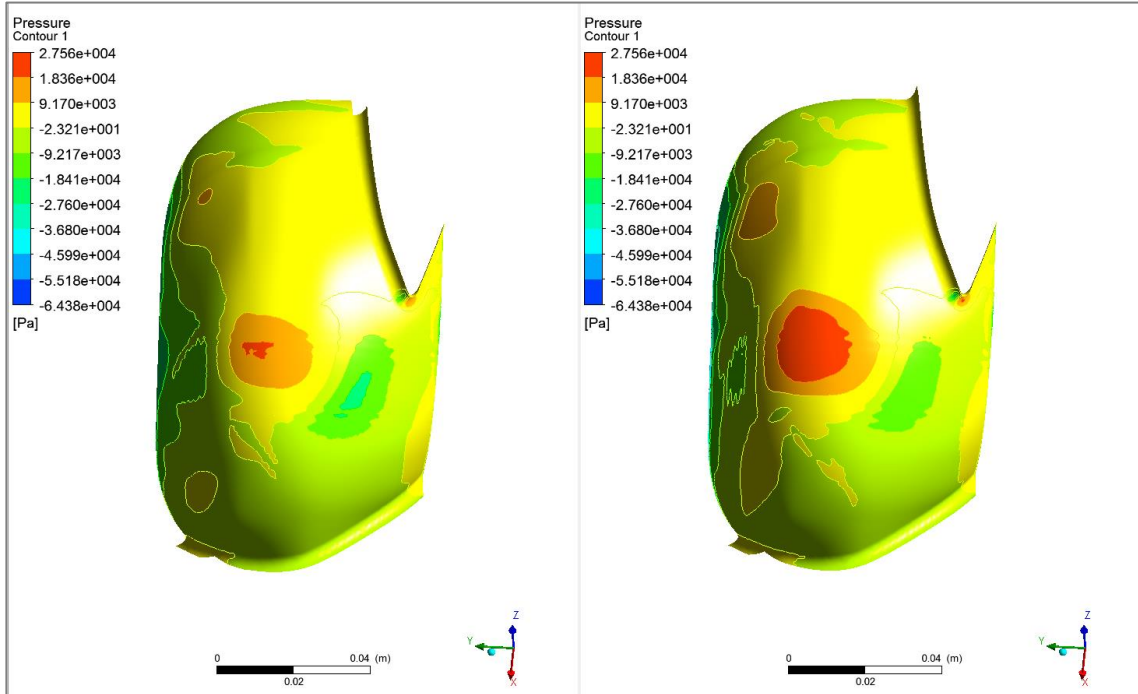


Fig. 4.35. Pressure contours on outside blade surface at 83.45° 22 blades (left) and 24 blades (right)

4.2.6 Blade thickness

Previous work carried out by (MacDuff 1969) has showed that the thickness of the blades is more than sufficient from a strength perspective and it may be beneficial to the hydraulic efficiency to reduce the thickness of the blades. This study was carried out without any changes to the inlet and exit angles and the leading edge thickness was left unchanged as it is already very thin at around 1.2mm for the 7.5" runner. The blade thickness was altered in four ways initially:

1. Leaving the inside surface and TE unchanged and reducing the thickness by 20% as shown in Fig. 4.36.
2. Leaving the outside surface and TE unchanged and reducing the thickness by 20%
3. Leaving the inside surface unchanged and reducing the thickness by 20%
4. Leaving the outside surface unchanged and reducing the thickness by 20%

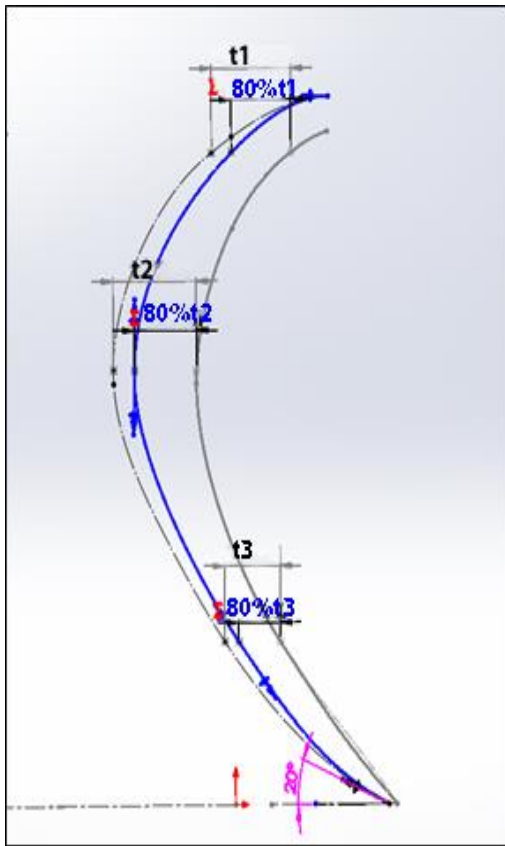


Fig. 4.36. Blade thickness variation for one cross section leaving leading and trailing edges unchanged

The results for these four initial runs are shown in Fig. 4.37 below. It can be seen from these results that there is a small gain (~0.10% normalised efficiency) to be made by reducing the thickness of the blades while keeping the inside surface and the TE fixed. When the outside surface is fixed and the inside surface altered, there is always a reduction in efficiency which is even more profound when the TE width is changed with the reduction in thickness. This shows how crucial the TE width is to the hydraulic performance of the Turgo and re-enforces the results of the previous study *4.2.3 Trailing edge width*.

The geometry with the reduced thickness was also run with 24 blades shown by the red curve. The results show that the 20% thinner blade (with fixed inside and TE) gives a greater increase in efficiency with 24 blades which indicates that the optimum blade number (Fig. 4.33) is restricted by the blade thickness, as postulated, and reducing the thickness of the blades means that greater gains can be achieved with an increase in the number of blades

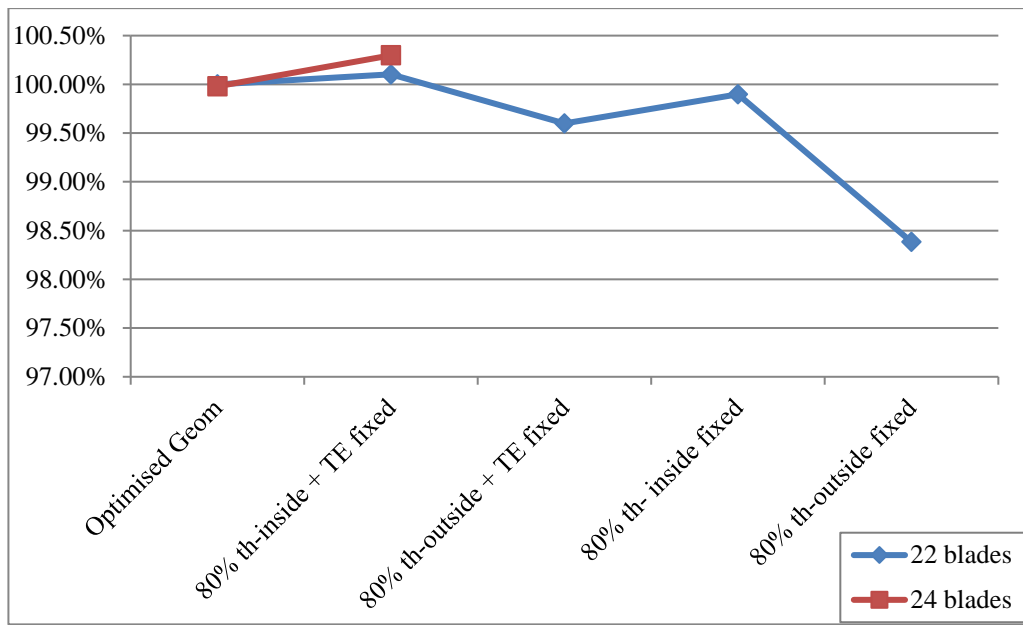


Fig. 4.37. Blade thickness study- initial runs

The geometry was cleaned up and parameterised again for this study and the blade thickness was reduced further in order to see the effect on the performance. The blade thickness was reduced to 60% of the original as shown in Fig. 4.38. This reduction only saw a 0.03% increase in efficiency compared to the 0.17% increase by reducing the thickness to 80%. It was therefore decided that the optimisation study will continue using the 20% reduction in blade thickness which doesn't affect the strength by as great a degree and leaves open the option for an increase in the number of blades.

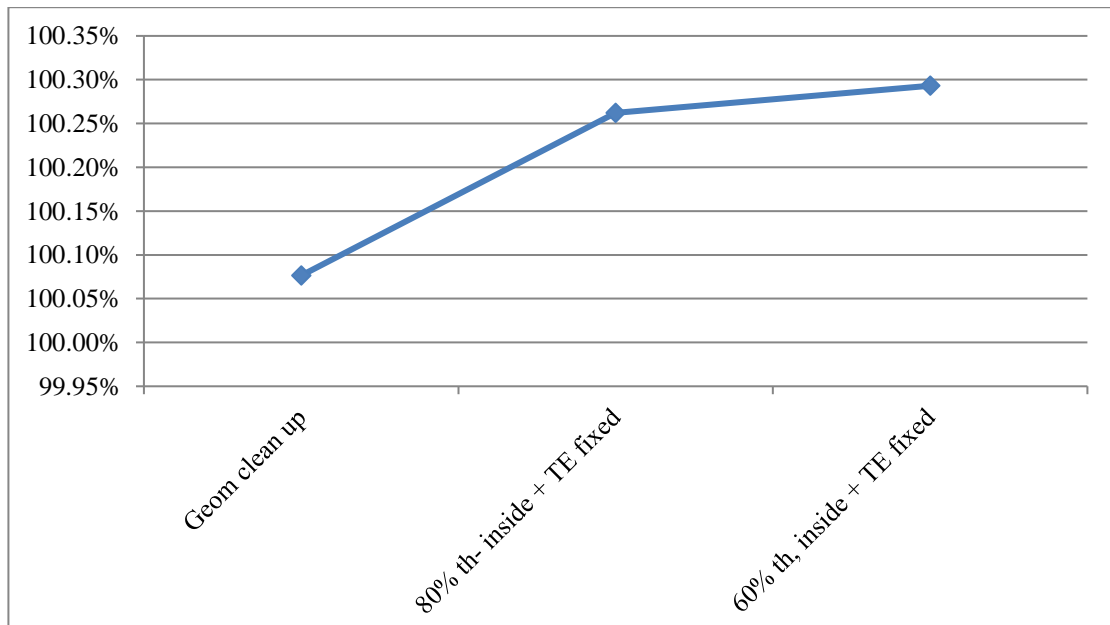


Fig. 4.38. Blade thickness study- further runs

4.3 Phase 2: Blade shape DOE study (DOE2)

4.3.1 DOE Study Setup

Phase 2 of the HCTI optimisation study looks at the shape of the blades and control of the flow once it has reached the inlet to the blade. The parameters being investigated are the depth of the blades in the peripheral direction, the width of the blades in the axial direction and the exit angles along the axial and radial control curves. The variation of these parameters will be based around the current optimised design with some modifications from Phase 1 of the optimisation study.

The DOE parameters, *Depth Factor (DF)*, *Width Factor (WF)* and *Exit Angles Factor (EAF)* are variations of the blade design as shown in Fig. 4.39, where the radial height of the blade, H , is kept constant.

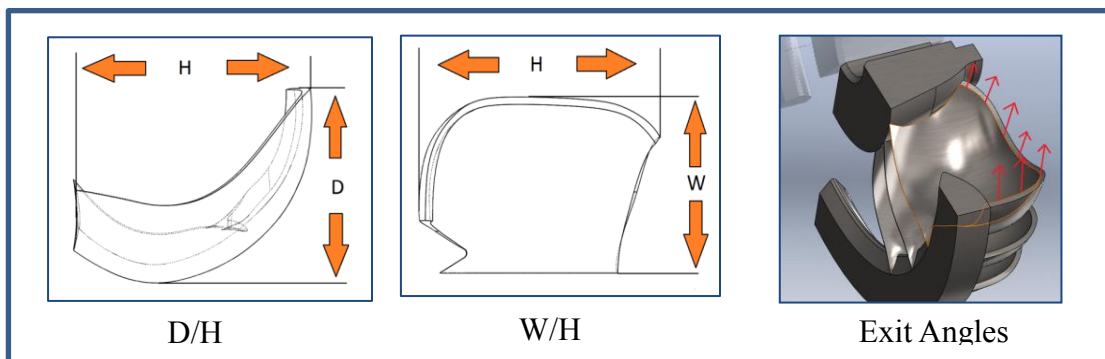


Fig. 4.39. DOE2 Parameters, left to right, DF, WF and EAF

The width of the blade, W , is varied by changing the distance between the 2 axial planes in the centre of the blade as shown in Fig. 4.40. This allows the width of the blades to be varied without affecting the inlet and exit angles. The range of blade widths used in this DOE study are defined by multiplying the original blade width between these two planes by a range of WFs ranging from 0.6-1.2. The limits were defined by changing the width of the geometry in either direction until a point is reached where the axial curves are no longer smooth.

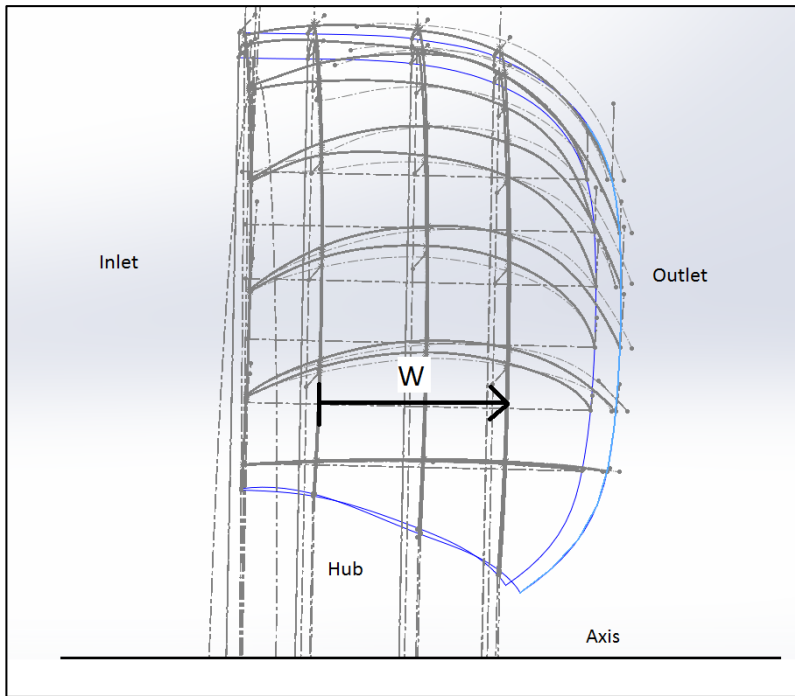


Fig. 4.40. Variation of DOE2 parameter blade width W

The blade depth, D , was varied by stretching the axial control curves (which lie on the axial planes used to control the width) in the horizontal direction. The depth variation is achieved by multiplying the horizontal distance from a fixed vertical plane of each point on the control curve by DF as shown in Fig. 4.41. Using this method ensures that the original profile of the control curves and thus the surface of the blades is maintained to a certain degree and simple stretched in either direction around the original shape. The range of DFs for the initial DOE2 study were set by changing the depth of the geometry in either direction until a point is reached where the axial curves are no longer smooth. The DFs used in the initial DOE study range from 0.9-1.2.

The exit angles were varied by multiplying both the axial and radial control curve exit angles by the EAF. This method helps to maintain the distribution of exit angle values across the TE. The initial range of exit angles was set using a range of EAFs from 0.7-1.1.

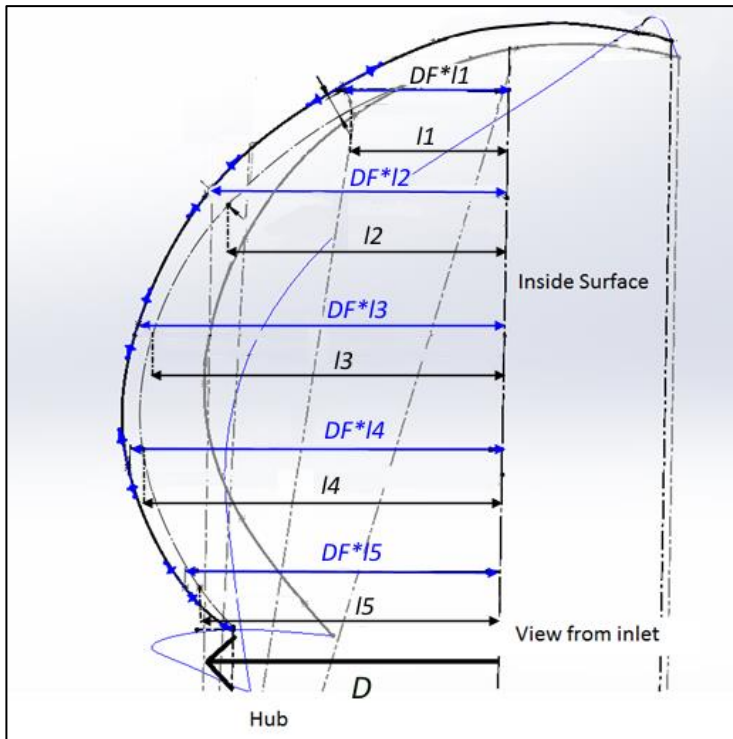


Fig. 4.41. Variation of DOE2 parameter blade depth D

Using these three DOE parameters with the ranges defined above, a DOE study was set up using the Design Expert software to look at the relationship between the blade depth, width and exit angles and their impact on the Turgo runner performance.

The details of the initial experiment design are given in Table 4.2, below.

Study Type	Response Surface	Runs	26
Design Type	Central Composite	Simulation Time	39 Days
Design Model	Quadratic		

Table 4.4- DOE2 initial study design details

Fig. 4.42 to Fig. 4.44 show the distribution of the DF, WF and EAF, which will be used in the initial DOE2 study to generate a response surface. 12 additional runs have been added to the initial DOE design which can be seen in the figures. These are the 4 points spaced equidistant between the centre point and the horizontal and vertical limits, for each chart. These points were added in order to improve the resolution of the response surface.

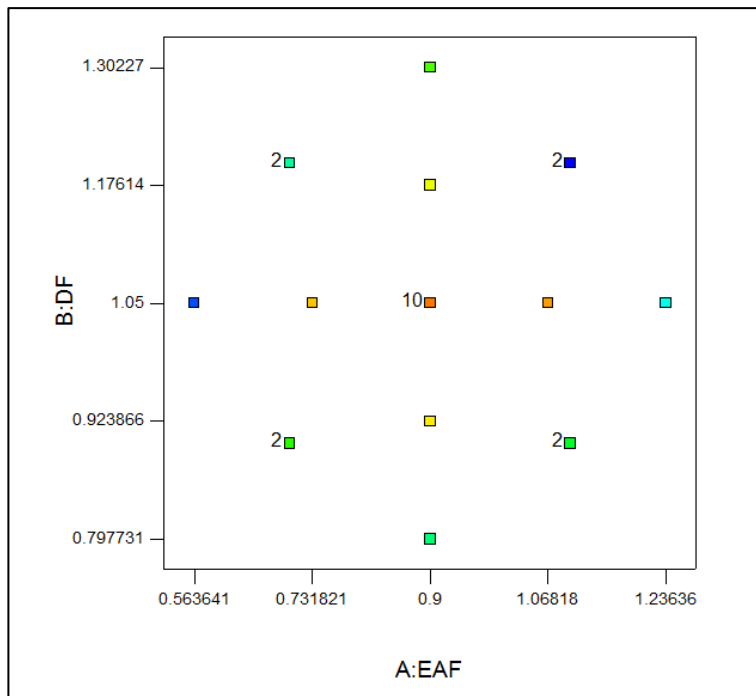


Fig. 4.42. Graph columns for *Depth Factor (DF)* against *Exit Angles Factor (EAF)*

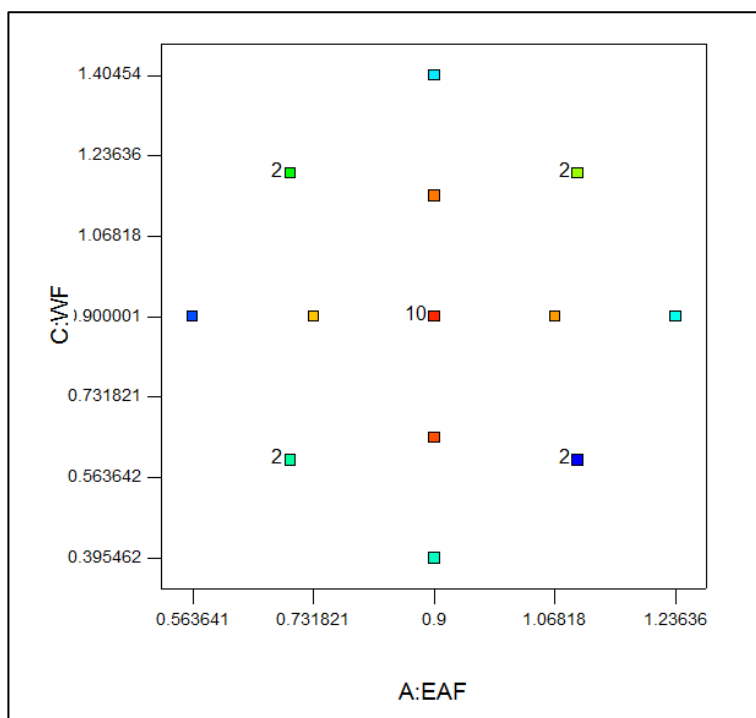


Fig. 4.43. Graph columns for *Width Factor (WF)* against *Exit Angles Factor (EAF)*

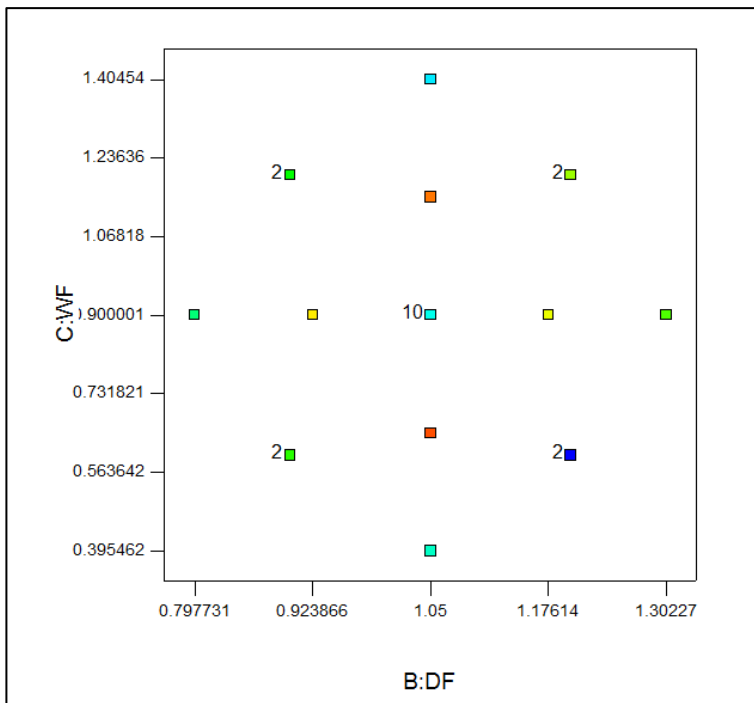


Fig. 4.44. Graph columns for *Depth Factor (DF)* against *Width Factor (WF)*

4.3.2 DOE Study Results

The results for this DOE study (excluding the repeated design points) are given in Table 4.5 below. The efficiencies are normalised against the previous optimum runner design efficiency.

Run	Exit Angle Factor	Depth Factor	Width Factor	Normalised efficiency
1	1.10	1.20	0.60	72.16%
2	0.90	1.05	0.90	97.94%
3	0.56	1.05	0.90	96.71%
4	0.90	1.05	1.40	95.67%
5	1.24	1.05	0.90	72.16%
6	0.90	1.05	0.40	80.54%
7	0.70	1.20	0.60	72.55%
8	0.90	0.80	0.90	97.99%
9	1.10	0.90	1.20	100.03%
10	0.70	0.90	1.20	99.37%
11	0.70	0.90	0.60	98.22%
12	0.90	1.30	0.90	72.28%
13	0.70	1.20	1.20	85.41%
14	1.10	1.20	1.20	86.59%
15	1.10	0.90	0.60	98.23%
16	0.90	1.18	0.90	86.10%
17	0.90	0.92	0.90	100.41%
18	0.73	1.05	0.90	96.60%
19	1.07	1.05	0.90	97.17%
20	0.90	1.05	1.15	97.83%
21	0.90	1.05	0.65	94.36%

Table 4.5- Blade shape and exit angles DOE study results- normalised against previous optimum

4.3.2.1 *Torque curve analysis*

Before analysis of the DOE response surface, some of the torque curves were compared for the designs where only a single parameter is varied giving a good understanding of the behaviour of the flow for these designs and how changing a single parameter affects the torque curves.

4.3.2.1.1 Varying Exit Angle Factor (EAF)

Fig. 4.45 below shows the normalised torque curves for two of the designs (runs 2&3) which have a DF of 1.05, a WF of 0.9 and an EAF which is varied from 0.56 to 0.9. The results show that the steeper EAF of 0.56 is less efficient than the EAF of 0.9 by around 1%. Even though the torque on the inside of the blade is greater for the steeper angled design, the flow leaving the inside blade surface causes a reduction in the outside torque due to flow interference and the overall torque is lower. The same can be seen for runs 9 and 10 in Fig.

4.46 where the shallower angled design is around 0.5% more efficient due to a larger torque on the outside blade surface.

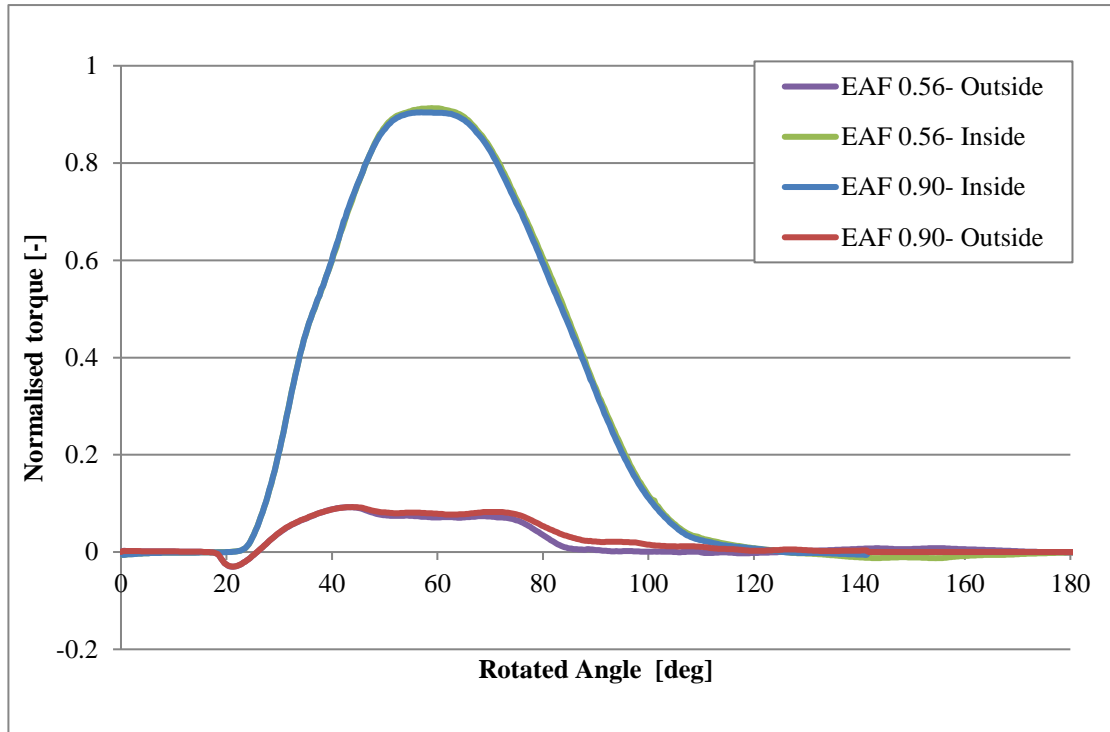


Fig. 4.45. Torque curves for runs 3 and 2 where the $DF=1.05$ and $WF=0.9$ and the EAF is varied

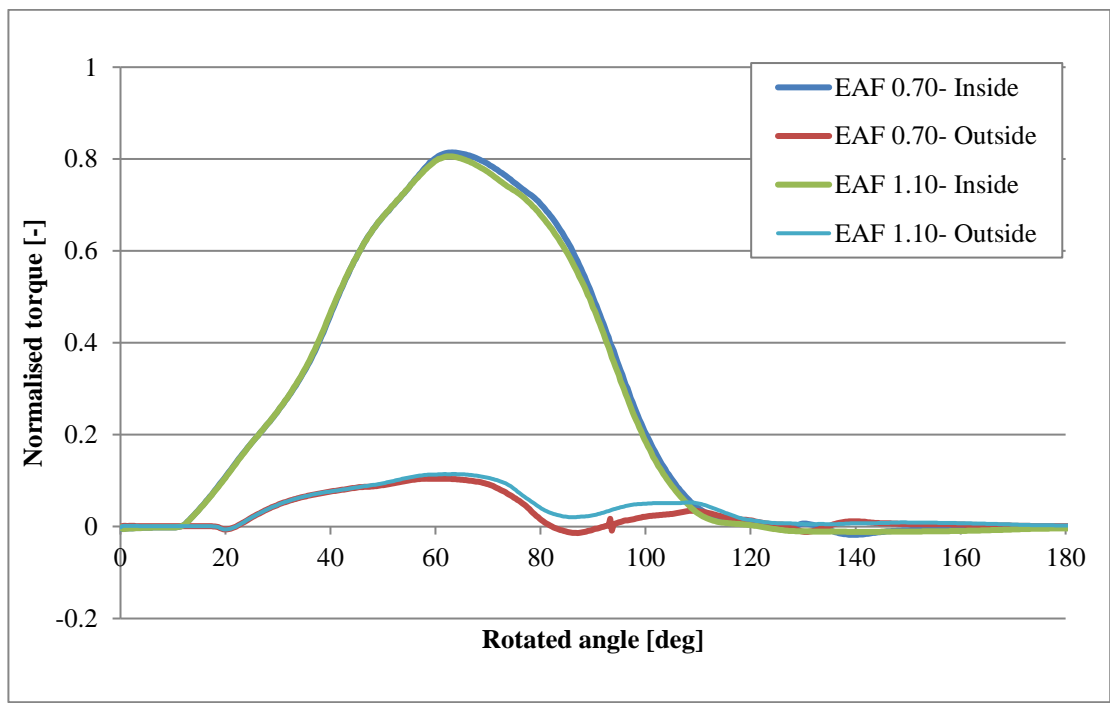


Fig. 4.46. Torque curves for runs 10 and 9 where the $DF=0.9$ and $WF=1.2$ and the EAF is varied

4.3.2.1.2 Varying Depth Factor (DF)

Fig. 4.47 shows the impact of varying the DF on the torque curves for runs 2, 8 and 17. The results show the shallower blade designs giving a much wider torque curve with a higher initial torque as the water jet reaches the blade surface sooner producing useful torque earlier in the rotation. It is interesting to note how the efficiency of designs 8 and 2 varies very little despite the large difference in the shapes of the torque curves whereas design 17 is around 2.1% more efficient than 2 and 8.

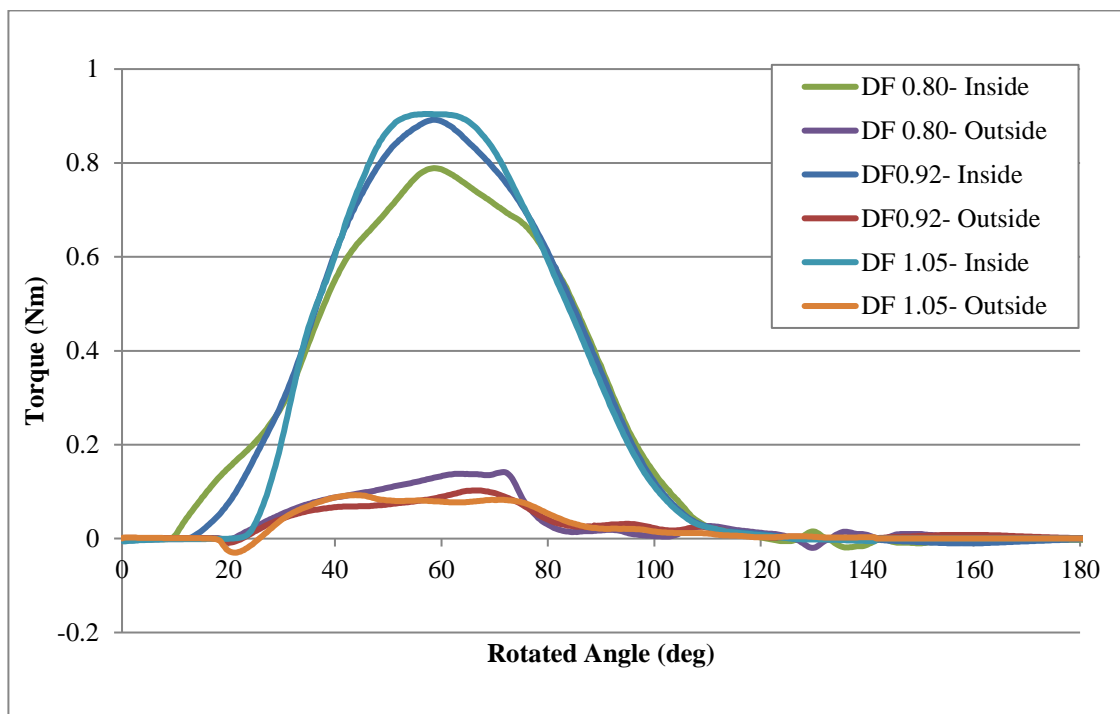


Fig. 4.47. Torque curves for runs 2, 8 and 17 where the EAF=0.9 and WF=0.9 and the DF is varied

4.3.2.1.3 Varying Width Factor (WF)

Fig. 4.48 shows the effect of varying the WF on the torque curves (runs 11 and 10). As is expected, the wider design has a wider torque curve width a lower peak as the flow takes longer to pass across the blade and the change in direction is less pronounced. The wider design is around 1% more efficient in this instance.

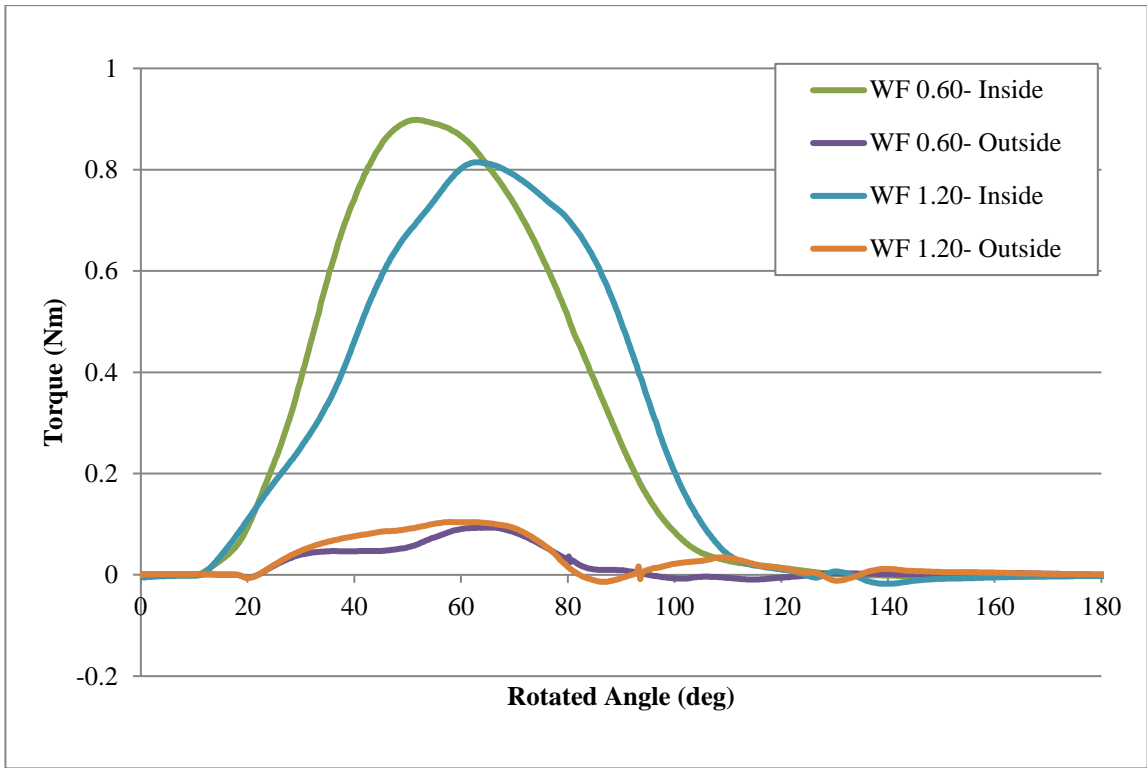


Fig. 4.48. Torque curves for runs 11 and 10 where the EAF=0.7 and DF=0.9 and the WF is varied

4.3.2.2 Full DOE results

The quadratic model was suggested by the Design Expert software as the most suitable for the DOE results, giving an adjusted R-squared value of 0.98 and a predicted R-squared value of 0.91. The predicted results are shown against the actual results in Fig. 4.49 showing a reasonable fit to the data points. Fig. 4.50 to Fig. 4.52 show the interaction between the DOE parameters. The results show no interaction between the EAF and the DF or WF and a slight interaction between the WF and DF.

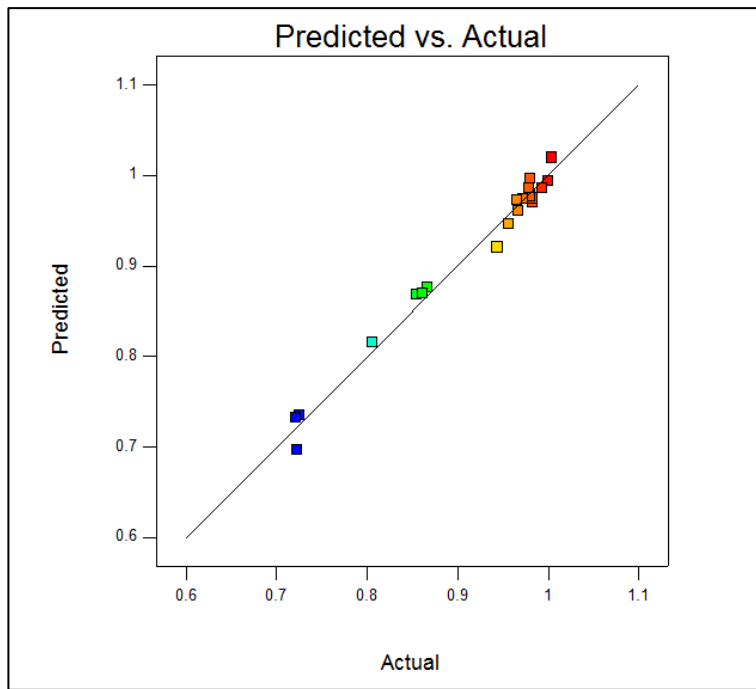


Fig. 4.49. Predicted vs. Actual DOE results

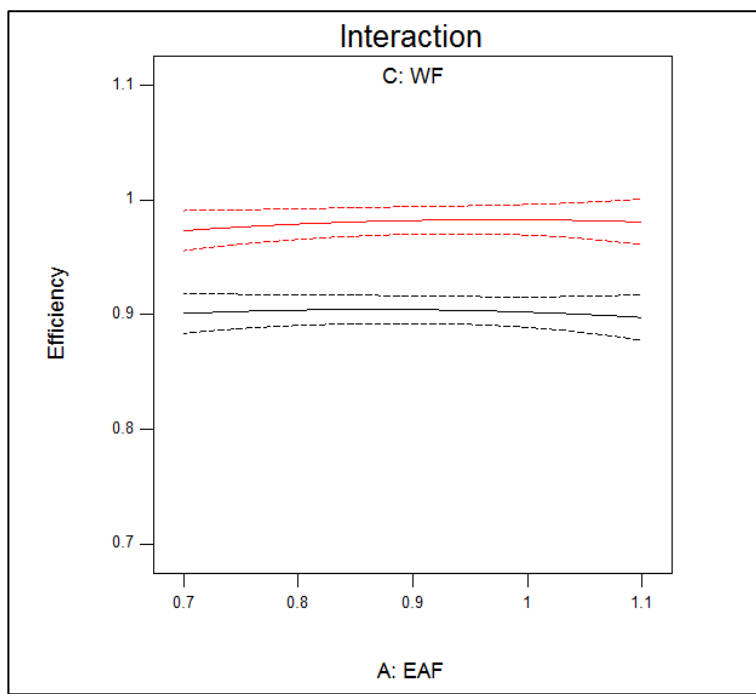


Fig. 4.50. Interaction between Width Factor (WF) and Exit Angles Factor (EAF)

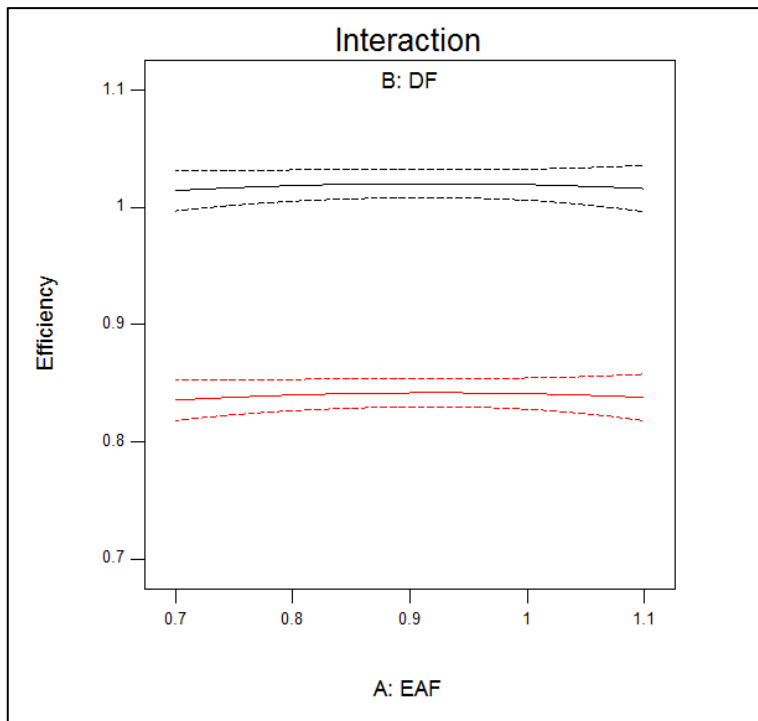


Fig. 4.51. Interaction between Depth Factor (DF) and Exit Angles Factor (EAF)

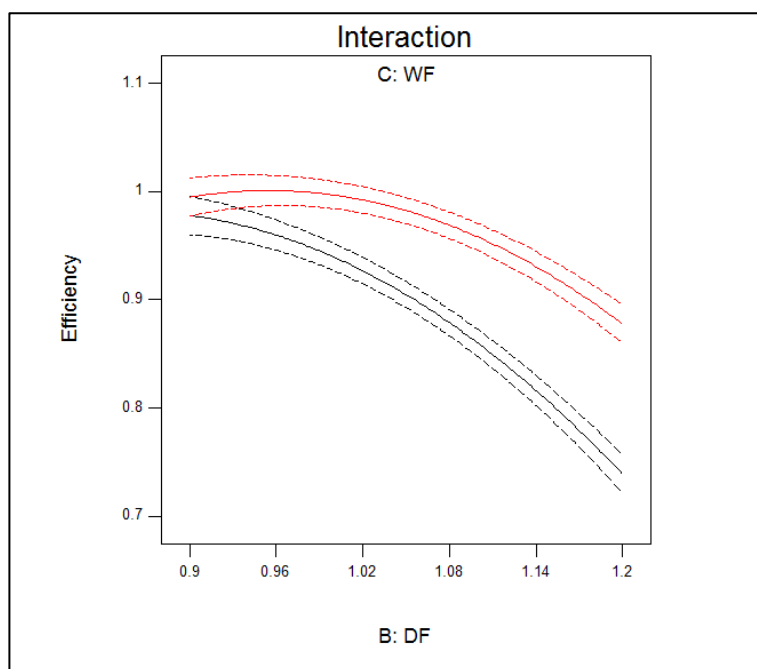


Fig. 4.52. Interaction between Width Factor (WF) and Depth Factor (DF)

4.3.2.2.1 Depth Factor (DF)/ Exit Angles Factor (EAF)

The impact of the DF and the EAF on the efficiency is shown by the contour plots in Fig. 4.53 to Fig. 4.55. The contours are plotted for WFs of 0.9, 1.05 and 1.2. The contours indicate the lack of interaction between the DF and the EAF with the DF having no impact on the optimum EAF of just over 0.9. This shows that the optimum exit angle is independent of the depth of the blades. The highest efficiency is predicted at a width factor of 0.9 of around 102% and as the width is increased, the optimum depth and exit angle factors are also higher.

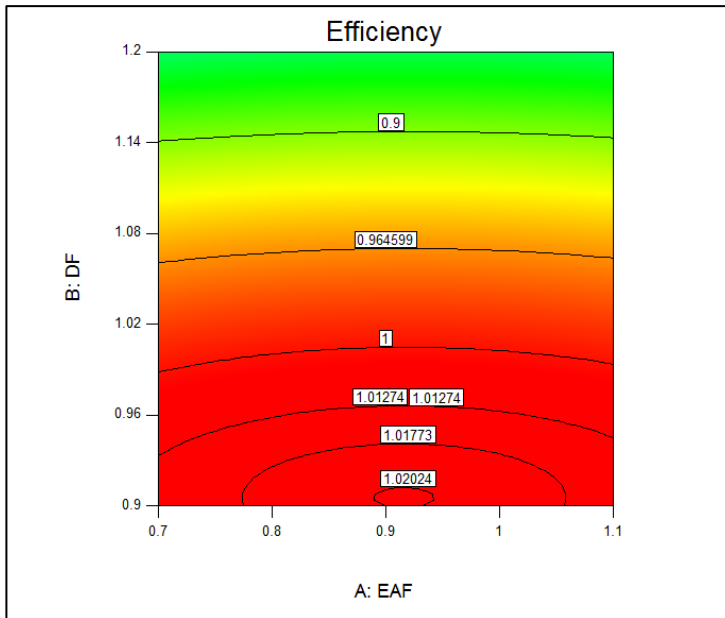


Fig. 4.53. DF/EAF contours for a WF of 0.9

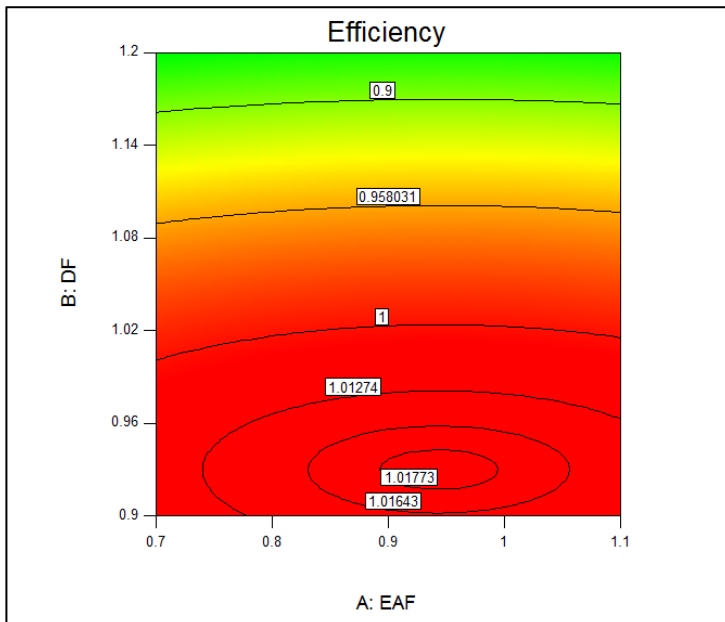


Fig. 4.54. DF/EAF contours for a WF of 1.05

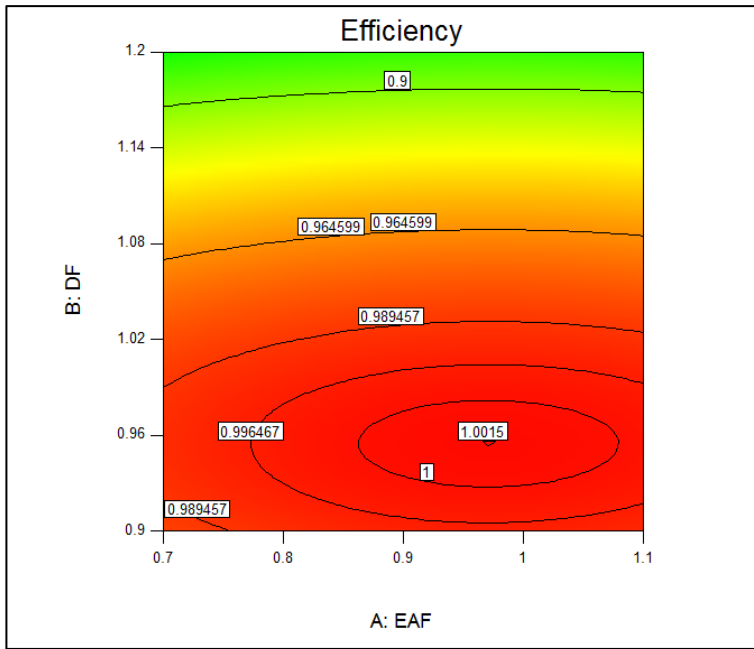


Fig. 4.55. DF/EAF contours for a WF of 1.2

4.3.2.2.2 Width Factor (WF)/ Exit Angles Factor (EAF)

The WF/EAF contours are shown in Fig. 4.56 to Fig. 4.58 for DFs of 0.90, 1.05 and 1.2. The results show the highest efficiency at a DF of 0.9 with a WF of around 0.95 and an EAF of just over 0.9. The results also show that as the DF is increased, the optimum WF also increases along with the EAF showing that wider deeper blades require a larger exit angle and are less efficient than narrower shallower blades.

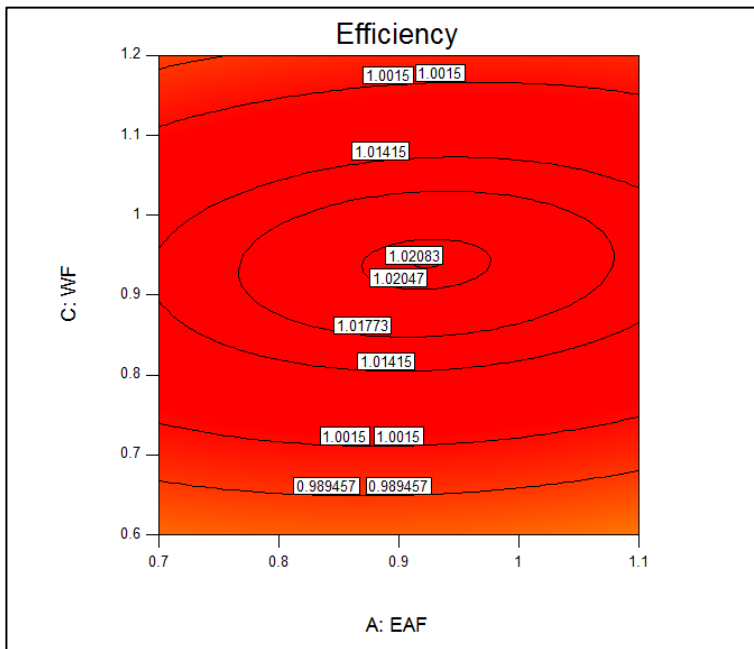


Fig. 4.56. WF/EAF contours for a DF of 0.90

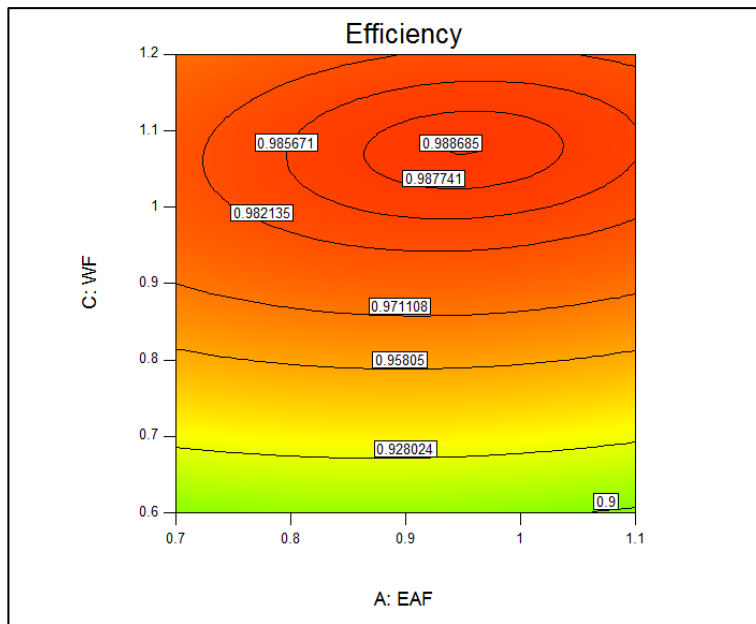


Fig. 4.57. WF/EAF contours for a DF of 1.05

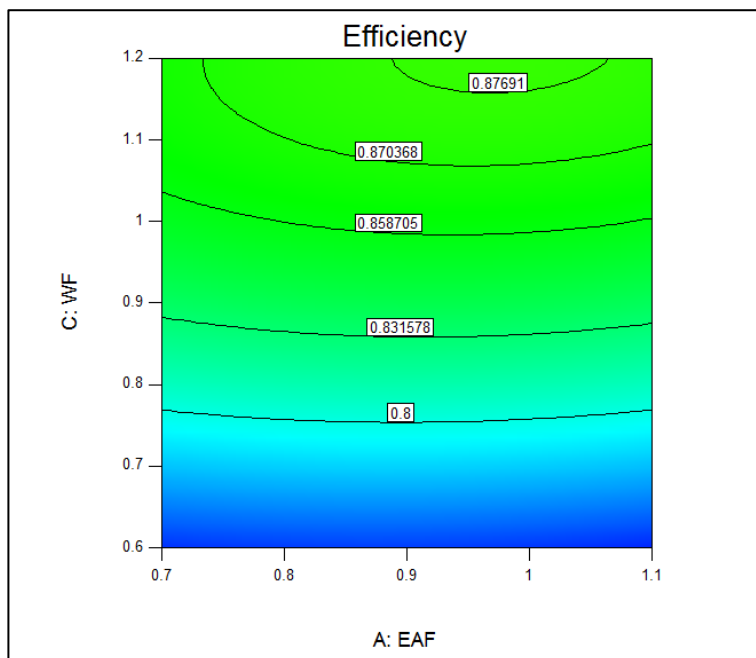


Fig. 4.58. WF/EAF contours for a DF of 1.2

4.3.2.2.3 Width Factor (WF)/ Depth Factor (DF)

The WF/DF contours are shown in Fig. 4.59 to Fig. 4.61. The results show that the EAF has little effect on the optimum WF and DF with the maximum efficiency at an EAF of 0.9. This shows an optimum WF and DF independent of the EAF.

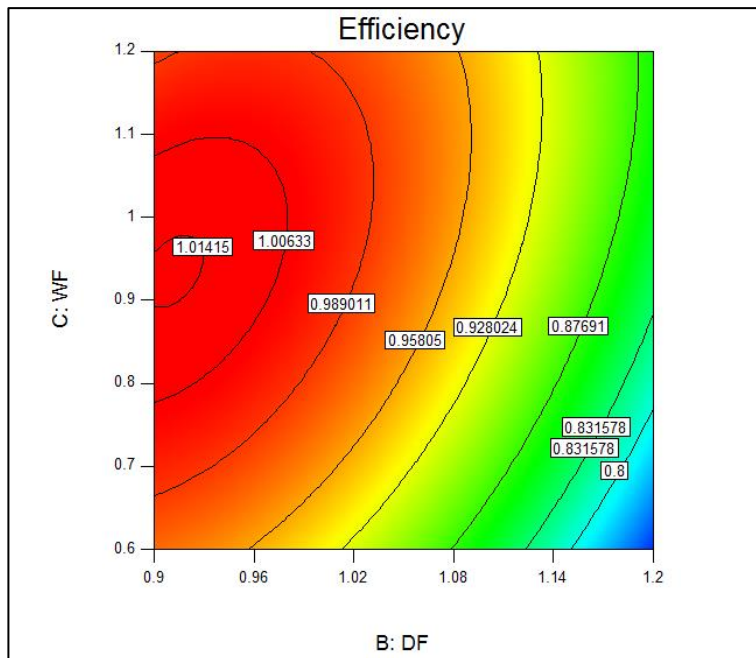


Fig. 4.59. WF/DF contours for an EAF of 0.7

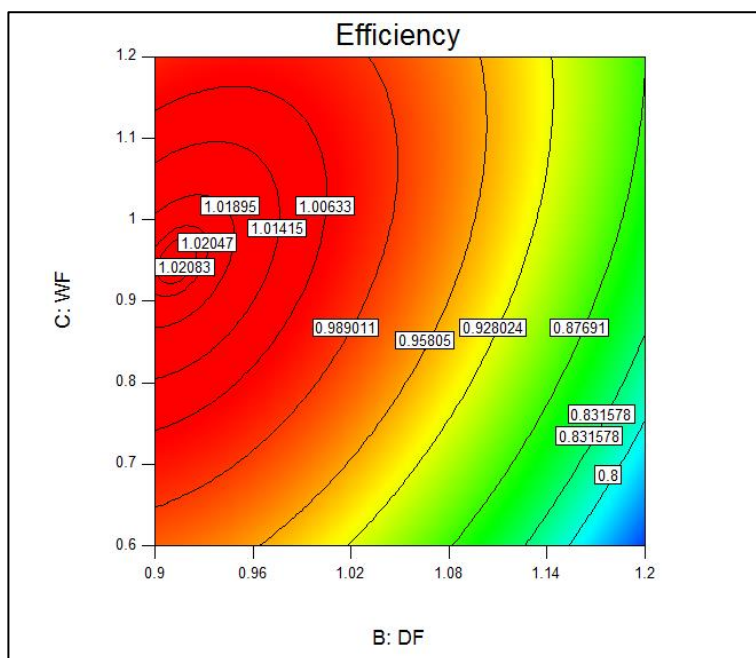


Fig. 4.60. . WF/DF contours for an EAF of 0.9

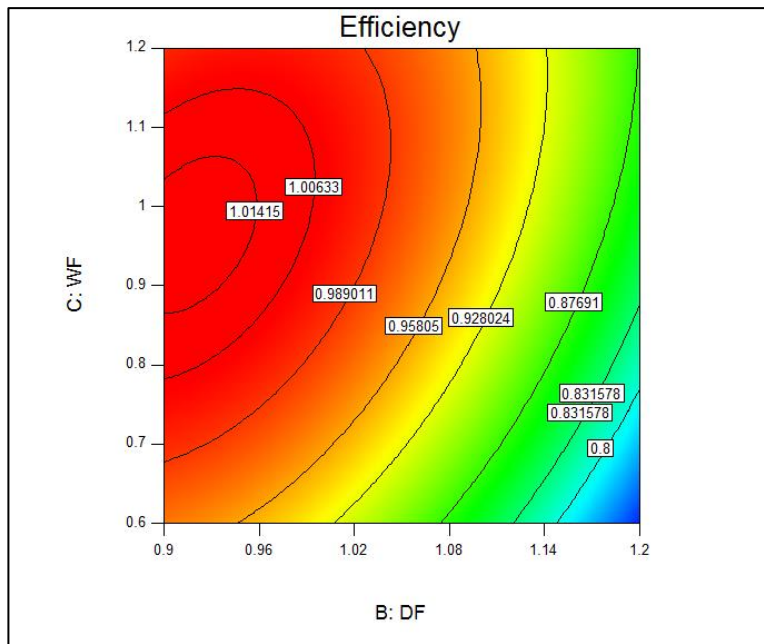


Fig. 4.61. . WF/DF contours for an EAF of 1.1

4.3.2.3 Optimisation

Based on the DOE2 results, an optimum design was suggested with an EAF of 0.926, a DF of 0.914 and a WF of 0.951. The modified geometry is shown in Fig. 4.62 laid over the original HCTI geometry. The torque curves for the previous optimised design (P036) and the optimised design based on the DOE study (DOE2.22) are shown in Fig. 4.63.

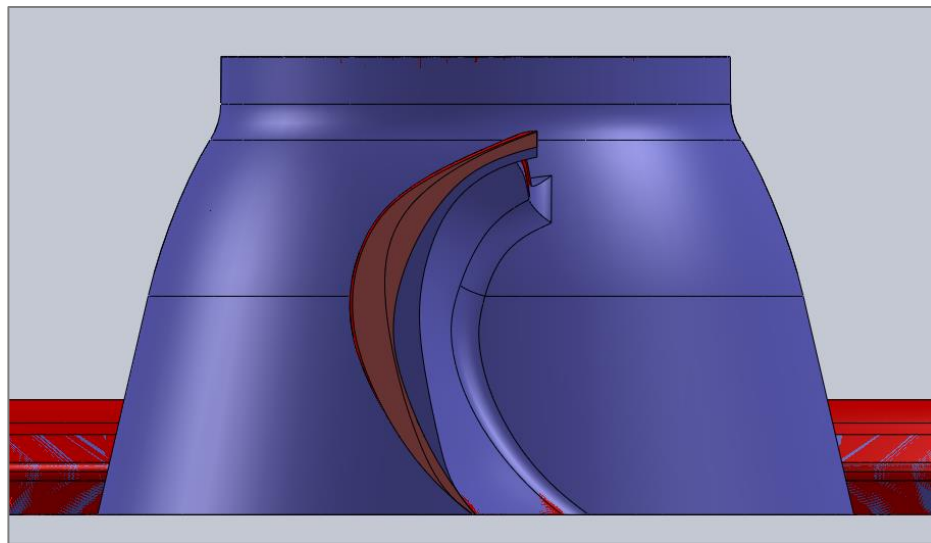


Fig. 4.62. Modified HCTI geometry shown in blue over original HCTI geometry in red- cut section at jet pitch circle radius

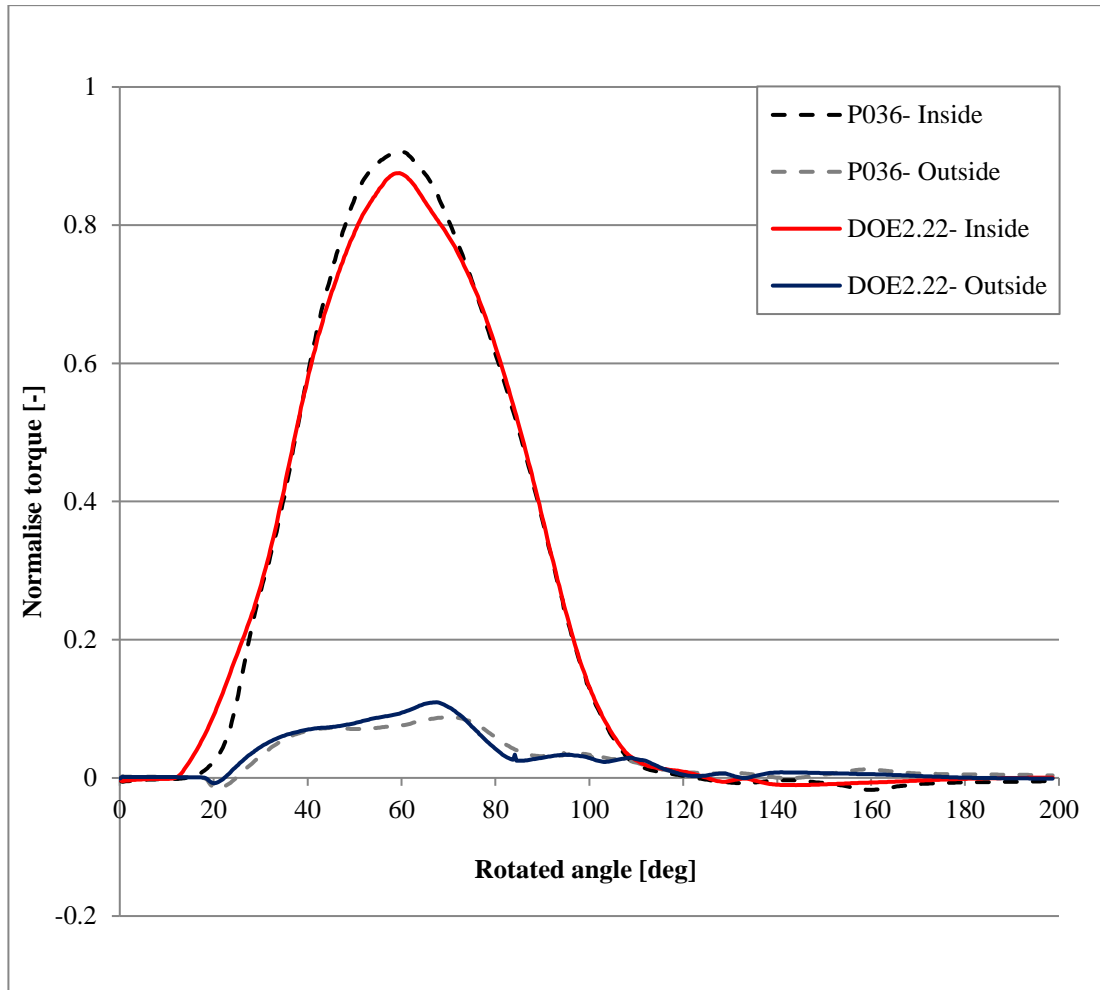


Fig. 4.63. Comparison between P036 design (optimum from TE width study) and DOE2.22 (the DOE2 study optimum design) normalised torque curves

The optimised DOE2.22 design gave an increase in efficiency of 0.56% compared to the previous P036 design. It can be seen by the torque curves that the modified design, with shallower, slightly narrower blades causes the jet to change direction sooner in the rotation giving a wider torque curve at the start of the rotation. The change in the design also produces a higher peak in the torque on the outside surface of the blade and although the peak torque on the inside surface is lower, the total torque is higher. This design point was then added to the DOE study results and although it is lower than the predicted optimum, it didn't change the position of the peak showing that this design result follows the trend in the prediction.

The optimised design was run with the *fine mesh* setup (~9M elements) which showed a smaller increase in efficiency of 0.33% from this study, with an overall increase of 1.41% from the original design using the refined mesh setup.

4.4 Phase 3: Additional Parameters

Based on the results of the previous optimisation studies and analysing the flow around the optimised geometry, some additional studies were carried out as detailed below.

4.4.1 Outside surface exit angles

Although the exit angles of the inside blade surface were studied and adjusted in 4.3- *Phase 2: Blade shape DOE study (DOE2)*, the outside surface exit angles were unchanged from the original design. As there is a significant portion of the flow tracing the outside surface of the blade, generating the positive torque on the outside blade surface as shown in the torque curves it was predicted that this would be an important parameter to investigate. The outside surface exit angles were varied by multiplying the original exit angles by an *exit angle factor*. The outside surface exit angle factors (OEAF) were varied from 1.2 to 0.1 in 0.1 intervals, generating 11 new runner geometries as shown in Table 4.6. These geometries were meshed and simulated and the results are shown in the table as well as in Fig. 4.64, below. The efficiencies are normalised against the initial P055 design with an OEAF of 1.

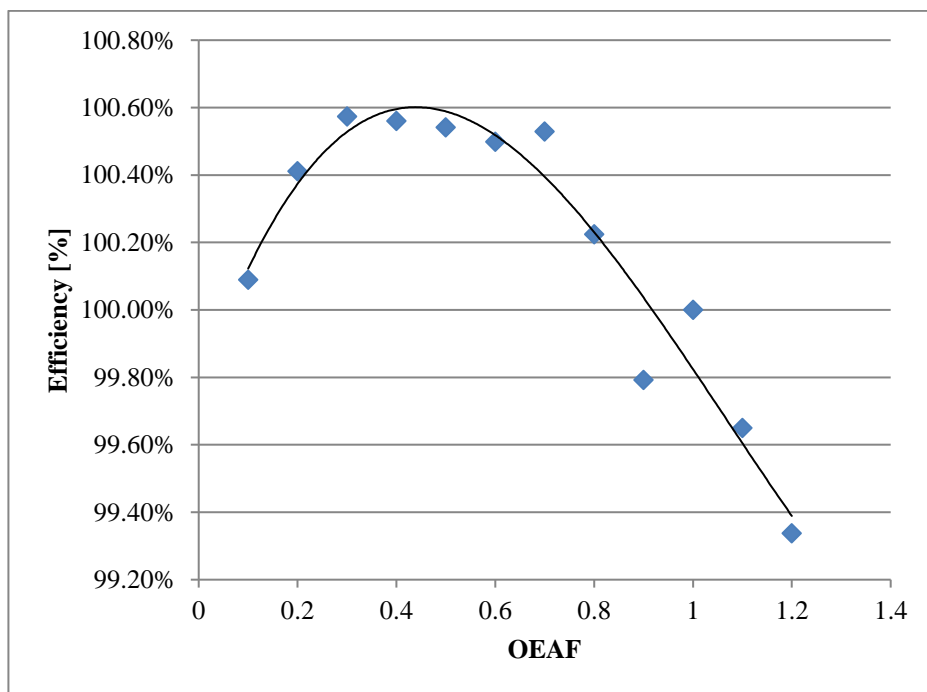


Fig. 4.64. Outside surface exit angles (OEAF) study- results

The results show that there is a significant gain in efficiency (over 0.5%) to be had by reducing the OEAF from 1 to 0.5 (OEAF7) which is the optimum value based on this study. The results also show that some flexibility in the accuracy of the outside surface exit angles is

permitted with values between 0.3 and 0.7 still giving high efficiencies compared to the original values.

The torque curves were also compared for the first half of the curve in Fig. 4.64 (OEAF 0.1-0.5) and the second half of the curve (OEAF 0.5-1.2) on either side of the optimum (Fig. 4.65 & Fig. 4.66). The torque curves show that as the OEAF is increased from 0.1-0.5 (Fig. 4.65), the torque on the outside blade surface is increased between 50° and 100° rotation which explains the increase in efficiency. As the OEAF is increased from 0.5-1.2 (Fig. 4.66), the torque on the outside surface of the blades remains high between 50° and 100° but decreases between 80°and 120°, with little change to the rest of the torque curves, showing that this is the region where the efficiency drop is occurring as the OEAF is increased beyond the optimum.

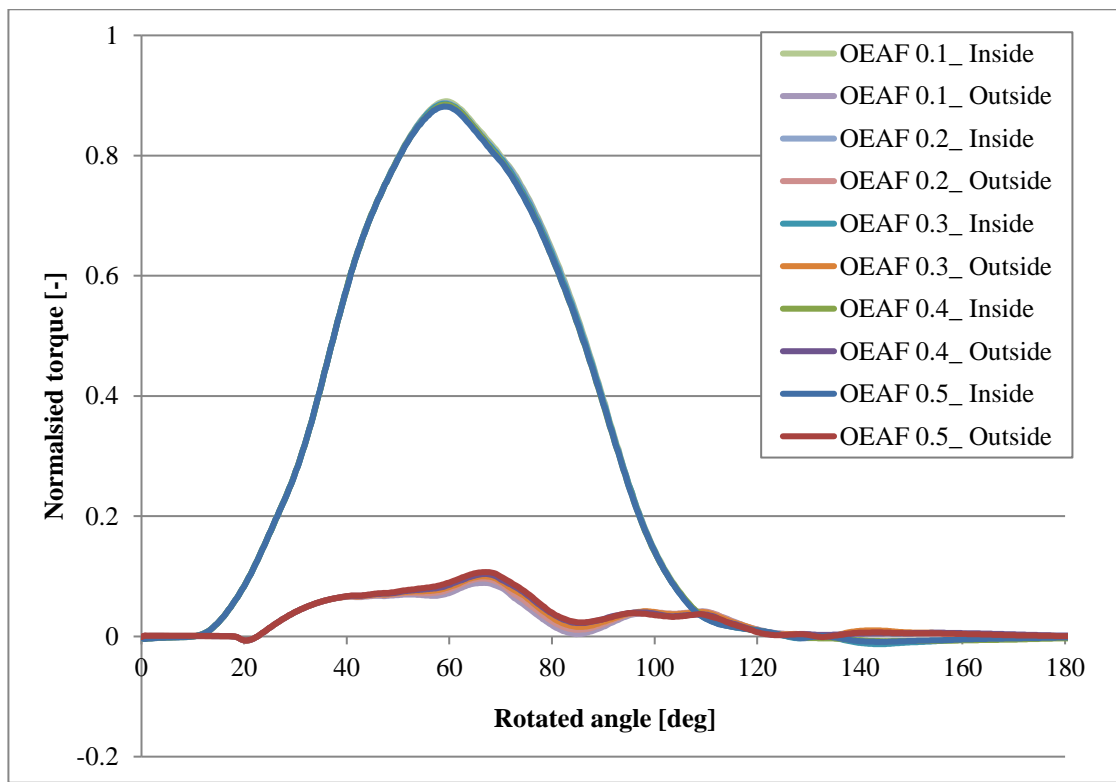


Fig. 4.65. Normalised torque curves for OEAF 0.1-0.5

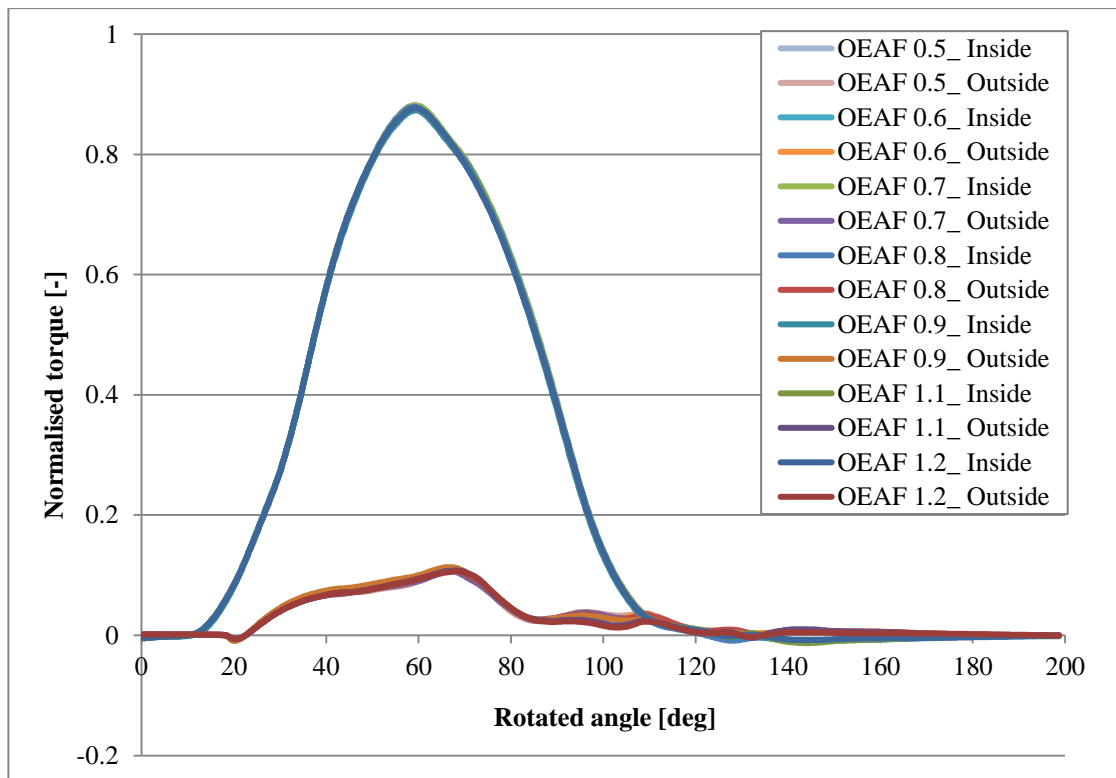


Fig. 4.66. Normalised torque curves for OEAFAF 0.5-1.2

Geometry	Outside Exit Angle Factor (OEAF)			Control curve							Normalised efficiency
				CR1	CR2	CR3	CR4	CR5	CR6	CR7	[%]
P055	1	Inside exit angles	[deg]	14.4	13.4	11.6	10.2	14.8	15.3	13	100.00%
		Outside exit angles	[deg]	2	22	22	19	20	20	20	
P055_OEA1	1.2	Inside exit angles	[deg]	14.4	13.4	11.6	10.2	14.8	15.3	13	99.34%
		Outside exit angles	[deg]	2	26.4	26.4	22.8	24	24	24	
P055_OEA2	1.1	Inside exit angles	[deg]	14.4	13.4	11.6	10.2	14.8	15.3	13	99.65%
		Outside exit angles	[deg]	2	24.2	24.2	20.9	22	22	22	
P055_OEA3	0.9	Inside exit angles	[deg]	14.4	13.4	11.6	10.2	14.8	15.3	13	99.79%
		Outside exit angles	[deg]	2	19.8	19.8	17.1	18	18	18	
P055_OEA4	0.8	Inside exit angles	[deg]	14.4	13.4	11.6	10.2	14.8	15.3	13	100.22%
		Outside exit angles	[deg]	2	17.6	17.6	15.2	16	16	16	
P055_OEA5	0.7	Inside exit angles	[deg]	14.4	13.4	11.6	10.2	14.8	15.3	13	100.53%
		Outside exit angles	[deg]	2	15.4	15.4	13.3	14	14	14	
P055_OEA6	0.6	Inside exit angles	[deg]	14.4	13.4	11.6	10.2	14.8	15.3	13	100.50%
		Outside exit angles	[deg]	2	13.2	13.2	11.4	12	12	12	
P055_OEA7	0.5	Inside exit angles	[deg]	14.4	13.4	11.6	10.2	14.8	15.3	13	100.54%
		Outside exit angles	[deg]	2	11	11	9.5	10	10	10	
P055_OEA8	0.4	Inside exit angles	[deg]	14.4	13.4	11.6	10.2	14.8	15.3	13	100.56%
		Outside exit angles	[deg]	2	8.8	8.8	7.6	8	8	8	
P055_OEA9	0.3	Inside exit angles	[deg]	14.4	13.4	11.6	10.2	14.8	15.3	13	100.57%
		Outside exit angles	[deg]	2	6.6	6.6	5.7	6	6	6	
P055_OEA10	0.2	Inside exit angles	[deg]	14.4	13.4	11.6	10.2	14.8	15.3	13	100.41%
		Outside exit angles	[deg]	2	4.4	4.4	3.8	4	4	4	
P055_OEA11	0.1	Inside exit angles	[deg]	14.4	13.4	11.6	10.2	14.8	15.3	13	100.09%
		Outside exit angles	[deg]	2	2.2	2.2	1.9	2	2	2	

Table 4.6- Phase 3: Outside exit angles geometry and results table

4.4.2 Jet inclination angle

As part of the Turgo runner optimisation, it was recommended that the jet inclination angle also be investigated to determine whether it would be possible to counter some of the outward radial movement of the flow due to the centrifugal forces as it moves across the blade surface by inclining the jet towards the rotational axis. The 1D model developed by Webster showed that a large portion of the losses can be attributed to this outward spreading of the flow and the resultant increase in the radius ratio (Webster 1971).

In order to investigate the impact of changing the jet inclination angle on the efficiency, the inclination angle of the jet, from the horizontal plane, about the point where the jet meets the runner, was varied from -10° to $+10^\circ$ from the horizontal in 2° increments as shown in Table 4.7. The efficiencies are normalised against the P055 design efficiency with an inclination angle of 0° .

Design #	Jet inclination angle [deg]	Normalised efficiency [%]
P055_JA1	-10	98.21%
P055_JA2	-8	98.98%
P055_JA3	-6	99.38%
P055_JA4	-4	99.79%
P055_JA5	-2	99.95%
P055	0	100.00%
P055_JA6	2	99.94%
P055_JA7	4	99.78%
P055_JA8	6	99.44%
P055_JA9	8	98.90%
P055_JA10	10	98.25%

Table 4.7- Jet inclination angle study results table

The results of this study (Fig. 4.67) show that the optimum inclination angle of the jet is horizontal and the efficiency drops off gradually as this is changed in either direction suggesting that there is no benefit to changing the inclination angle of the jet. The results also show that the turbine remains insensitive to a slight change in the inclination angle, with a variation of 2° either side of the horizontal only reducing the efficiency by around 0.1%. This shows the robustness of this Turgo design, with slight changes in the inclination angle which could arise from tolerance stacking etc. having little effect on the efficiency.

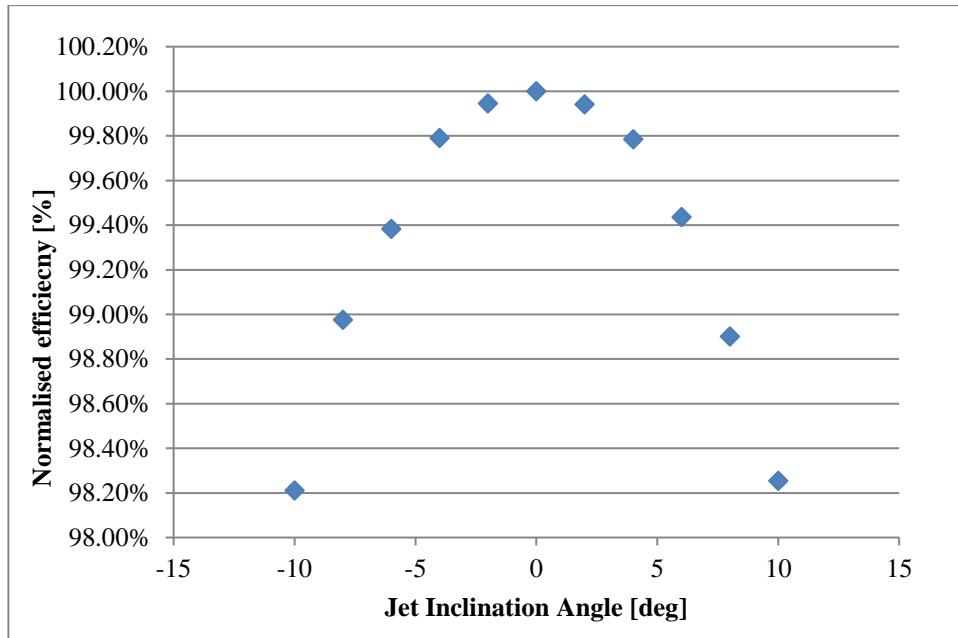


Fig. 4.67. Jet inclination angle study results

4.5 Runner optimisation summary

The design changes carried out during the runner optimisation study were verified using the *fine mesh* simulation which showed an increase in normalised efficiency of 2.28% between the original HCTI Turgo runner and the optimised Turgo runner. The design studies carried out on the Turgo runner which showed improvement in performance are plotted in Fig. 4.68. The efficiencies are normalised against the *fine mesh* efficiency of the original HCTI runner.

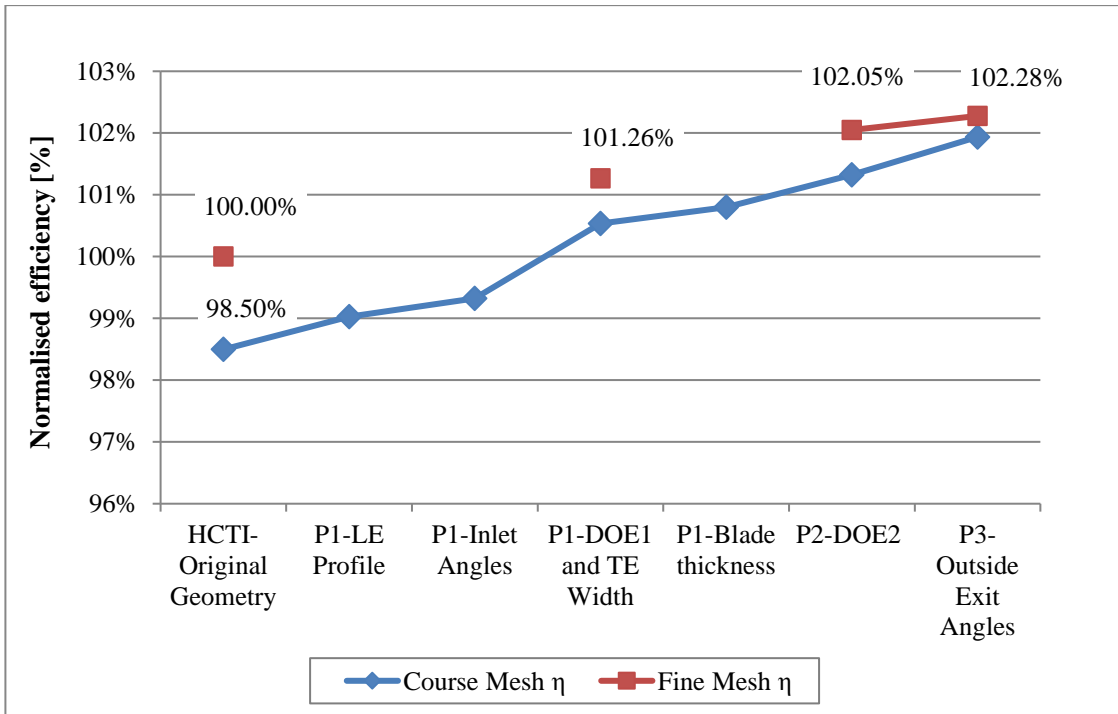


Fig. 4.68. Turgo numerical runner optimisation summary showing *coarse mesh* and *fine mesh* results

The normalised torque curves for the original and optimised designs are shown in Fig. 4.69 below. The torque curves show that the negative torque on the outside blade surface has been reduced substantially and the overall shape of the inside torque curve is more uniform as well as being wider as a result of the wider, slightly shallower blade design. The absolute velocity contours in the centre of the jet are also compared for each runner design in Fig. 4.69 at the peak inside torque position. The results show less restriction in the flow through the optimised runner as a result of the shallower blades as well as the exit flow leaving at a steeper angle, reducing the leaving losses.

This study has shown how an accurate CFD model can be utilised in the optimisation of Turgo impulse turbine runners, giving the ability to not only compare different designs but provide a better understanding of why specific design changes impact the performance. This is possible by being able to compare the torque curves and internal flow phenomena in great detail and at specific time periods which is not possible with experimental testing.

Although the runner design has been optimised with a view for maintaining the mechanical strength where possible, this needs to be verified before carrying out experimental tests. The strength of the optimised runner is analysed in detail and compared to the original runner design in the following chapter 5 *Turgo runner Finite Element Analysis (FEA)*.

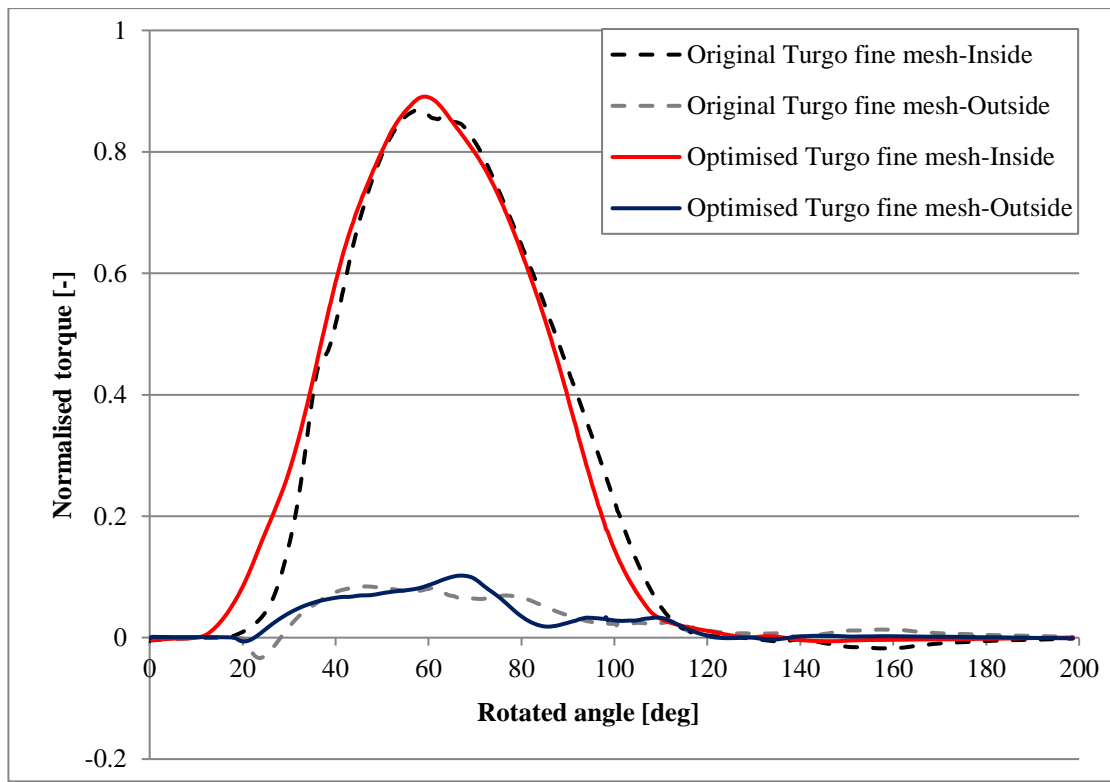


Fig. 4.69. Normalised torque curve comparison between the original HCTI Turgo runner and the optimised Turgo runner designs using the *fine mesh*

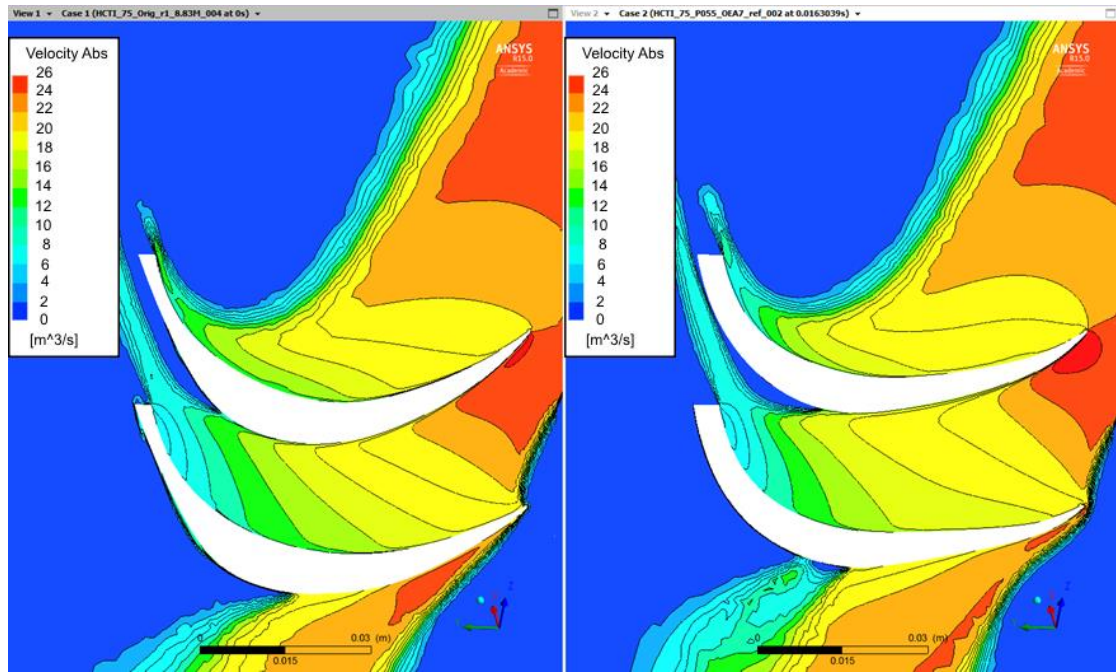


Fig. 4.70. Absolute velocity contours on axial plane through centre of jet for the original HCTI Turgo runner (left) and the optimised runner (right) plotted at the peak inside torque position

5 Turgo runner Finite Element Analysis (FEA)

Before manufacturing the optimised Turgo runner, a full Finite Element Analysis (FEA) was carried out using ANSYS® Mechanical in order to ensure the optimised runner still has sufficient strength to withstand the loads experienced by the runner during operation. These can be broken down into three cases;

1. Runaway speed or overspeed, where the load on the turbine shaft is lost (usually a result of a power cut) and the runner peripheral speed at the PCD approaches the free jet velocity. Here the stresses, which are usually of the greatest magnitude, are induced by the centrifugal forces acting on the runner.
2. Jet loading-normal operation, where the jet applies a load to the runner during normal operation combined with the centrifugal forces resulting from the rotation of the runner.
3. Jet loading- locked operation, where the jet applies a load to the blades while the runner is locked in place with no rotation.

A $\frac{1}{4}$ runner section was first analysed and the design was strengthened based on the results of the $\frac{1}{4}$ runner FEA. The design changes were verified with CFD simulations of the new runners in order to ensure there is no significant reduction in hydraulic efficiency with the imposed design changes. Design for Manufacture and Assembly (DFMA) was then applied to the strengthened runner by changing the LE width to aid the manufacturing process. FEA was then carried out on the two resulting designs, with varying LE widths, looking at a $1/4$ and $1/3$ runner sections and finally the full runner. CFD was also carried out on these runner designs.

5.1 $\frac{1}{4}$ Runner FEA

5.1.1 Mesh refinement study

For the initial FEA case, a $\frac{1}{4}$ runner section was used with the stresses measured on the middle three blades. The FEA was carried out using ANSYS® Mechanical and the densest meshes for the two geometries are shown in Fig. 5.1.

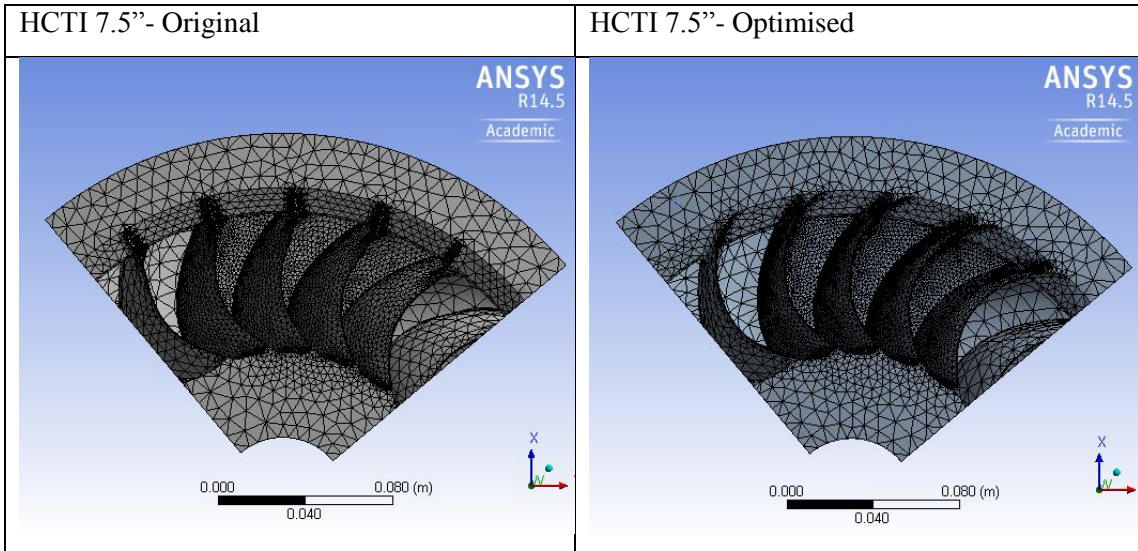


Fig. 5.1. Quarter runner mesh (~130k elements), ANSYS® Mechanical, showing refinement on blade edges

The mesh size was varied by increasing the mesh density on the edges of the blades up to the mesh limit which was restricted by the software license. The setup for the Runaway speed FEA is shown in Fig. 5.2 with supports added to the adjacent faces shown in blue and a rotational speed of 4988rpm corresponding to the runaway speed at a 150m head.

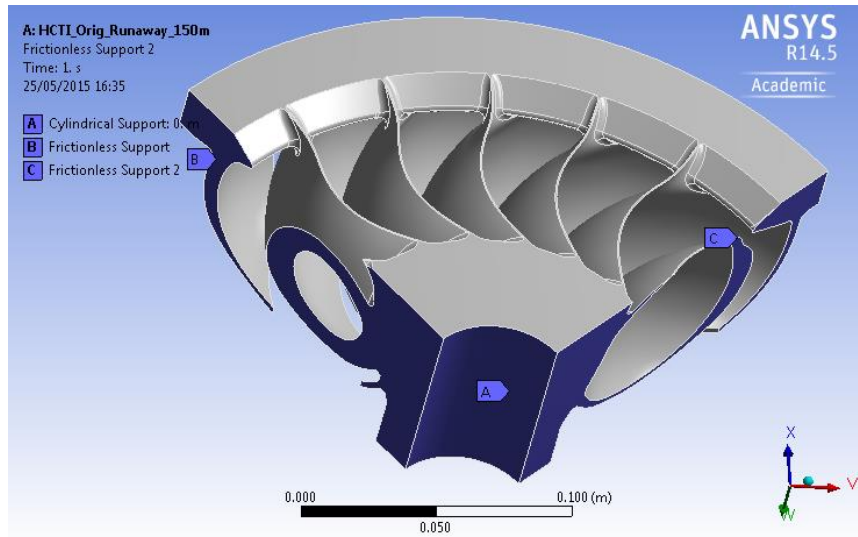


Fig. 5.2. Quarter Runner FEA Setup showing cylindrical and frictionless supports

The impact of the mesh density on the maximum von Mises stress is shown in Fig. 5.3. The results show that the mesh used (containing around 130k elements) is almost mesh independent and differs from the previous mesh size by only 3% and should be accurate enough for comparative purposes.

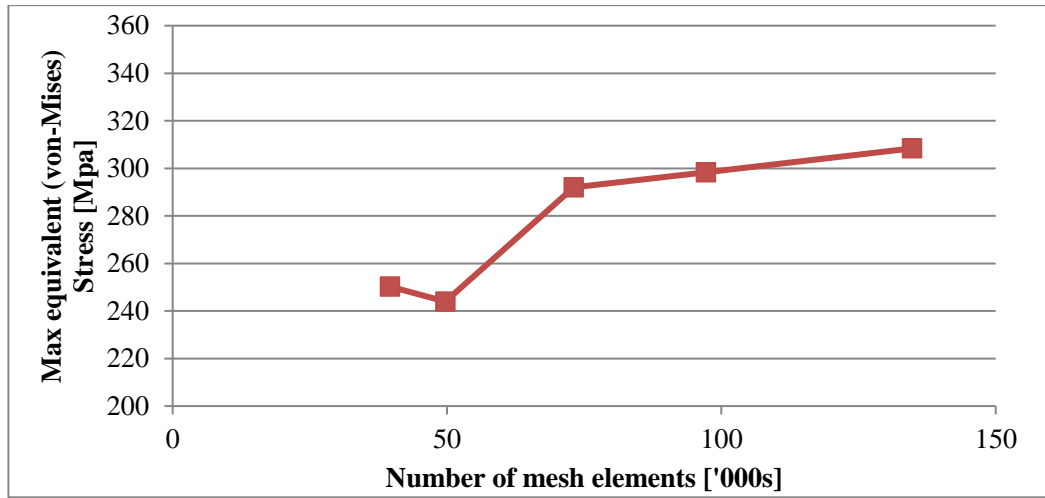


Fig. 5.3. 1/4 runner FEA mesh refinement study for the original 7.5" HCTI runner at 150m head runaway speed

5.1.2 Runaway speed

Using the mesh setup of around 130k elements, the original (HCTI) and optimised (HCTI-opt1) runner geometries were analysed at a runaway speed of 4988rpm (150m maximum design head for 7.5" runner). Initial analysis of the optimised runner, HCTI-opt1, showed that the maximum stress at overspeed is 15.44% higher than the original (HCTI) design as shown in Fig. 5.4.

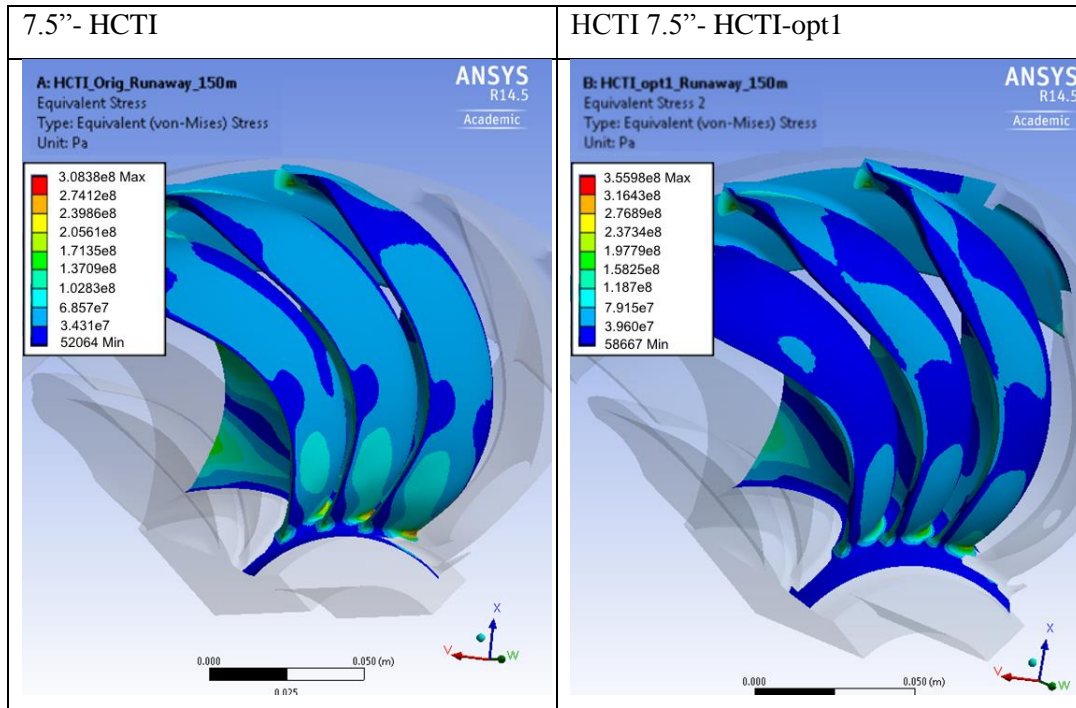


Fig. 5.4. Equivalent (von-Mises) Stress plot for the original and optimised Turgo geometries at runaway speed of 4988rpm

5.1.3 Jet loading

The stresses in the runner as a results of the jet impacting the blades was analysed initially by splitting the three middle blades using the maximum rated flow jet diameter at a head of 150m and a Q11 of 0.25 ($Q=0.111 \text{ m}^3/\text{s}$) as shown in Fig. 5.5 below.

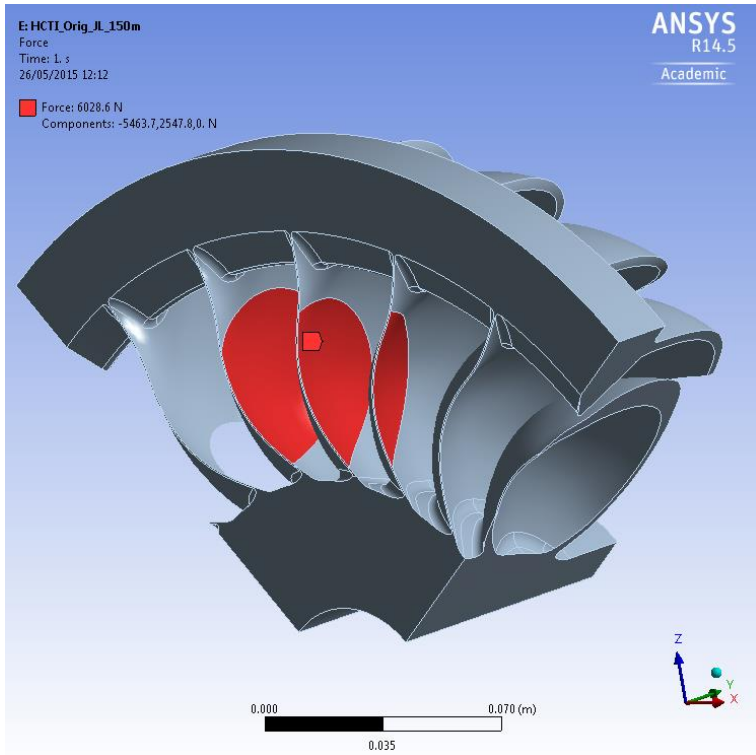


Fig. 5.5. Jet loading applied to area cut out by jet diameter (shown in red) at maximum flow

The force of the jet was applied to these faces under normal and locked operation. The results show that the maximum stress during normal operation in the HCTI-opt1 design is 29.33% higher than the original HCTI design and 3.28% lower in locked operation.

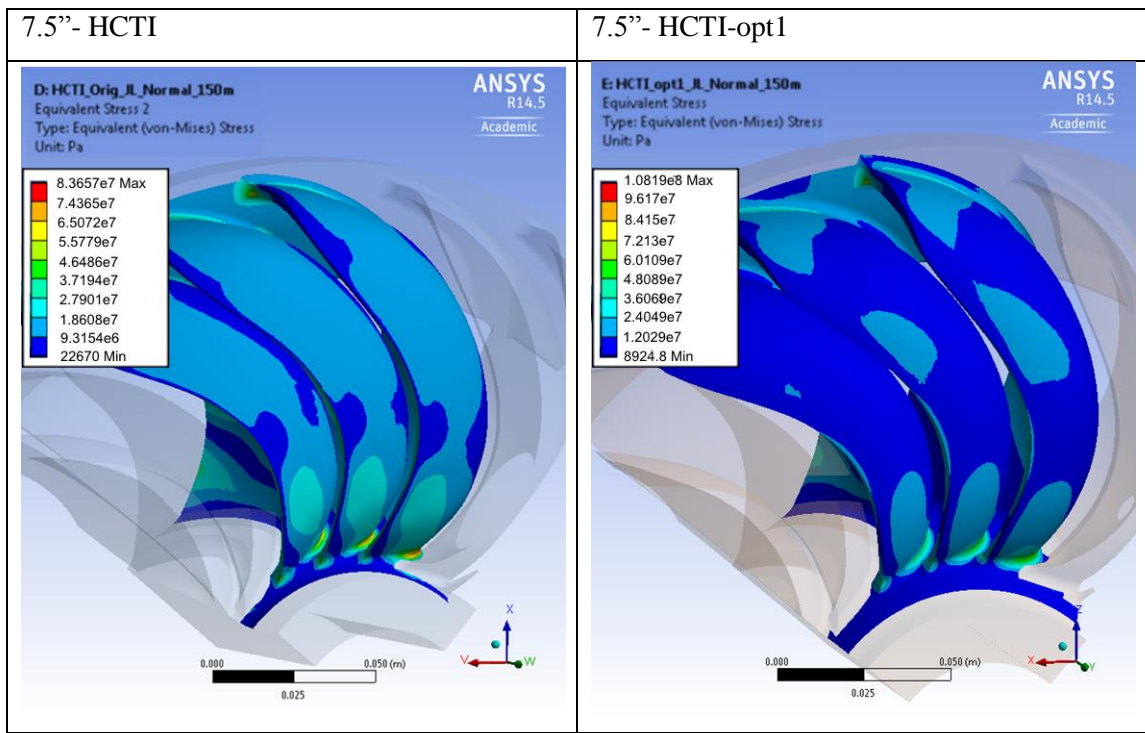


Fig. 5.6. Jet loading in normal operation at 150m head and max flow (111 l/s)

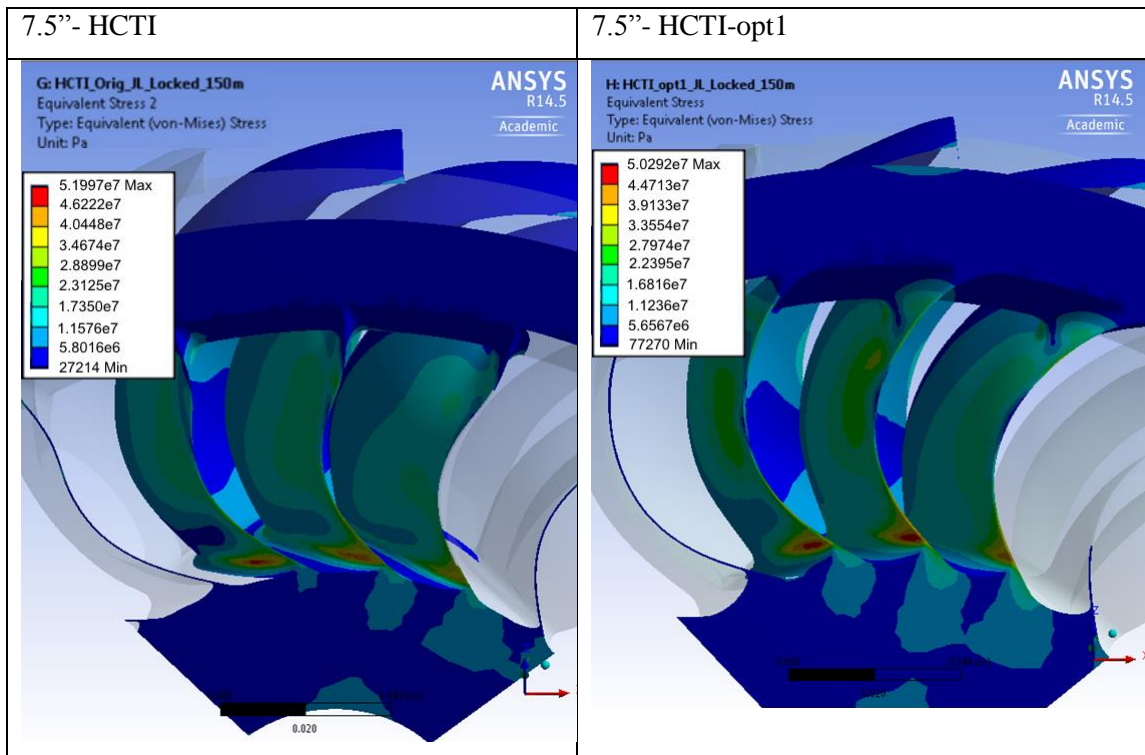


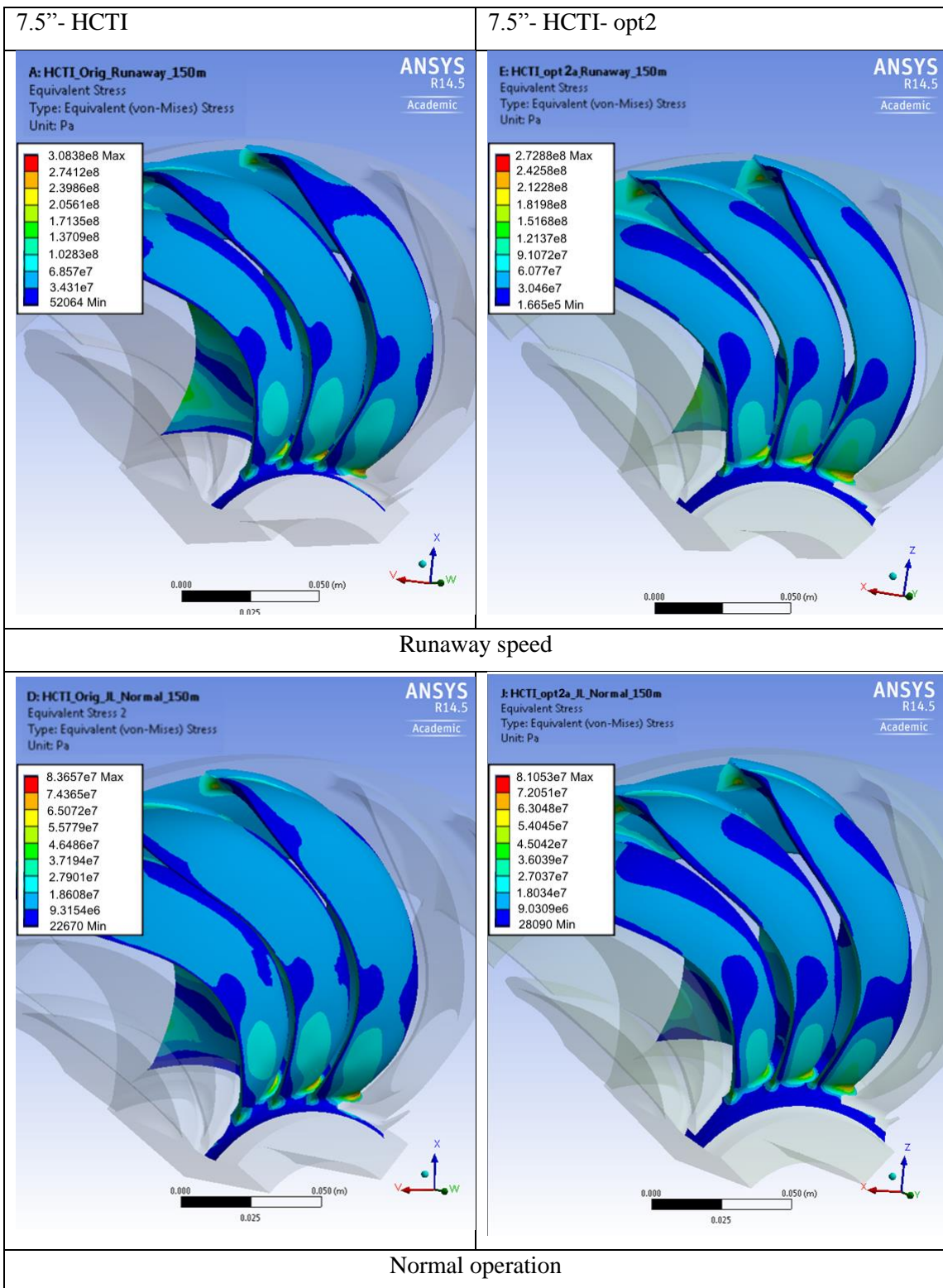
Fig. 5.7. Jet loading in locked operation at 150m head and max flow (111 l/s)

5.1.4 Strengthening the runner

Based on the location of the stresses as a result of overspeed and jet loading, the HCTI-opt1 design was modified further to add strength to the regions of high stress concentration . This was achieved primarily by increasing the radii of the fillets where the blades meet the hub and ring. The stress contours for the strengthened runner design, HCTI-opt2 are compared to the original design for runaway speed, normal operation and locked operation in Fig. 5.8. The peak stresses are also compared in Fig. 5.9.

The results showed the new strengthened (HCTI-opt2) design has reduced the maximum stress at runaway speed to 16.29% lower than original (HCTI) design. At normal operating conditions, the peak stress is 6.49% lower and 8.52% higher during locked operation. The stresses during locked operation are however the lowest overall and it was decided, following discussions with Gilkes, that the overall strength of the Optimised 2 design is sufficient.

The HCTI-opt2 design was also analysed using the coarse mesh and fine mesh CFD models in order to analyse the impact of the design changes to strengthen the runner on the runner efficiency (Fig. 5.9). The results showed a reduction in normalised efficiency, as a result of strengthening the design, of 0.07% using the coarse mesh setup and 0.09% using the fine mesh setup showing that the strengthening design changes have had little impact on the hydraulic performance of the runner.



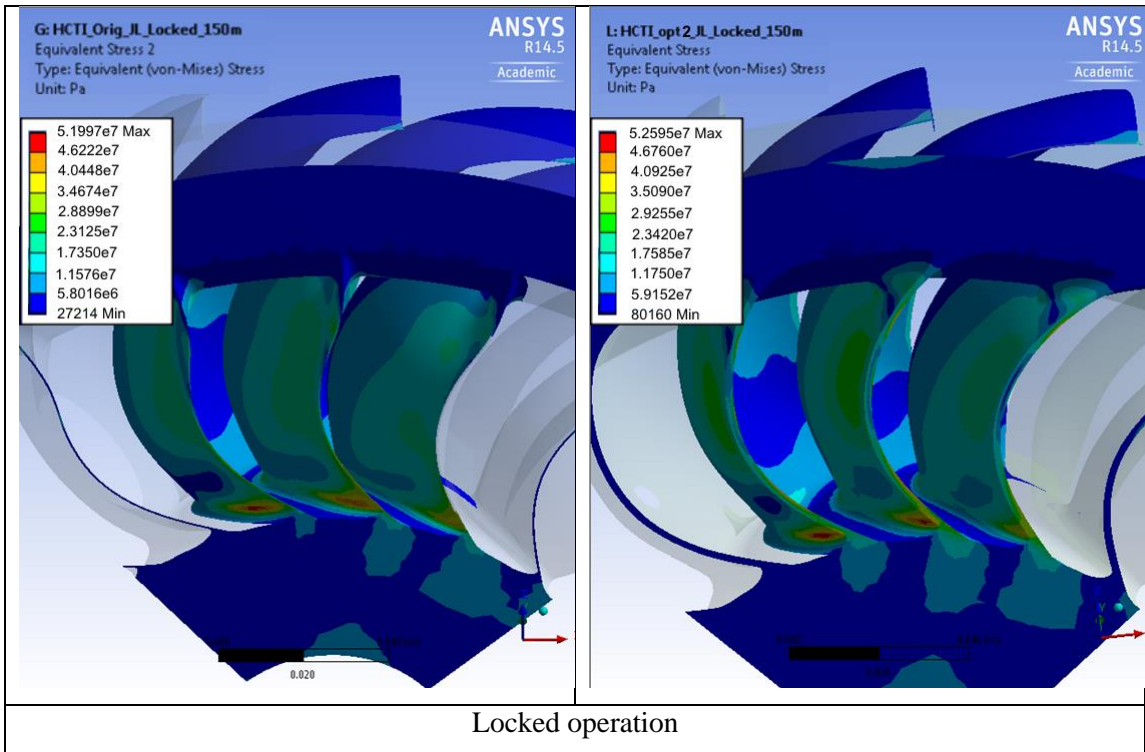


Fig. 5.8. Stress contour comparison between original HCTI runner and strengthened HCTI-opt2 runner designs for runaway speed, normal operation and locked operation

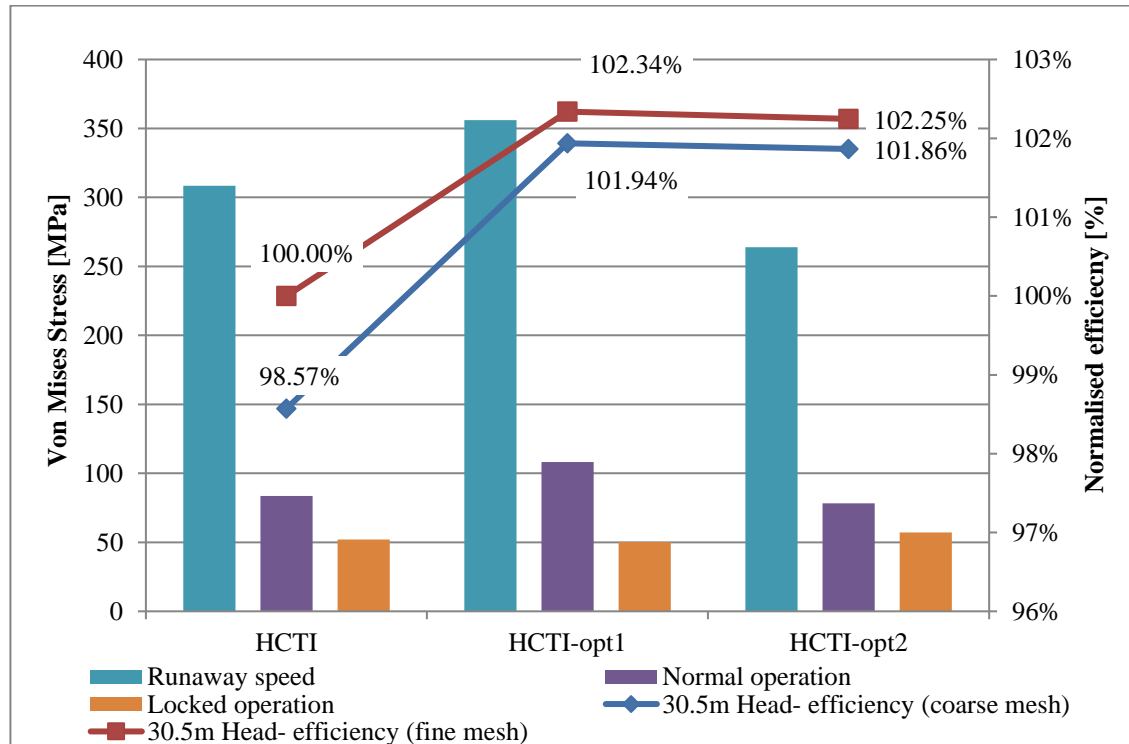


Fig. 5.9. Maximum stresses and normalised efficiencies for the original (HCTI), optimised (HCTI-opt1) and optimised and strengthened (HCTI-opt2) runners

5.2 DFMA- Leading edge width

The FEA of the Turgo was extended to include some DFMA (Design for Manufacture and Assembly) modifications in order to aid the investment casting process which will be used to build the 9" runner for experimental testing. Casting of the original HCTI runner showed some problems along the relatively thin leading edge (LE) (less than 1mm on the 9" runner). The manufacturing company being used have said they can cast accurately down to 2mm along this edge which suggests that some machining or grinding of this edge after casting is required. In order to investigate the impact of the LE width on the strength and performance of the optimised HCTI-opt2 Turgo, the LE was modified to give three geometries (HCTI-opt2-LE4, HCTI-opt2-LE2, HCTI-opt2-LE1) with LE widths of 1.67mm, 0.83mm and 0.42mm (7.5" runner). These LE widths correspond to 2mm, 1mm and 0.5mm on the 9" runner. The HCTI-opt2 runner is equivalent to the HCTI-opt2-LE1 runner.

5.2.1 1/4 Runner FEA and CFD

The same FEA operating conditions used in the previous chapters were used on these designs which were also strengthened further based on the results of the previous FEA. CFD simulations at the BEP were also run using the coarse and fine mesh setups. The results of the FEA are shown in Table 5.1 and Fig. 5.10 below. The FEA results show that the stresses in all three designs (HCTI-opt2-LE1, HCTI-opt2-LE2, HCTI-opt2-LE4) are lower than the original HCTI design at runaway speed (16.3%, 12.8% and 8.7% lower respectively) and under normal operation with jet loading (6.5%, 3.2% and 1.2% lower respectively). The jet loading FEA at the 'locked' condition, however showed higher stresses (1%, 16% and 8.5%) respectively, however the stresses under this condition are the lowest overall.

Design	Description	Runaway Stress [MPa]	Diff [%]	Jet loading-Normal [MPa]	Diff [%]	Jet loading-Locked [MPa]	Diff [%]
HCTI	Original HCTI design	308.38		83.66		52.00	
HCTI-opt1	Optimised design	355.98	15.44%	108.19	29.33%	50.29	-3.28%
HCTI-opt2-LE1	LE width 1mm, Radii and TE width increased at ring	263.94	-16.29%	78.40	-6.49%	57.15	8.52%
HCTI-opt2-LE2	LE width 2mm, Radii and TE width increased at ring	272.88	-12.79%	81.05	-3.16%	60.44	16.06%
HCTI-opt2-LE4	LE width 4mm, Radii and TE width increased at ring	277.60	-8.65%	82.33	-1.22%	52.60	1.19%

Table 5.1- DFMA LE width ¼ runner FEA results

The CFD results (Fig. 5.10) for the *fine mesh* simulations showed a large drop in normalised efficiency (1.06%) with the 1.67mm LE (2mm on 9" runner) compared to the HCTI-opt2-LE1 design with a 0.42mm LE. As the width of the LE is reduced, the efficiency increases substantially, and is 0.19% lower than the HCTI-opt1 design for the 0.83mm LE. This shows that the LE width has a considerable impact on the efficiency of the runner and it is recommended that the cast runner be ground down or machined to achieve a LE width close to 0.5mm for the 9" runner.

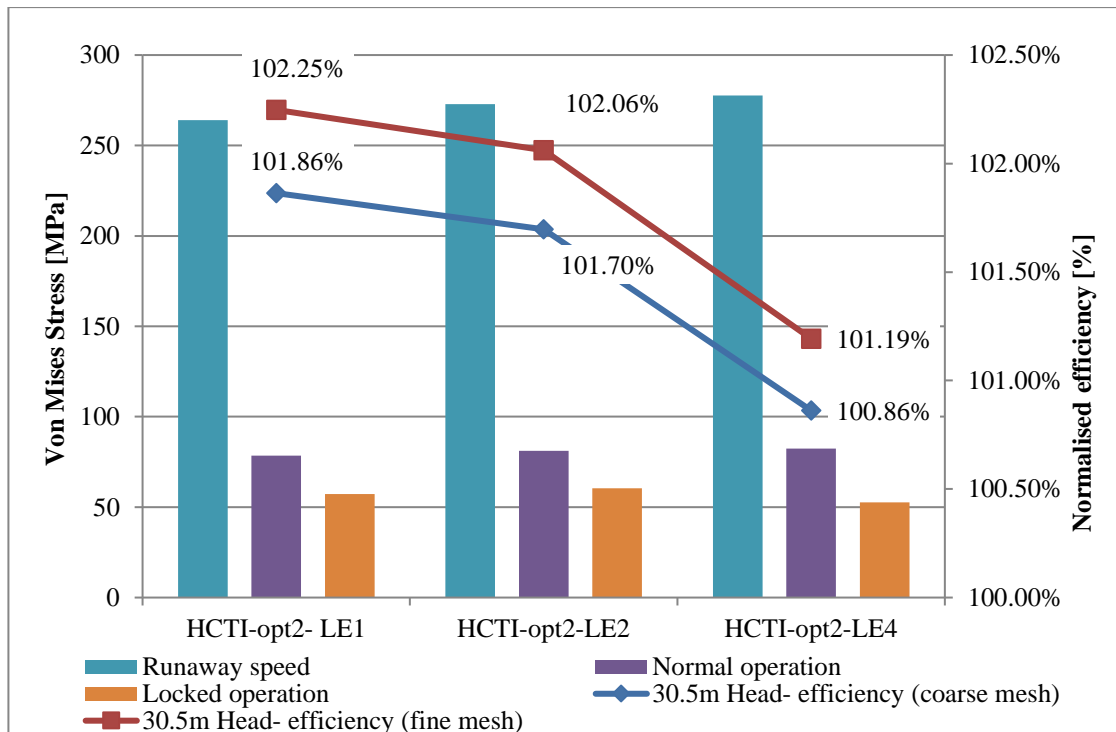


Fig. 5.10. DFMA LE width study FEA (1/4 runner) and CFD results

5.2.2 1/3 Runner FEA

The FEA on these designs was extended to look at a 1/3 runner section to see if the stresses being calculated are affected by the size of the runner section used. The same mesh settings and FEA conditions were used as in the previous section. The results are shown alongside the 1/4 runner FEA results in Fig. 5.11 below.

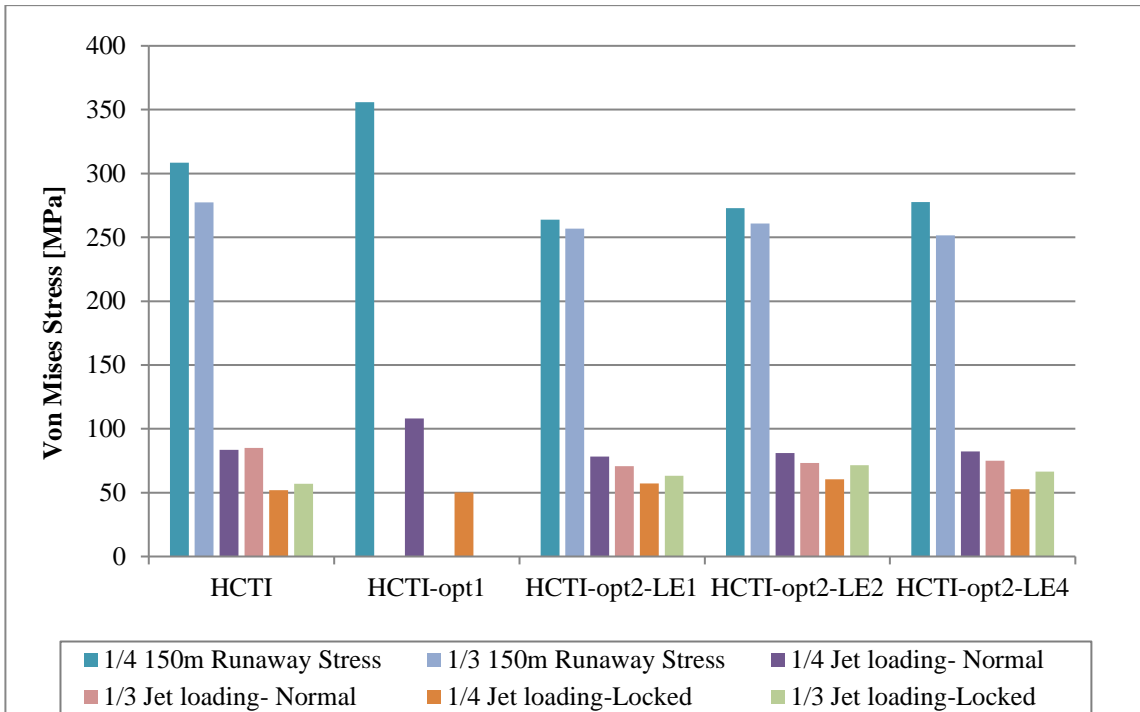


Fig. 5.11. DFMA LE width study FEA (1/4 and 1/3 runner) and CFD results

The results show that under runaway speed and normal operation (where the centrifugal forces are the primary driver of the stresses) the stresses are slightly lower, with the exception of the original (HCTI) runner where the stresses are slightly higher under normal operation. However under the locked condition, the stresses increase for all designs.

The regions of stress concentration do not change between the 1/4 and 1/3 runner sections; it is only the value of the peak von-Mises stress. It would appear that the general trend is a reduction in the stresses using the larger runner section however this doesn't apply to the locked condition.

Overall it seems that the non-uniformity in the difference between the stresses is being caused by the mesh resolution which was restricted by the license at the time and in order to carry out a more thorough comparison, the license was extended to allow the use of more nodes in the regions of high stress concentration.

5.2.3 Full Runner FEA

Following the $\frac{1}{4}$ and $\frac{1}{3}$ runner FEA, the ANSYS® Mechanical licence was extended to cover larger meshes which allowed the analysis of the full runner to be carried out as described in this chapter.

5.2.3.1 Mesh refinement study

Before beginning the FEA, a mesh refinement study was carried out using the runaway speed operating conditions, with a rotational speed of 4988rpm corresponding to the runaway speed at a 150m head. It was found that a mesh of around 2.1m elements produced almost mesh independent results, with the maximum stress at runaway speed differing from the 4.7m element mesh by only 0.4% (Fig. 5.12).

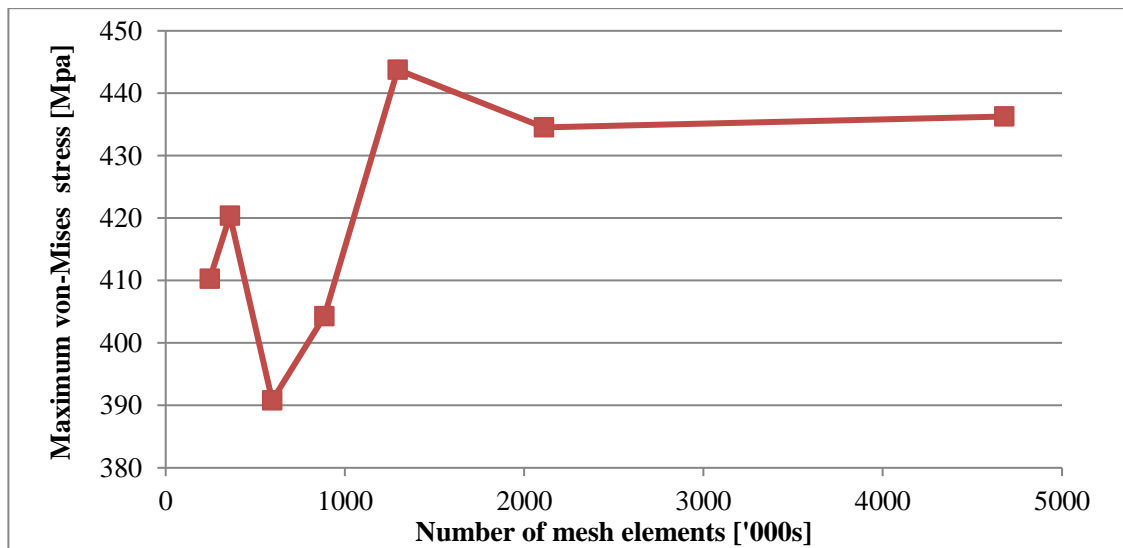


Fig. 5.12. Full runner FEA Mesh study for the original 7.5" HCTI runner at 150m head runaway speed

The mesh independent full runner mesh is shown in Fig. 5.13 and Fig. 5.14, below. The mesh has a minimum orthogonal quality of 0.2 and a maximum aspect ratio of 16.2.

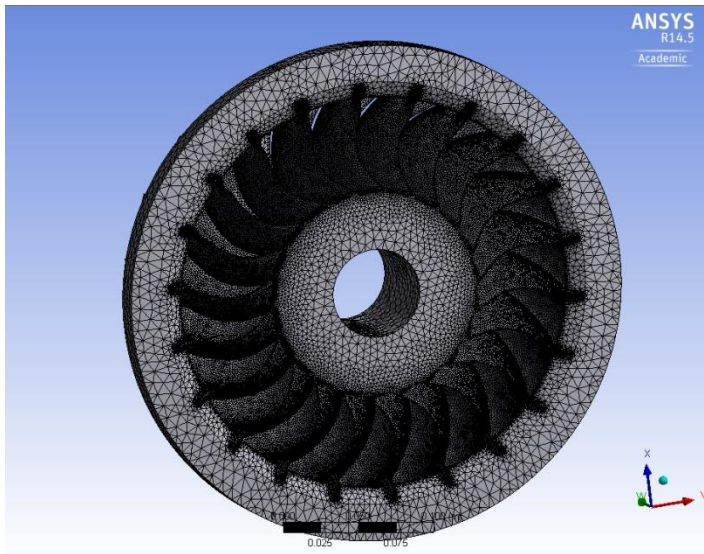


Fig. 5.13. Mesh independent full runner mesh- 2.1M elements- Inlet view

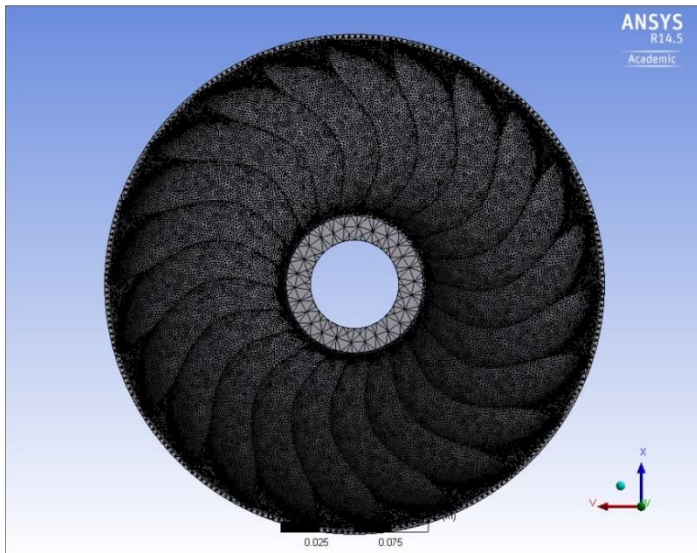


Fig. 5.14. Mesh independent full runner mesh- 2.1M elements- Outlet view

5.2.3.2 FEA model comparison

FEA was carried out on the full runner under the same conditions as used previously with the runner sections at runaway speed, normal operation and locked operation. The areas of stress concentration were observed to be the same as in the previous studies (Fig. 5.15 to Fig. 5.17) however the stresses were found to be considerably larger as shown in Fig. 5.18 below. This difference in the maximum stresses shows the importance of using the entire runner when carrying out FEA on turbines of this nature.

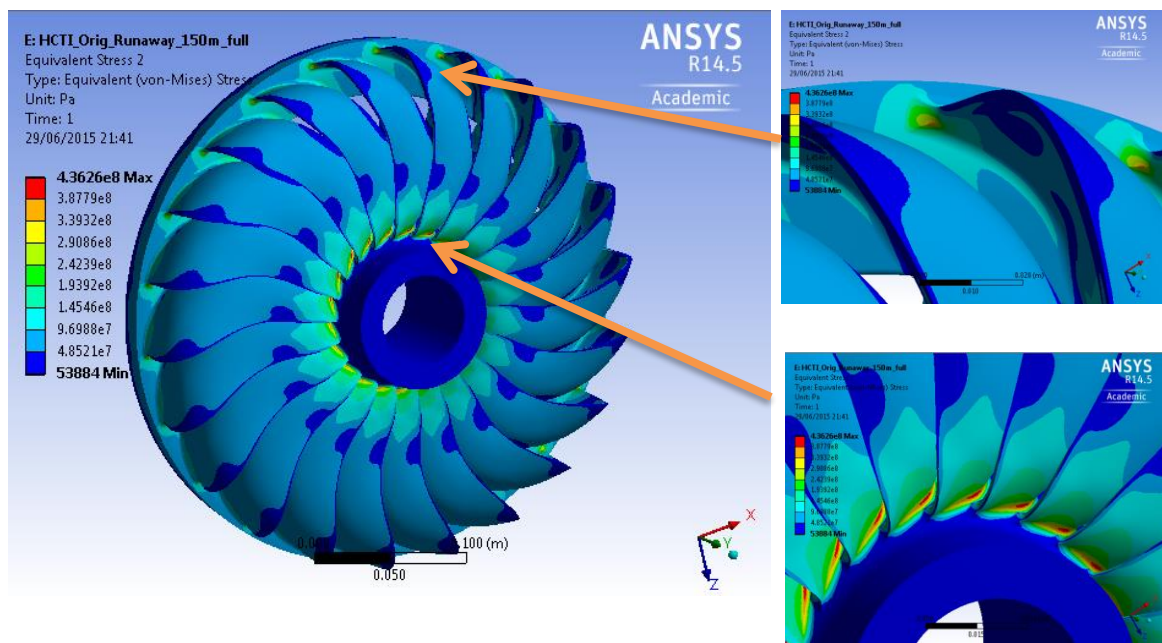


Fig. 5.15. Full HCTI-Orig runner FEA at Runaway speed showing stress concentrations

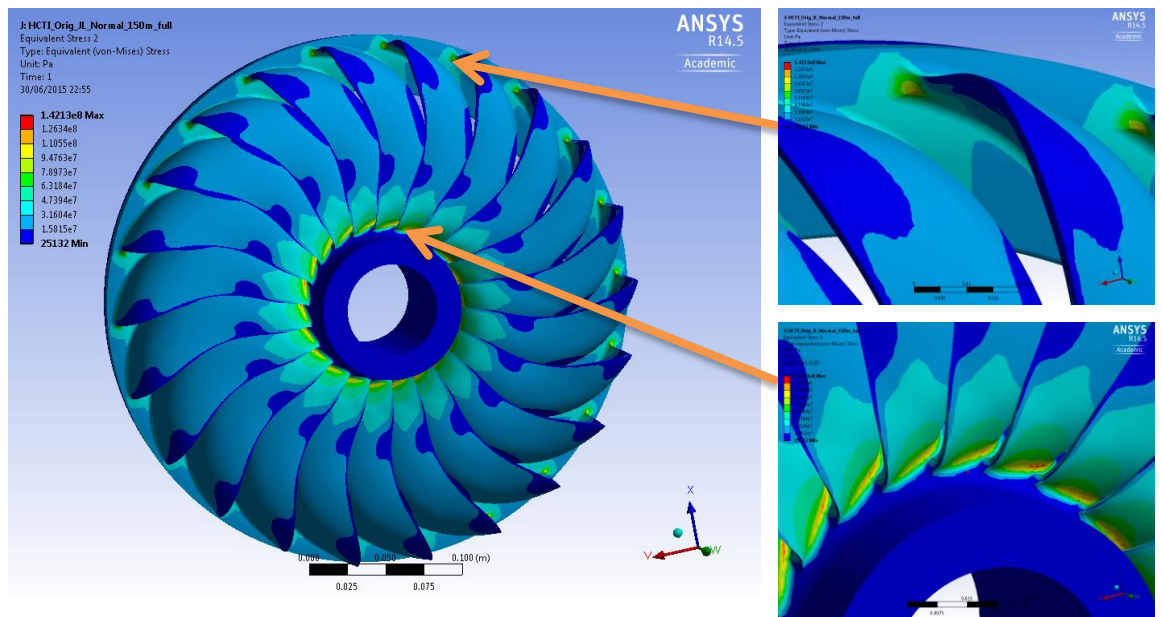


Fig. 5.16. Full HCTI-Orig runner FEA under normal operation showing stress concentrations

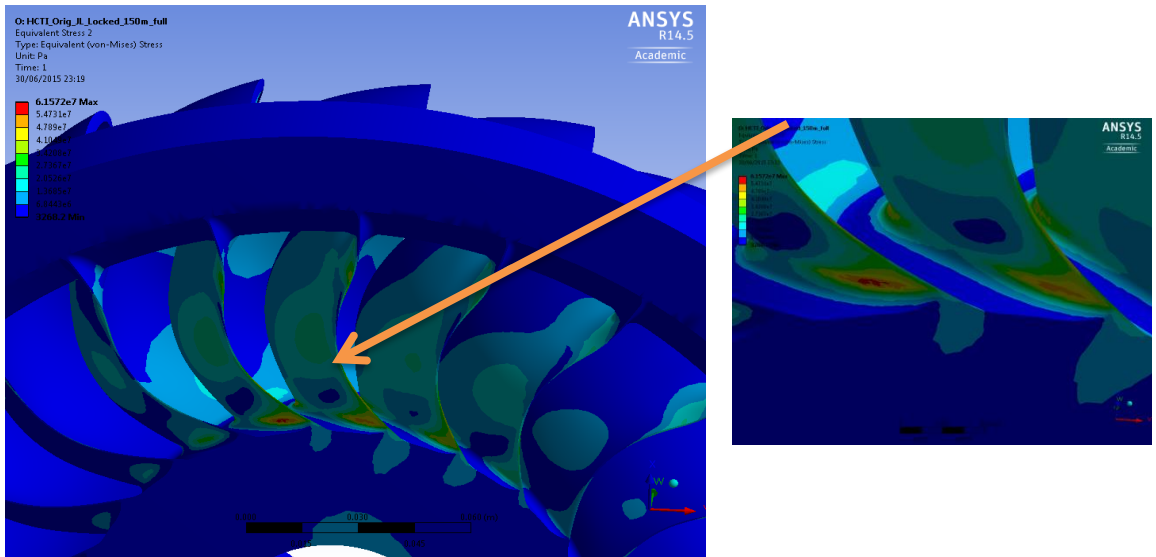


Fig. 5.17. Full HCTI-Orig runner FEA under locked operation showing stress concentrations

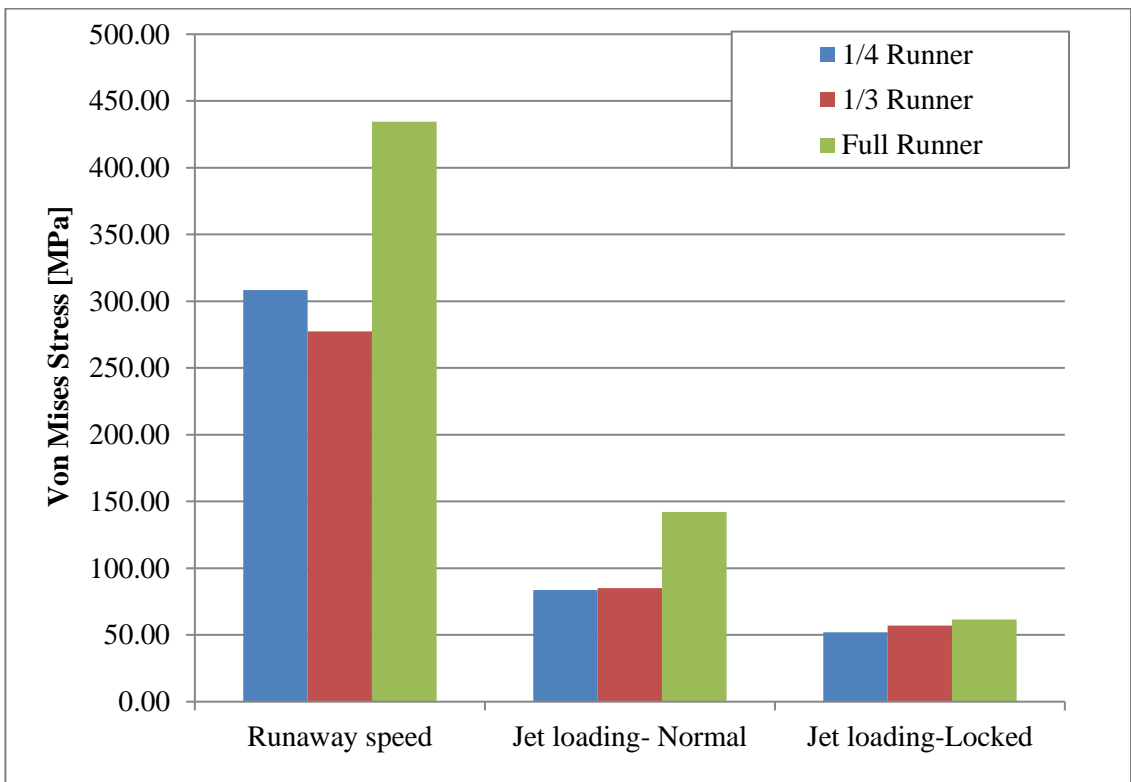


Fig. 5.18. Comparison between stresses under runaway speed, normal operation and locked operation using the full runner, 1/3 runner and 1/4 runner sections for the original HCTI runner

5.3 Final runner design comparison

Using the mesh independent full runner FEA conditions, the HCTI, HCTI-opt2-LE4 and HCTI-opt2-LE1 designs were compared as these are the designs which will be manufactured for experimental testing. The areas of stress concentration were found to be in the same regions as shown in the 1/4 runner analysis however the values differed slightly as shown in Fig. 5.19 below. The results show that at runaway speed, the HCTI-opt2-LE4 and HCTI-opt2-LE1 designs are 6.5% and 9.2% stronger than the original HCTI design and under normal operation 6.1% and 6.8% stronger respectively.

Under the locked condition however, the FEA showed an increase in the stresses for the HCTI-opt2-LE4 and HCTI-opt2-LE1 designs compared to the original HCTI design by 9% and 21% respectively. This is due to the reduction in the blade thickness as part of the optimisation study (4.2.6). Although this has weakened the optimised designs, the stresses due to blade loading are nearly 1/10th of the runaway speed stresses and it is unlikely that the runner will fail as a result of this.

It was decided based on discussions and further stress and fatigue analyses carried out by Gilkes that both the HCTI-opt2-LE1 and HCTI-opt2-LE4 designs have sufficient strength and will be manufactured for testing. The *fine mesh* simulations showed the efficiency improvement of the LE1 runner is 2.25% and the LE4 runner 1.19% of the original runner efficiency.

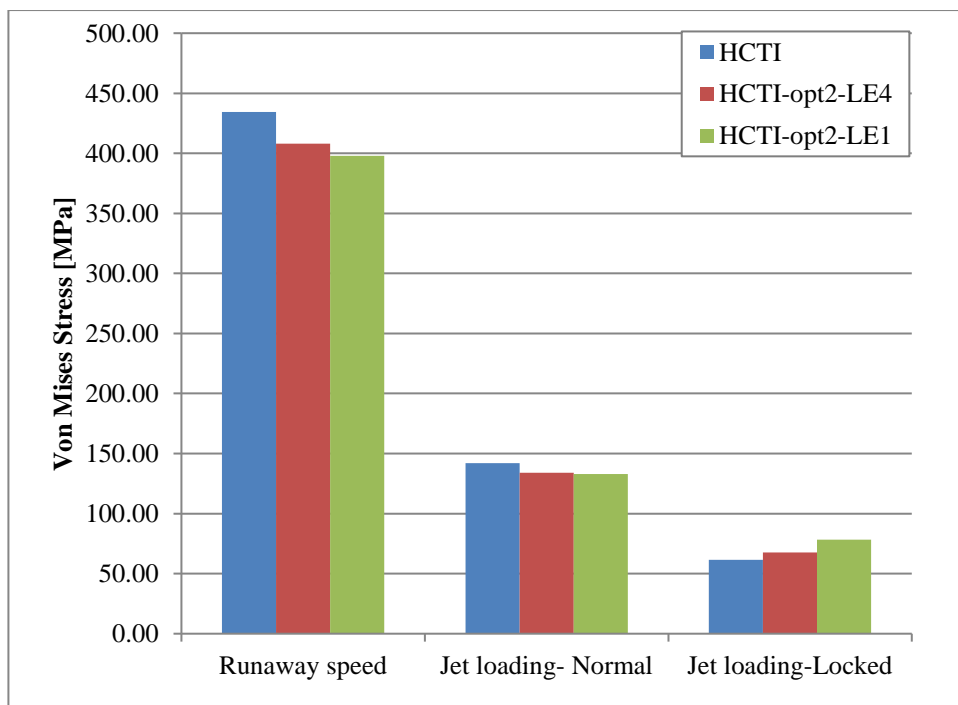


Fig. 5.19. Full runner FEA design comparison

6 Injector design optimisation and further analysis

This section covers the 2D axisymmetric CFD analysis and optimisation of the spear/valve assembly of a generic impulse turbine injector for a range of heads and flow rates. The results of this optimisation study are then taken further by applying the optimisation design changes to a standard Gilkes Turgo injector. The standard (d65) and optimised (d65mod-scaled) injectors are compared using a 2D axisymmetric simulation as well as 3D straight pipe and full 3D simulation, including the branch pipe and guide vanes upstream of the nozzle and spear.

This research resulted in the publication of two academic papers in the ASME journal of Fluids Engineering (Benzon, Židonis et al. 2014; Benzon, Židonis et al. 2015).

6.1 2D generic injector optimisation using CFD

Although some studies have been carried out in the past where injector geometries have been modified to improve the performance (Veselý and Varner 2001; Gass and Water 2002; Peron, Parkinson et al. 2008; Staubli T., Abgottspion A. et al. 2009; Zhang and Casey 2009; Xiao, Wang et al. 2014), there has been no thorough investigation of the basic injector design parameters together with the importance they have on the performance of an injector. This study utilises ANSYS® CFX® to analyse the basic geometric factors affecting the efficiency of a typical impulse turbine injector. A Design of Experiments study is used to look at the impact of four primary nozzle and spear design parameters on the injector losses over a range of inlet pressures. An optimum injector design is suggested based on the results and comparisons are made. The results for both CFD tools suggest that steeper nozzle and spear angles than current literature describes will reduce the losses by up to 0.6%. The study is taken further by looking at the impact of spear tip curvature and scaling on the injector losses. Additional simulations showed that adding curvature to the spear tip can reduce these losses further however it is the nozzle and spear angles which have the greatest impact on the losses.

6.1.1 Design analysis and modelling

In order to investigate the effect that the main design parameters of the injector have on the performance, a straight pipe was assumed upstream of the injector without the branch pipe and bifurcation geometry. The nozzle opening diameter, D_n , and the injector opening diameter, G , shown in Fig. 6.1, were fixed at 36mm and 82.5 mm respectively.

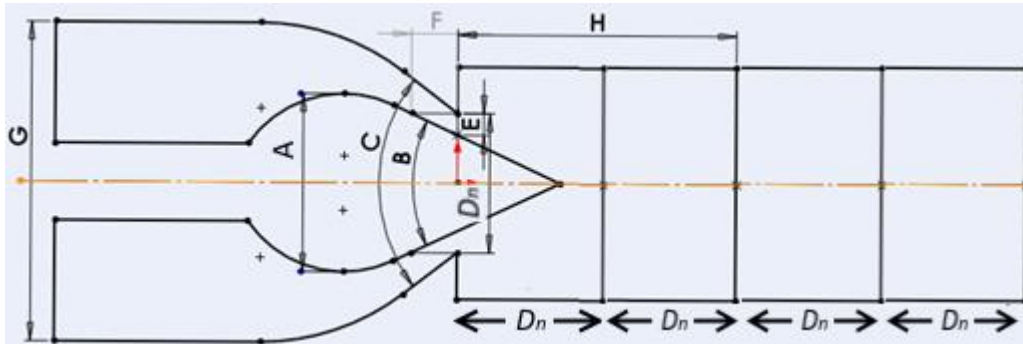


Fig. 6.1. 2D injector geometry showing fixed and variable operational and geometric parameters

The injector losses, which are the main focus of this study, were calculated by comparing the power at the inlet with the power at a distance of 2 nozzle opening diameters ($2D_n$) downstream of the nozzle, as shown in Fig. 6.1 with dimension 'H', using equations (6.1) to (6.3).

$$N = \int_A \left(p + \frac{\rho \cdot u^2}{2} \right) \cdot u \cdot dA \quad (6.1)$$

$$N = \sum_{i=1}^n \left(p_i + \frac{\rho \cdot u_i^2}{2} \right) \cdot u_i \cdot A_i \quad (6.2)$$

$$\text{Injector Losses} = \frac{N_{in} - N_{out}}{N_{in}} \quad (6.3)$$

Where N is the power in J/s, p_i is the static pressure in Pa, ρ_i is the density of fluid in kg/m^3 , u_i is the velocity of fluid at the individual mesh cell i in m/s , A is the area at the cross-section in m^2 and n is the number of cells at the cross-section.

The Reynolds (Re) number was calculated at the inlet for the peak velocity (when nozzle is fully open) using equation (6.4) below.

$$Re = \frac{\rho v D}{\mu} \quad (6.4)$$

Where D is 82.5mm and v is derived from the maximum flow rate of 40.7 l/s, giving

$Re = 5.6e^6$. From this the turbulence intensity I at the centre of the flow can be estimated using equation 6.5 (derived from an empirical correlation of pipe flows (ANSYS 2013b)).

$$I = 0.16(Re)^{\frac{1}{8}} \quad (6.5)$$

This gives a turbulence intensity of 3%. As this is an estimated and will vary in reality, the turbulence intensity at the inlet was varied within the ranges recommended from *low* (intensity 1%, viscosity ratio 1) to *high* (intensity 10%, viscosity ratio 100). It was found that the difference in the efficiency at 2 diameters from the nozzle exit between low and high turbulence was less than 1e-3 % showing that the turbulence intensity at the inlet for this flow regime, which experiences such a great change in velocity through the nozzle, is negligible. It was therefore decided the *medium* (intensity 5%, viscosity ratio 10) option would be used.

Based on the available published research in this area discussed in *2.4 Impulse turbine injector research*, the homogeneous multiphase method was used in ANSYS® CFX®. The *high resolution* advection scheme was also used. The simulations were run in steady state and the convergence criteria were a residual target of 1e-6. The boundary layer conditions used are detailed in Table 6.1, below.

Location	Boundary	CFX Details
Injector inlet	Inlet	<i>Mass and Momentum:</i> Total Pressure (stable) <i>Turbulence option:</i> k- ω SST Medium intensity (intensity 5%, viscosity ratio 10)
Nozzle and spear surfaces	Wall	<i>Mass and Momentum:</i> No slip wall <i>Wall roughness:</i> Smooth wall
Injector Outlet	Opening	<i>Mass and Momentum:</i> Entrainment <i>Turbulence option:</i> k- ω SST Zero Gradient

Table 6.1- Boundary conditions for injector simulations

As CFX® does not accept 2D meshes an equivalent 3D wedge of only one cell thickness was used for the CFX® simulations as advised by the ANSYS® CFX®-Pre User Guide (ANSYS 2013b). The wedge angle used was 1° as this was the angle which produced angle-independent results. All meshes were produced using the ANSYS® ICEM® CFD mesh generation software with a minimum element orthogonal quality greater than 0.3.

As with the runner simulations discussed in *3 Turgo runner analysis*, it was decided that the K- ω SST turbulence model would be used for all the simulations in the optimisation study. The size of the mesh cells near the wall was restricted in order to maintain a Y+ value under 10. Simulations were also run with very small mesh cells close to the wall and a Y+ value below 1 however no noticeable difference in the losses was measured compared to the aforementioned mesh. In addition, a simple mesh refinement study was performed using the baseline injector design with a nozzle angle of 90° and a spear angle of 50° (Fig. 6.2). The results show that the injector losses are very similar for meshes with around 100,000 cells (0.022% lower than the 3M cell mesh) while the results become almost identical for meshes with over 1 million cells (0.006% and 0.001% lower than the 3M cell mesh for ~1M and ~2M cells respectively).

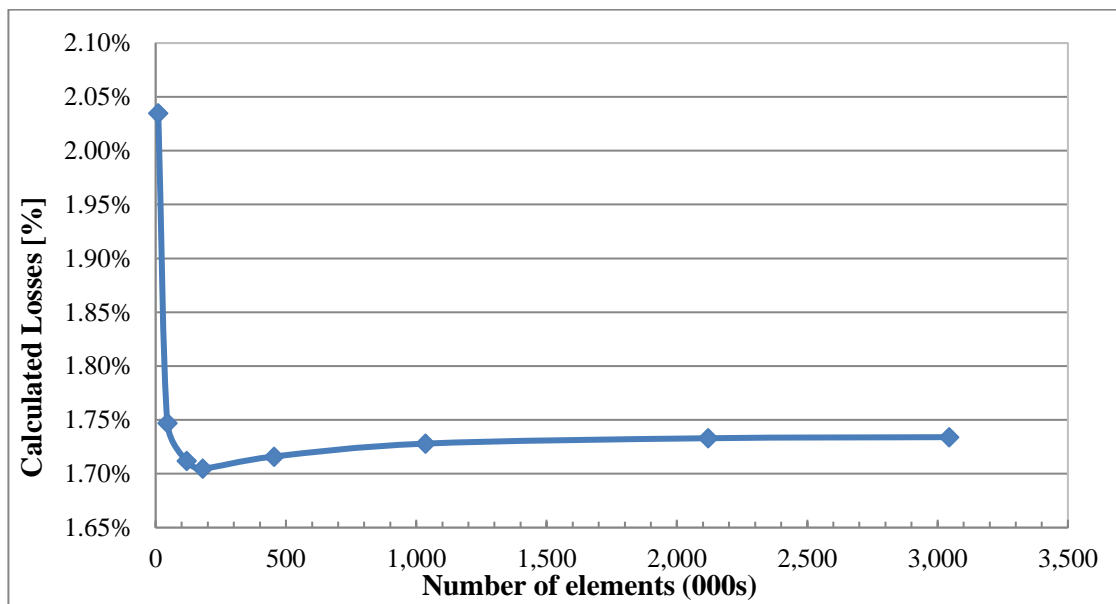


Fig. 6.2. Mesh refinement study- 2D injector losses at $2D_n$

It should be mentioned that the incremental increase of the jet diameter after the point known as Vena Contracta which was observed during experimental tests (Staubli and Hauser 2004) was not observed in any of the computational results. The reason for this could be due to the influence of the air on the water jet as the formation of droplets was not calculated using this CFD model which is the likely cause of this apparent jet expansion (Zhang and Casey 2009). However as the runners of impulse turbines are positioned close to the injector, where the losses in this research are calculated, this inaccuracy is not expected to have any significant influence on the results.

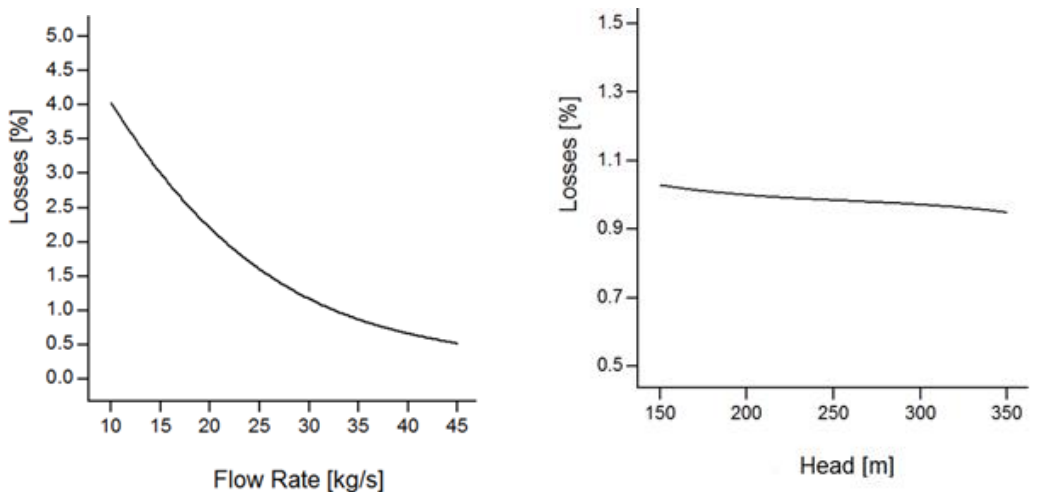
After verifying the accuracy of the CFD models, the influence the geometric parameters have on the performance of the injector, for a range of operating conditions could be investigated. In order to do this, a *Design of Experiment* (DOE) study was carried out using the Design-

Expert® software (Stat-Ease®. 2013). The Nozzle Angle, Spear Angle and Spear Width were chosen as the primary geometric parameters for this study, having been identified as the most important design characteristics according to the current literature (Gass and Water 2002; Peron, Parkinson et al. 2008; Nesiadis, Papantonis et al. 2011). The exact definition of these factors are shown in Fig. 6.1, where B and C are the Nozzle and Spear Angles, A is the Spear Width and E is the Spear Opening which was used instead of the Spear Travel, F, to regulate the flow rate. The Spear Opening and the total inlet pressure were selected as the operational parameters as they are linked directly to the head and flow rate. By varying these 5 factors more than 120 cases suggested by the DOE were simulated with each simulation relating the losses to the operational and geometric parameters.

The range of inlet pressure used was 1.5-3.5 MPa (~150-350 m Head). All the simulations were performed with the same turbulence and mesh settings with a structured mesh of around 150,000 cells.

6.1.2 Design of Experiments (DOE) study

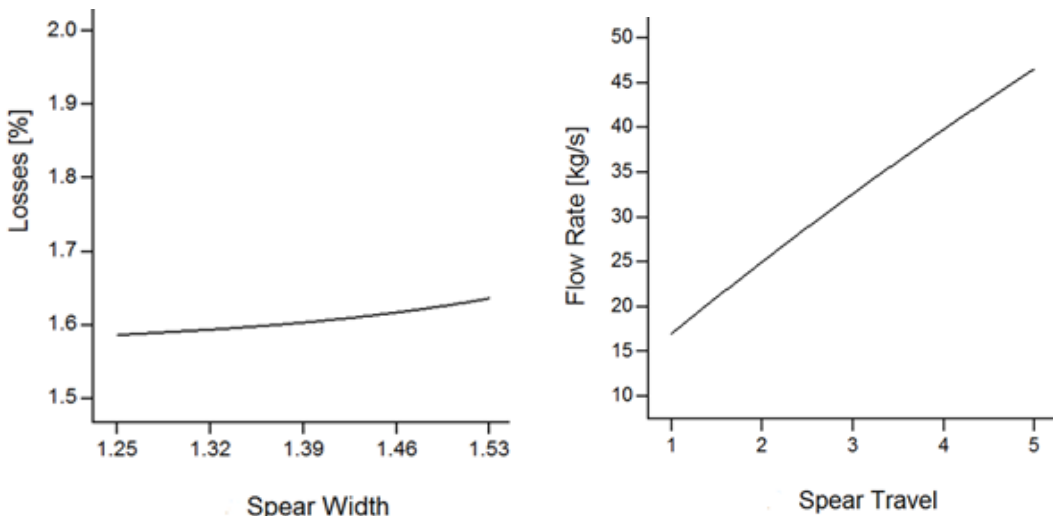
The DOE study was set up using Nozzle Angles of 70°-110° and Spear Angles of 30°-70° as the tendency of modern designs are towards steeper angles (Gass and Water 2002; Staubli and Hauser 2004) than those suggested by Nechleba and Bovet (Bovet 1957; Nechleba 1957). The relative non-dimensional Spear Width was varied from 1.11-1.67 as a factor of the maximum Spear Opening. The Spear Opening was varied from 3.3 mm to a maximum value of 18mm (due to geometric constraints). The DOE method was employed to analyse the injector efficiency response to the five input parameters and the interaction between those parameters. Three of five input parameters were found to be independent by showing the same injector losses response for any combination of the remaining 4 parameters. The response curves for these independent parameters: Spear Opening (expressed as Flow Rate), Pressure Head and Spear Width are presented in Fig. 6.3 and Fig. 6.4 respectively. Fig. 6.4 also provides information on the Flow Rate response to the Spear Travel for spear openings 1-5. While one parameter is plotted per graph the remaining parameters are fixed at the median of their ranges and listed in the figures.



Nozzle Angle = 90°, Spear Angle = 50°, Head = 200 m,
Spear Width = 1.39 (or 25 mm).

Nozzle Angle = 90°, Spear Angle = 50°, Spear Travel = 3,
Spear Width = 1.39 (or 25 mm).

Fig. 6.3. Injector Losses vs. Spear Travel (Expressed as Flow Rate)-left and Injector Losses vs. Pressure Head- right.



Nozzle Angle = 90°, Spear Angle = 50°, Head = 200 m, Nozzle Angle = 90°, Spear Angle = 50°, Head = 200 m,
Spear Width = 1.39 (or 25 mm), Flow Rate = 25 kg/s Spear Width = 1.39 (or 25 mm).

Fig. 6.4. Injector Losses vs. Spear Width-left and Flow Rate vs. Spear Travel-right

It can be seen that larger Spear Travel values reduce the restriction and hence reduce the losses. The losses also decrease slightly as the Pressure Head is increased for a fixed spear travel. The losses are shown to increase slightly as the Spear Width increases for a fixed Nozzle and Spear Angle, Head and Flow Rate. The Nozzle Angle and the Spear Angle on the other hand are related to one another and must be analysed together. It was anticipated that different Spear Travels will have an influence on optimum angles however, it is not the Spear

Travel but the Flow Rate which is important and therefore the combinations of Nozzle Angles and Spear Angles were analysed over a range of 4 corresponding Flow Rates as presented in Fig. 6.5 and 6.6. The Pressure Head was fixed at 200 m and the Spear Width was fixed at 25 mm.

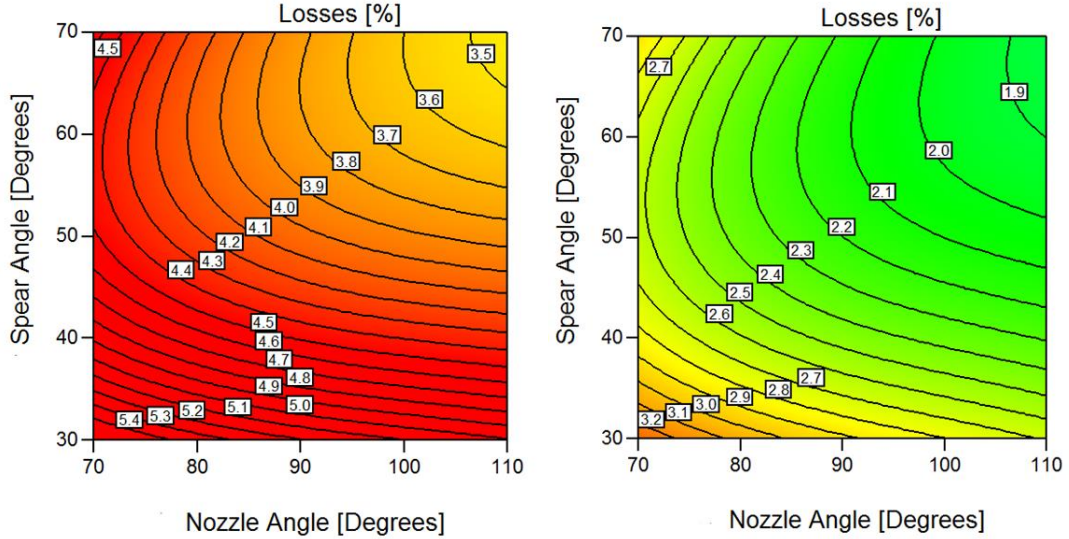


Fig. 6.5. Injector Loss contours for Nozzle and Spear Angles at $Q = 10 \text{ kg/s}$ (left) and 20 kg/s (right).

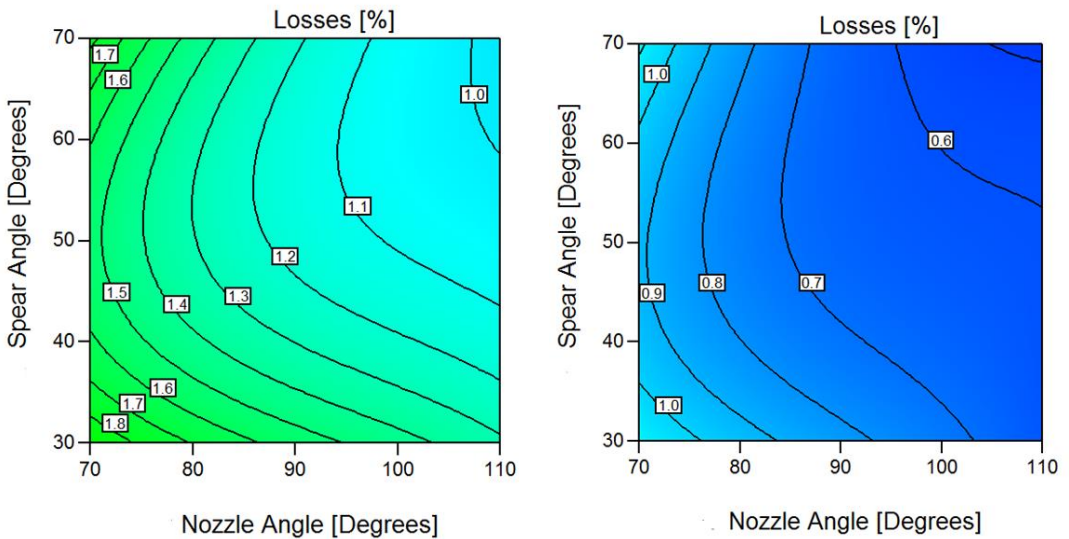


Fig. 6.6. Injector Loss contours for Nozzle and Spear Angles at $Q = 30 \text{ kg/s}$ (left) and 40 kg/s (right).

The flow rate of 40 kg/s was the highest flow rate to be analysed as the effect of the nozzle and spear angles on the losses decreases with increasing the flow as can be seen in the

contours in Fig. 6.6. All of the contours show the lowest losses to be at the top right hand corner of the graph where the angles are 110° for the nozzle and 70° for the spear.

Since the optimised design with nozzle and spear angles of 110° and 70° was acquired from the surfaces fitted onto the CFD data, a direct comparison was made using CFD results at the 5 different openings in order to verify this design. Fig. 6.7 shows the comparison between the optimised $110^\circ/70^\circ$ and the initial $90^\circ/50^\circ$ nozzle and spear geometry.

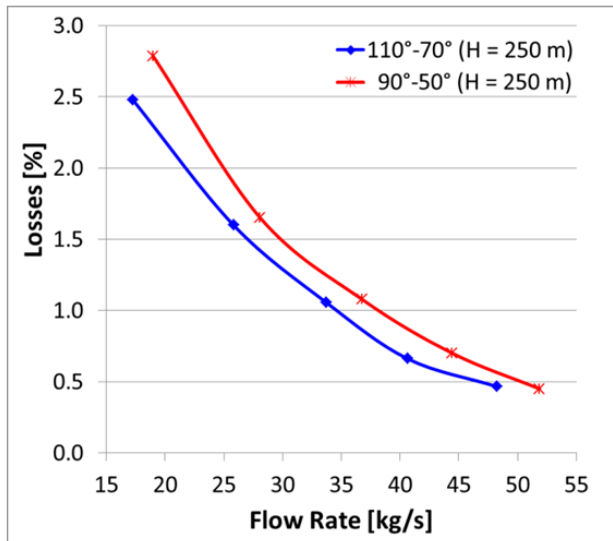


Fig. 6.7. Comparison between the initial and optimised injector geometries using CFD results at 5 different openings

The results show that at a head of 250m, the optimised injector design reduces the losses by over 0.5% at smaller flow rates. At larger flow rates the spear is closer to the maximum opening position where the losses as well as the difference in losses between the two designs are smaller.

During the optimisation study it was observed that by changing the angles of the nozzle and spear, the flow rate was also changed slightly meaning that the maximum flow rate that the compared injectors can accommodate is also slightly different. In order to verify that the difference in the flow rate is small enough to have no major influence on the above results, the optimum nozzle was scaled up by 3.2% in order to produce the same flow rates as the $90^\circ/50^\circ$ design (Fig. 6.8). This does have the effect of increasing the losses slightly as the spear travel has to be reduced in order to produce a similar flow rate for the larger nozzle. However the optimum design still shows lower losses, with the scaled up injector's losses increasing by around 0.1 %.

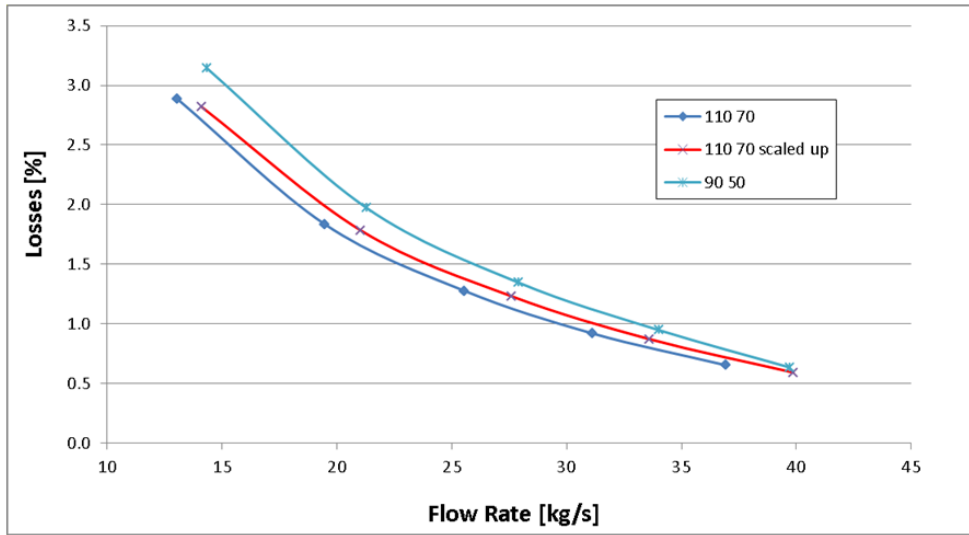


Fig. 6.8. Comparison between the original 90-50 and optimised 110-70 nozzles with the same maximum flow rate

It is useful to observe the way in which the optimised injector geometry has affected the velocity profiles of the jet at the five opening positions. Fig. 6.9 shows the velocity profiles of the jet about the symmetrical axis at the five opening positions for the initial 90°/50° design and the improved 110°/70° design. The 90°/50° design shows lower velocities in the centre of the jet for all openings but the difference is most prominent for opening 1, where the 90-50 design has a minimum velocity of 50m/s and the 110/70 design has a minimum velocity of around 55m/s. The velocity profiles concur with the experimental work carried out by Zhang and Casey where the axial velocities are shown for a jet connected to a straight pipe (Zhang and Casey 2009).

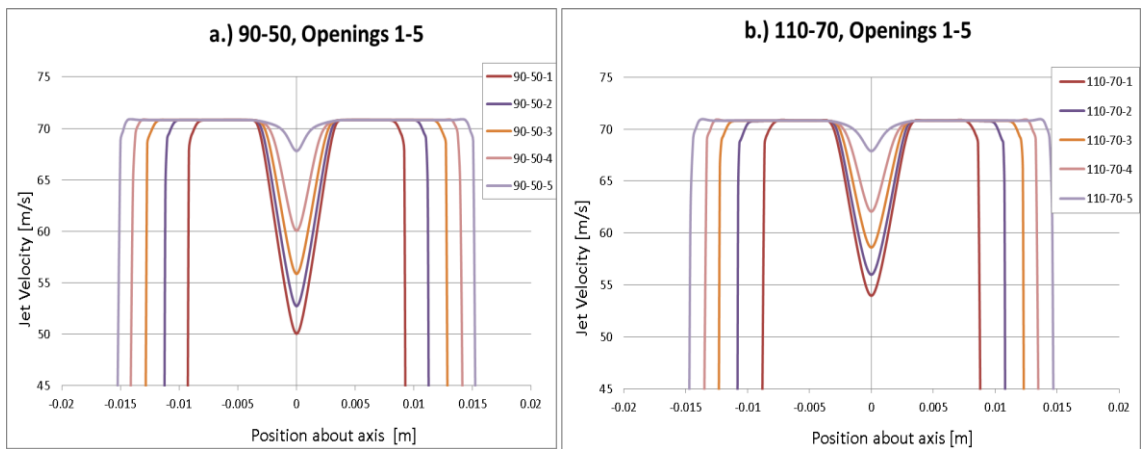


Fig. 6.9. Jet velocity profile comparison for original 90-50 nozzle and spear design and the optimised 110-70 design

For the full range of flow rates, the design of experiment surfaces predicted optimum nozzle and spear angles at the upper limit of this study at 110° and 70° respectively. The accuracy of this prediction was confirmed by the additional CFD results comparison between the original 90-50 and optimised 110-70 injector design at each opening. A possible explanation for why the larger injector and spear angles incur lower losses can be suggested when it is considered that the primary cause of the losses is a result of the boundary layer interaction between the solid surfaces of the nozzle and spear and the high speed fluid. Fig. 6.10 shows this interaction taking place in zones A and B where the high speed fluid meets the solid boundary for the two injector designs with the same inlet pressure and flow rate. The results show that by increasing the nozzle and spear angle, the length of the interaction zones A and B are reduced which could be the reason for the reduction in losses.

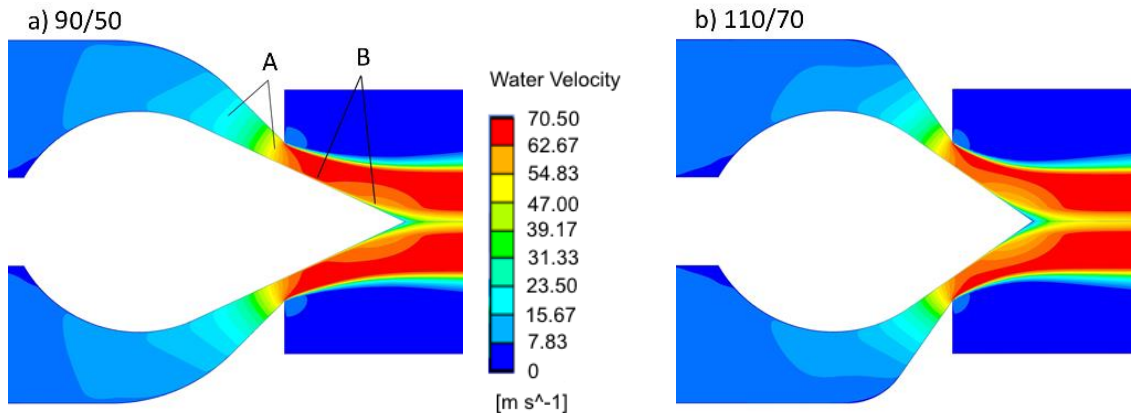


Fig. 6.10. Velocity field comparison for (a) small and (b) large nozzle and spear angles

6.1.3 Further investigation

In addition to the above investigation of the basic geometric and operational parameters, the impact of the level of spear tip curvature and the size of the nozzle on the flow rate and injector losses was investigated for the optimised 110-70 injector design.

6.1.4 Spear tip curvature

All geometries in the above investigation have the spear ending as a straight cone as shown in Fig. 6.1. In practice, curvature can be applied to this edge as used in older designs (Bovet 1957; Nechleba 1957). Several curvatures were investigated for an inlet pressure of 2.5MPa using the case of the optimised 110-70 nozzle geometry. Fig. 6.11 shows the half symmetrical

cross section of some spear geometries as well their influence on the velocity contours and Fig. 6.12 shows the resultant losses.

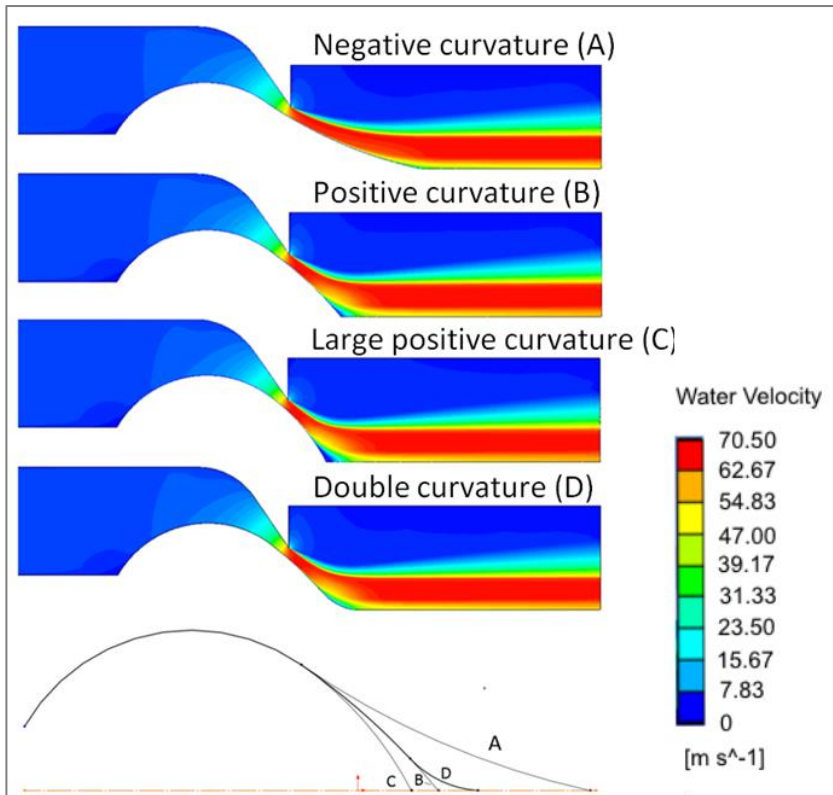


Fig. 6.11. Velocity magnitude contours for spear curvatures A-D

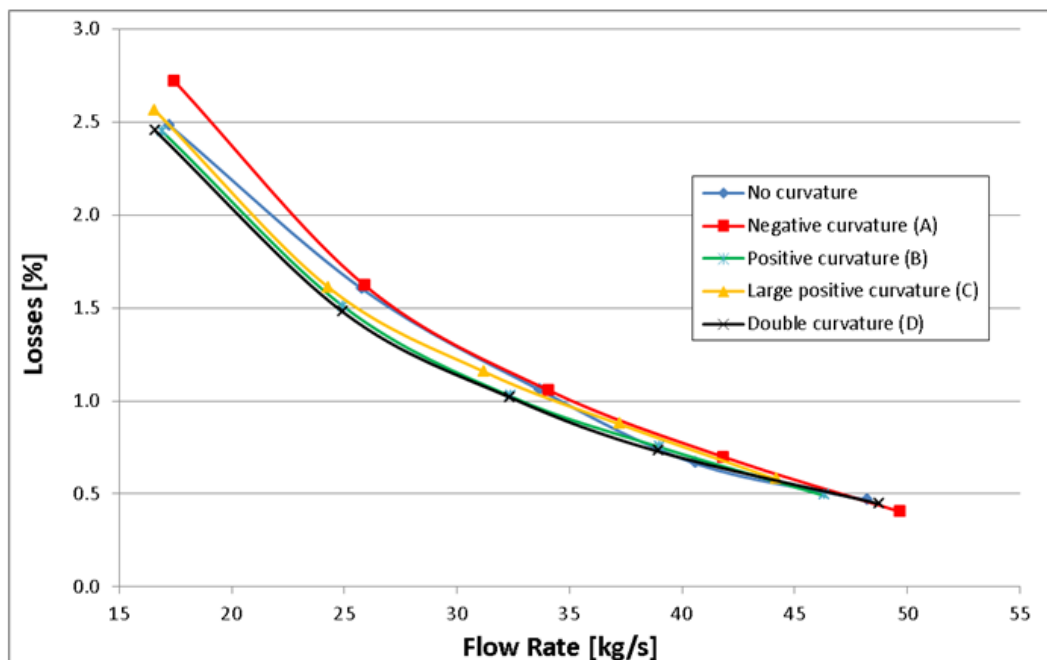


Fig. 6.12. Injector losses for spear curvatures A-D

The results showed that adding positive curvature to the spear tip, making the shape more bulbous, can reduce the losses up to a threshold as shown in Fig. 6.12. A double curvature

design, with positive curvature applied to the spear slope and negative curvature to the tip, was also simulated. Although Fig. 6.12 shows marginal improvements in efficiency for this design, the difference is close to the simulation error, showing that it is the curvature of the slope of the spear which impacts the losses more than the tip. These results give a good indication of the impact of spear tip curvature on the injector losses however more work could be done in this area to give a more holistic analysis.

6.1.5 Injector scaling

The size of the injector has a major effect on the flow rate according to the equation $Q = k^2 \cdot Q'$ where Q' is the flow rate for the 36mm nozzle opening diameter and k the scaling factor. As this analysis was only carried out for a relatively small injector, the impact of scaling the geometry was also investigated. This showed a minor decrease in the calculated losses as the injector is scaled up maintaining the same relative position of the spear in order to accommodate larger flow rates Fig. 6.13.

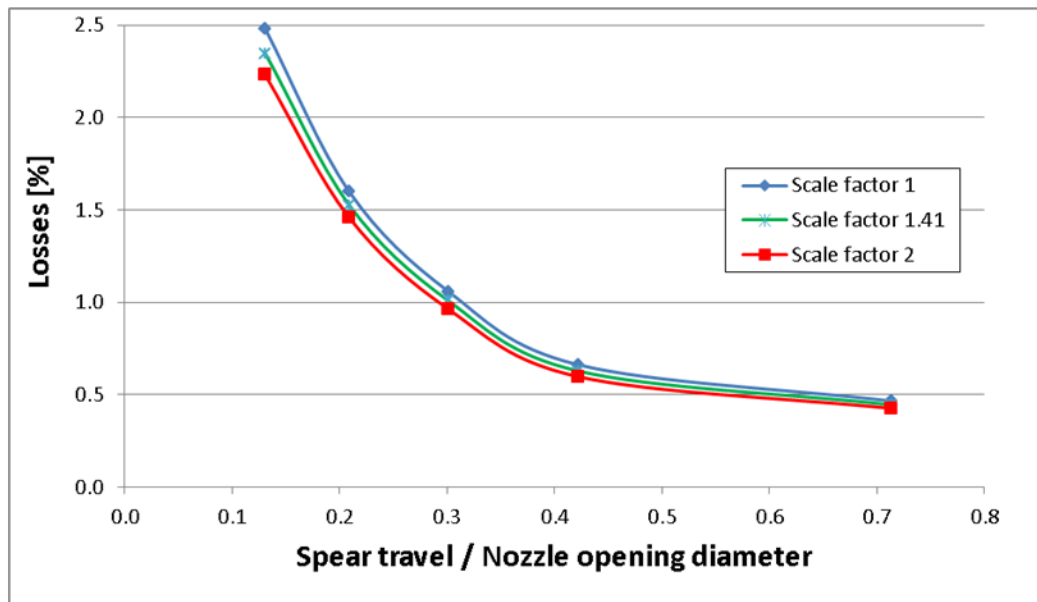


Fig. 6.13. Impact of scaling on injector losses

6.2 HCTI Injector design study

This chapter applies the results of the design changes from the optimisation study carried out in the previous chapter (*6.1- 2D generic injector optimisation using CFD*) to the Gilkes HCTI Turgo injector design to improve the performance. The study is extended further by looking at the injector with a straight pipe in 3D as well as including the branch pipe and guide vanes upstream of the nozzle and spear which have been shown to have significant impact on the injector performance and quality of the resulting water jet.

6.2.1 2D Straight pipe study

Using the 2D mesh independent setup (2M elements) and solver control (Table 6.1) which was verified in the previous chapter (*6.1- 2D generic injector optimisation using CFD*), the HCTI injector geometry was studied using ANSYS® CFX® in order to calculate the impact of the spear travel on the flow rate and the efficiency.

The HCTI injector geometry (HCTI-d78) has nozzle and spear angles of 80° and 55° degrees, which is close to the baseline design used in the previous study which had angles of 90° and 50° degrees respectively . The 2D generic injector optimisation showed that increasing the nozzle and spear angles to 110° and 70° can reduce the injector losses by up to 0.6% for the 2D straight pipe case. This study was carried out at much higher heads (150-350m) than the 30.5m used in the 7.5" HCTI performance testing however as Fig. 6.3 indicates, there is little change to the injector losses in 2D with an increase in the head.

The original (HCTI-d78) injector, with a nozzle diameter D_n of 78mm, was modified (HCTI-d78mod) accordingly and the nozzle and spear angles were increased to 110° and 70° respectively. The geometries were also scaled down to a nozzle diameter D_n of 65.25mm (HCTI-d65 and HCTI-d65mod) to match the nozzle diameter used for the 7.5" HCTI injector performance testing. These four injector designs were run at 5 spear travels (T_s) from a T_s/D_n ratio of 0.1-0.9. The relationship between the spear travel ratio T_s/D_n and the mass flow rate for the $D_n=78\text{mm}$ and $D_n=65\text{mm}$ designs are shown in Fig. 6.14, below. The $D_n=65\text{mm}$ results are also compared to the experimental results for the HCTI performance testing and show good correlation giving confidence in the CFD methodology used.

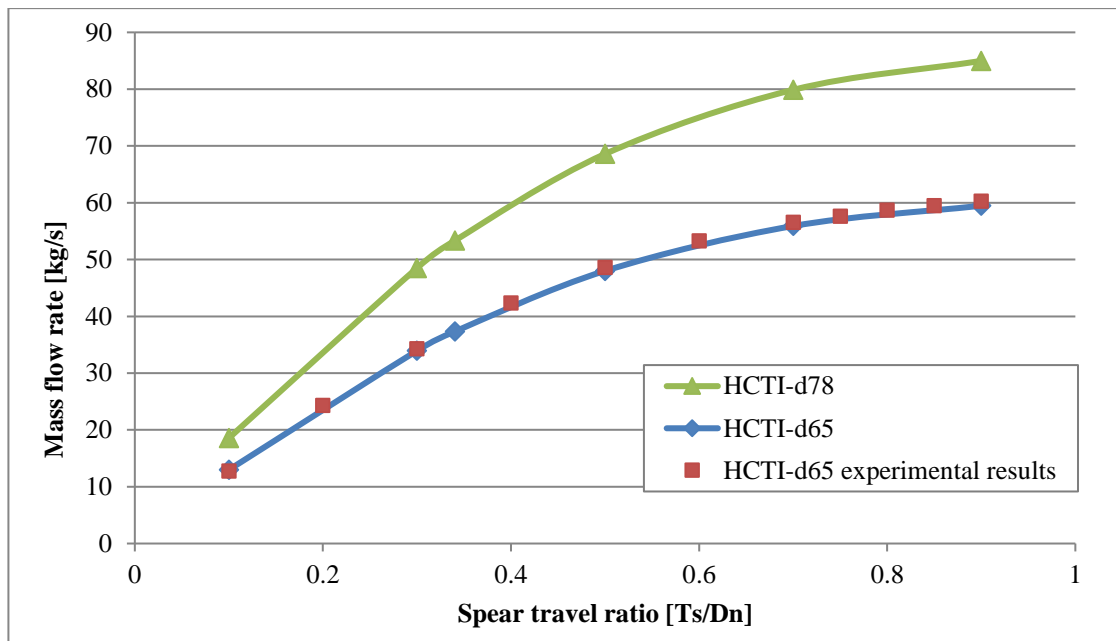


Fig. 6.14. Spear travel ratio against flow rate for 2D J608 $D_n=78\text{mm}$ and $D_n=65\text{mm}$ injectors-comparison with experimental results

Using these results, the spear travel required for the BEP flow rate for the 7.5" HCTI design could be calculated using fit curves for the spear travel/flow rate results as shown in Fig. 6.15.

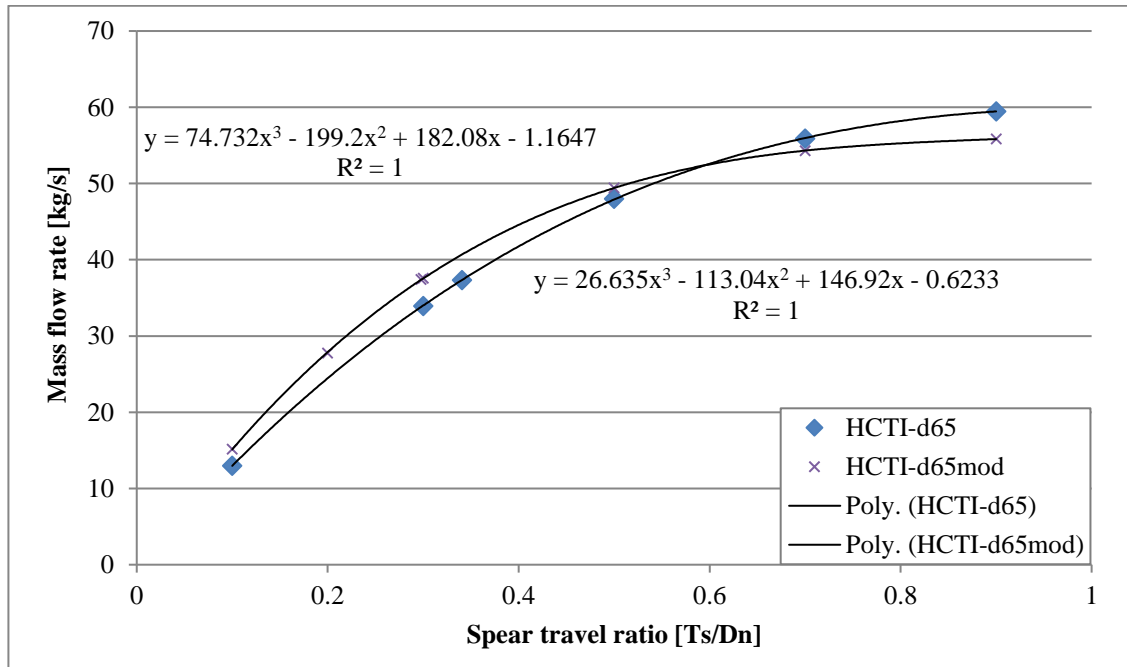


Fig. 6.15. Spear travel ratio $[Ts]/[D_n]$ against flow rate for the original J608 and the modified $D_n=65\text{mm}$ injectors with polynomial fit curves

As in the previous study, the modifications to the nozzle and spear angles have resulted in changing the maximum flow rate which the injector can accommodate slightly. In order to

account for this, the modified injectors were scaled up to match the maximum flow rates of the original injectors (Fig. 6.16 & Fig. 6.17). The modified and scaled injectors (HCTI-d78mod-scaled and HCTI-d65mod-scaled) showed a reduction in the losses of over 1% at smaller flow rates for both injectors and at the BEP for the 7.5" HCTI runner, the modified and scaled HCTI-d65mod-scaled injector is 0.34% more efficient than the original HCTI-d65 design.

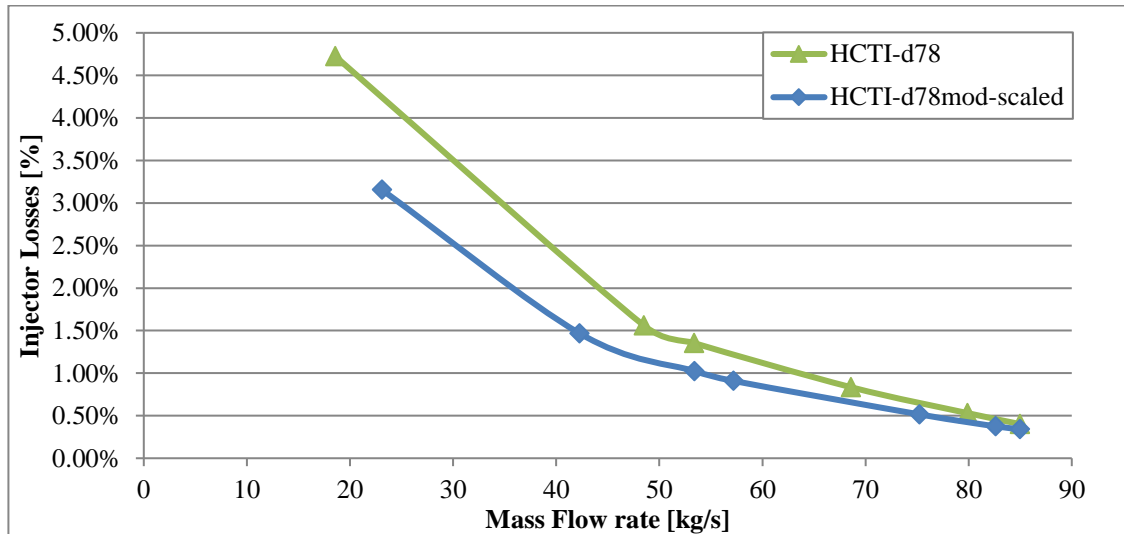


Fig. 6.16. Flow rate against losses for the original HCTI-d78 and the modified and scaled HCTI-d78mod-scaled, $D_n=78\text{mm}$ injectors

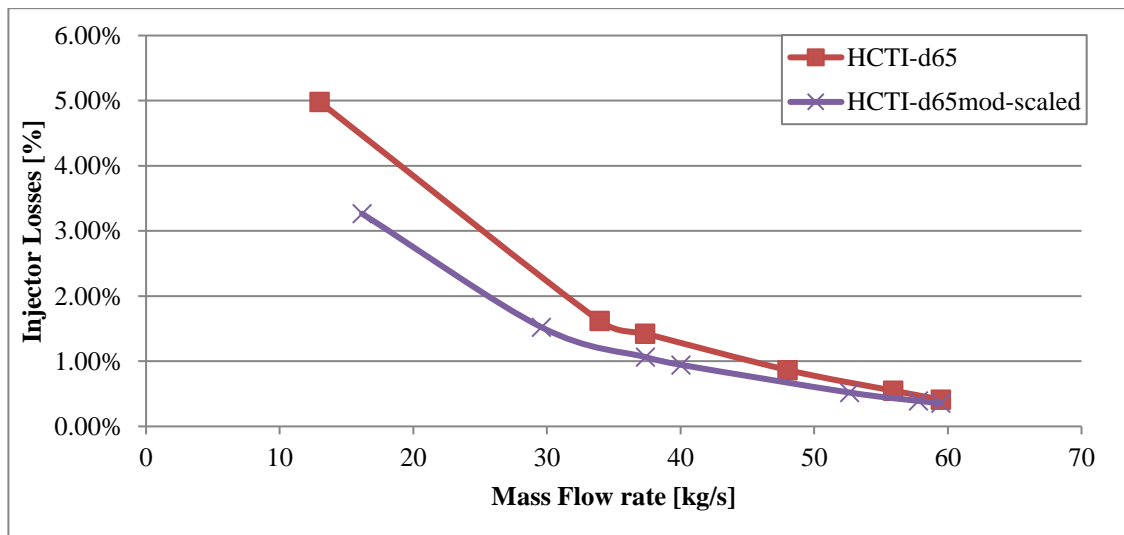


Fig. 6.17. Flow rate against losses for the original HCTI-d65 and the modified and scaled HCTI-d65mod-scaled, $D_n=65\text{mm}$ injectors

6.2.2 3D Straight pipe study

The 2D straight pipe study was extended by simulating the original HCTI-d65 and the optimised HCTI-d65mod-scaled injectors at the BEP flow rate in 3D. The domain was drawn as half of a full 3D straight pipe injector with symmetry conditions applied to the cut plane.

The mesh and simulation setup was the same as used in 6.2.1- 2D Straight pipe study with further refinement along the boundary layers. The surface mesh on the symmetry plane for the 80-55 injector is shown in Fig. 6.18 and Fig. 6.19. The mesh had around 6.8M cells before mesh adaption.

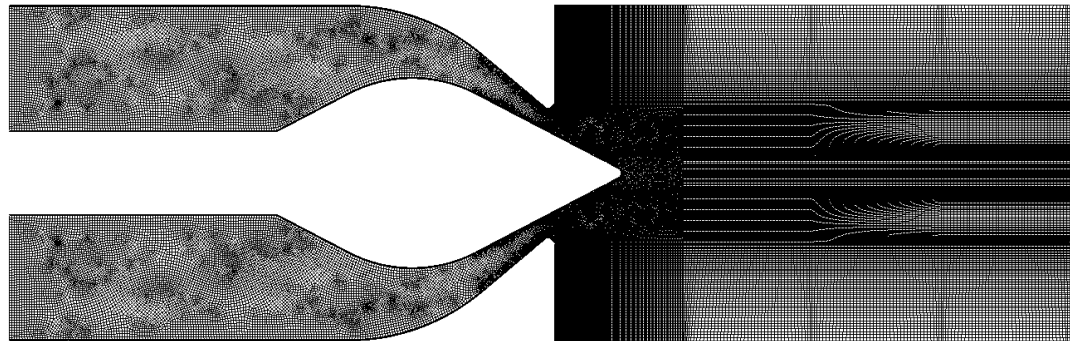


Fig. 6.18. HCTI-d65 injector mesh

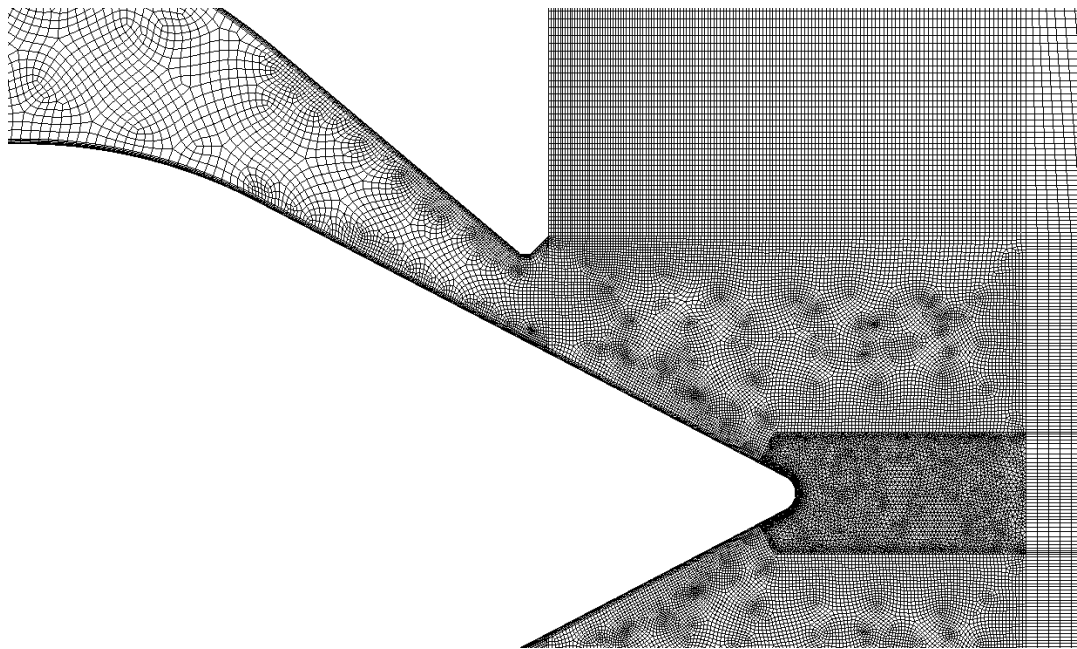


Fig. 6.19. HCTI-d65 injector mesh- detail view

The convergence criteria were set to 1e-6 for these simulations with mesh adaption taking place after the residuals reach 1e-5. Mesh adaption based on velocity and volume fraction was run with a node factor of 2 (producing around 19M cells) in order to investigate the impact of the mesh density on the results. The node factor is the factor by which the cell edge length is divided if the conditions within the cell meet the adaption criteria. The HCTI-d65 injector mesh is shown after mesh adaption with a node factor of 2 in Fig. 6.20.

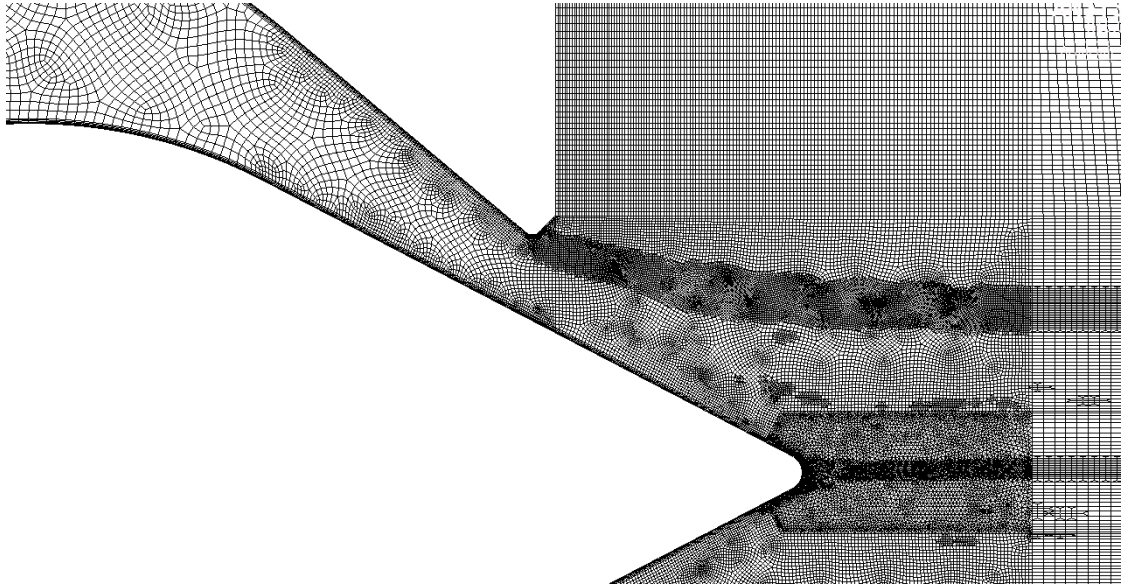


Fig. 6.20. HCTI-d65 injector mesh- detail view after mesh adaption with Node Factor 2

The losses at the planes 1D, 2D, 3D and Opening ($1D_n$, $2D_n$, $3D_n$ and $4D_n$ respectively) are shown in Fig. 6.21 for the *HCTI-d65* and *HCTI-d65mod-scaled* injectors using a 3D straight pipe (SP) simulation with, no mesh adaption and mesh adaption with node factors of 2 (NF2). All the simulations converged with a residual target of 1e-6.

The results show that the difference in efficiency between the two injector designs increases slightly as the mesh is refined from no mesh adaption (0.17%) to NF2 (0.19%) taken at the 2D plane. It is also apparent from the results, that using active mesh adaption makes little difference with the original HCTI-d65 injector however for the optimised HCTI-d65mod-scaled injector; the losses are reduced as the distance from the nozzle increases. The active mesh adaption is critical in order to capture the detailed flow in the regions where the velocity and volume fraction is changing the most, particularly when upstream geometry induces secondary velocities and more disturbances on the outside of the jet as discussed in the following chapter, 6.2.3 3D Full injector study.

Although the results of the 3D straight pipe simulations show the HCTI-d65mod-scaled injector to be more efficient than the HCTI-d65 injector, the difference between the losses for

each design is smaller than the 2D axisymmetric case at 0.2% compared to 0.51% respectively. These differences are explored further in *6.2.4 2D/3D Injector study comparison*.

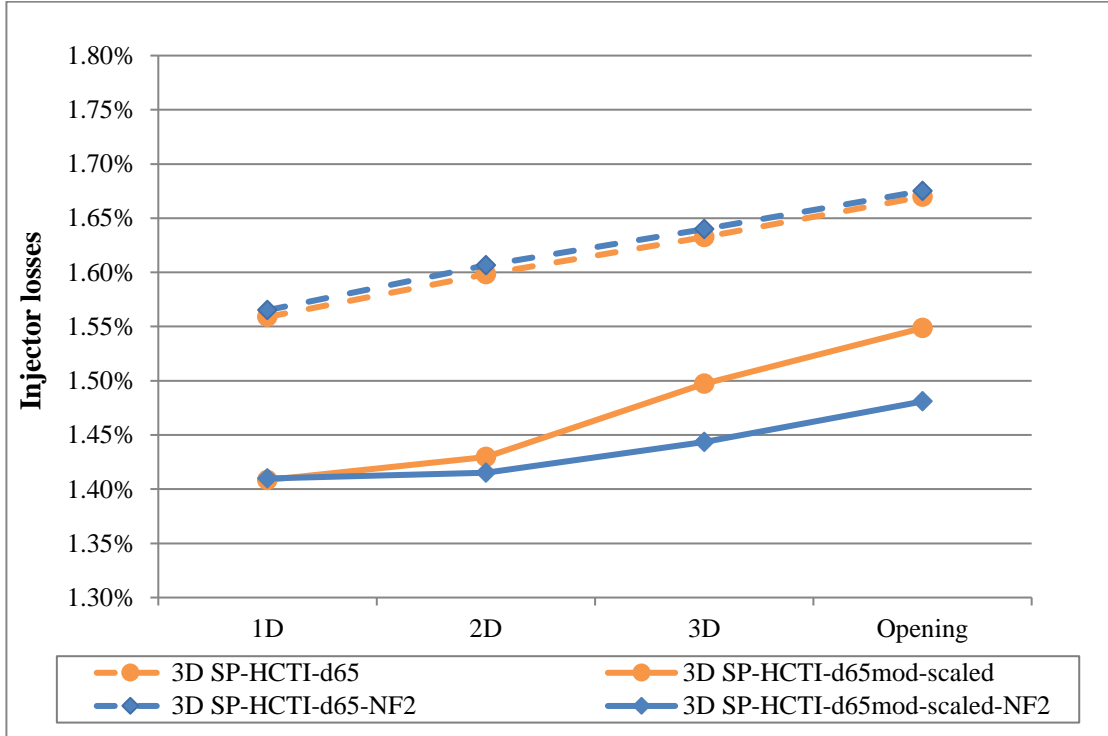


Fig. 6.21. 3D Straight pipe efficiency at planes 1D, 2D, 3D and with and without active mesh adaption (NF2)

6.2.3 3D Full injector study

The HCTI Turgo injector study was taken further by looking at the performance of the full 3D injector including the branch pipe and guide vanes upstream of the nozzle and spear. The full injector assembly containing the bend and the spear holding vanes was modelled in 3D, as shown in Fig. 6.22. The domain geometry was blocked to assist the meshing process. The injectors were meshed using the ANSYS® Workbench Mesh tool with the same sizing parameters used in the 3D straight pipe study. The minimum orthogonal quality was above 0.2. Fig. 6.23 provides an image of a complete mesh and Fig. 6.24 and Fig. 6.25 give a more detailed mesh view of the nozzle exit and spear tip. Tetrahedral elements were used to mesh the geometry region at the bend that contains the spear shaft and the region around the spear holding vanes. Tetrahedral elements were also used at the spear tip and 10 inflation layers were used on all the wall boundaries.

The mesh was semi-structured containing ~12 million cells before mesh adaption and ~20 million cells after mesh adaption. Mesh adaption was applied with a node factor of 2 (NF2) which was found in the previous study to give accurate results. Using a NF2 gave convergence of the RMS momentum and mass residuals below 7.5e-6 for both injectors in steady state.

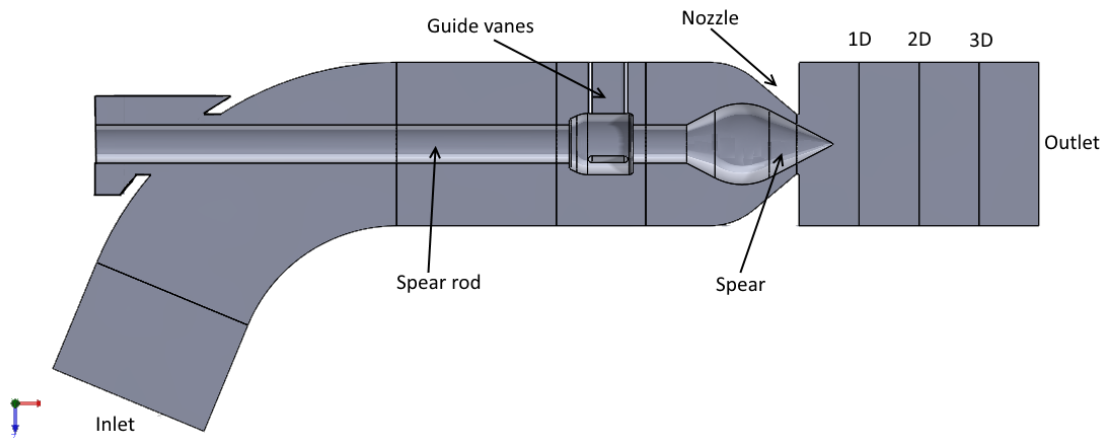


Fig. 6.22. Full 3D injector domain geometry

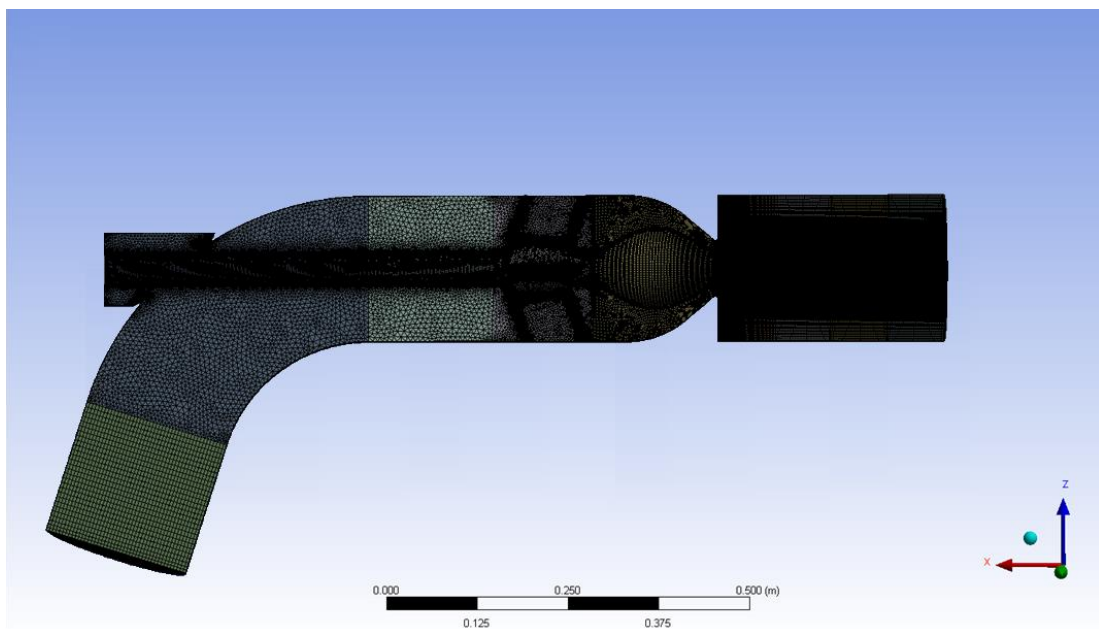


Fig. 6.23. 3D mesh for complete HCTI-d65 injector geometry

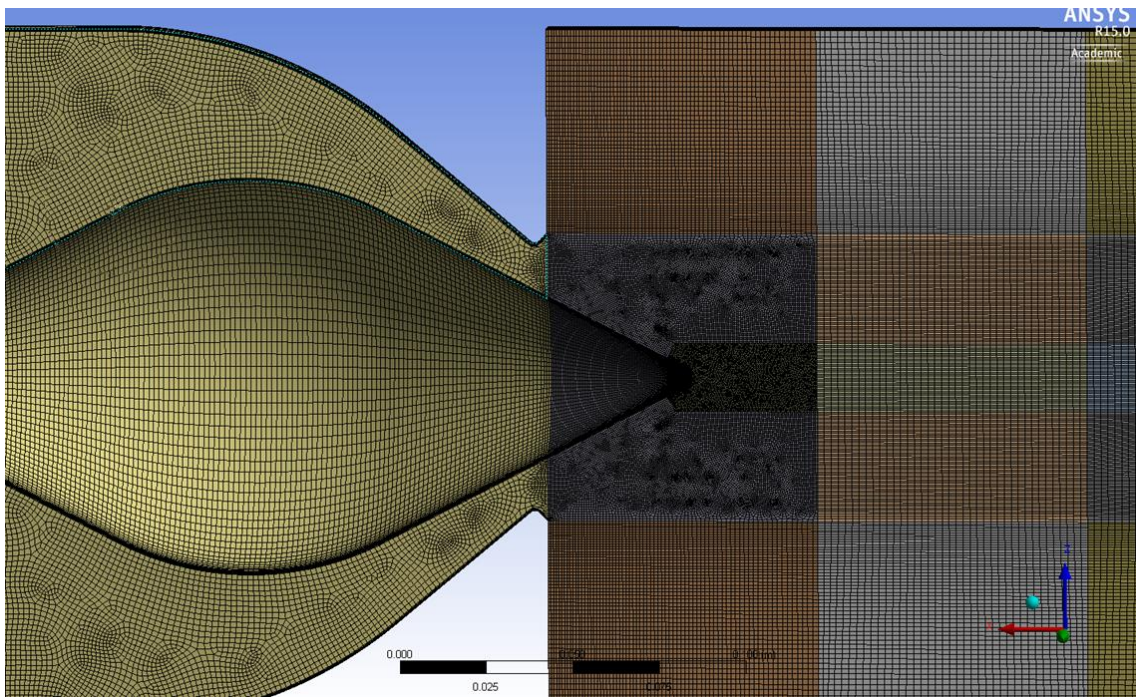


Fig. 6.24. 3D mesh for complete HCTI-d65 injector geometry- spear and nozzle view

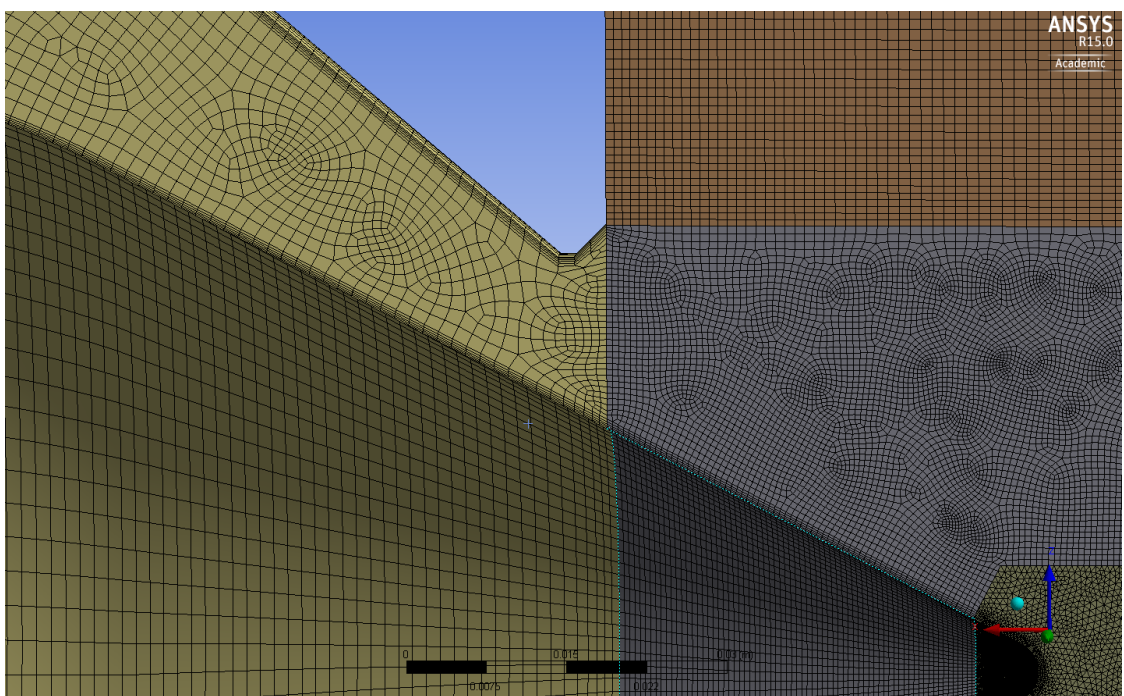


Fig. 6.25. 3D mesh for complete HCTI-d65 injector geometry- detailed view of restriction

The full 3D injector was simulated with a symmetry plane vertical to the axis of the pipe bend, as used in the 3D straight pipe study while the rest of the simulation settings were the same as in the 2D case given in Table 6.1. The streamlines and jet surface, at a water volume fraction of 0.5, for the HCTI-d65 injector design at a head of 30.5m and the BEP flow rate are shown in Fig. 6.26 as well as the planes on which the secondary velocities are plotted.

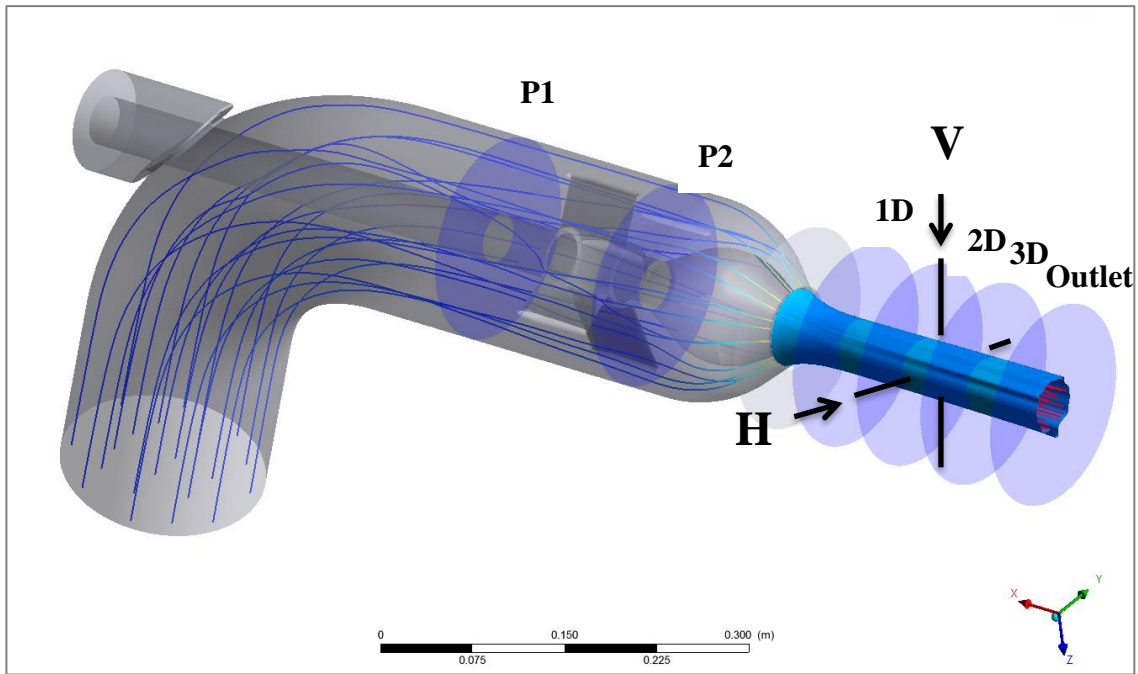


Fig. 6.26. HCTI-d65 3D injector simulation showing the planes used in the analysis

The 300 16 core node Lancaster University HEC (High End Computing Cluster) was used to cope with the large mesh sizes running the simulations on 36 or 48 cores. The partitioning was set to linear, with the domain partitioned perpendicular to the flow direction which reduced the occurrence of residual spikes. The solver was set to mesh adaption after 500 iterations with a total of 2000 iterations and a 1e-6 residual target giving a solution time of around 15hours on 36 cores.

The same BEP design points were used as the 2D straight pipe and 3D straight pipe studies, using a 65mm injector at the 7.5" HCTI Turgo BEP test conditions operating at a head of 30.5m and a flow rate of 39kg/s. The results of these simulations are shown in Fig. 6.27, below. The results show that the 110-70 design is 0.22% more efficient than the original 80-55 design which agrees with the 2D study carried out previously as well as the work done on the generic injector design.

Overall it proved difficult getting these full injector simulations to converge to below 5e-6 which may suggest that the flow is not steady state and requires a full transient analysis however this is beyond the scope of this research and as an initial comparison, the steady state simulations have proven adequate.

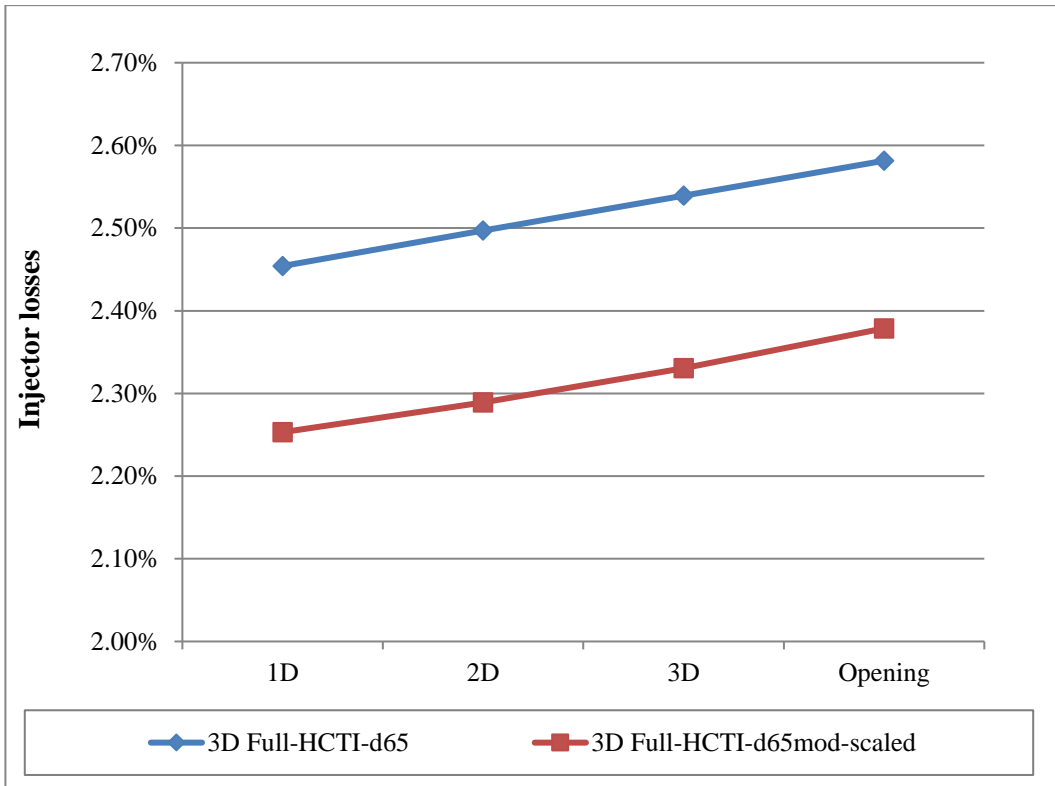


Fig. 6.27. Full 3D Injector losses measured at 2 diameters from the nozzle

In order to investigate the differences between these designs further, the velocity and pressure profiles are plotted in Fig. 6.28 and Fig. 6.29. The velocity contours show a more even distribution of velocity for the 110-70 designs, with the low velocity region in the centre of the jet not extending as far as the 80-55 design. This is more apparent when comparing the velocity profiles on a plane through the jet as shown in Fig. 6.33 and Fig. 6.36. The pressure profiles are more similar for the two designs, but show the zone in which the pressure change takes place to be smaller for the 110-70 design as discussed previously in Fig. 6.10 .

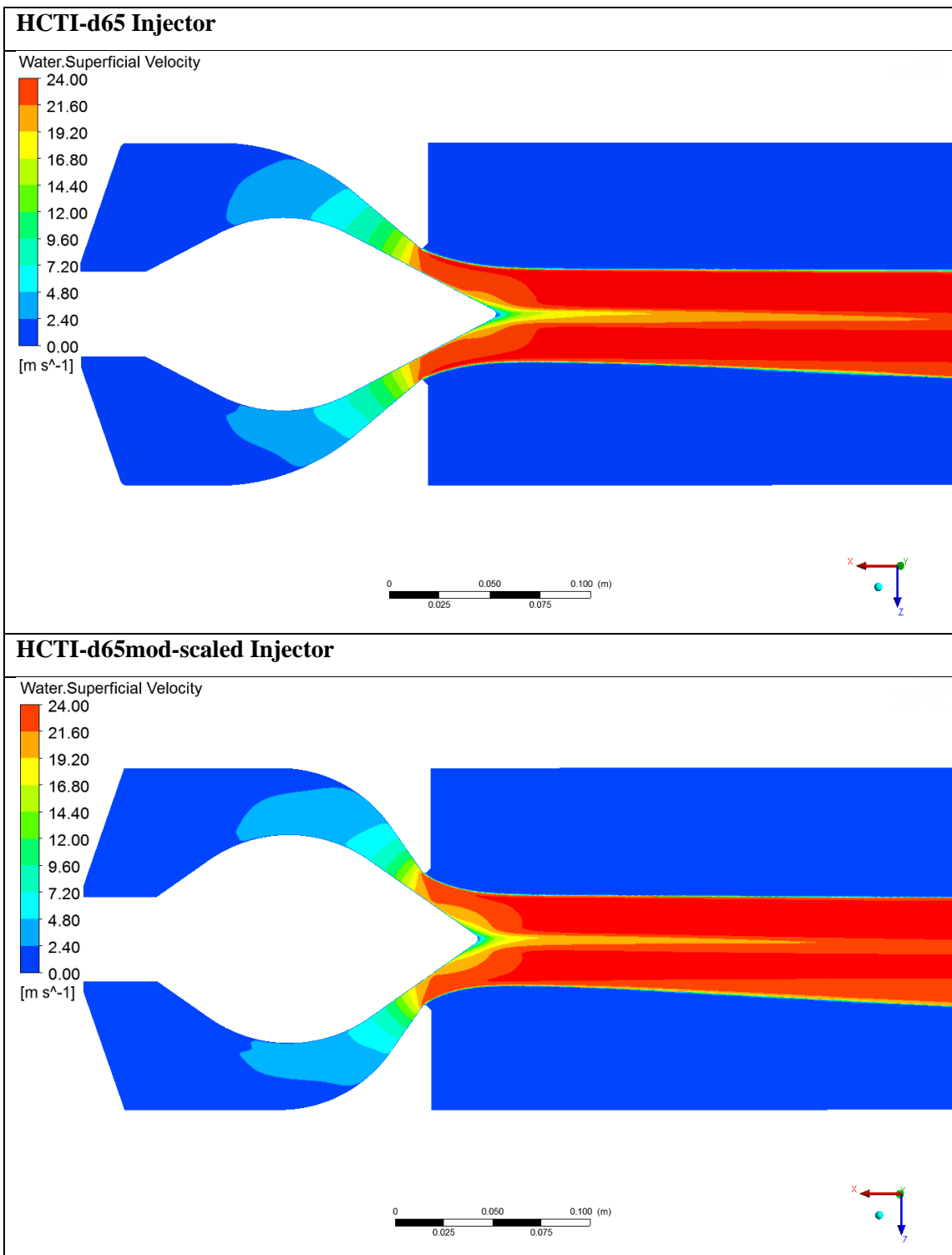


Fig. 6.28. Velocity contours on the symmetry plane for the full 3D injectors

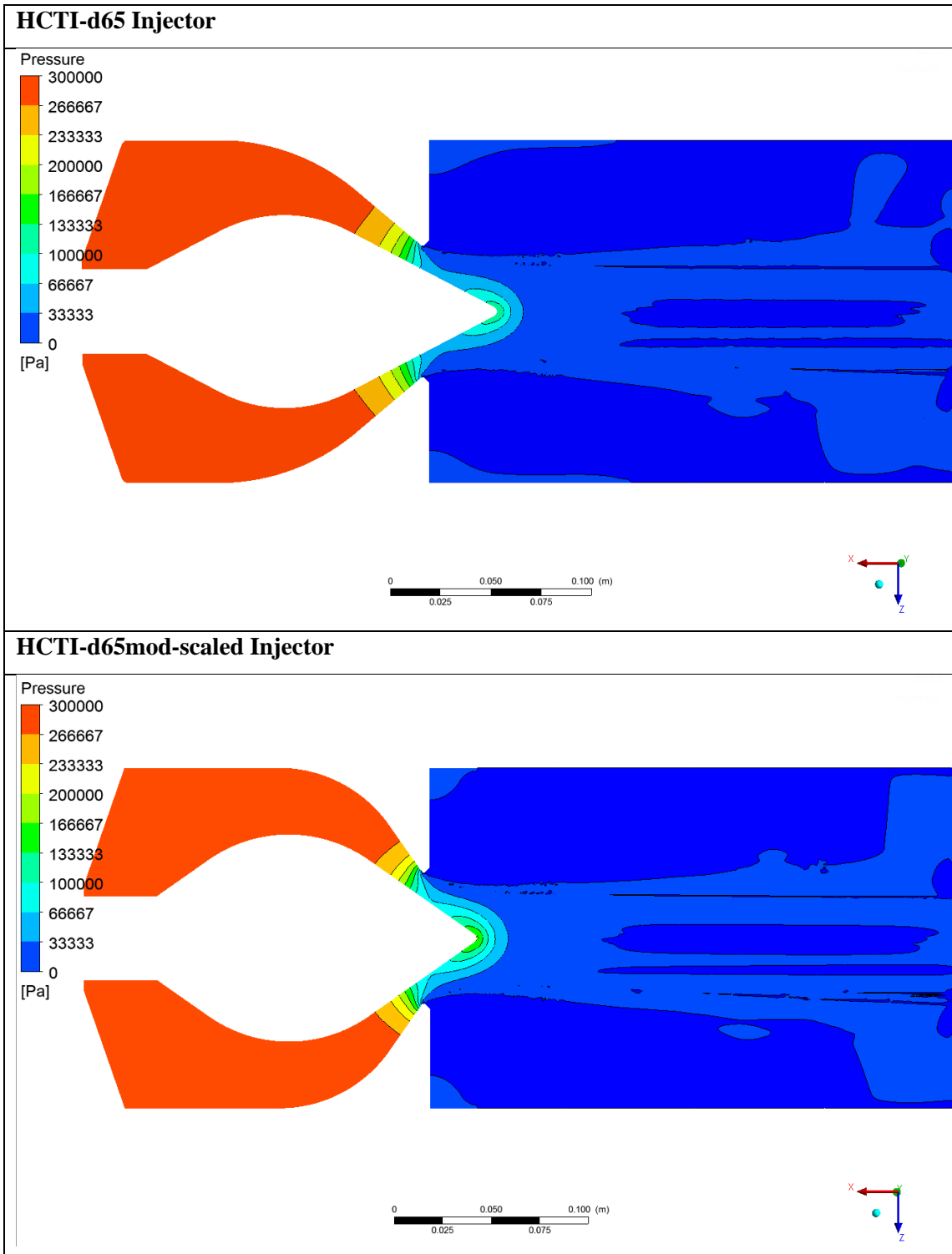
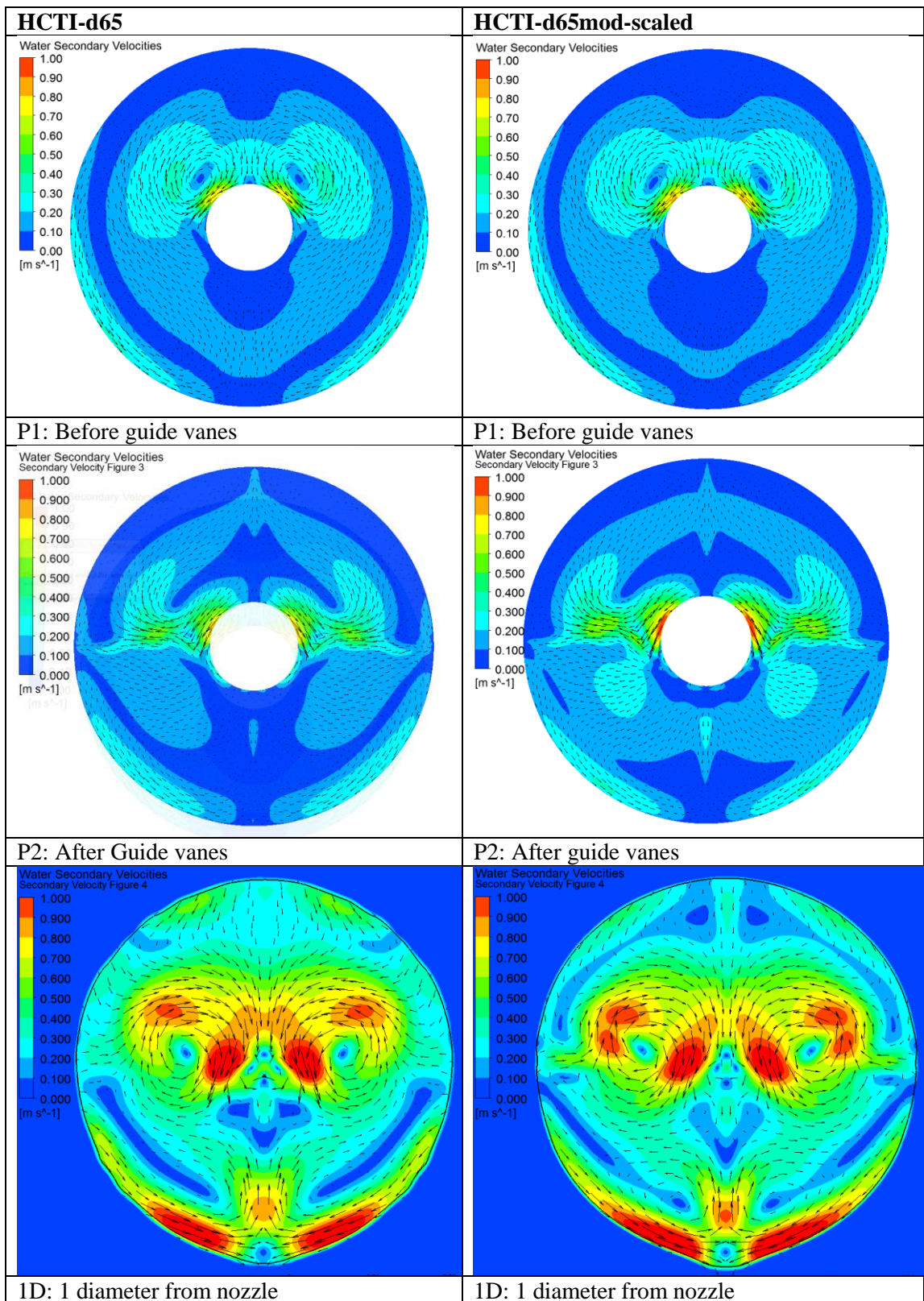


Fig. 6.29. Pressure contours on the symmetry plane for the full 3D injectors

The secondary velocities were plotted on a series of planes through the injector and free jet as shown in Fig. 6.26. The development of the secondary velocities through the injector from plane P1 through to the Outlet is shown in Fig. 6.30.



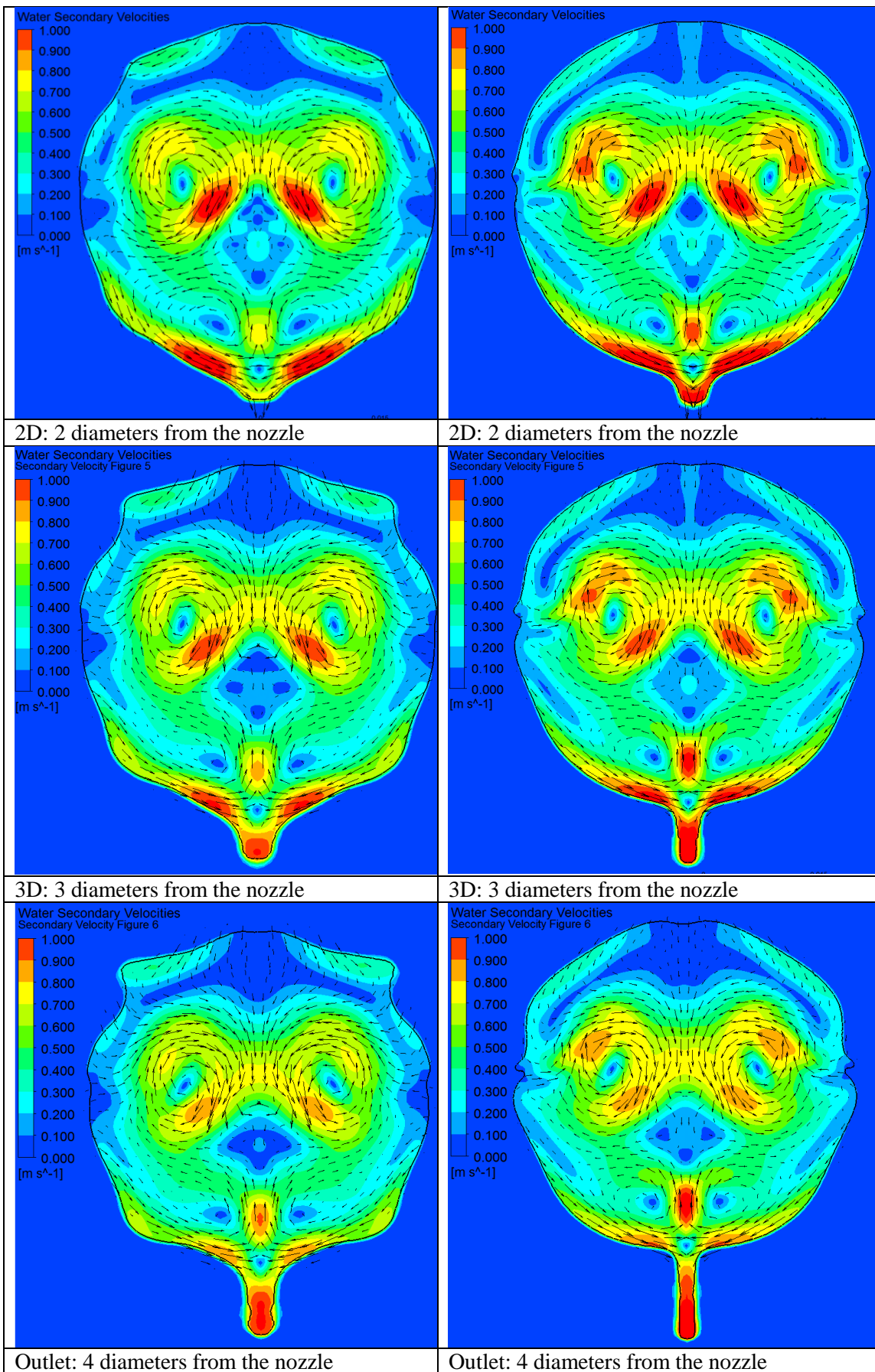


Fig. 6.30. Secondary velocities for the two injectors from P1-Outlet

The secondary velocities for the HCTI-d65 and HCTI-d65mod designs show some interesting disturbances in the jet as a result of the secondary velocities such as the bead which forms at the bottom, corresponding to the inside of the bend in the pipe and the disturbances on the corners corresponding to the guide vanes. These disturbances concur with previous experimental studies which showed similar disturbances (Staubli and Hauser 2004; Perrig, Avellan et al. 2006; Perrig 2007; Peron, Parkinson et al. 2008; Staubli T., Abgottsporn A. et al. 2009; Zhang and Casey 2009). Although the losses through the steeper angled HCTI-d65mod-scaled injector are lower, when comparing the shape of the jet and the secondary velocities, the HCTI-d65mod-scaled injector seems to develop a slightly longer bead/disturbance at the bottom of the jet and the maximum localised secondary velocities seem higher. In order to investigate this further, the secondary velocities are compared graphically in Fig. 6.31 below.

Although the maximum secondary velocity is 6.4% higher for the 110-70 design at 2D, the average secondary velocity (derived from the magnitudes only) is 35.18% lower than the 80-55 design. With it being difficult to get the residuals of these simulations lower than 5e-6, the average secondary velocity provides a more stable comparison between the designs and suggests that the 110-70 design produces a more uniform jet with lower secondary velocities albeit with a more extended bead forming at the bottom of the jet.

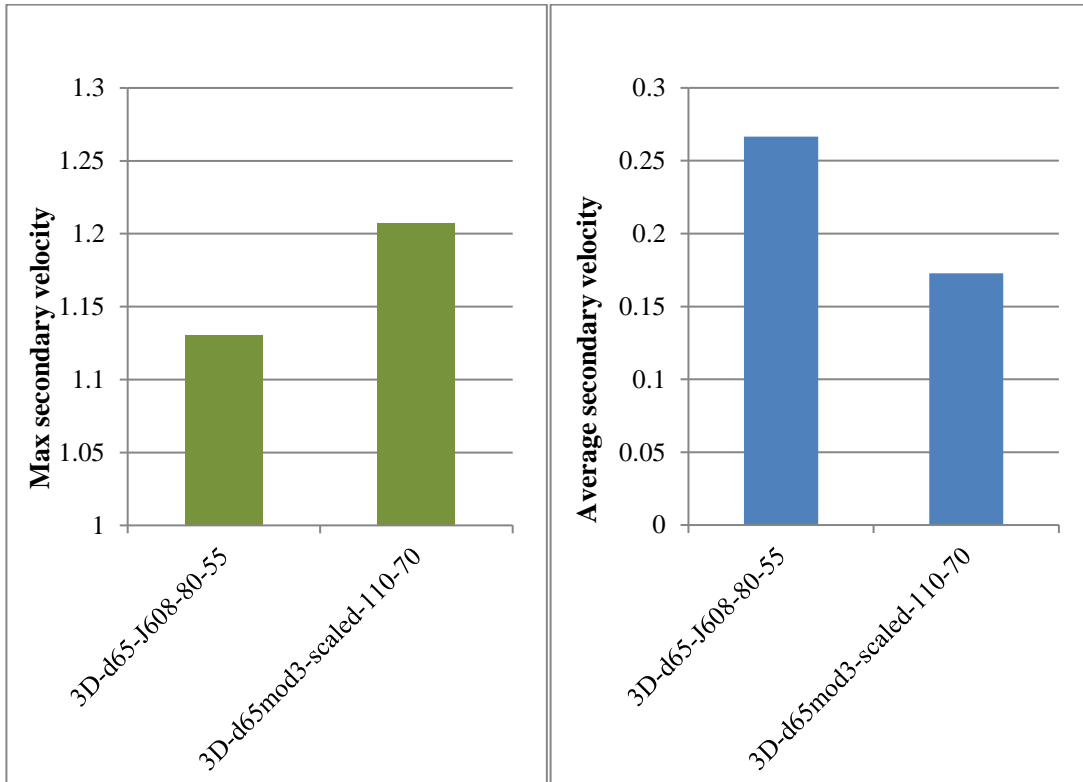


Fig. 6.31. Maximum and average secondary velocities at 2D for each injector design

Previous studies (Veselý and Varner 2001; Staubli T., Abgottsporn A. et al. 2009; Zhang and Casey 2009) have shown that it is these secondary velocities, induced by the pipework and geometry upstream of the spear/valve, which cause increased jet dispersion and reduce the performance of the runner. The injector design which reduces these secondary velocities the most overall is likely to perform better when combined with the runner. This is explored further through experimental testing of both the Standard (80/55) and the Novel (110/70) injector designs with both a Pelton and a Turgo runner (*8- Injector experimental testing*) as well as numerically comparing the performance of the Turgo runner with the jets produced by each injector (*9.3.1- Full injector and runner simulations*).

6.2.4 2D/3D Injector study comparison

During the course of this injector analysis, some minor differences were found in the injector comparisons using the 2D axisymmetric case, the 3D straight pipe case and the 3D full injector case (including the branch pipe and guide vanes). These differences and the reasons for them are covered in more detail in this section.

The losses for the HCTI-d65 and the optimised HCTI-d65mod-scaled injectors are shown in Fig. 6.32 for the 2D straight pipe study, the 3D straight pipe study and the full 3D injector study. The results show that the losses increase by around 0.5% from 2D to 3D (straight pipe), for both injectors, and nearly 1% when the guide vanes and upstream bend in the pipe are included. This seems logical as more of the disturbances and secondary flows are accounted for as the simulations move from the simple 2D axisymmetric case to the full 3D case.

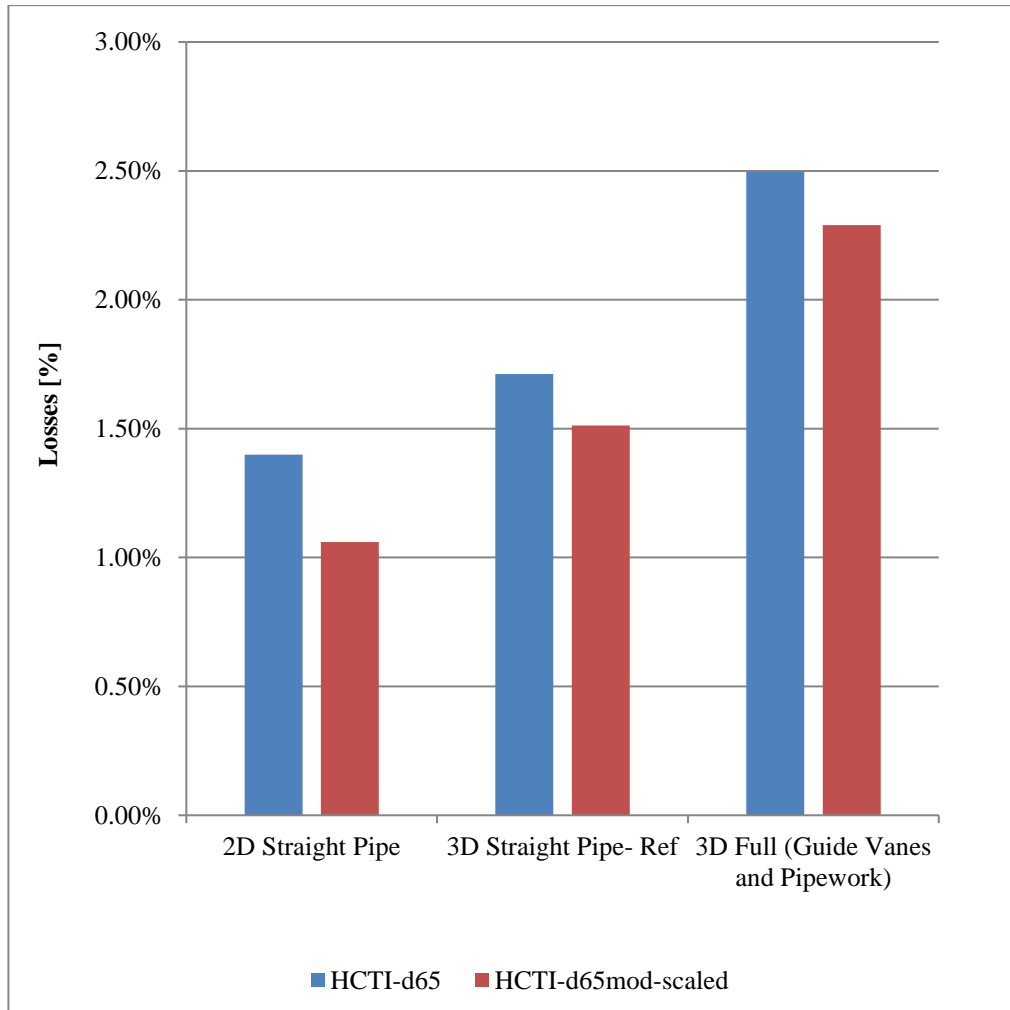


Fig. 6.32. HCTI-d65 and HCTI-d65mod injector losses for 2D Straight Pipe, 3D Straight Pipe and 3D Full injector studies

The difference in the losses between the HCTI-d65 and HCTI-d65mod injector designs is greater for the 2D axisymmetric case (0.34%) than the 3D straight pipe and full 3D cases at 0.20% and 0.21% respectively. In order to investigate the reasons for this, the velocity profiles through the centre of the jet are compared as shown in Fig. 6.33 to Fig. 6.36. Fig. 6.33 shows the velocity profiles for the 2D axisymmetric simulations using a straight pipe. The velocity profiles are very uniform showing a clear difference between the dip in the centre of the jet between the 80-55 and 110-70 designs. The 3D straight pipe study profiles are shown in Fig. 6.34. The results are very similar to the 2D case however the differences in the low velocity dip in the centre of the jet are slightly less pronounced.

Fig. 6.35 and Fig. 6.36 show the horizontal and vertical jet profiles for 3D Full injector simulations. The results show concurrence with the 2D straight pipe and 3D straight pipe simulations where the HCTI-65mod-scaled design reduces the dip in velocity in the centre of the jet giving a more uniform jet in both the horizontal and vertical planes. The bead which

forms as a result of the secondary velocities can be seen clearly by the wider profiles seen in the vertical plane. The horizontal (H) profiles indicated by the solid lines show a uniform cross section with a well-defined difference between the 80-55 and 110-70 injectors. The vertical profiles (V) indicated by the dashed lines show a smaller difference in the dip in the centre of the jet between the two designs. The losses are still lower however and the dip in the centre of the jet is still smaller for the HCTI-d65mod-scaled injector but this may contribute to the smaller difference in the losses between the two designs for the 3D full injector case compared to the 2D case.

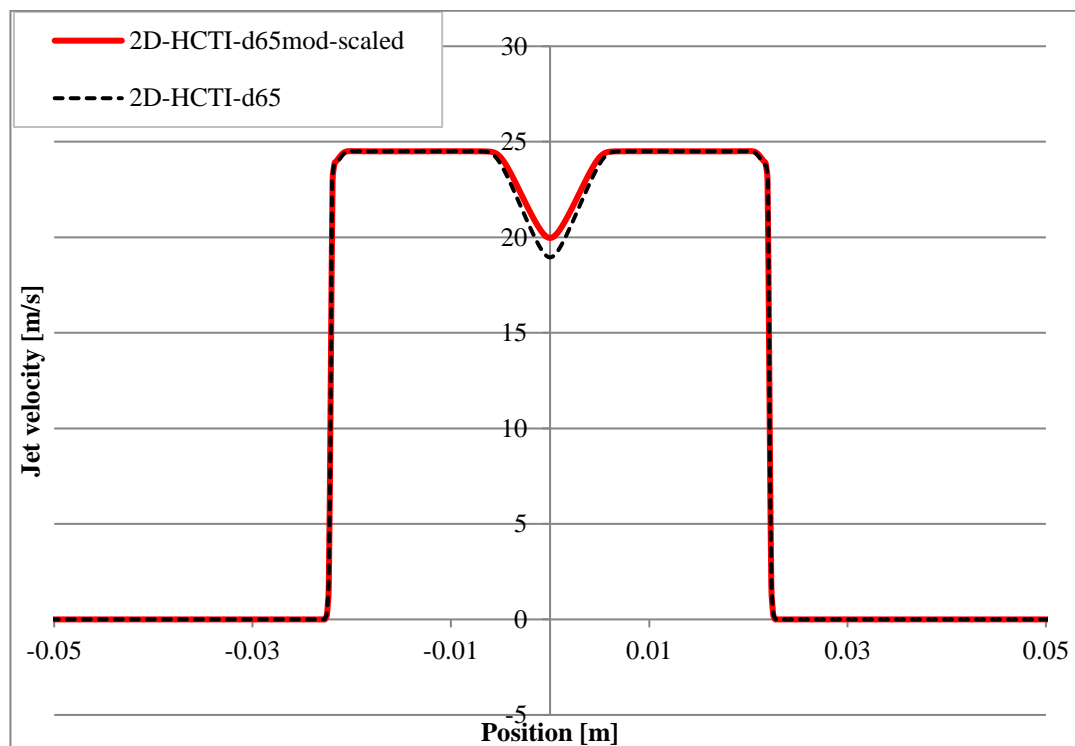


Fig. 6.33. 2D straight pipe injector study- velocity profile comparison at $2D_n$

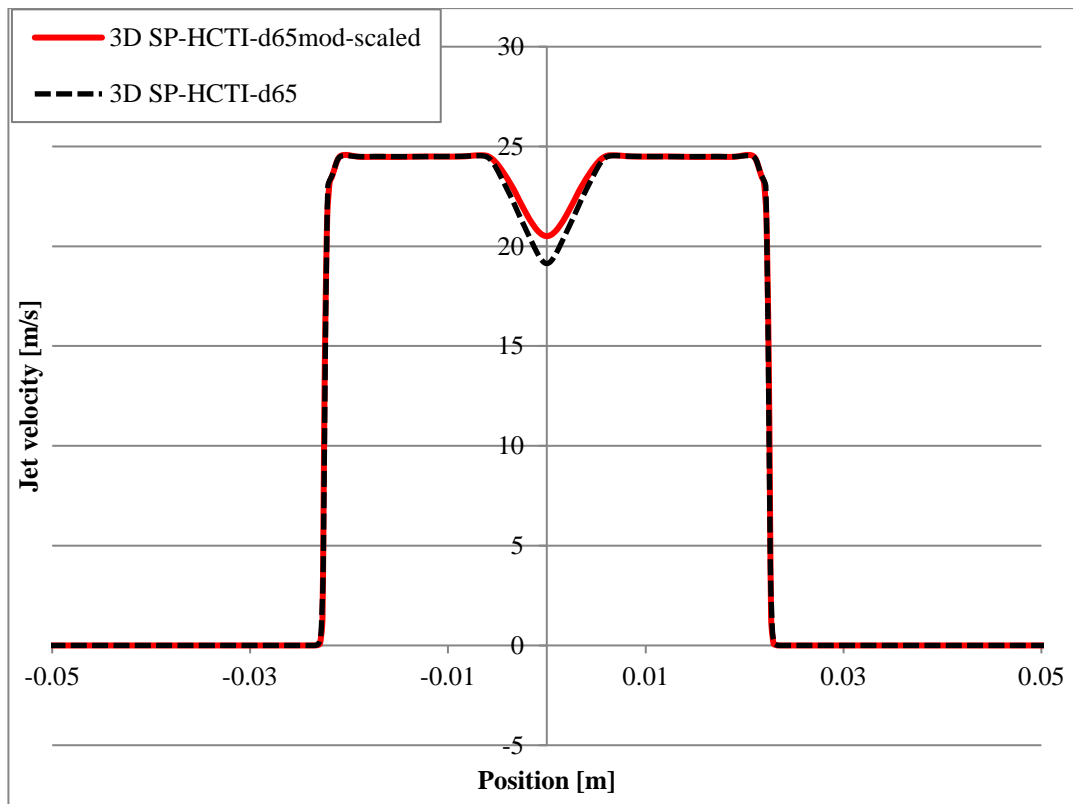


Fig. 6.34. 3D straight pipe injector study- velocity profile comparison at $2D_n$

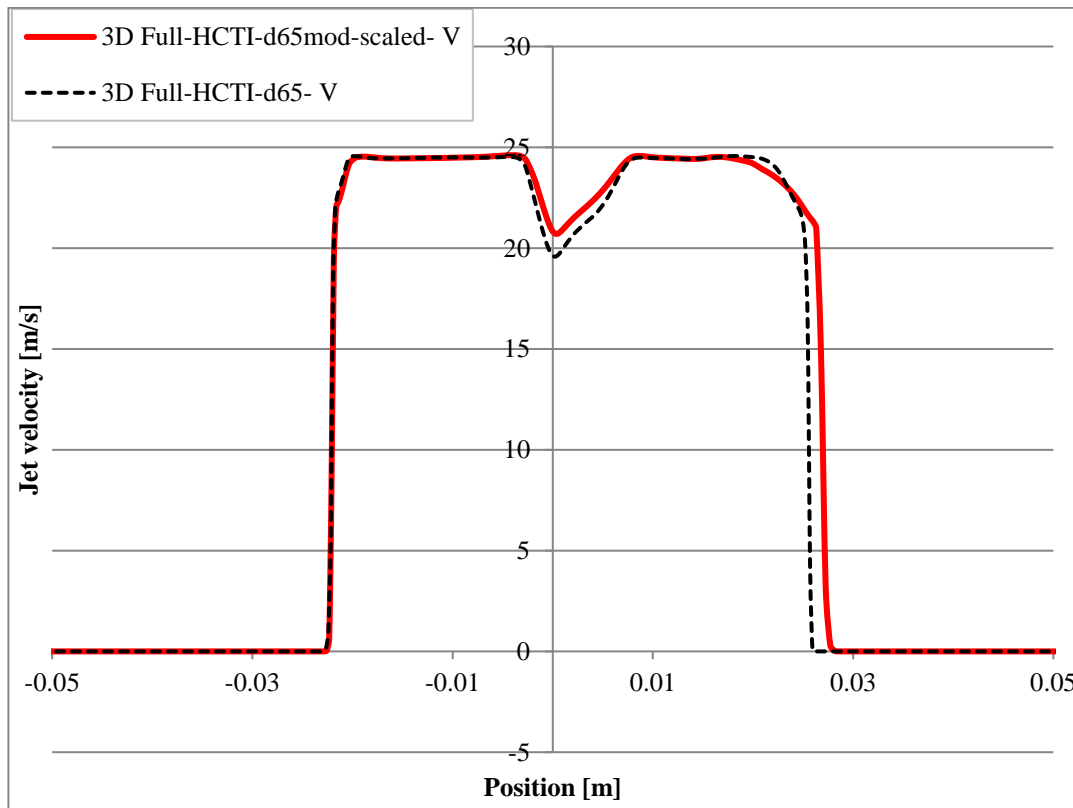


Fig. 6.35. 3D Full injector study- Vertical velocity profile comparison at $2D_n$

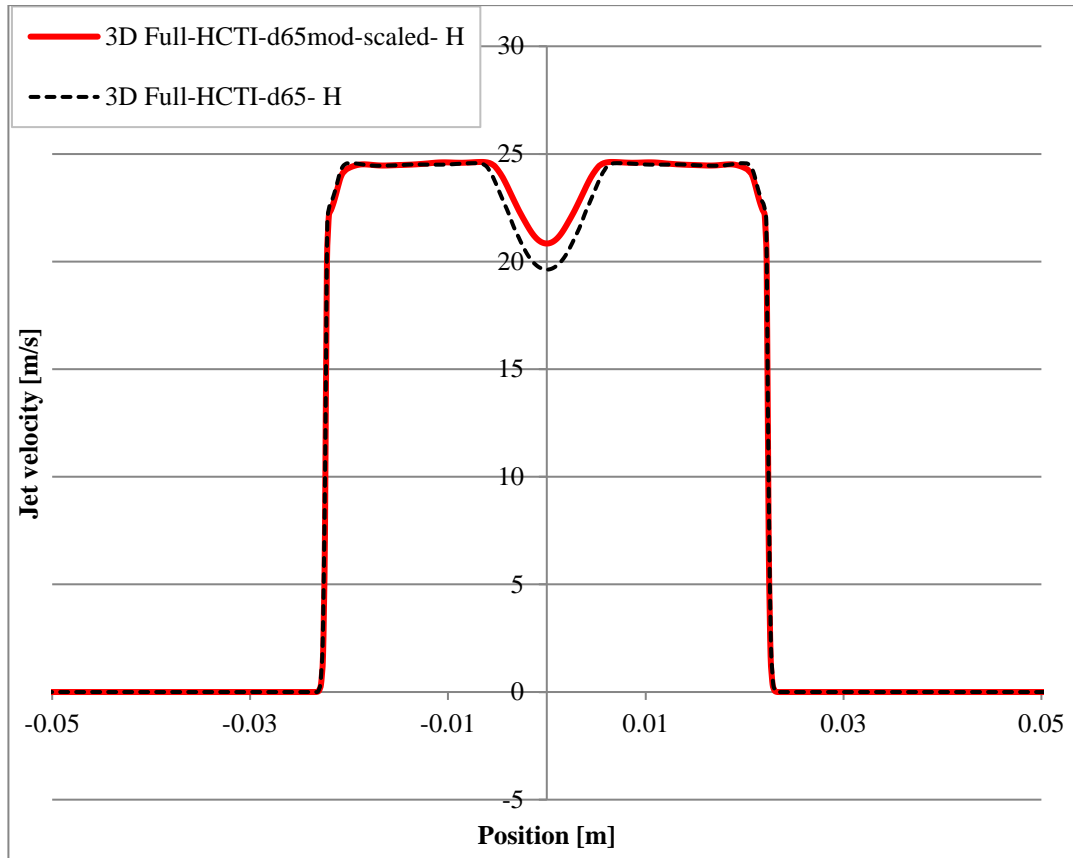


Fig. 6.36. 3D Full injector study- Horizontal velocity profile comparison at $2D_n$

Overall it seems that the reasons why the difference between the losses for the HCTI-d65 and HCTI-d65mod-scaled designs is greater in the 2D axisymmetric cases compared to the 3D cases is primarily due to the stability of the simplified flow field in the 2D case which better captures the subtle differences in the flow through the injectors. Despite this, the difference in the losses between the two designs of around 0.2% for the full 3D case should be significant enough to capture experimentally.

The impact that the jets produced by each injector have on the performance of the runner is also significant as discovered when importing the ‘real jet’ profiles in to the runner simulations as opposed to the ‘ideal jet’ used in the optimisation. The impact these varying jet profiles have on the numerical runner performance is explored in *9.3.1 Full injector and runner simulations* and compared to the experimental injector test results.

7 Turgo runner experimental testing

This chapter describes the experimental testing of the original HCTI Turgo runner and the optimised LE4 and LE1 designs which was carried out at the Laboratory of Hydraulic Machines, National Technical University of Athens (NTUA) according to IEC60193 testing standards. A short summary of the manufacture of the runners is provided followed by details of the Turgo test rig and equipment used during testing. The characteristic equations used to calculate the performance of the runners and plot the performance envelopes or ‘hill charts’ are also provided. The systematic, random and total uncertainties are then established followed by the test plan and procedure used. Following this, the results are presented, compared and discussed.

7.1 Runner manufacturing

Based on the optimisations carried out on the original HCTI runner design, the new runner design was manufactured by a Gilkes supplier. The optimised runner was manufactured using investment or lost-wax casting. This process involves 3D printing of the runner in Poly Methyl Methacrylate (PMMA) Plastic, with adjustments for shrinkage of the cast etc. This model is then ‘shelled’ by coating the model in layers of ceramic and left to dry in ambient conditions. Once dry, the shell is baked in an oven to harden the cast and remove the PMMA model. The cast is then filled with molten 17-4 PH (Precipitation Hardened) stainless steel and once set; the cast can be broken away, leaving the stainless steel runner behind. The rough cast runner face is then machined to the specified width, shot blasted to remove any remaining cast and x-rayed to look for defects in the material.

As the minimum recommended wall thickness for the lost-wax casting used to manufacture this runner is 2mm, the optimised runner geometry was adjusted to increase the thickness of the leading edge. This resulted in three runner designs, detailed below, which were tested consecutively.

1. **HCTI-9” PCD**, original Gilkes High Capacity Turgo design manufactured in the normal manner for a runner of this size which is sand casting and then grinding down to match templates.
2. **LE4- 9” PCD** optimised design which has a 2mm leading edge on the 9” runner. This design is investment cast and the front face and hub is machined to match the drawings. No additional machining or dressing is carried out on the blades.
3. **LE1- 9” PCD** optimised design which is the LE4 design after dressing of the leading edges to 0.5mm which is closer to the optimised CAD.

The 9" HCTI and LE4 runners used in this testing are shown in Fig. 7.1 and Fig. 7.2 below. The dressed LE1 runner with the 0.5mm leading edges is shown in Fig. 7.3.



Fig. 7.1. Dressed 9" HCTI design (left) and optimised LE4 design (right)- inlet side



Fig. 7.2. Dressed 9" HCTI design (left) and optimised LE4 design (right)- outlet side



Fig. 7.3. Optimised LE1 design showing dressed leading edges

Both designs were tested using upper, lower and twin jet operation and compared to the original Gilkes HCTI Turgo which is sand cast and then dressed, the normal manufacturing process for this runner size.

7.2 Turgo test rig

For the purposes of this research, Gilkes have invested in a brand new 9" Turgo test rig at the Laboratory for Hydraulic Machines, NTUA, the 3D CAD design of the test rig is shown in Fig. 7.4 and the physical rig in Fig. 7.5.

A high head adjustable speed multistage pump of nominal operation point $Q=290 \text{ m}^3/\text{h}$, $H=130 \text{ mWG}$, coupled via a hydraulic coupler to a 200 kW induction motor is used to feed the model turbine, pumping from the 320 m^3 main reservoir of the Lab. The runner is coupled to a variable speed generator as shown in Fig. 7.4.

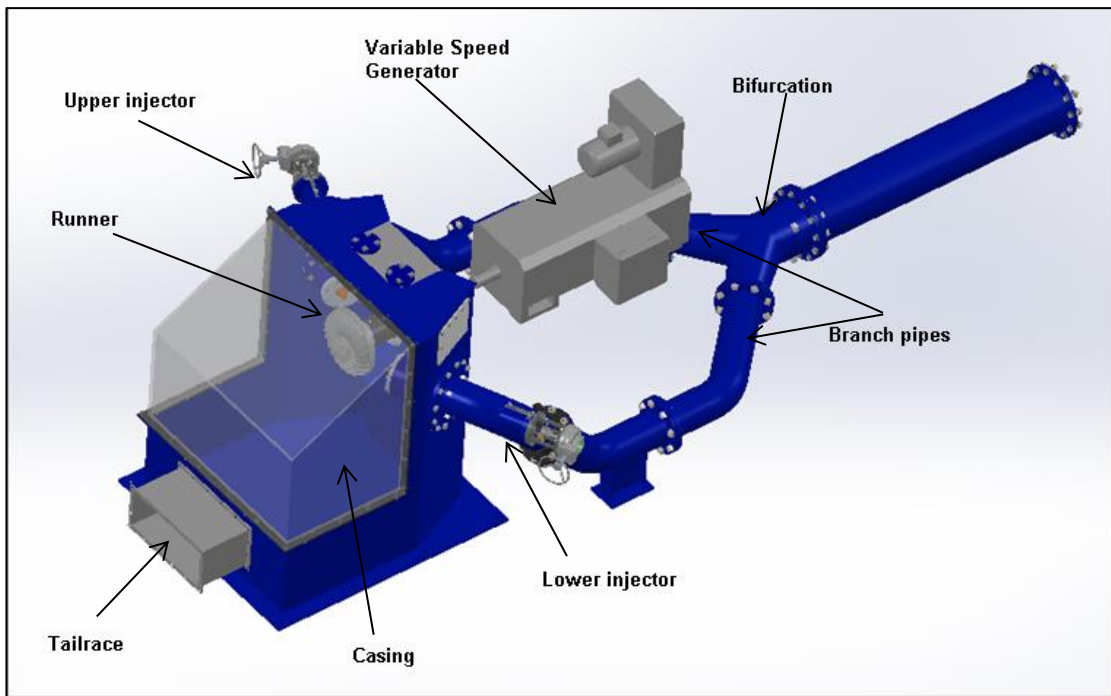


Fig. 7.4. 3D CAD model of new 9" Turgo test rig



Fig. 7.5. New Gilkes 9" Turgo test rig, Laboratory for Hydraulic Machines, NTUA

7.3 Sensors and instrumentation

Testing and calibration of all the sensors was carried out according to testing standard *IEC 60193 Hydraulic turbines, storage pumps and pump-turbines – Model acceptance tests* (IEC 60193:1999).

The location of the pressure, torque and speed sensors in relation to the test rig are shown in Fig. 7.6, below. The flow meter was located upstream of the pressure sensor and is not shown in the diagram.

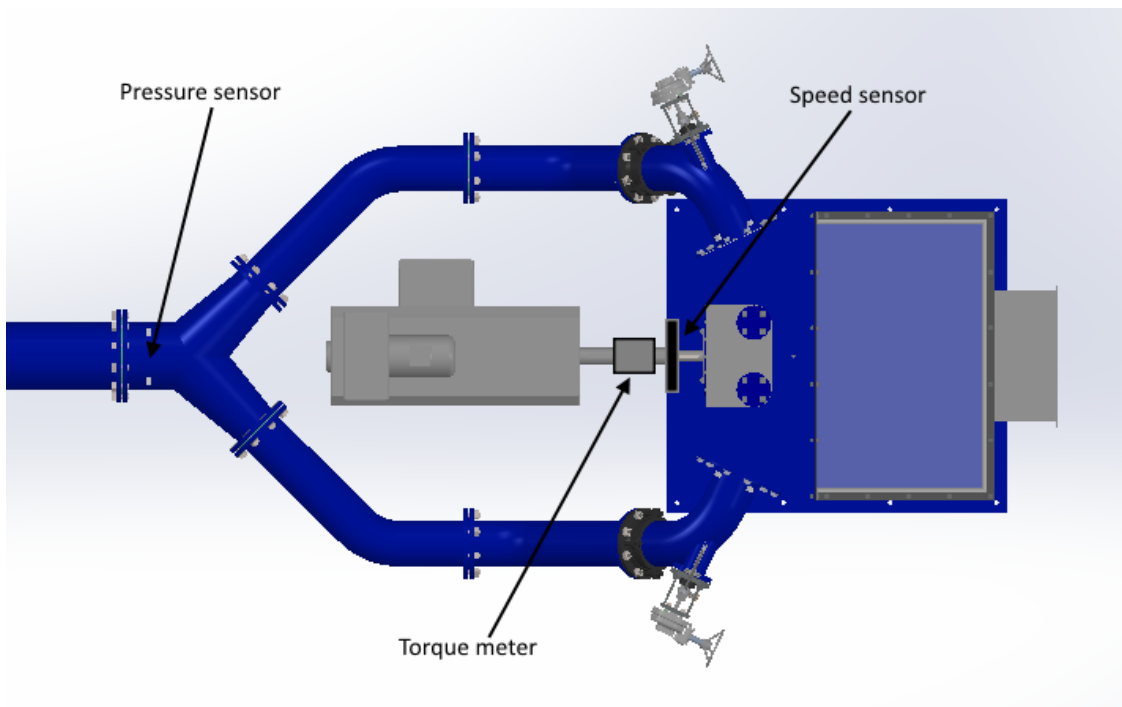


Fig. 7.6. Schematic of Turgo test rig showing location of pressure, torque and speed sensors

The sensors used on the Turgo test rig and the details of their operation are given in Table 7.1 below.

Instrument	Manufacturer and Model	Measured parameter	Range	Calibration error
Pressure sensors	ESI Technology Ltd., model: Ellison-Pr3200	Net head (H)	0-10bar	±0.1%
Flow meter	ABB, model: DE41F	Flow rate (Q)	0-600m ³ /hr	±0.5%
Speed sensor	Efectron, model: GA3005-ANKG	Rotational speed (n)	100 pulses/rev	±0.05%
Torque meter	Datum electronics, model: M425	Torque (M)	0-600Nm	±0.1%

Table 7.1- details of the sensors used for the generation of the turbine hill charts

7.4 Characteristic equations

The characteristic equations (7.1)-(7.5) used to define the operation and performance of the turbine, are given below. The pitch circle diameter, D , of the Turgo runners used in this testing was 229m.

$$n_{11} = \frac{n \times D}{\sqrt{H}} \quad (7.1)$$

$$Q_{11} = \frac{Q/N_j}{D^2 \times \sqrt{H}} \quad (7.2)$$

$$P_{out} = M\omega \quad (7.3)$$

$$P_{in} = \rho g H Q \quad (7.4)$$

$$\eta = \frac{P_{out}}{P_{in}} \quad (7.5)$$

Where n_{11} is the unit speed, Q_{11} is the unit flow rate, η is the efficiency, n is the rotational speed of the runner, H is the net head, Q is the flow rate, N_j is the number of jets, M is the torque measured on the turbine shaft, ρ is the density of water and g is the acceleration due to gravity. ρ and g were calculated according to the tables provided in the testing standards (IEC60193:1999).

7.5 Establishing the uncertainty

7.5.1 Systematic Uncertainty

The systematic uncertainty for each instrument used during this testing is given in Table 2, below. The calibration error for each instrument becomes the systematic uncertainty when used for determining the uncertainty.

Instrument	Symbol	Systematic Uncertainty
Pressure Transducer (H)	δ_p	$\pm 0.1\%$
Flow meter (Q)	δ_Q	$\pm 1.0\%$
Torque meter (M)	δ_M	$\pm 0.1\%$
Speed Sensor (n)	δ_n	$\pm 0.05\%$

Table 7.2- Systematic error of each instrument

The total systematic uncertainty for the hydraulic efficiency, δ_s , can be calculated using equation (7.6), below. The total systematic uncertainty in the efficiency, η , was calculated as $\pm 1.01\%$.

$$\delta_s = \sqrt{\delta_p^2 + \delta_Q^2 + \delta_M^2 + \delta_n^2} \quad (7.6)$$

7.5.2 Random and Reproducibility Uncertainty

The random uncertainty was determined by taking repeat measurements at a single operating point following the procedure described in Annex L (*Analysis of random uncertainties for a test at constant operating conditions*) of the international testing standard (IEC 60193:1999). The operating point used was the BEP for the HCTI runner, used as the control point and taken twice at the start, middle and end of each test. Three tests were used, taken on different days in order to account for random fluctuations in the measurements from day to day and thus include the reproducibility error.

#	Y _i	\bar{Y} -Y _i	(\bar{Y} -Y _i) ²
1	0.998774	0.001226	1.50362E-06
2	0.999005	0.000995	9.90274E-07
3	0.998511	0.001489	2.21851E-06
4	0.999548	0.000452	2.03869E-07
5	0.999825	0.000175	3.06614E-08
6	0.999222	0.000778	6.056E-07
7	0.998332	0.001668	2.78179E-06
8	0.997938	0.002062	4.25316E-06
9	0.999301	0.000699	4.88182E-07
10	0.999061	0.000939	8.82433E-07
11	0.997777	0.002223	4.94318E-06
12	1.000304	-0.0003	9.2446E-08
13	1.002347	-0.00235	5.50836E-06
14	1.003221	-0.00322	1.03742E-05
15	1.003169	-0.00317	1.00395E-05
16	1.003154	-0.00315	9.94941E-06
17	1.000132	-0.00013	1.75097E-08
18	1.00038	-0.00038	1.44549E-07
	$\bar{Y} = 1$		$\Sigma = 5.50272\text{E-}05$

Table 7.3- Control points, normalised to $\bar{\eta}$, used to determine standard deviation, s_y

The standard deviation, s_y , is calculated as 0.003028 using equation (7.7) below.

$$s_y = \sqrt{\frac{1}{n-1} \sum_{i=1}^n (\bar{Y} - Y_i)^2} \quad (7.7)$$

The random uncertainty associated with the mean value at the 95% confidence level, using the Student's T distribution, is given by equation (7.8).

$$s_r = \frac{t \cdot s_y}{\sqrt{n}} \quad (7.8)$$

Where t is the Student's T factor and can be approximated using equation (7.9)

$$t = 1.96 + \frac{2.36}{n-1} + \frac{3.2}{(n-1)^2} + \frac{5.2}{(n-1)^{3.84}} \quad (7.9)$$

The total random uncertainty at 95% confidence was calculated using this method as $\pm 0.087\%$.

7.5.3 Total uncertainty

The total uncertainty, δ_t , was calculated as **±1.02%** using equation (7.10) below.

$$\delta_t = \sqrt{\delta_s^2 + \delta_r^2} \quad (7.10)$$

The total uncertainty of ±1.02% for the experimental testing using the Turgo test rig was acceptable for the purpose of this research as the main objective is to compare the three runner designs for which the systematic uncertainty can be cancelled out and it is only the random uncertainty which determines the error in the comparison.

7.6 Test plan and procedure

The Turgo runner test plan can be seen in Fig. 7.7 below, showing the range of n_{11} and Q_{11} values which were tested. A total of 48 test points were measured excluding the six control points. The control point for each test was the design BEP for lower jet operation which was taken twice at the start, middle and end of each test. The control points not only determine the random uncertainty but can be used to monitor any large fluctuations in the readings during the testing.

For each Q_{11} value, the head and flow rate is set by adjusting the spear travel and the speed of the pump. The rotational speed is then varied by adjusting the speed of the brake and the n_{11} values are measured for each Q_{11} value. This is the approach suggested in the IEC60193 standards. For each test point, 180 readings are taken from the pressure, torque, flow and speed sensors over a period of 90 seconds. From these voltage readings, the pressure, torque, flow rate, and speed can be calculated using the calibration curves for each instrument and used to determine the efficiency.

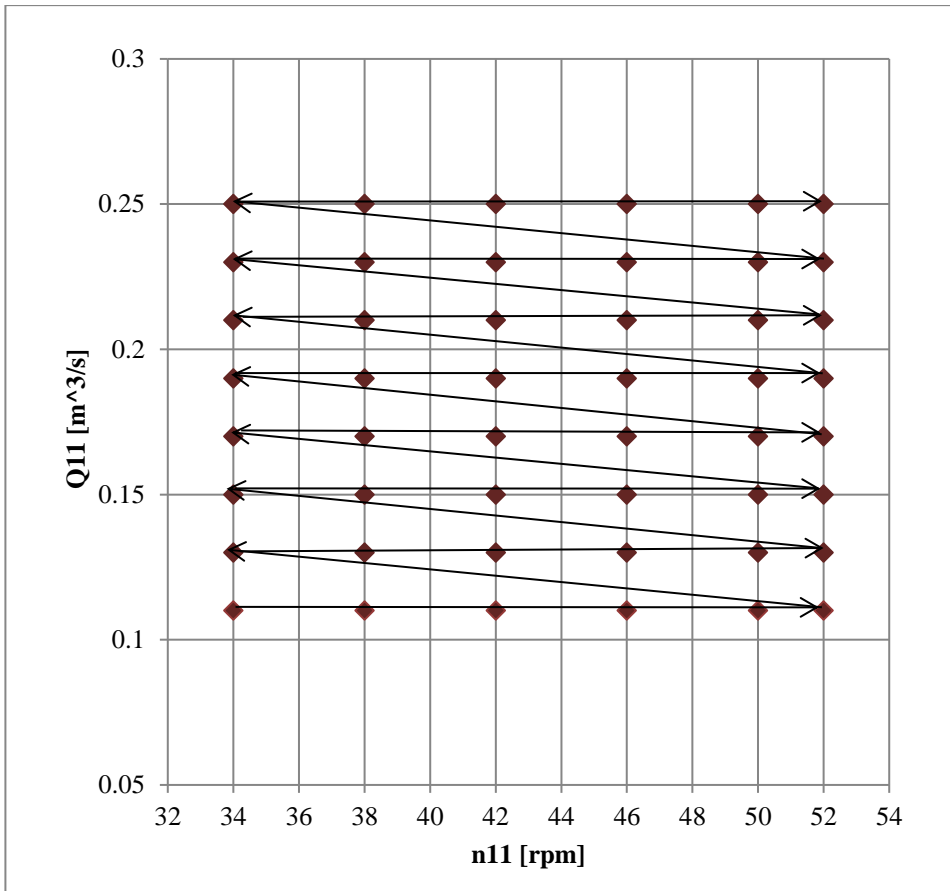


Fig. 7.7. Turgo runner test plan

7.7 HCTI runner test results

The original Gilkes HCTI runner results are plotted in the hill charts shown in Fig. 7.8 and Fig. 7.9 for single jet and twin jet operation respectively. All of the efficiencies in this chapter are normalised against the peak efficiency of the LE1 runner during twin jet operation. The hill charts are drawn from the test data using MatLab with a fixed contour interval of 1.0%. The normalised maximum efficiency point is also plotted from the test data giving an indication of where the BEP lies.

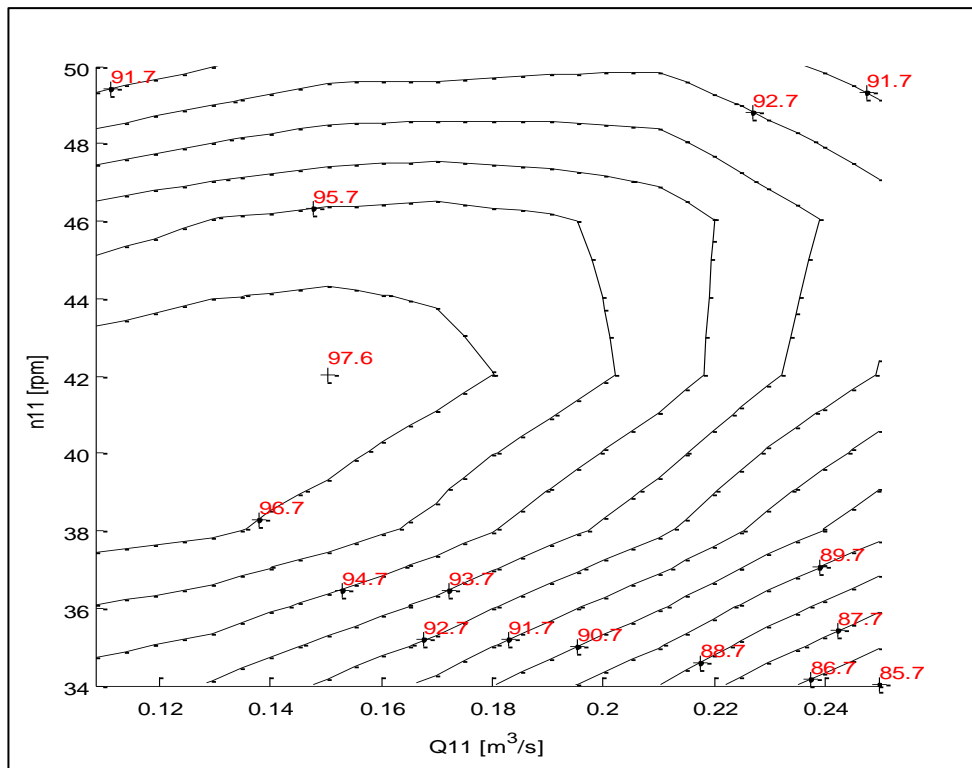


Fig. 7.8. 9" HCTI runner, single jet operation

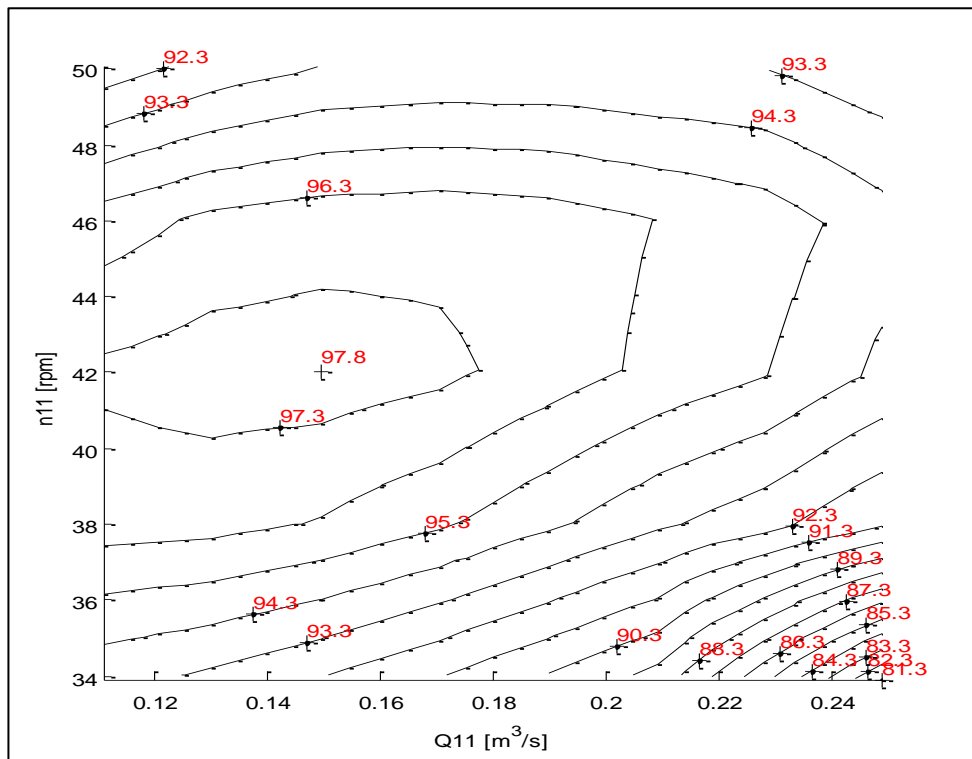


Fig. 7.9. 9" HCTI runner, twin jet operation

7.8 LE4 runner test results

The LE4 runner experimental test results for lower jet, and twin jet operation are plotted in the hill charts shown in Fig. 7.10 and Fig. 7.11 respectively.

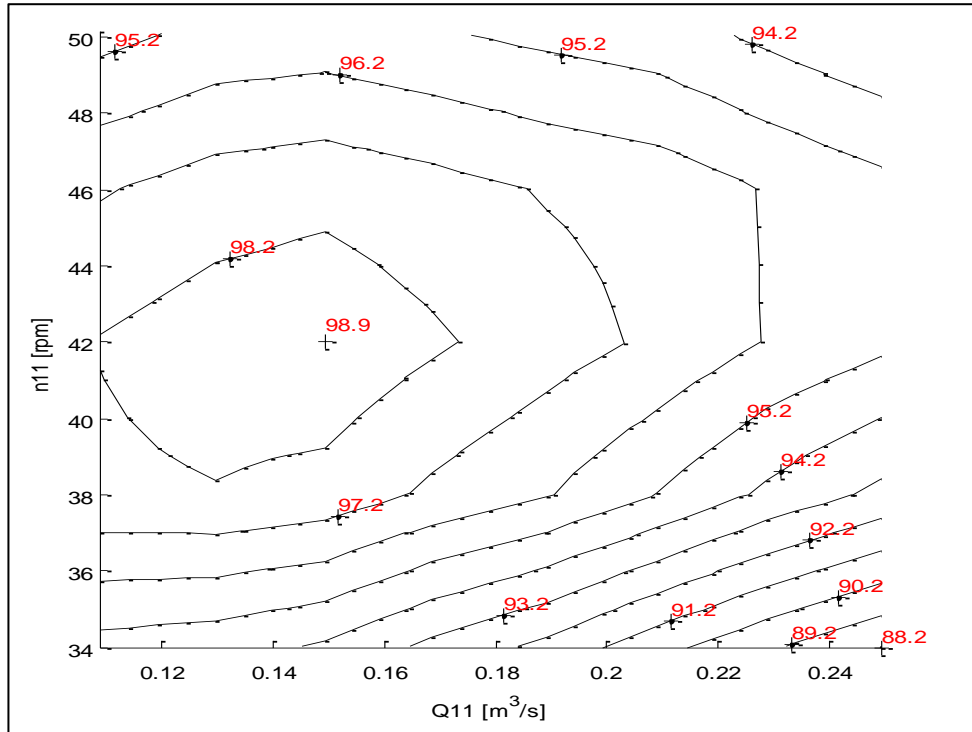


Fig. 7.10. 9" LE4 runner, single jet operation

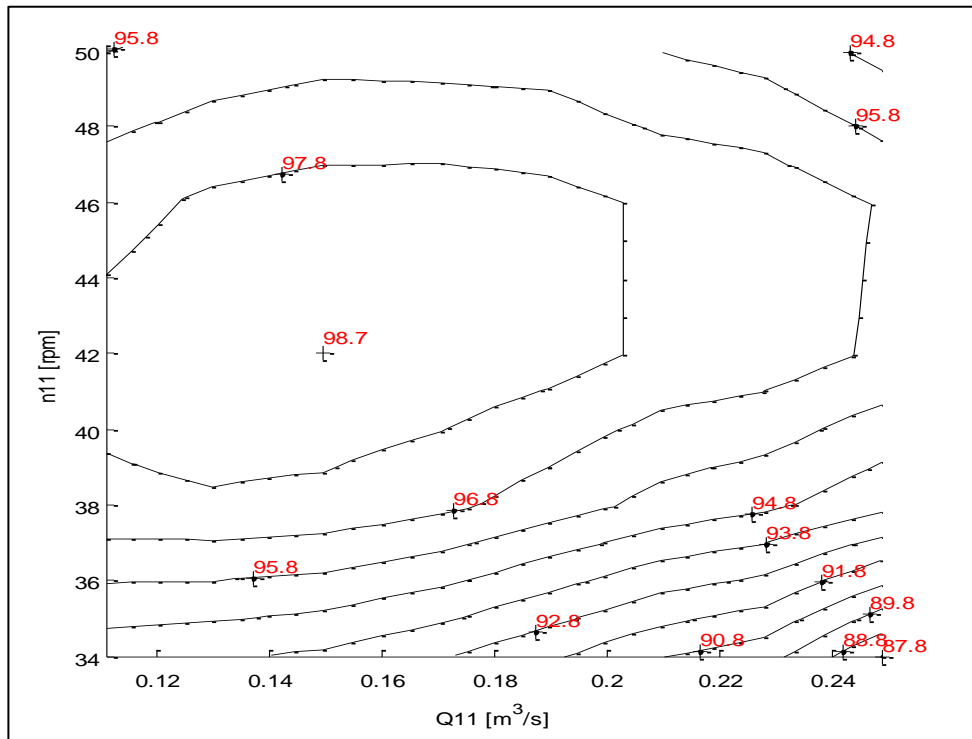


Fig. 7.11. 9" LE4 runner, twin jet operation

7.9 LE1 runner test results

The LE1 runner experimental test results for lower jet and twin jet operation are plotted in the hill charts shown in Fig. 7.12 to Fig. 7.13 respectively.

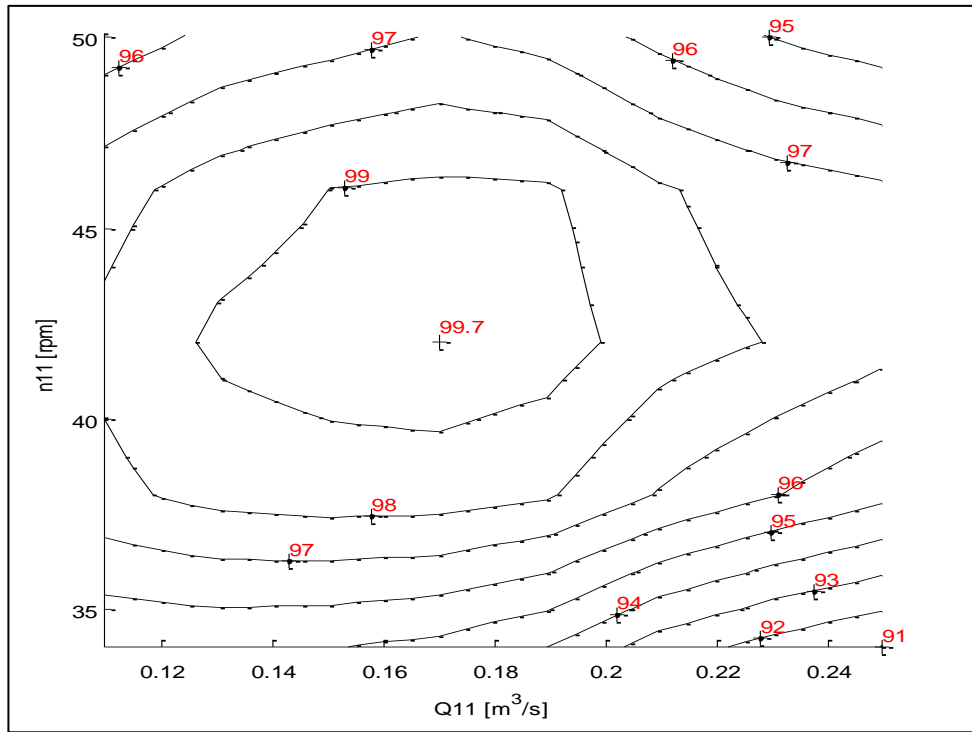


Fig. 7.12. 9" LE1 runner, single jet operation

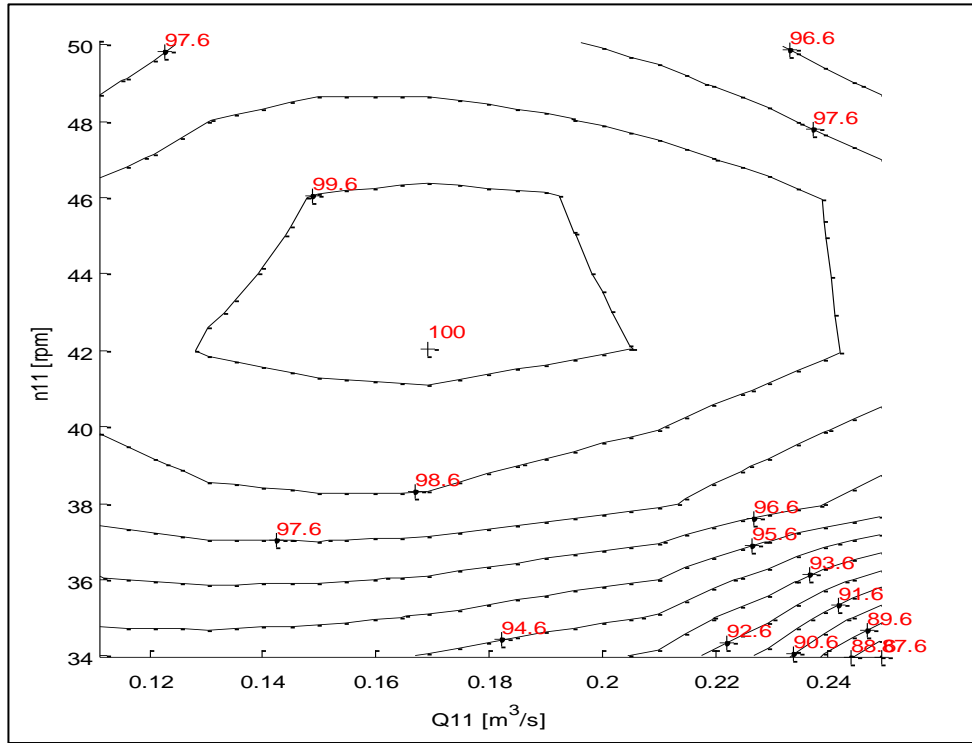


Fig. 7.13. 9" LE1 runner, twin jet operation

7.10 Results comparison and discussion

The experimental results of the three Turgo runner tests (HCTI, LE4 and LE1) are compared and discussed in this chapter looking at the effectiveness of the optimisations carried out.

The hill charts (Fig. 7.8 to Fig. 7.13) show very similar normalised peak efficiencies for single and twin jet operation for all three designs, with less than 0.3% difference; however the twin jet results show a much flatter peak, with the efficiencies staying higher than single jet operation as the flow rate increases. This will be partially due to the radial loading on the bearings being cancelled out by the opposing jet directions. For single jet operation, as the flow rate increases the axial and radial load on the bearings increases proportionally, causing an increase in mechanical losses. For twin jet operation, only the axial loading increases as the radial loading is cancelled out which could explain the flatter performance curve.

It is interesting to note that the peak efficiency point for the HCTI and the LE4 designs occurs at a lower flow rate ($Q_{11} \sim 0.15 \text{ m}^3/\text{s}$) than the design BEP ($Q_{11}=0.177 \text{ m}^3/\text{s}$ and $n_{11}=43 \text{ rpm}$). The LE1 design peak efficiency occurs at a higher flow rate ($Q_{11} \sim 0.17 \text{ m}^3/\text{s}$), closer to the design BEP which suggests that having a thicker leading edge obstructs the flow through the runner, causing a choking effect which not only reduces the total efficiency but shifts the peak efficiency point towards lower flow rates.

The LE4 runner hill charts (Fig. 7.10 and Fig. 7.11) show that there is a significant improvement in the performance of the LE4 design compared to the HCTI design for single and twin jet operation, with the differences being more pronounced at higher speeds and flow rates. The peak efficiencies are around 1% higher overall, with much flatter curves indicated by the wider spacing between the contour lines. The LE1 runner hill charts (Fig. 7.12 and Fig. 7.13) show even flatter shaped contours than the LE4 runner, with much wider spacing between the contour lines indicating that there is a much smaller drop in efficiency as the flow rate and speed deviates from the BEP. The peak efficiencies are also around 1% higher than the LE4 runner and 2% higher than the HCTI runner on average.

The difference between the three designs as the flow rate increases is made clearer by plotting the normalised efficiency against Q_{11} for a fixed speed of $n_{11}=42 \text{ rpm}$ which is closest to the nominal speed of $n_{11}=43 \text{ rpm}$. These curves provide a good comparison between the designs and show that for single jet operation, (Fig. 7.14) the efficiency of the LE4 runner is around 1% greater than the HCTI runner at lower flow rates ($Q_{11}=0.11-0.15$) and increases to over 2% at maximum flow ($Q_{11}=0.25$). The LE1 runner showed significant improvements in efficiency in comparison to the original (HCTI) design, ranging from around 1.5% at lower flow rates to over 4% at higher flows for single jet operation ($Q_{11}=0.25$).

The same trend is seen for twin jet operation (Fig. 7.15) however the overall efficiencies are around 0.2% higher than single jet operation at the BEP flow rate ($Q_{11}=0.177\text{m}^3/\text{s}$) for all three designs. The efficiency curves are also much flatter, showing around a 1% increase in efficiency at the maximum flow $Q_{11}=0.25\text{m}^3/\text{s}$ between single and twin jet operation.

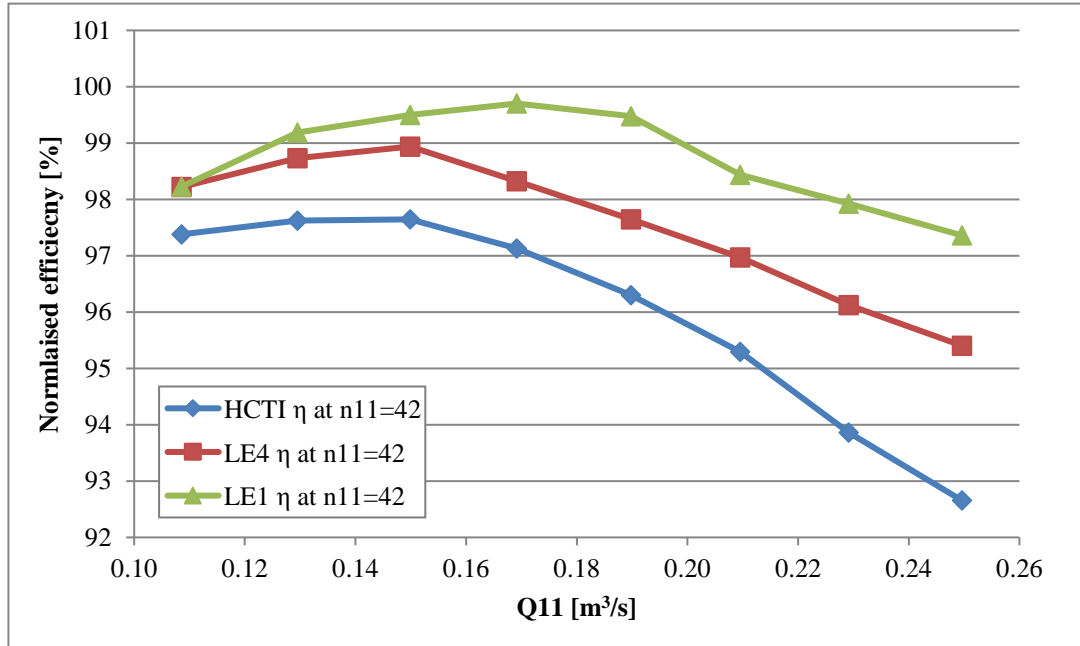


Fig. 7.14. 9" HCTI, LE4 and LE1 runner normalised efficiency comparison for $n_{11}=42$ - single jet

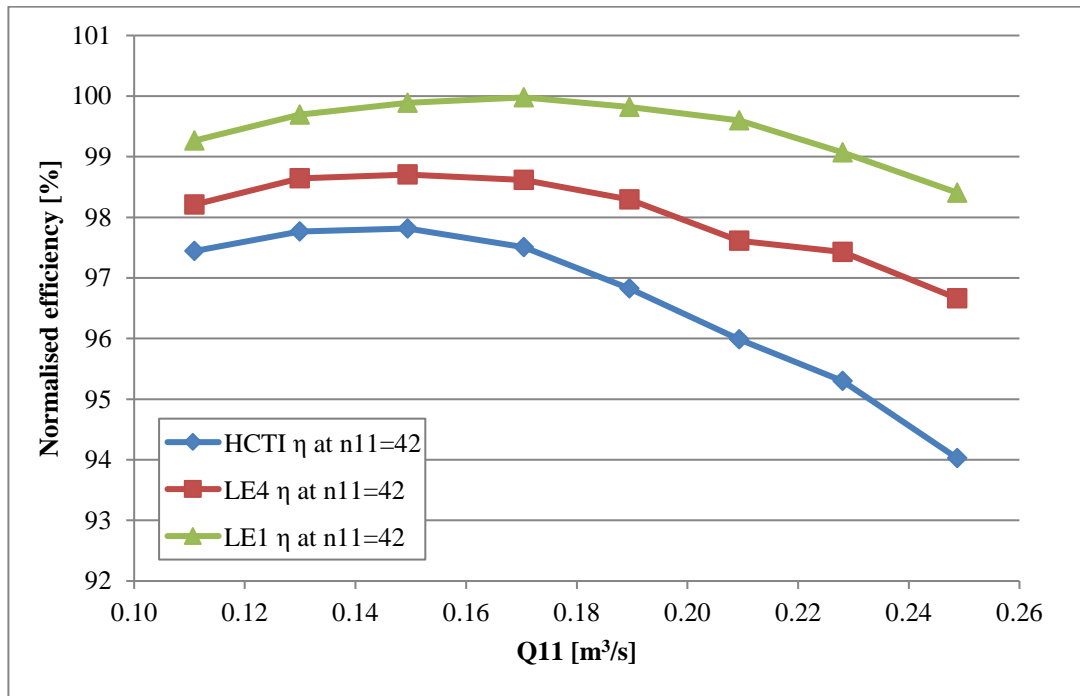


Fig. 7.15. 9" HCTI, LE4 and LE1 runner normalised efficiency comparison for $n_{11}=42$ - twin jet

8 Injector experimental testing

This chapter presents the experimental testing of the injectors based on the optimisations carried out in chapter 6- *Injector design optimisation and further analysis*. The injector designs tested were the Standard (80/55) design, with nozzle and spear angles of 80° and 55° and the Novel (110/70) design with nozzle and spear angles of 110° and 70°.

These two injector designs were manufactured for testing on both the Pelton test rig and the Turgo test rig at the Laboratory for Hydraulic Machines, National Technical University of Athens (NTUA). The testing procedure and results for the Pelton injector tests are presented in 8.1- *Pelton injector testing* followed by the Turgo injector tests in 8.2- *Turgo injector testing*.

8.1 Pelton injector testing

Two injector designs were manufactured by Gilbert Gilkes & Gordon Ltd for experimental testing using the Pelton test rig at the Laboratory for Hydraulic Machines, National Technical University of Athens (NTUA). The injector designs tested were the Standard (80/55) design, with nozzle and spear angles of 80° and 55° and the Novel (110/70) design with nozzle and spear angles of 110° and 70° based on the scaled HCTI-d65mod-scaled design. The nozzles and spears used in these tests are shown in Fig. 8.1 and Fig. 8.2.

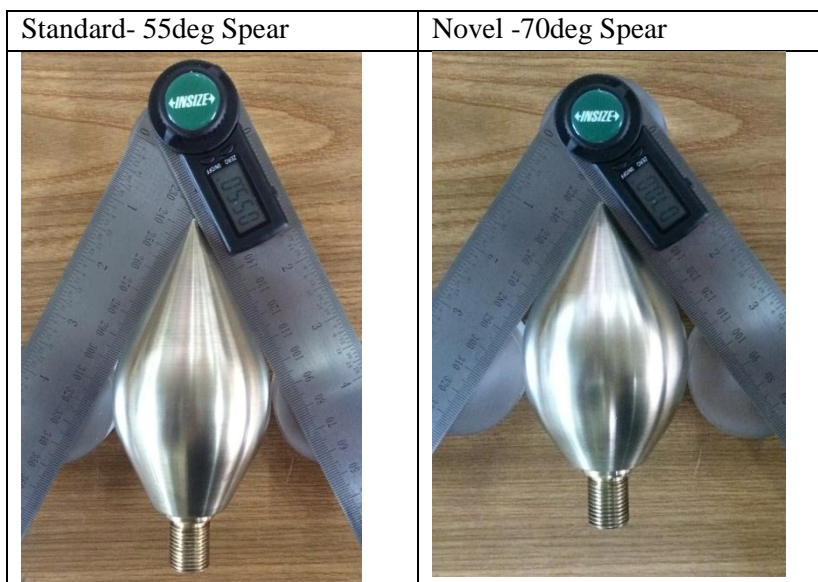


Fig. 8.1. Pelton spears used for experimental tests

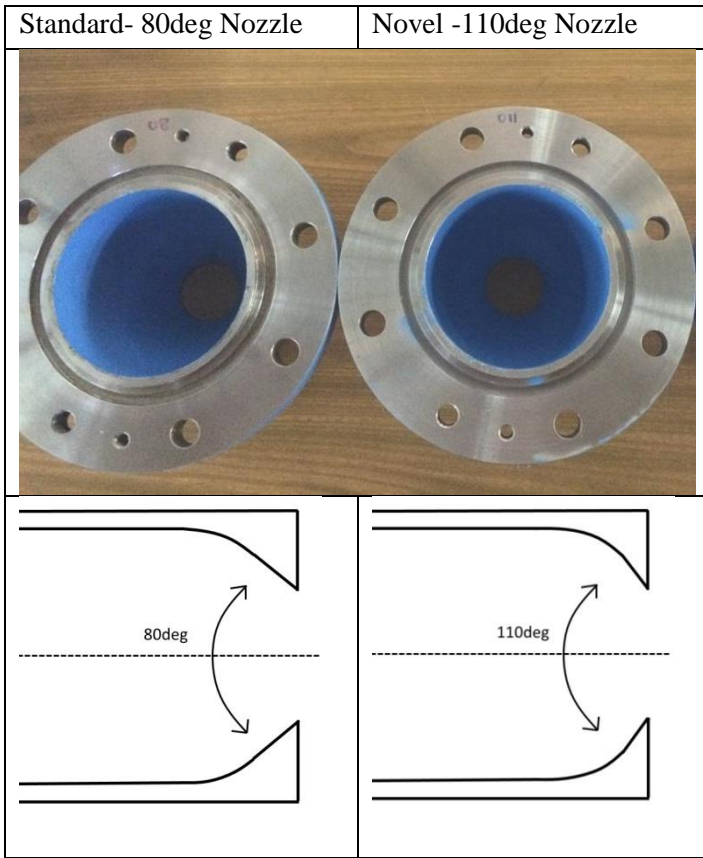


Fig. 8.2. Pelton nozzles used for experimental testing

8.1.1 Pelton test rig

The first injector tests were carried out using the Pelton test rig at the Laboratory for Hydraulic Turbomachinery, NTUA. The tests were carried out using the Gilkes Z120 Pelton runner.

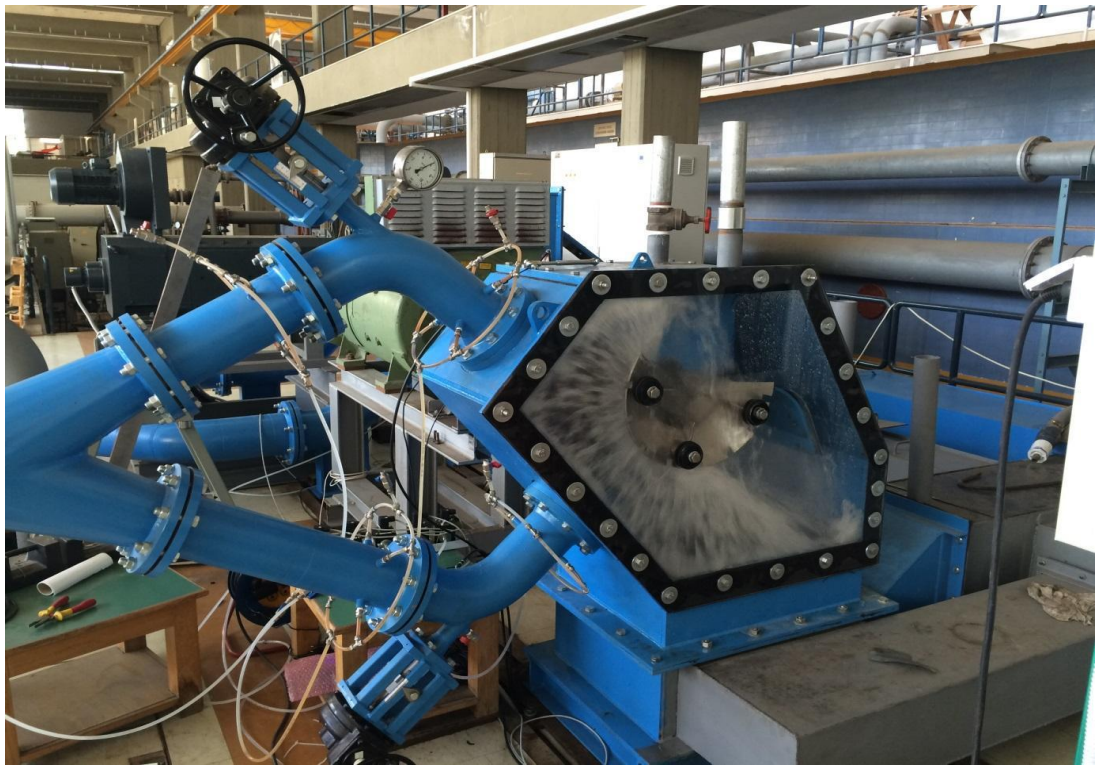


Fig. 8.3. Gilkes twin jet Pelton test rig in operation at NTUA

Testing and calibration of all the sensors was carried out according to testing standard *IEC 60193 Hydraulic turbines, storage pumps and pump-turbines – Model acceptance tests* (IEC 60193:1999).

The testing was carried out in single jet operation using the upper jet where the least interference of the flow leaving the runner and the oncoming jet takes place and the efficiencies are the highest.

The characteristic equations used to define the operation and performance of the turbine, are the same at those used in the Turgo runner tests, given in equations (7.1) to (7.5). However as the ratio of the runner diameter to the width of Pelton machines can vary significantly from one machine to another, the unit flow rate, Q_{11k} , is calculated using the bucket width, B , given in equation (8.1) below. The pitch circle diameter, D , of the Pelton runner used in this testing was 320mm and the bucket width, B , was 120mm.

$$Q_{11k} = \frac{Q/N_j}{B^2 \times \sqrt{H}} \quad (8.1)$$

The systematic uncertainty for each instrument used during this testing is given in Table 8.1, below. The total systematic uncertainty in the efficiency, η , was calculated as $\pm 1.01\%$.

Instrument	Systematic Uncertainty δ
Pressure Transducer (H)	$\pm 0.1\%$
Flow meter (Q)	$\pm 1.0\%$
Torque meter (M)	$\pm 0.1\%$
Speed Sensor (n)	$\pm 0.05\%$

Table 8.1- Systematic error of each instrument

As the purpose of these experimental tests is to compare the two injector designs, the systematic uncertainty can be cancelled out and it is the random uncertainty which determines the error bars. The random uncertainty in the efficiency, η , was calculated as $\pm 0.2\%$ at the 95% confidence interval.

8.1.2 Injector test plan

The injector test plan can be seen in Fig. 8.4 below, showing the range of n_{11} and Q_{11k} values which were tested. A total of 32 test points were measured excluding the control points. For each Q_{11k} value, the head and flow rate is set by adjusting the spear travel and the speed of the pump. The rotational speed is then varied by adjusting the speed of the brake and n_{11} values are measured for each Q_{11k} value. This is the approach suggested in the IEC60193 standards. For each test point, 180 readings are taken from the pressure, torque, flow and speed sensors over a period of 90 seconds. From these voltage readings, the pressure, flow rate, speed and torque can be calculated using the calibration curves for each instrument and used to determine the efficiency.

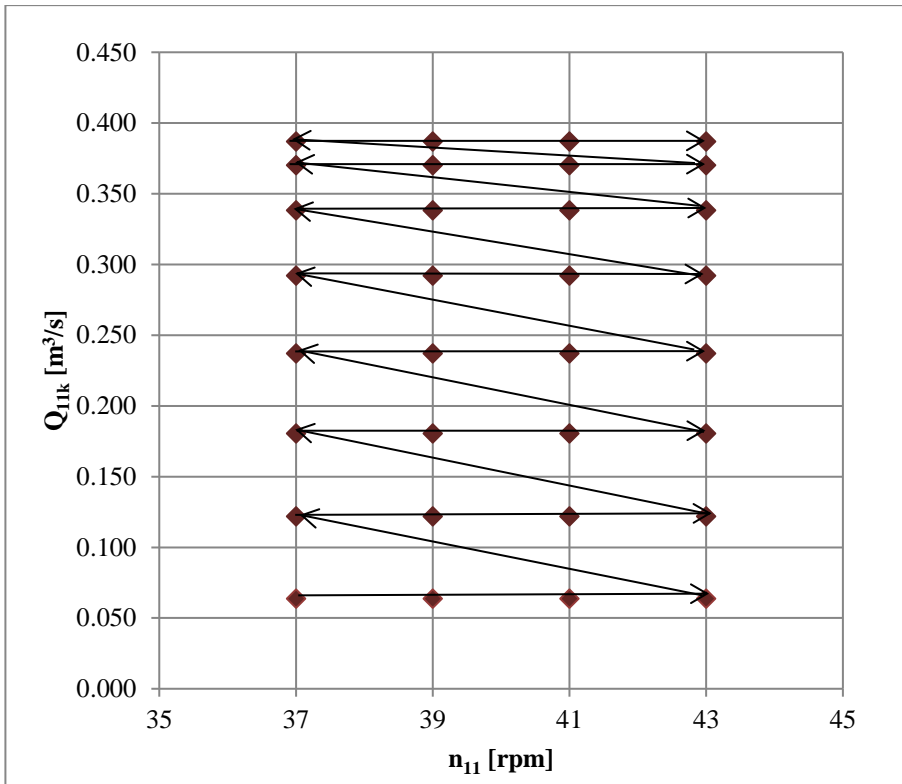


Fig. 8.4. Pelton injector test plan

8.1.3 Flow curve comparison

As the increase in the nozzle and spear angles reduces the maximum flow rate the injector can accommodate slightly, the Novel (110/70) injector was scaled up in order to match the maximum flow rate of the Standard (80/55) injector. The scaling used can be seen in Table 8.2, below.

Injector design	Nozzle Angle	Spear Angle	Nozzle Diameter
	[deg]	[deg]	[mm]
Standard (80/55)	80	55	46.9
Novel (110/70)	110	70	48.9

Table 8.2- Pelton injectors- geometric details

The flow rate for each test point is plotted against the spear travel over the nozzle diameter (s/D_s) for each injector as shown in Fig. 8.5. The results show that although the maximum flow rates are within 1.6% of one another and the slight discrepancy is likely to be due to the accuracy of the spear positioning being limited to 0.25mm.

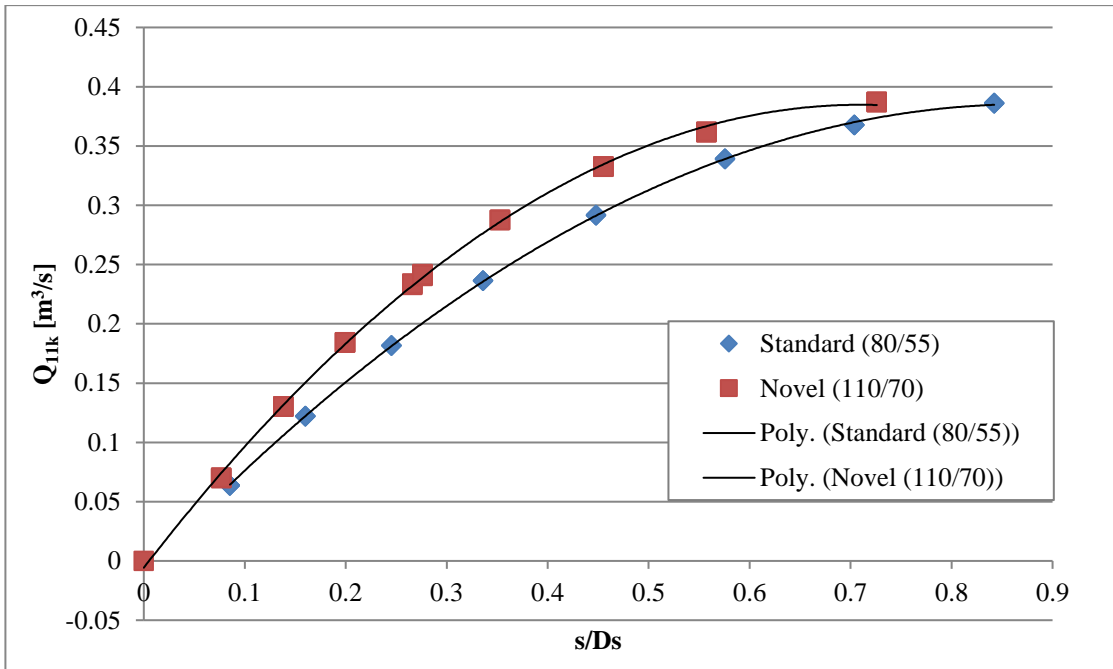


Fig. 8.5. Pelton injector flow curves comparison

8.1.4 Results comparison and discussion

The normalised efficiency curves for the upper jet are plotted against the Q_{11k} for each unit speed n_{11} in Fig. 8.6 to Fig. 8.9. The efficiencies are normalised against the best efficiency test point.

The results show that at all speeds, the steeper angled Novel design performs better than the Standard (80/55) design, with the differences being more pronounced at lower flow rates where the losses through the injectors are greater. The Novel design shows quite a substantial increase in efficiency compared to the original 80-55 design, with a 1% increase at the BEP flow $Q_{11k}=0.234$ and speed $n_{11}=39$.

To summarise, the results show that the Novel (110/70) injector performs better than the Standard (80/55) injector across the range of flows except at the maximum flow ($Q_{11k}=0.388$) where the Standard (80/55) design performs slightly better. However the difference between the designs is very small here as the spear is in the fully open position where the geometry of the injector has the least impact on the performance. The very large difference between the Novel and the Standard (80/55) injectors, shown at the lowest flow rate ($Q_{11k}=0.07$) is not a true indication of the differences here as the flow rate is slightly lower for the 80-55 injector in this portion of the curve where the efficiency drops rapidly with a small decrease in flow rate. However for the rest of the test points, the flow rates are much closer for each injector and the curves much flatter, making the points more comparable.

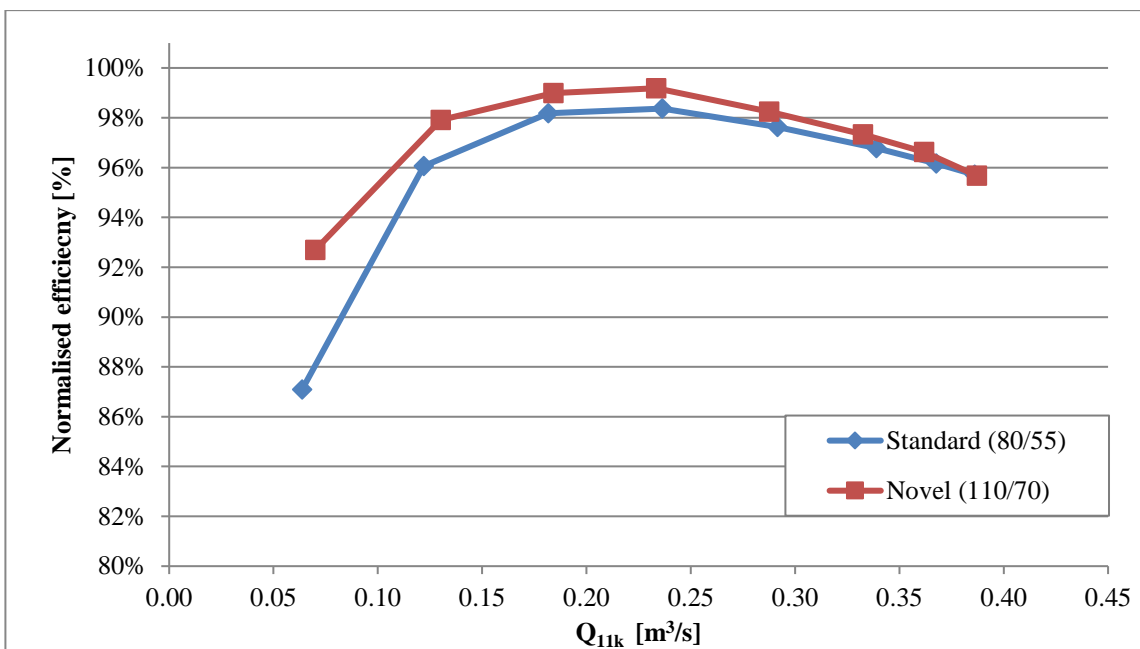


Fig. 8.6. Pelton normalised efficiency curves for Standard (80/55) and Novel (110/70) injectors at $n_{11}=37\text{rpm}$

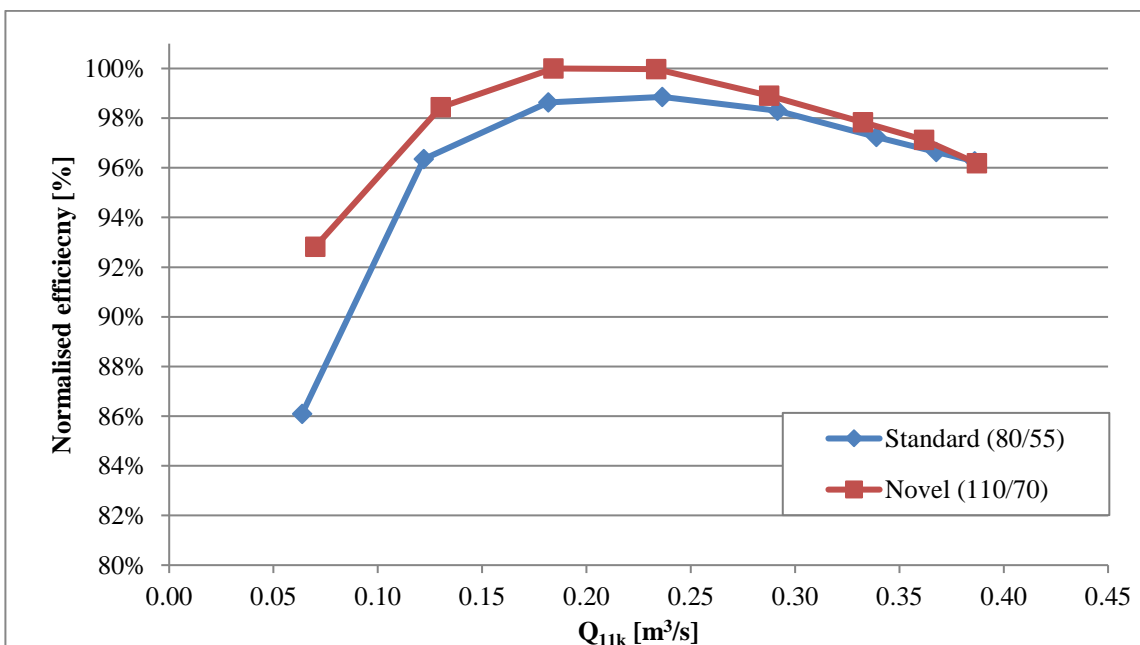


Fig. 8.7. Pelton normalised efficiency curves for Standard (80/55) and Novel (110/70) injectors at $n_{11}=39\text{rpm}$

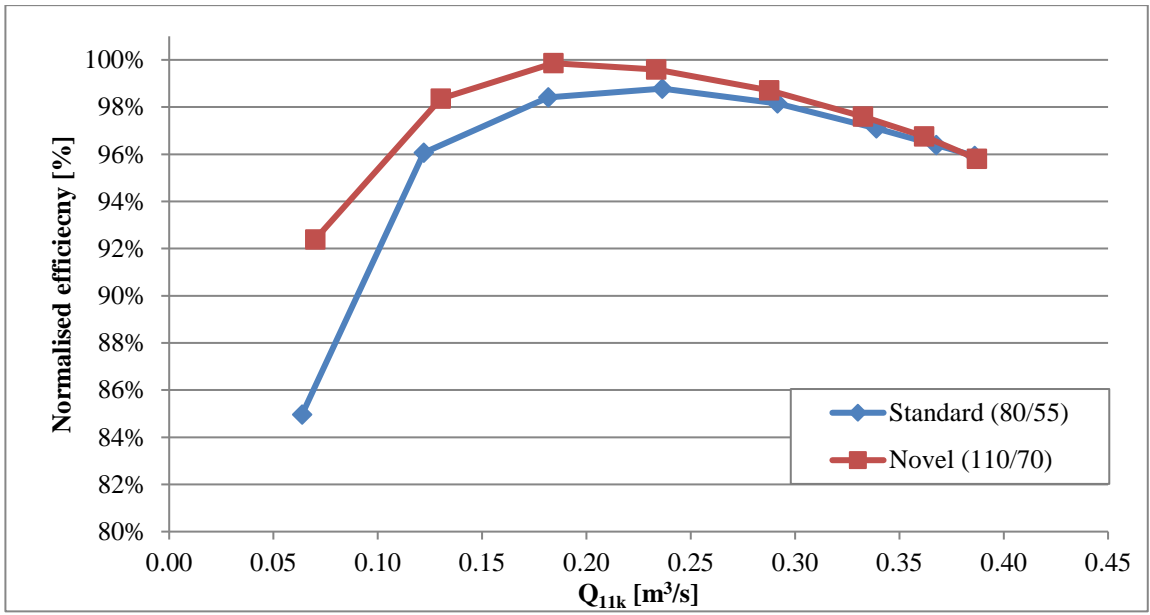


Fig. 8.8. Pelton normalised efficiency curves for Standard (80/55) and Novel (110/70) injectors at $n_{11}=41\text{rpm}$

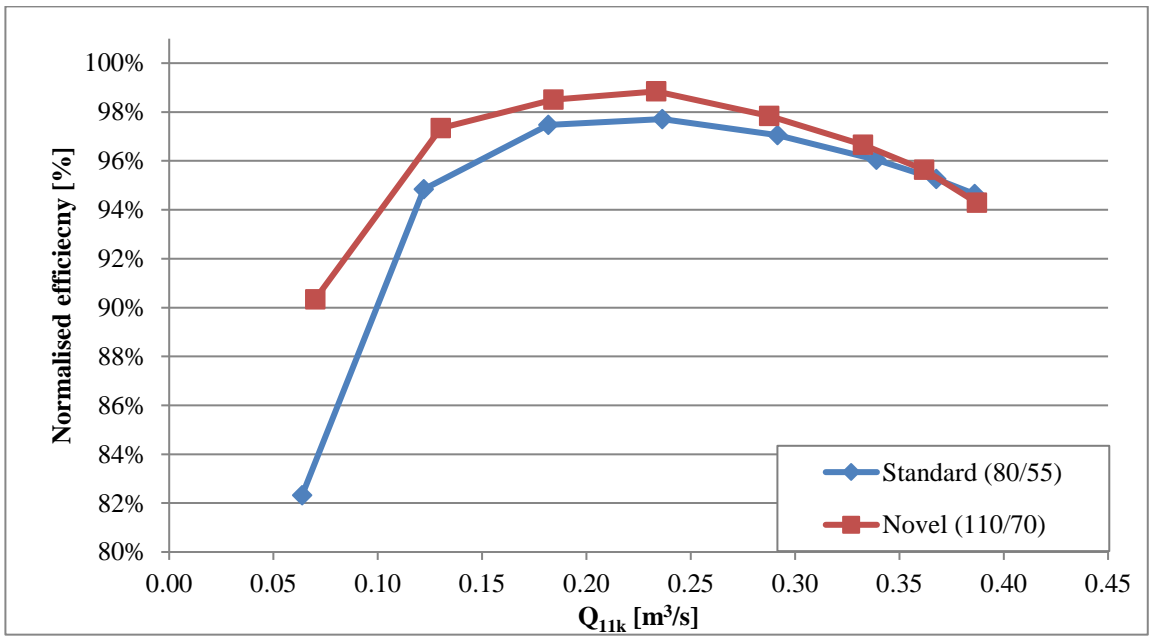


Fig. 8.9. Pelton normalised efficiency curves for Standard (80/55) and Novel (110/70) injectors at $n_{11}=43\text{rpm}$

Overall the results show much greater improvements in the performance of the Novel (110/70) injector experimentally than in the numerical analysis. This is likely to be a result of the impact of the quality of the jet on the Pelton runner performance which is beyond the scope of this research. This is however looked at in the Turgo case, in *9.3.1- Full injector and runner simulations*, which gives some indication of how the injector affects the whole turbine system performance numerically.

8.2 Turgo injector testing

Following on from the previous injector CFD analysis in *6- Injector design optimisation and further analysis* and the testing of the Pelton injectors in *8.1- Pelton injector testing*, two similar ,Standard (80/55) and Novel (110/70), Turgo injector designs with larger diameters were manufactured for testing at the Laboratory for Hydraulic Machines, National Technical University of Athens. The tests were carried out using the optimised, dressed 9" LE1 Turgo runner design with the 13.5" Turgo casing.

As the increase in the nozzle and spear angles reduces the maximum flow rate the injector can accommodate (as with the Pelton injectors), the Novel (110/70) injector was scaled up in order to match the maximum flow rate of the Standard (80/55) injector. The scaling used can be seen in Table 8.3, below.

Injector design	Nozzle Angle	Spear Angle	Nozzle Diameter
	[deg]	[deg]	[mm]
Standard (80/55)	80	55	84.68
Novel (110/70)	110	70	81.25

Table 8.3-Turgo injector main dimensions

8.2.1 Injector test plan

The Turgo injector test plan was modified from the previous test plan in order to investigate the performance of the injectors at lower flow rates than previously studied with the Turgo rig ($Q_{11}=0.03\text{m}^3/\text{s}$, $0.05\text{m}^3/\text{s}$ and $0.07\text{m}^3/\text{s}$) as shown in the test plan (Fig. 8.10). Two control points were also measured at the start, middle and end of each test. The control points were taken at the BEP (single jet $Q_{11}=0.177\text{m}^3/\text{s}$ and $n_{11}=43\text{rpm}$).

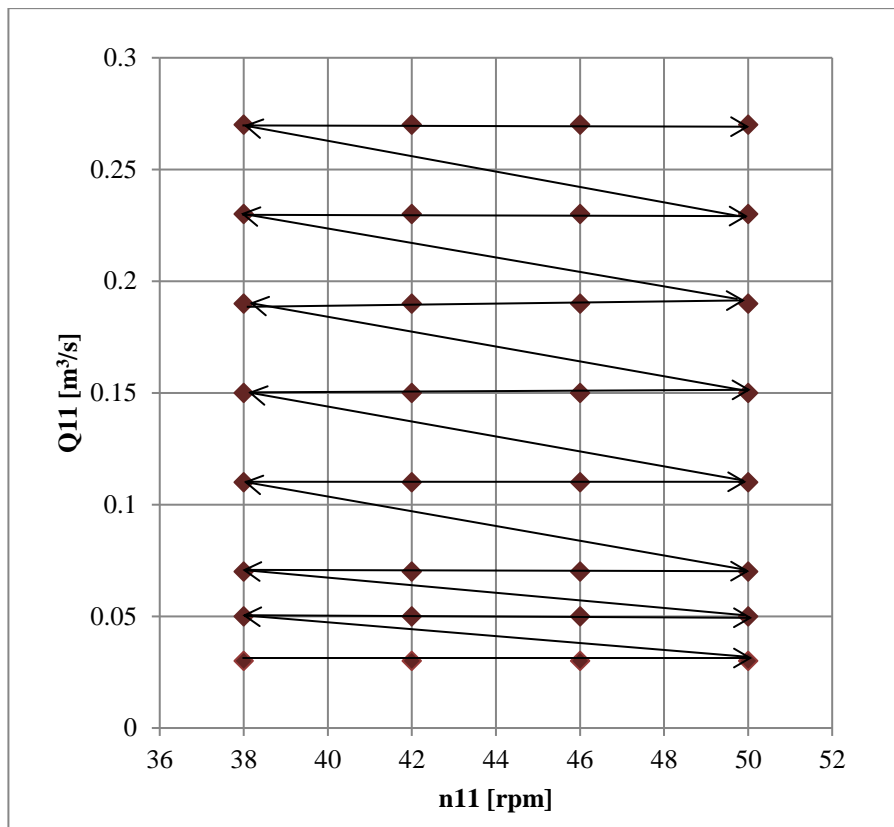


Fig. 8.10. Turgo injector test plan

8.2.2 Flow curve comparison

The unit flow rate Q_{11} is plotted against the spear travel/Standard (80/55) injector diameter (s/D_s) for each injector during single jet operation in Fig. 8.11. As the maximum spear travel is restricted by the worm gear to around 43.5mm it was not possible to test the injectors up to the fully open position so instead they were tested to a maximum flow rate of 99.71/s.

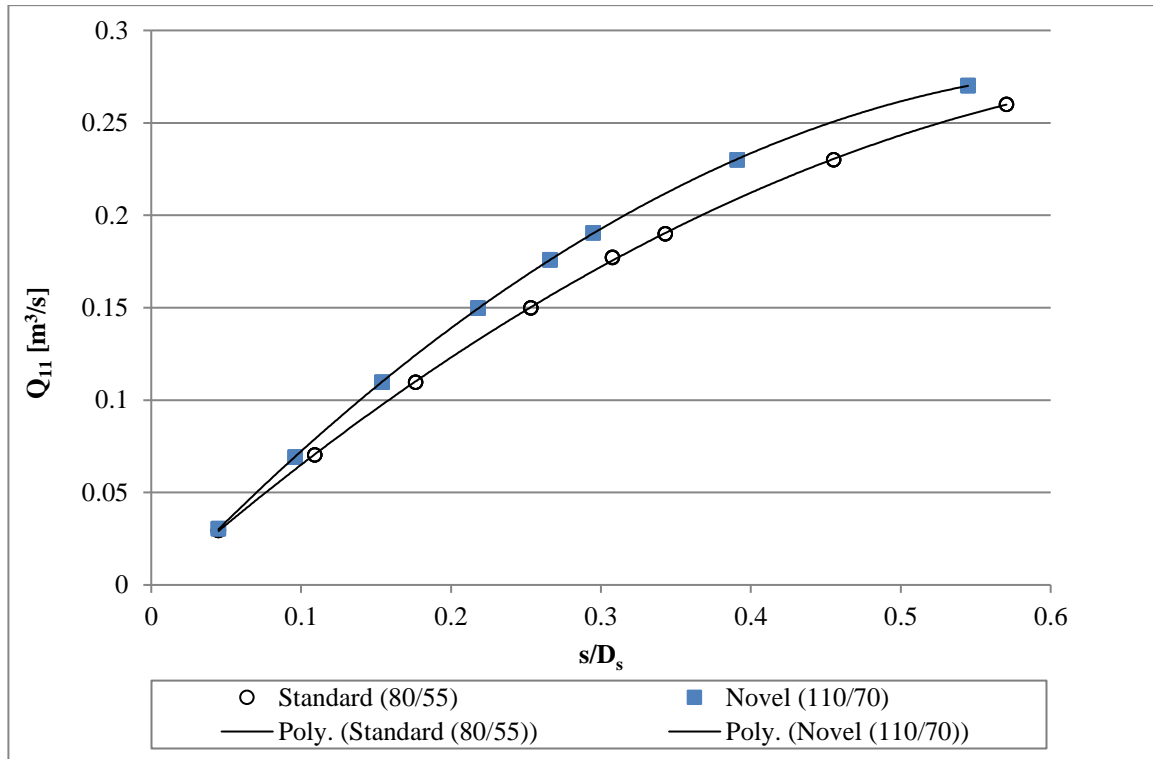


Fig. 8.11. Flow curve comparison for the Standard (80/55) and Novel (110/70) injectors

8.2.3 Results comparison and discussion

For each single jet flow rate at $n_{11}=42$ rpm (which is the closest test speed to the nominal n_{11} of 43 rpm) the jet was photographed in order to investigate the impact of the nozzle and spear angles on the jet quality. The two lowest flow rates ($Q_{11}=0.03-0.07$ m^3/s), where the disturbances on the outside of the jet and the jet dispersion are greatest, are shown in Fig. 8.12. The higher flow rates ($Q_{11}=0.11-0.25$ m^3/s), where there are less disturbances in the jet, are shown in Fig. 8.13. What is interesting from these images is that for the steeper angled Novel (110/70) design the jet dispersion (beyond the vena Contracta) is more pronounced, particularly at the lowest flow rate (Fig. 8.12).

The higher jet dispersion seen for the Novel designs at low flow rates is likely due to the steeper nozzle angles that cause a more sudden change in direction of the water at the nozzle exit. Moreover, the spear travel from closed position for a particular low flow rate becomes smaller for steeper angles, and this may give rise to non-symmetric effects of possible very small imperfections or tolerances in the spear valve injector manufacture.

As the spear opening is increased, the jets of the two injectors become more similar, although the disturbances on the outside of the steeper angled design are slightly more pronounced (Fig. 8.13).

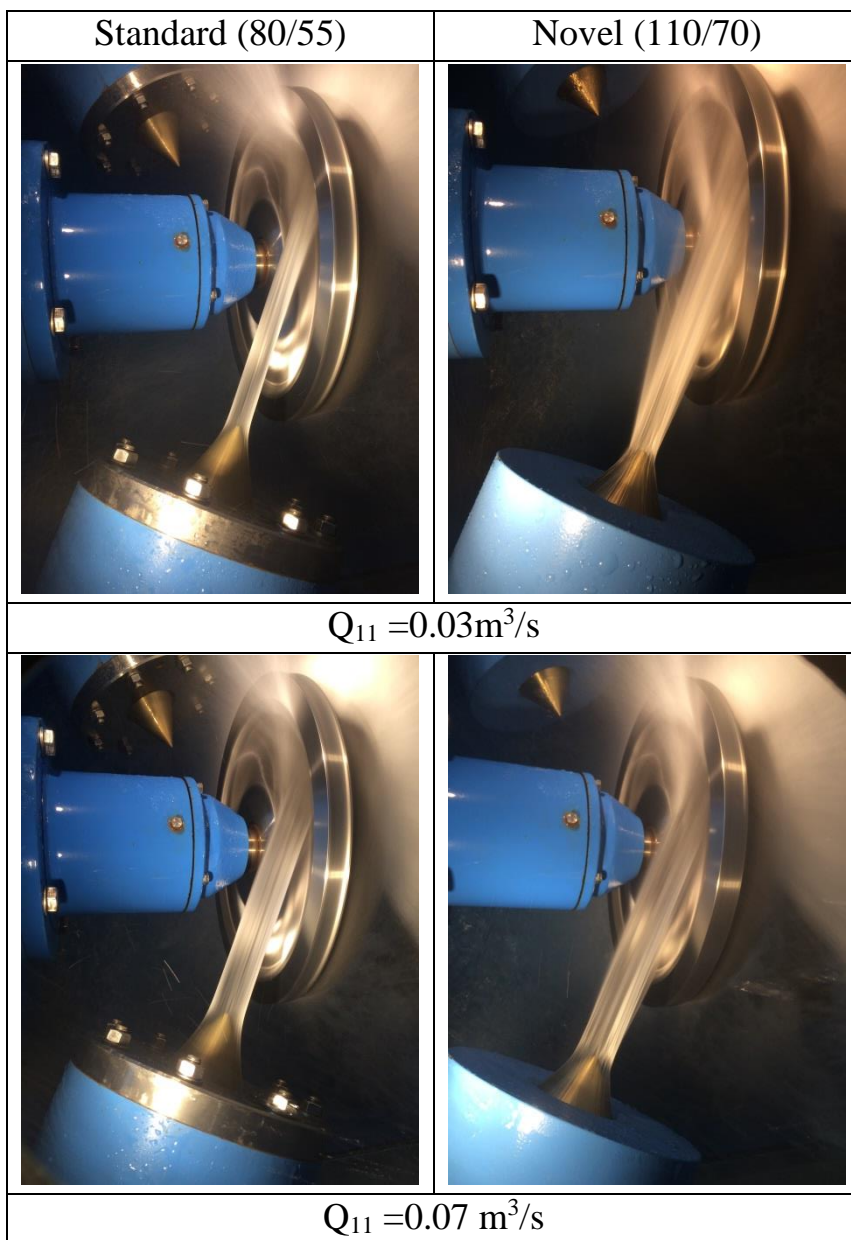


Fig. 8.12. Single jet operation for $Q_{11}=0.03-0.07\text{m}^3/\text{s}$ at $n_{11}=42\text{rpm}$

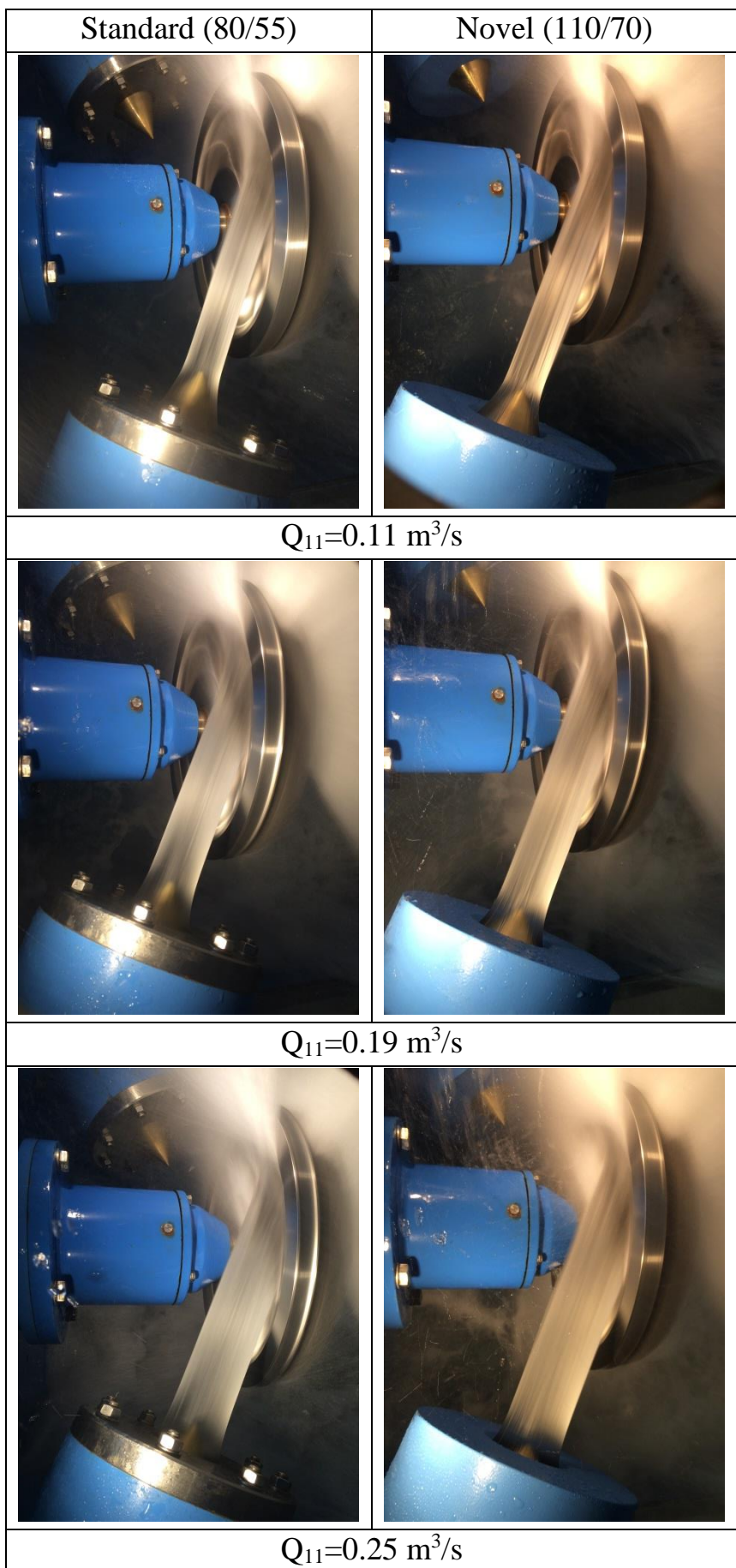


Fig. 8.13. Single jet operation for $Q_{11}=0.11-0.25\text{m}^3/\text{s}$ at $n_{11}=42 \text{ rpm}$

The efficiencies are normalised against the twin jet BEP of the LE1 runner with the Standard (80/55) injectors. For the lowest flow rate ($Q_{11} = 0.03 \text{ m}^3/\text{s}$ or $\sim 10\%$ of the maximum flow rate), the normalised efficiencies were very low (below 85%) as shown in Fig. 8.14 and Fig. 8.15. For this very low flow rate, the Novel (110/70) injector shows slightly lower efficiencies than the Standard (80/55) injector for single jet operation. This is likely to be a result of the Standard (80/55) injector producing a more stable jet at these very low flows as shown in Fig. 8.12. For twin jet operation the differences between the Novel (110/70) and the Standard (80/55) injectors are very similar however the overall efficiencies are around 3% higher compared to single jet operation. This is likely to be a result of the radial forces acting on the bearings being cancelled out during twin jet operation, reducing the mechanical losses.

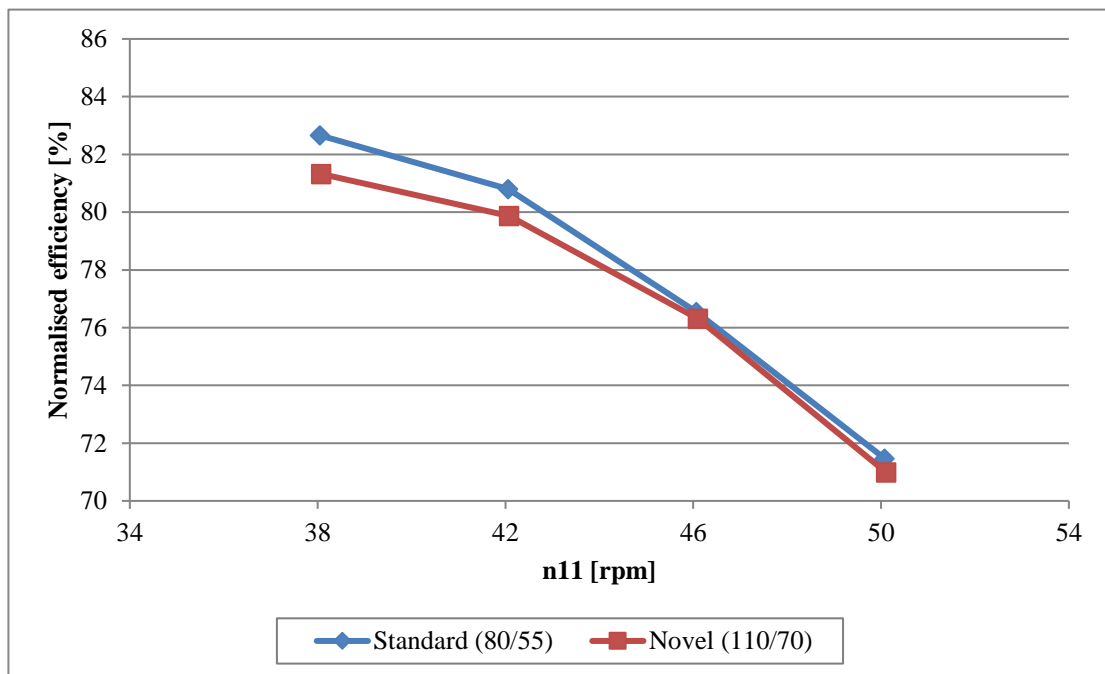


Fig. 8.14. Single jet operation at $Q_{11}=0.03\text{m}^3/\text{s}$

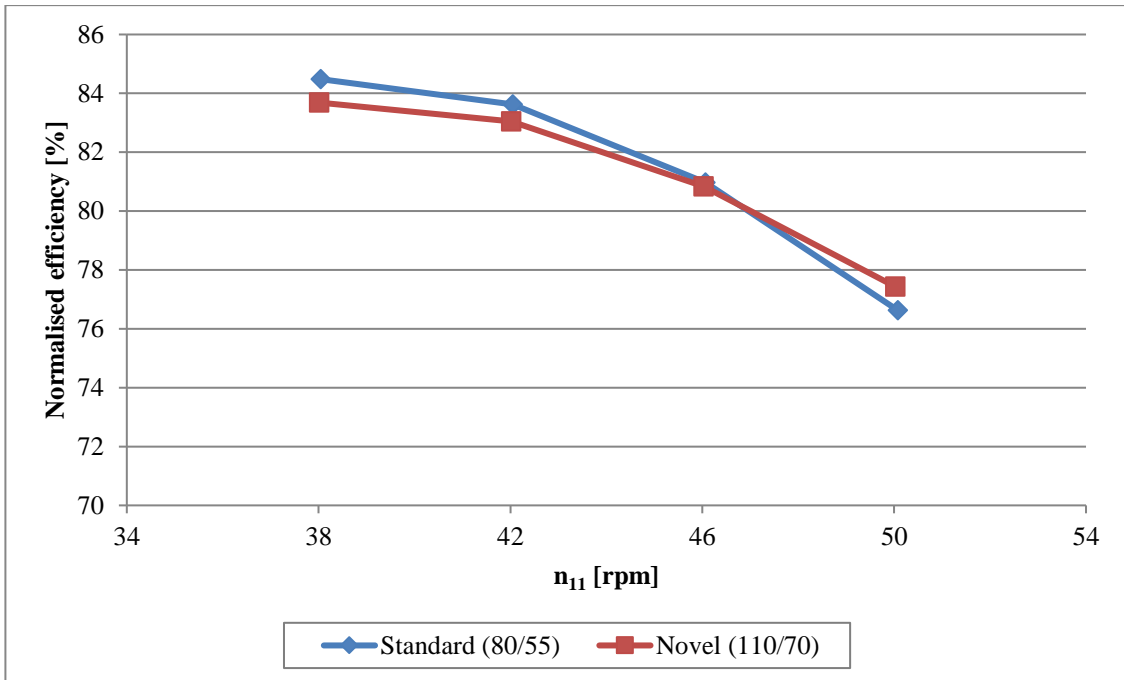


Fig. 8.15. Twin jet operation at $Q_{11}=0.03\text{m}^3/\text{s}$

The attainable efficiencies become quite high in the entire loading range of the turbine above that lowest flow rate, namely for $Q_{11}=0.07-0.27 \text{ m}^3/\text{s}$, as can be seen in Fig. 8.16 and Fig. 8.17. Although the images in Fig. 8.13 give the impression that the Standard (80/55) design produces a cleaner looking jet overall, the turbine efficiency with the steeper angled designs are overall higher up to about $Q_{11}=0.2 \text{ m}^3/\text{s}$.

The results show the Novel (110/70) injector performs best overall, which is consistent with the numerical results obtained in *6-Injector design optimisation and further analysis* as well as the Pelton injector results in *8.1- Pelton injector testing*. The normalised turbine efficiency with this injector is of the order of 0.2-0.8% higher than Standard (80/55) design, for both single and twin jet operation (Fig. 8.16 and Fig. 8.17, respectively). The slight dip in the efficiency curve for the Novel (110/70) injector during single jet operation (Fig. 8.16) at $Q_{11}=0.15\text{m}^3/\text{s}$ is likely to be an anomaly as the average of the 12 control points (BEP single jet $Q_{11}=0.177\text{m}^3/\text{s}$ and $n_{11}=43\text{rpm}$) measured across each injector test show the Novel (110/70) design giving an increase in normalised efficiency of 0.80% over the Standard (80/55) injector.

Overall it appears that the steeper angled Novel (110/70) design creates more disturbances on the outside of the jet (particularly at very low flow rates) but gives higher overall efficiencies at flows above $Q_{11}=0.03\text{m}^3/\text{s}$. This could explain why historically shallower angled injectors have been used, producing a cleaner looking jet which, although it looks better, is less efficient across most flow rates.

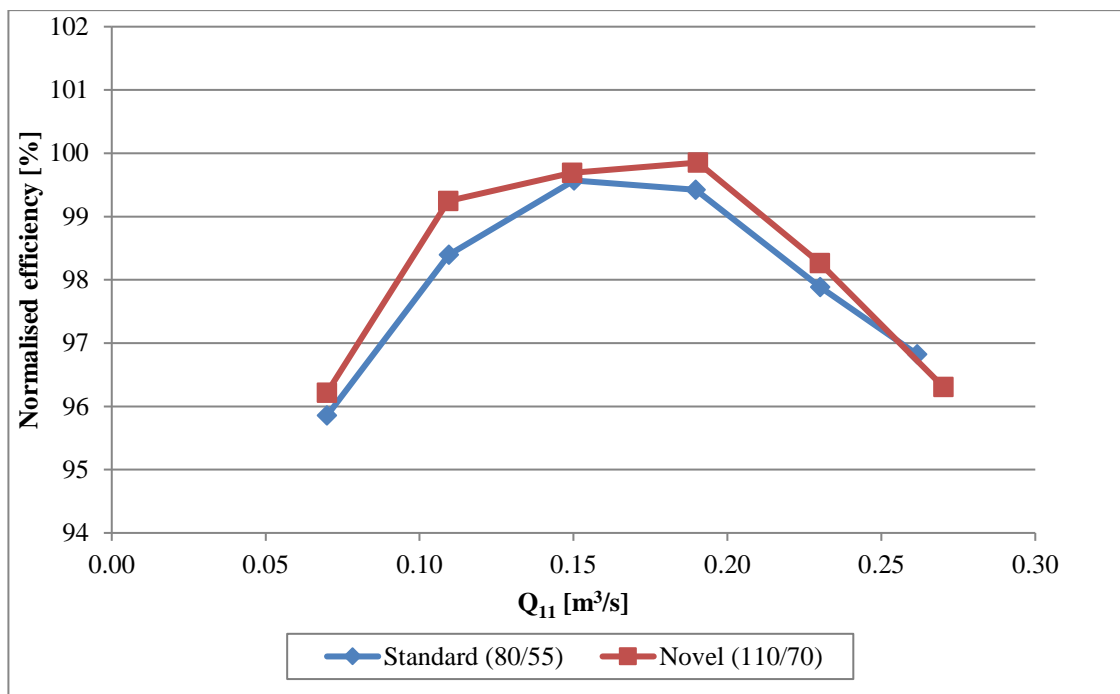


Fig. 8.16. Turgo injector efficiency comparison at $n_{11}=42\text{rpm}$ - single jet

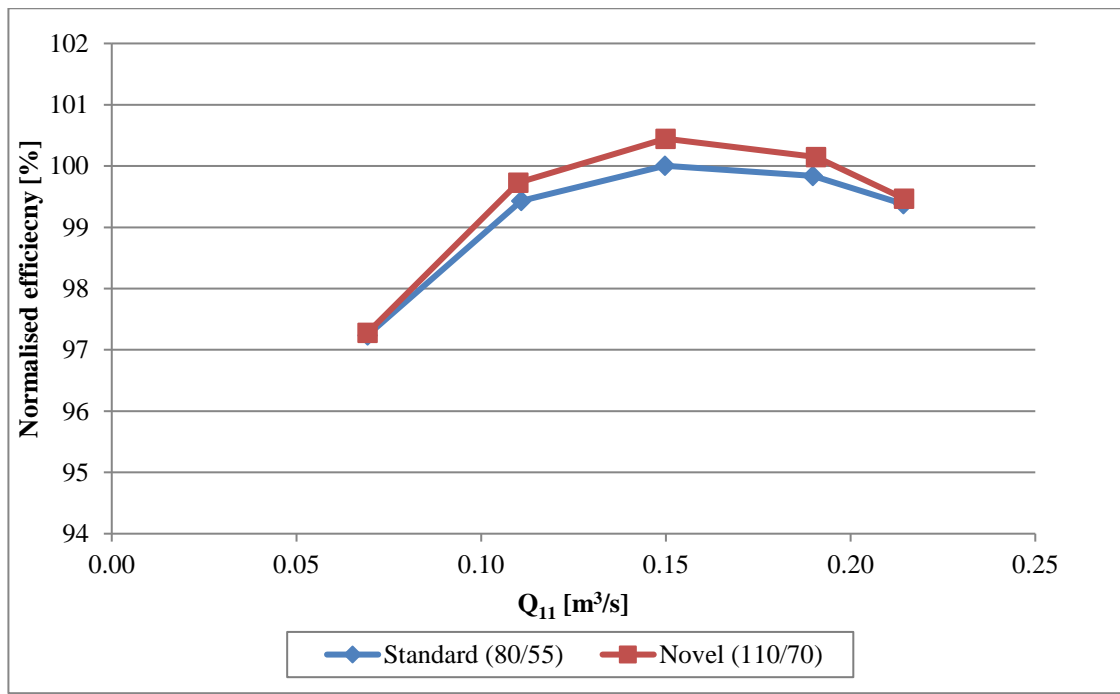


Fig. 8.17. Turgo injector efficiency comparison at $n_{11}=42\text{rpm}$ - twin jet

Fig. 8.18 and Fig. 8.19 show the variation in normalised efficiency with n_{11} at $Q_{11} = 0.19 \text{ m}^3/\text{s}$ which is closest to the BEP flow of $Q_{11}=0.177 \text{ m}^3/\text{s}$. The results show that the Novel (110/70) injector performs better than the Standard (80/55) injector across all unit speeds, for both single and twin jet operation, with the differences being greater at higher speeds.

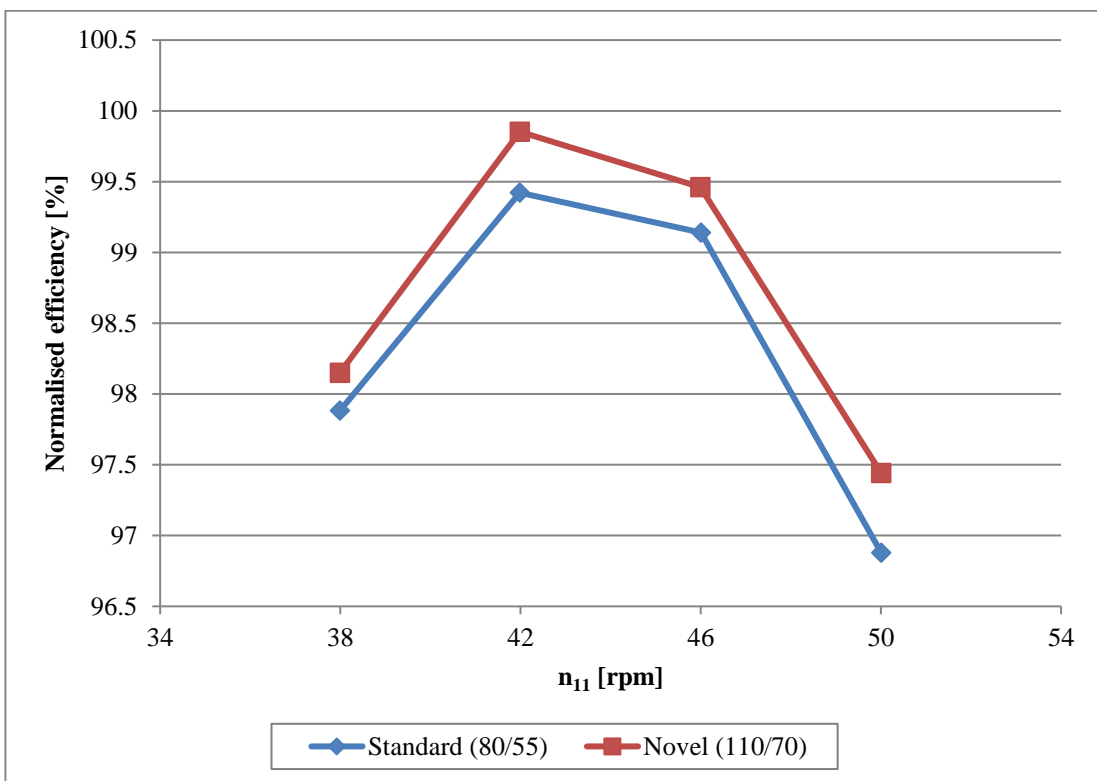


Fig. 8.18. Single jet operation at $Q_{11} = 0.19 \text{ m}^3/\text{s}$

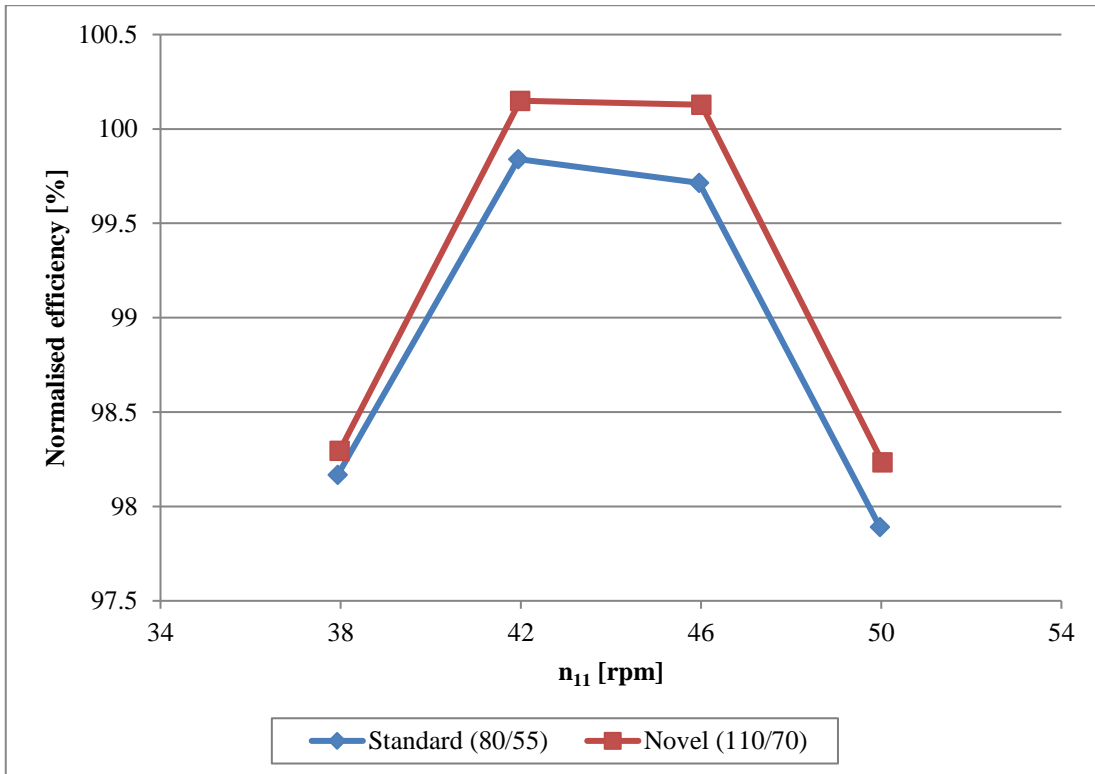


Fig.8.19. Twin jet operation at $Q_{11} = 0.19 \text{ m}^3/\text{s}$

9 CFD model verification

This chapter compares the numerical runner and injector analyses to the experimental tests in order to verify the accuracy of the numerical predictions. Before comparing the numerical and experimental results, the mechanical losses in the Turgo system are estimated so they can be accounted for in the comparison.

The CFD models used in this research are verified in three ways:

1. Turgo full system modelling: Comparing the absolute experimental hydraulic efficiency to the numerical hydraulic efficiency, taking into account the losses through the pipework and injector as well as the impact of the resultant real jet profile on the runner performance.
2. Turgo injector modelling: By comparing the numerical improvements to the runner performance as a result of changes in the injector spear/valve geometry to the measured experimental improvements.
3. Turgo runner modelling: By comparing the numerical improvements between the runner designs to the experimentally measured improvements.

Although the numerical model is based on a 7.5" Turgo runner and the experimental testing was carried out on a 9" Turgo runner, the dimensionless BEP conditions are the same and it is assumed that there is hydraulic similitude between the two designs.

9.1 Estimating the mechanical losses

As the measured efficiency η includes the mechanical losses in the system, as a result of the windage losses and the frictional forces within the bearings, it is important to try and establish these losses in order to compare the numerical and experimental results.

A method is proposed for determining the mechanical losses from the mechanical friction torque M_m which uses a combination of the experimental measurements of the frictional torque of the runner and the difference in measured torque for single and twin jet operation.

The measured torque M_t , used to calculate the efficiency, η , given by equation (7.3) can be defined as:

$$M_{t(Nj)} = N_j \cdot M_j - M_{m(Nj)} \quad (9.1)$$

For a number of jets, N_j , where M_j is the torque induced by each jet and M_m is the mechanical friction torque. M_m can be defined as the sum of the bearing friction torque, M_b , and the disk friction torque, M_d .

$$M_{m(Nj)} = M_d + M_{b(Nj)} \quad (9.2)$$

This disk friction torque is defined as the frictional torque arising from the frictional losses of the outer surface of the runner not in contact with the flow passage (IEC 60193:1999). The assumption is made that this does not vary with the number of jets used.

9.1.1 Disk friction torque, M_d

In order to aid in the understanding of the mechanical losses, some torque measurements were made by rotating the turbine shaft at varying speeds with and without the runner in order to measure the torque on the shaft as a result of the disk friction as well as the bearings with no loading. The results for these tests are given in Fig. 9.1 below.

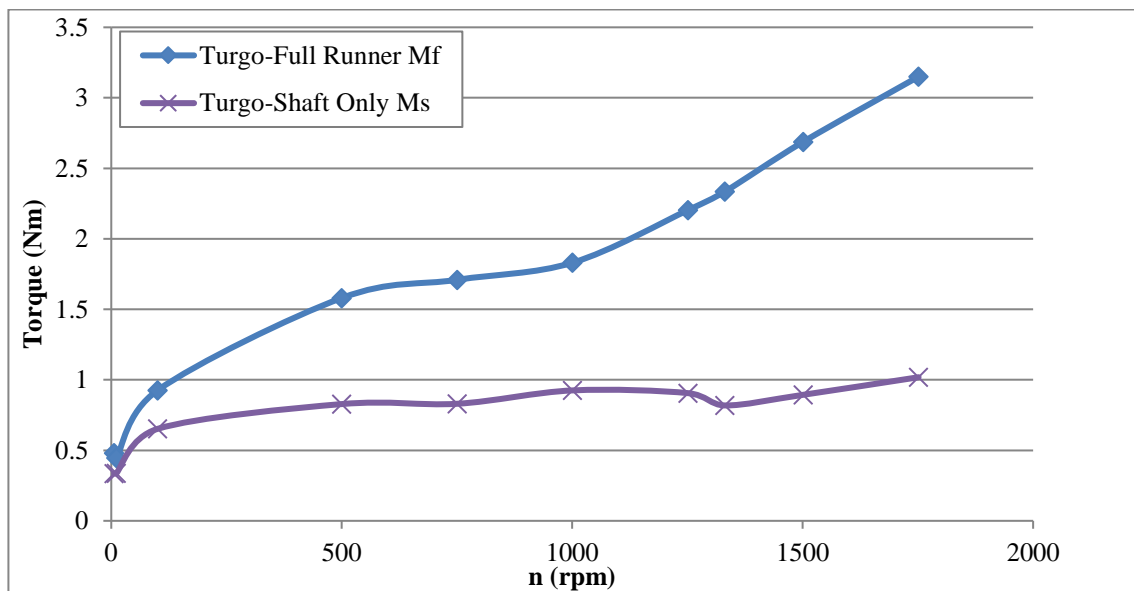


Fig. 9.1. Torque measurements taken at $Q=0\text{m}^3/\text{s}$, with and without runner at varying speeds

Assuming that the bearing friction doesn't change significantly with the load induced by the mass of the runner (31.2kg), the disk friction, M_d , can be approximated as:

$$M_d = M_f - M_s \quad (9.3)$$

Where M_f is the friction torque of the full runner in rotation and M_s is the friction torque from only the shaft rotating. At the BEP rotational speed, this gives a disk friction of $M_d=2.33-0.82=1.51\text{Nm}$.

9.1.2 Bearing friction torque, M_b

The force acting on the runner as a result of the jet loading force \vec{F}_j , for an ideal jet can be represented as:

$$\vec{F}_j = \dot{m} \cdot \vec{v} \quad (9.4)$$

Where \dot{m} is the mass flow rate of the fluid and \vec{v} is the velocity vector.

For a number of jets, N_j , the axial and radial forces ($F_{a(Nj)}$ and $F_{r(Nj)}$) acting on runner as a result of the jet loading force F_j and jet angle, α , from the radial plane, can be defined as.

$$F_{a(Nj)} = |\overrightarrow{F_{j(Nj)}}| \cdot \sin\alpha \quad (9.5)$$

$$F_{r(Nj)} = |\overrightarrow{F_{j(Nj)}}| \cdot \cos\alpha \quad (9.6)$$

During twin jet operation, $N_j=2$, the axial force acting on the runner is doubled, $F_{a2}=2F_{a1}$ and the radial force is cancelled out by the opposing jet directions, $F_{r2}=0$.

Although the frictional forces within the bearings are measured in the tests shown in Fig. 9.1 there is no loading applied to the shaft apart from the mass of the runner. Fig. 9.2 shows the bearing arrangement of the Turgo test rig the details of each bearing are given below:

- B1- SKF Spherical Roller Bearing (SKF 22312CC)- designed to support axial and radial loading
- B2- SKF Cylindrical Roller Bearing (SKF NU3212ECM)- designed to support radial loading

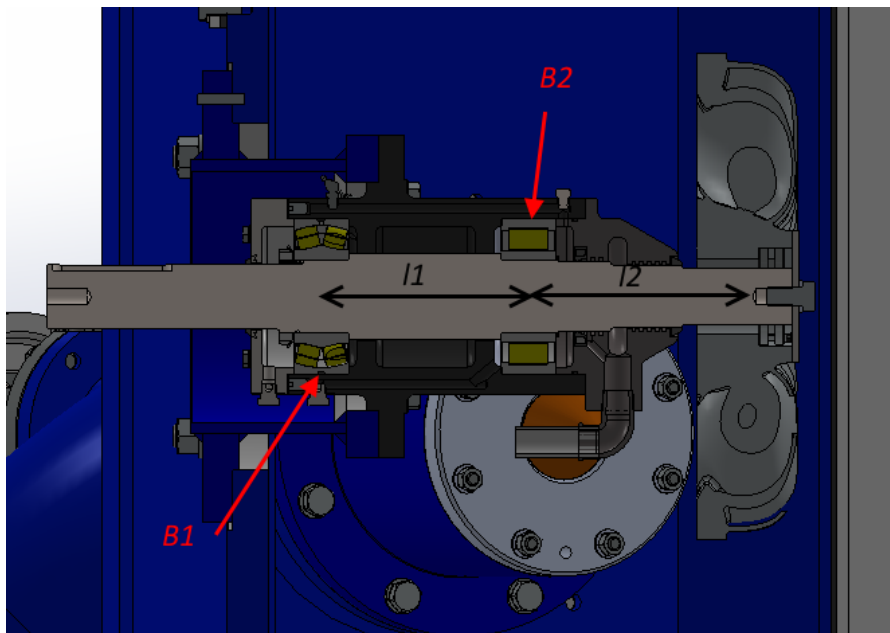


Fig. 9.2. Turgo test rig bearing arrangement

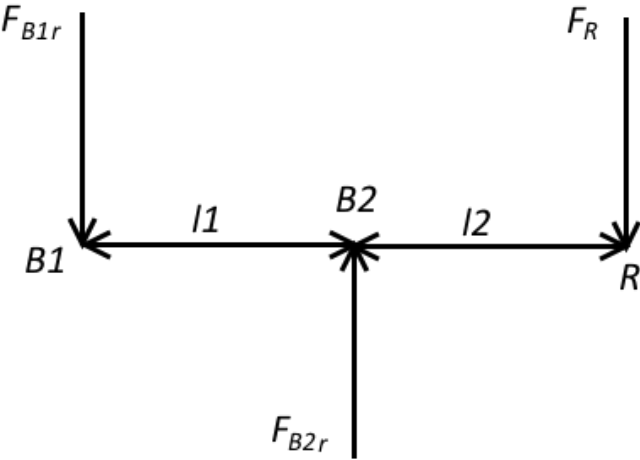


Fig. 9.3. Bending moment diagram for showing radial loading on bearings

Using the bending moment diagram above, (Fig. 9.3) the forces acting on each bearing can be resolved using the radial force acting on the runner, F_R , and the lengths $l1$ and $l2$ where:

$$F_{B1r} = \frac{F_R \cdot l_2}{l_1} \quad (9.7)$$

$$F_{B2r} = \frac{F_R(l_1 + l_2)}{l_1} \quad (9.8)$$

The radial force, F_R , acting on the shaft is the resultant of the radial jet loading force F_r and F_m , the force due to the mass of the runner, m_r . As these forces are perpendicular, F_R can be written as:

$$F_R = \sqrt{F_r^2 + F_m^2} \quad (9.9)$$

The axial forces acting on each bearing (F_{B1a} and F_{B2a}) are a direct result of the axial forces acting on the runner given by equation (9.5).

The forces acting on each bearing at the BEP conditions can be resolved using equations (9.7) to (9.9), as shown in Table 9.1 below.

		$N_j = 1$	$N_j = 2$
\dot{m}	[kg/s]	65.4	130.8
H	[m]	50	50
v	[m/s]	31.3	31.3
α	[deg]	25	25
m_r	[kg]	31.2	31.2
F_m	[N]	306.1	306.1
F_r	[N]	1561.2	0
F_a	[N]	859.0	3433.5
F_R	[N]	1867.3	306.1
l_1	[mm]	181	181
l_2	[mm]	173	173
F_{B1r}	[N]	1953.7	320.3
F_{B2r}	[N]	3821.0	626.3
F_{B1a}	[N]	859.0	3433.5
F_{B2a}	[N]	0	0

Table 9.1- Bearing forces for single and twin jet operation

Following a meeting with the bearing manufacturers, SKF, it was recommended that the online tool *SKF Bearing Calculator* (SKF Group 2016) be used to estimate the bearing friction losses. The tool requires the following input data:

- The axial and radial loads on each bearing- given in Table 9.1 .
- The operating temperature- this was not measured, however a range of values are looked at in order to establish the impact of the temperature on the performance. The value used for the losses was taken as 40°C.
- Viscosity of lubricant- The lubricant used on these bearings is a Lithium soap, LGEP-2, which has a viscosity of 200mm²/s at 40°C and 16mm²/s at 100°C.

Enter input parameters



Note: The drawing displayed is only for general representation and may not be identical to the selected bearing variant.

Frictional moment - power loss

F_r Radial load	<input type="text" value="3.850"/> kN
n_i Rotational speed of the inner ring	<input type="text" value="1330"/> r/min
Operating temperature Bearing outer ring	<input type="text" value="30"/> °C
Viscosity calculation input type Select from list	<input type="button" value="Viscosity input at 40 °C and 100 °C"/>
Viscosity at 40 °C	<input type="text" value="200"/> mm ² /s
Viscosity at 100 °C	<input type="text" value="16"/> mm ² /s
Lubrication Select from list	<input type="button" value="Grease"/>
<input type="button" value="Calculate"/> <input type="button" value="Reset"/>	

Fig. 9.4. SKF Bearing Calculator, showing input values for BEP operation at 30°C

The variation in the friction torque for each bearing M_{b1} and M_{b2} are plotted against the temperature in Fig 9.5 below.

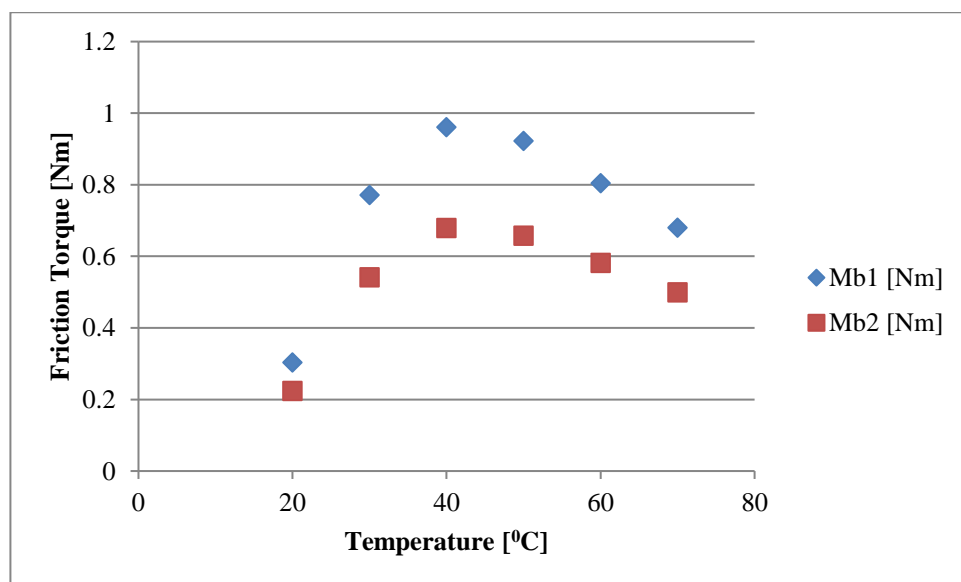


Fig 9.5. Variation in Friction torque with temperature for each bearing

An operating temperature of 40°C was chosen for this estimation as a worst case scenario. The resultant bearing friction torques are given in Table 9.2 below. The losses can be determined using M_b/M_t , where M_t is the total torque measured experimentally.

		$N_j = 1$	$N_j = 2$
M_{b1}	[Nm]	0.961	0.542
M_{b2}	[Nm]	0.679	1.318
$M_b = M_{b1} + M_{b2}$	[Nm]	1.64	1.86
M_t	[Nm]	180.48	362.98
M_b/M_t		0.91%	0.51%

Table 9.2- Bearing friction torques and losses using SKF bearing calculator

The results show that the frictional torques for single and twin jet operation are very similar, with the torques for twin jet operation slightly higher, however as the frictional losses are shared between each jet for twin jet operation, the overall losses are lower, at 0.36% compared to 0.91%.

The torque values given by the online calculator are only slightly larger than the torque measured at the BEP (Fig. 9.1) with no shaft, $M_s=0.82\text{Nm}$ and are lower than the torque measured with just the runner rotating at $M_f=2.33\text{Nm}$. This suggests that the friction torques calculated using the SKF bearing calculator are slightly lower than the real friction torques. This is likely to be down to the losses in the seals, which are not taken into account with the calculator tool.

9.1.3 Mechanical friction torque, M_m

Using the bearing frictions, M_b , from Table 9.2 and the disk friction, M_d , calculated in 9.1.1, we can calculate the mechanical friction torques using equation (9.2):

$$M_{m1} = 1.51 + 1.64 = 3.15\text{Nm} \text{ and } M_{m2} = 1.51 + 1.86 = 3.37\text{Nm}$$

Expressing this as a ratio between the friction torque and the total torque, $\frac{M_{m1}}{M_{t1}} = 1.75\%$ and $\frac{M_{m2}}{M_{t2}} = 0.93\%$, for single and twin jet operation respectively.

9.2 Turgo full system modelling

The numerical simulations were carried out at the design BEP of the HCTI runner at $n_{11}=43\text{rpm}$ and $Q_{11}=0.177\text{m}^3/\text{s}$. As the control points were taken at the same operating point for each runner, a direct comparison can be made between the numerical and experimental results at the BEP. The Turgo system was only analysed numerically for single jet operation as it was assumed that any hydraulic improvements made for a single jet would be apparent for twin jet operation as well.

The full Turgo system is broken into three primary regions of analysis for comparison with the experimental results as shown in Fig. 9.6.

1. This includes the bifurcation and first two bends in the pipe downstream of the pressure sensor. The flow in this region is relatively predictable in comparison to regions 2 & 3 and can be analysed with acceptable accuracy using pipe flow equations.
2. This includes the full injector, as modelled in Chapter 6.2 *Final runner design comparison* where the losses at the BEP are determined numerically.
3. This region includes the losses in the runner, which are modelled using the real jet profiles obtained in Chapter 6.2.

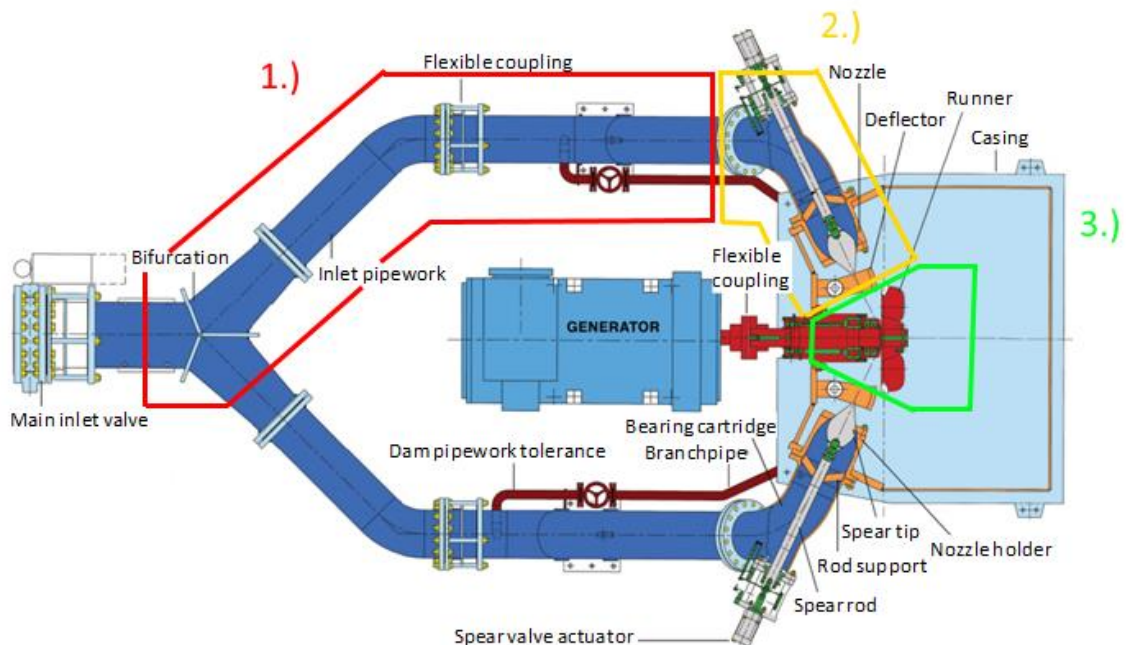


Fig. 9.6. Turgo turbine test rig, showing regions of analysis

9.2.1.1 Region 1

The flow in region 1 can be approximated by looking at the individual head losses, h_l , for each component using loss factors K .

$$h_l = K \cdot \frac{v^2}{2g} \quad (9.10)$$

Where v is the mean velocity in the pipe calculated from the internal diameter and the mass flow rate, which for the 8" pipe is calculated as 2.02m/s.

Region 1 can be broken down into 4 different loss features and 3 straight pipe sections as shown in Fig. 9.7. The loss features are defined as:

1. **Bifurcation:** This is treated as a 45deg metre bend as the upper injector is closed.
2. **Gradual contraction:** this is the section where the pipe diameter steps down from bifurcation to the 8" diameter pipe.
3. **45deg elbow bend 1:** this is the first elbow bend downstream of the bifurcation
4. **45deg elbow bend 2:** this is the second elbow bend downstream of the bifurcation

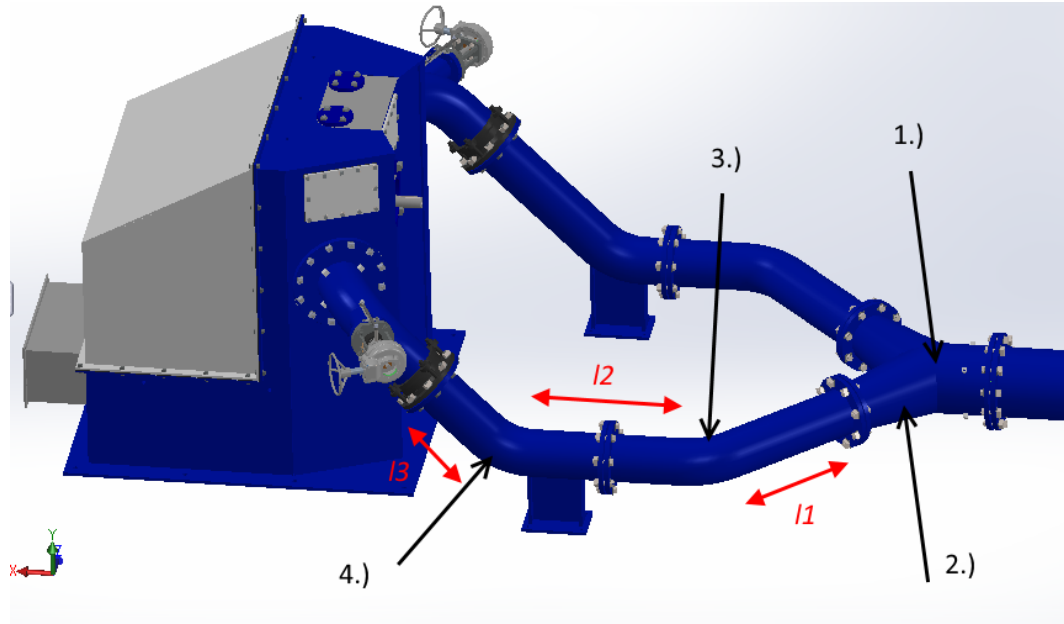


Fig. 9.7. Loss features (1-4) and straight pipe sections ($l1-l3$) in region 1

The loss factors (K) are given in (Metro Pumps & Systems Inc 2016) for each feature and from these the head loss, h_l , can be calculated using equation (9.10). The head loss for each feature as well as the total head loss is shown in Table 9.3 below.

Loss feature	Loss factor (K)	Head loss (h_l)
1	0.20	0.042m
2	0.04	0.008m
3	0.22	0.0458m
4	0.22	0.0458m
	Total	0.1415m

Table 9.3. Head loss from loss features

The head loss from the straight pipe sections can be calculated using:

$$h_l = \frac{4f l v^2}{2Dg} \quad (9.11)$$

Where l is the total pipe length, ($l_1 + l_2 + l_3$), which is measured as 1.795m and D is the 8" pipe diameter (0.203m). f is the friction factor determined by the surface roughness and Reynolds number, which is taken from a Moody diagram as 0.006. This gives a total head loss from the straight pipe sections as 0.0044m. The total head loss through region 1 can then be taken as $0.1415 + 0.0044 = 0.1459\text{m}$ which equates to **0.29%** losses from the inlet pressure head of 50m.

9.2.1.2 Region 2

The losses in region 2 are determined using a CFD analysis of the full 3D injector at the BEP (Chapter 6.2). For the original injector, these losses are calculated as **2.5%**.

9.2.1.3 Region 3

The losses in Region 3 are determined by importing the velocity profiles developed for region 2 into the runner simulation as shown in chapter 9.3.1 *Full injector and runner simulations*. For the original injector and optimised LE1 runner, the numerical efficiency at the BEP was calculated. The efficiency was normalised to **100%** for comparative purposes.

9.2.1.4 Total efficiency comparison

The total numerical hydraulic efficiency, η_{nh} , accounting for all the losses in the Turgo system can be calculated using equation (9.12) where η_{r3} is normalised to 100%.

$$\eta_{nh} = \eta_{r1} \cdot \eta_{r2} \cdot \eta_{r3} = 99.71 \times 97.50 \times 100 = \mathbf{97.22 \%} \quad (9.12)$$

The experimental hydraulic efficiency, η_{eh} , normalised against η_{r3} , excluding the mechanical efficiency, η_m , calculated in 9.1 can be calculated from the measured efficiency, η , as:

$$\eta_{eh} = \frac{\eta}{\eta_m} = \frac{94.28}{98.25} = \mathbf{95.96\%} \quad (9.13)$$

This shows the CFD model to be over predicting the efficiency by 1.26% which is inside of the total experimental uncertainty of 1.02% and the total numerical uncertainty of 0.62% however there are some uncertainties which are not included in the numerical model such as turbulence which could have an impact on the absolute numerical solution. There are several other possible explanations for this slight over prediction.

Firstly, the losses calculated in region 1 are treated separately and the influence of these bends (3 &4) and the bifurcation (1) on the jet quality and subsequent interaction with the runner is not modelled. Although the losses in this region are small ~0.29%, the secondary velocities induced by this pipework could have a significant impact on the jet quality and it is recommended that the entire branch pipe system from the pressure sensor location downstream should be modelled for a more accurate comparison.

Secondly, these simulations were carried out using a 2-bladed Turgo model (1 single blade passage) which was found during the periodicity study (*3.1.1.2 -Periodicity*) to give slightly higher efficiencies (0.41%) than the average of the 7 blade periodic case. This suggests that using more blade passages will reduce the numerical efficiency, bringing it closer to the experimental result. It is recommended that a larger runner section is modelled with a finer mesh in order to achieve a more accurate absolute numerical result although this will introduce a much higher computational cost.

Thirdly, the numerical model does not include the Turgo casing and any losses associated with interference between the flow leaving the casing walls and the oncoming jets and rotating runner. Although these losses are expected to be small due to the inclined nature of the Turgo turbine, expelling the water away from the oncoming jets, it is recommended that full runner simulations including the casing are carried out in order to establish the magnitude of these losses.

9.3 Turgo Injector modelling

The verification of the stand-alone injector models is difficult to carry out in isolation as the performance of each injector design was measured by analysing the effect of the spear/valve geometry on the entire Turgo system. This means that the measured differences between the designs are not simply the differences between the losses through each injector but include the effect each jet has on the performance of the runner as well.

For this reason, the injector model is verified by combining the injector results with a runner simulation which will include the impact of the quality of the jet produced by each injector on the performance of the runner.

9.3.1 Full injector and runner simulations

In order to try and numerically predict the overall performance of the original and optimised injector and runner designs, the real jet profiles at the BEP head and flow rate, produced in 6.2.3 - *3D Full injector study* are imported into the optimised LE1 runner simulation developed in 5.2- *DFMA- Leading edge width*.

The normalised torque curves for the ‘real jet’ simulations using the non-uniform velocity profiles shown in 6.2 for each injector design (d65 and d65mod-scaled) are compared to the ideal jet, with a uniform velocity profile, used for the runner optimisation in Fig. 9.8. The results show a significant change in the shape of the torque curves when using real jet profiles as well as a reduction in the peak torque on the inside blade surface and a drop in the torque on the outside blade surface. Comparing the real jet torque curves for each injector shows a very similar torque on the inside and outside blade surfaces for both real jets with a slightly higher peak torque for the d65mod-scaled jet profile.

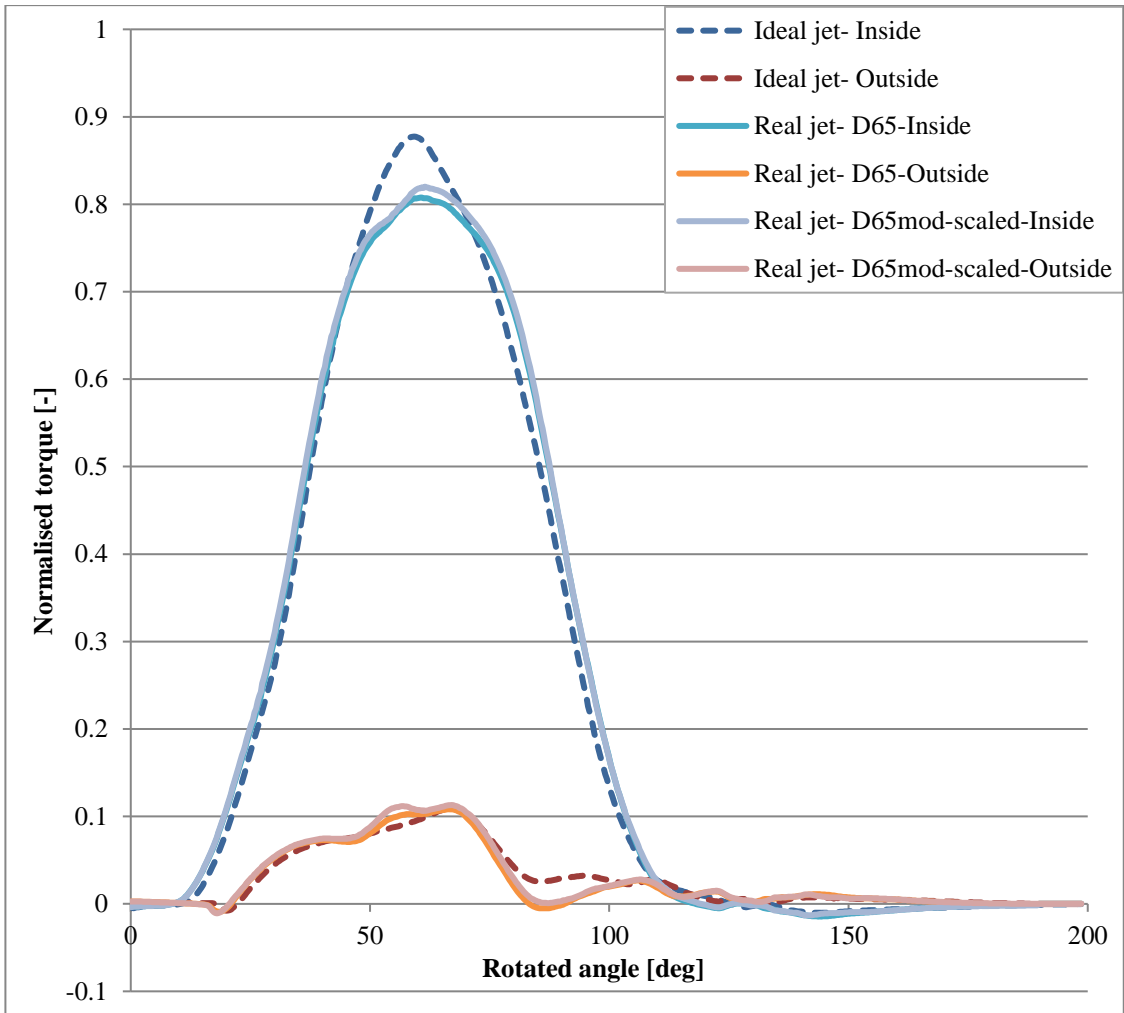


Fig. 9.8. Torque curves for Turgo runner using ideal jet and real jet profiles at the inlet

The efficiencies of the three runner simulations, using the ideal and real jet profiles are compared in Fig. 9.9 below. All of the efficiencies are normalised against the ‘Real jet-d65’ runner simulation efficiency, using the original d65 real jet profile (η_{r3}). The results show a significant decrease in normalised efficiency between the ideal and both real jet simulations, of over 2.00% for the d65 jet profile and 1.70% for the d65-mod-scaled jet profile. This shows that the secondary velocities induced by the injector geometry and the non-uniform velocity profile have a significant impact on the performance of the runner and should be minimised wherever possible.

Comparing the two injector designs, the d65mod-scaled injector jet performs slightly better in the runner simulation, giving an increase in runner efficiency of 0.27%.

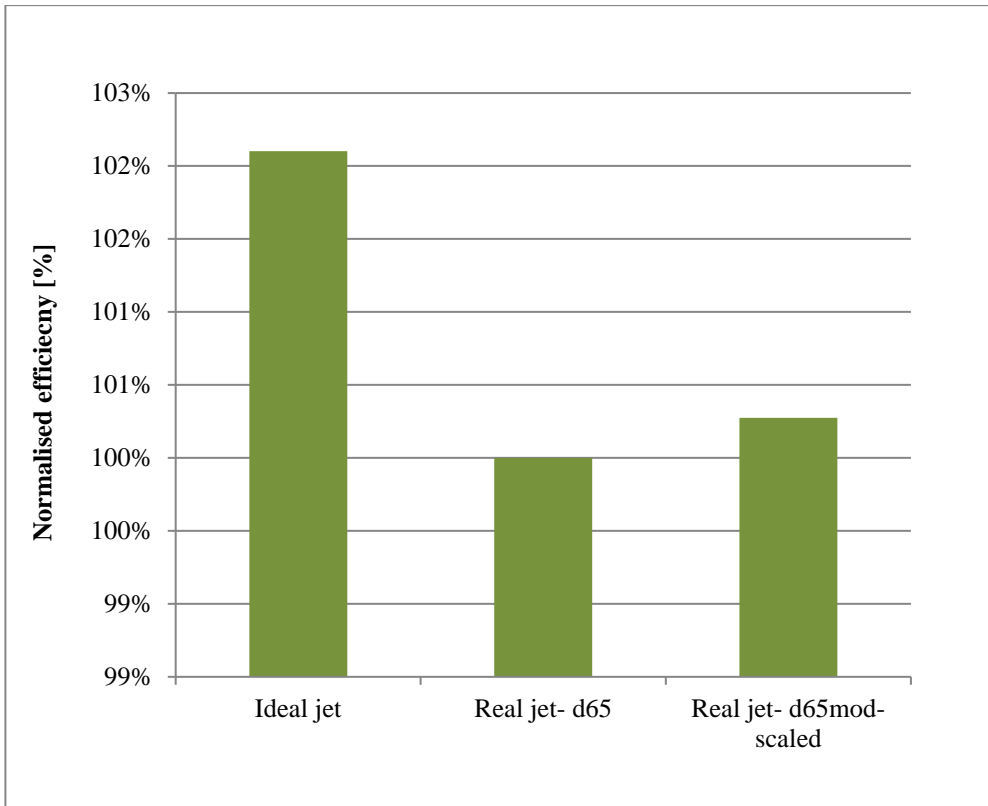


Fig. 9.9. 7.5" HCTI Runner efficiencies using real jet profiles

In order to compare the overall numerical performance of the injectors, the numerical hydraulic efficiency η_{nh} is calculated by substituting the full 3D injector efficiencies, η_{r2} , calculated in Chapter 6.2, the runner efficiencies, η_{r3} , and the region 1 efficiency, η_{r1} , into equation (9.12).

The numerical hydraulic efficiencies for each injector, d65 and d65mod-scaled, are compared to the experimental hydraulic efficiencies η_{eh} , calculated using equation (9.13) from the BEP performance in Chapter 8.2, in Fig. 9.10. The absolute comparison shows the numerical results to over predict the efficiency by a similar margin to the comparison in Section 9.2.1.4 at 1.44% for the d65 injector and 1.03% for the d65mod-scaled injector.

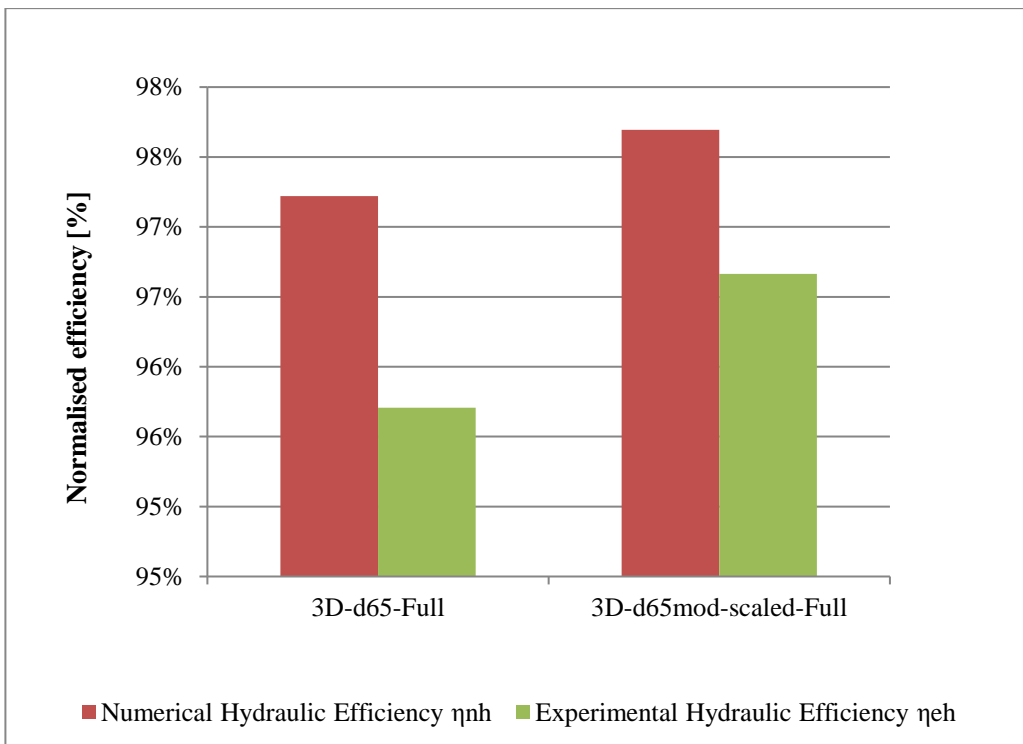


Fig. 9.10. Numerical and experimental total efficiency comparison for original (d65) and optimised (d65-mod-scaled) injectors, normalised against the numerical efficiency of the ‘Real jet-d65’ runner simulation (η_{r3}).

In order to verify the ability of the CFD model to accurately calculate the differences between the performances of different designs, the numerical improvements in the overall performance of the 65mod injector are compared to the experimentally measured improvements. The numerical modelling has shown that the d65mod-scaled injector is 0.48% more efficient than the d65 design, whereas experimentally, the difference is 0.87%. This shows the CFD model to be under-predicting the experimental improvement by 0.39%. Again there could be several reasons for this mismatch but the most likely are;

1. The injector CFD models only include the branch pipe (region 2) and not the two elbow bends and bifurcation (region 1) which will add further secondary velocities to the jet and impact the effect the real jet has on the runner performance.
2. The steady state injector CFD models require a very fine grid at the boundaries between air and water and at the regions of high velocity gradient in order to capture the shape and quality of the jet. This is achieved using mesh adaption in these regions however this is not possible in the transient runner simulations. It is likely that even though the density of the grid is increased in the jet path of the runner domain, some of the jet resolution is being lost in these larger cells resulting in a less defined difference between the jet profiles reaching the runner.

For a more accurate comparison between the injector CFD and experimental results, it is recommended that both regions 1 and 2 of the branch pipe are modelled to produce the jet profiles and a denser mesh is used for the runner domain or, if possible, the use of mesh adaption during the transient run. This is however likely to induce a much higher computational cost and will require significant computational resources if the simulations are to solve in reasonable timescales.

9.4 Turgo runner modelling

The verification of the Turgo runner numerical model used was carried out by comparing the differences between the original (HCTI) and the two optimised designs (LE1 and LE4) predicted by the CFD model with the differences measured experimentally at the BEP. By comparing the differences between the designs, the systematic error in the experimental tests are cancelled out providing a good verification comparison. As the injectors used are the same for the runner tests, the impact of the jet quality on the runner performance for each runner can also be treated as a constant allowing us to compare the experimental difference between the runners to the numerical difference from the *fine mesh* ideal jet runner simulations used for the optimisation. The numerically obtained normalised torque curves at the BEP for the three designs used in the experimental tests are compared in Fig. 9.11 below. The efficiencies calculated from these torque curves gave a 1.19% increase between the HCTI and LE4 designs and a 2.25% increase between the HCTI and LE1 designs as a percentage of the original HCTI numerical runner efficiency.

The average experimental difference between the HCTI and LE4 runners, as a percentage of the HCTI numerical efficiency, at the BEP for all 18 control points is 1.17% which is very close to the 1.19% predicted numerically. The average difference between the HCTI and LE1 runners at the BEP from all the control points is 2.16% which is also very close to but slightly less than the 2.25% calculated in CFD. The average difference between the LE4 and LE1 designs across all the control points is 0.98% which is in good agreement with the 1.06% predicted by CFD at the BEP and highlights the significance of having the leading edge dressed to as sharp an edge as possible in order to minimise disturbance of the flow at the inlet.

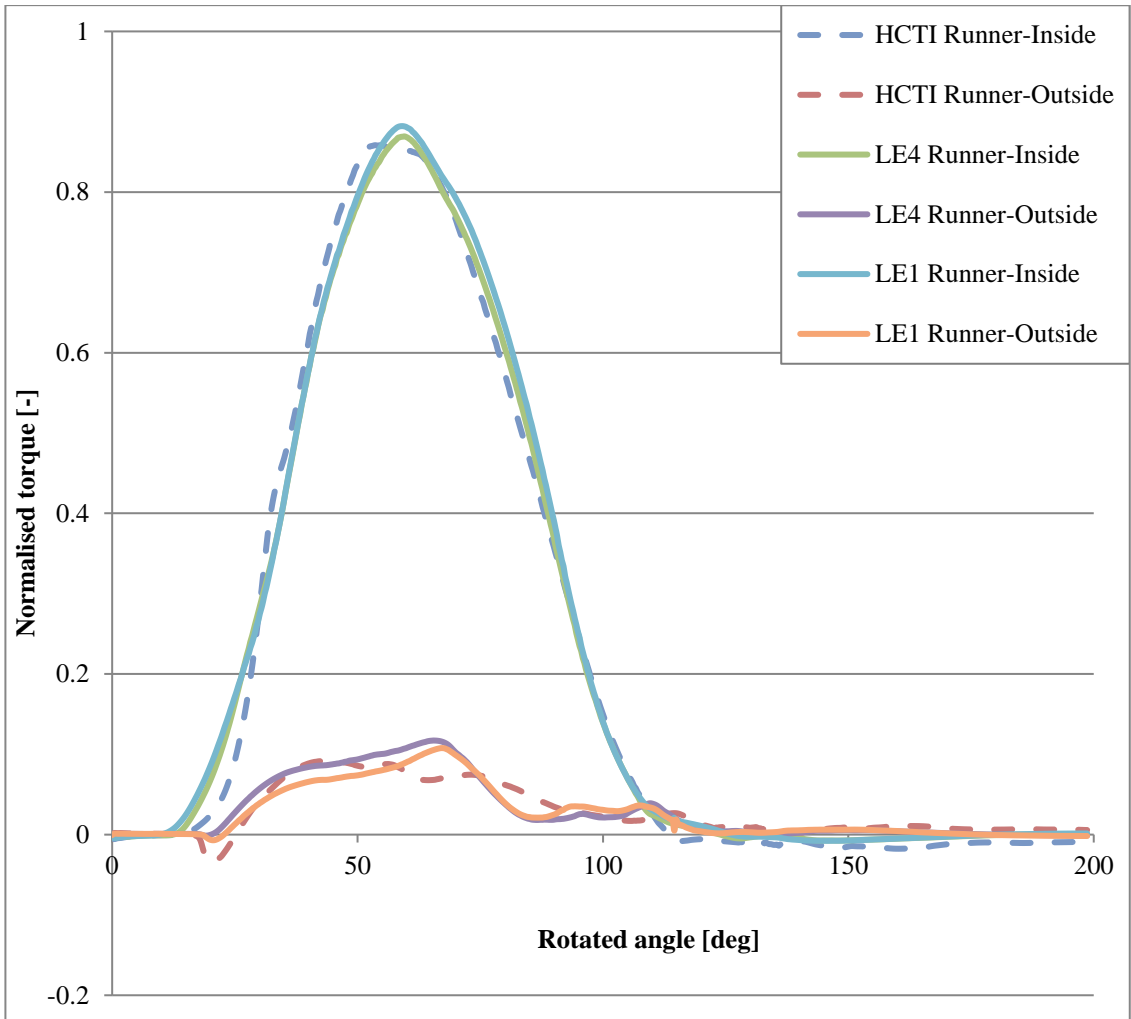


Fig. 9.11. Numerically obtained normalised torque curves for the original HCTI and optimised LE4 and LE1 runner designs at the BEP

The experimental differences between the runner designs at the BEP flow rate show very good agreement with the numerical model with an almost identical difference (0.02%) between the HCTI and LE4 designs. The HCTI and LE1 runner comparison showed a very small over prediction of the CFD model (0.09%) which could be a result of the experimental error or due to deviation between the CAD model of the runner and the manufactured runner. Overall these differences are small and this study has shown that the numerical model provides an accurate prediction of the differences in performance between different runner designs and is a useful tool for the optimisation of Turgo impulse turbine runners.

10 Conclusions

This chapter summarises the methodologies used and the outcomes of the research carried out during the course of this project. The initial aims and objectives (*1.6- Aims and objectives*) set out at the start of this research are also reflected upon and the degree to which these aims have been met are discussed.

10.1 Summary

The over-arching aim of this research was to use modern CFD tools to aid the better understanding and facilitate the hydraulic efficiency optimisation of the Turgo impulse turbine, including the runner and the spear/valve injectors (similar for both Pelton and Turgo turbines). This was carried out by separate analysis of the Turgo runner and the Injectors using the CFD modelling techniques deemed appropriate for the analysis and optimisation of each case. Following the separate CFD analysis of the Turgo runner and injectors, the models were combined in order to predict the impact the ‘real jets’ produced by the injectors have on the runner performance. This gave a more complete verification of the numerical models used when comparing the numerical and experimental results.

10.1.1 Turgo runner

Before analysing and optimising the Turgo runner, a detailed literature review was carried out covering the theoretical, numerical and experimental research on Turgo turbines since its invention in 1918. This review showed that although there have been some studies using CFD in the analysis of Turgo turbine runners, these have been unable to show a good correlation with experimental results and a complete analysis of the Turgo turbine using CFD, and capturing the high speed, highly turbulent, multiphase flow across the blades is yet to be carried out. There are also no studies looking at the specific geometric features of the Turgo runner and how these affect the performance. In order to analyse the behaviour of the Turgo runner numerically and carry out the optimisations a CFD model was required which could simulate the Turgo runner case accurately and in reasonable timescales. The commercial CFD solver, ANSYS® CFX® was selected based on previous research carried out on Pelton runners which require similar multi-phase free surface modelling with a rotating frame of reference. A series of geometric and modelling assumptions were introduced in order to simplify the numerical model and reduce the simulation time. The majority of these assumptions were validated and quantified by running higher cost comparative simulations. A two blade runner model was eventually chosen which models a single blade passage from which the periodic torque on the whole runner can be extrapolated. A mesh refinement study

was carried out on the 2 blade runner model which showed that a *coarse mesh* containing around 3.1 million elements and taking 2days and 1hour to solve on a quad core 3.4GHz Intel Xeon processor with 16BG of RAM gave a total numerical error of 1.55%. This mesh was shown to be sufficient to capture small incremental design changes and was used effectively throughout the runner optimisation. A more refined mesh (*fine mesh*) containing around 10M cells, and taking 8 days and 14hours to solve, was used to verify the design changes made using the *coarse mesh*. The runner optimisation was carried out in three phases with Phase 1 looking at selected initial design changes and studies based on previous Turgo research, Phase 2 carrying out a DOE study varying the blade shape and exit angles and Phase 3 looking at additional parameters which were varied based on observations of the flow field.

Following the runner optimisation a Finite Element Analysis (FEA) was carried out on the optimised design which was modified to increase the strength. With knowledge of the manufacturing process used to make the runners, following meetings and a site visit to the company used to manufacture the runners, Design for Manufacture and Assembly (DFMA) was carried out to improve the castability of the design. This resulted in two optimised runner designs; LE4, with a thicker leading edge and no dressing and LE1, which is the LE4 runner with the leading edge ground down to a sharper profile. The CFD models using the *fine mesh* simulations showed an efficiency improvement of 2.25% for the LE1 runner and 1.19% for the LE4 runner over the original runner numerical efficiency.

The original HCTI runner was manufactured and tested alongside the two optimised runner designs at the Laboratory for Hydraulic Machines, National Technical University of Athens (NTUA). The three runners were tested using single and twin jet operation. A total of 48 test points were measured for each test as well as 6 control points taken at the design BEP. From this test data, hill charts were produced comparing the three runner designs across a range of operating conditions. The experimental test results showed that the optimised LE1 design gave an efficiency improvement of 2.16% and the LE4 runner 1.17% of the original HCTI runner numerical efficiency. The improvements in runner efficiency predicted numerically are therefore only 0.02% and 0.09% higher than the experimental improvements at the BEP showing that the CFD model developed can predict to within 0.1% the difference in performance between runner designs. The optimised runner designs also showed even larger experimental improvements at higher flow rates at over 4% at $Q_{11}=0.25\text{m}^3/\text{s}$ for the LE1 runner. This shows that the optimisations carried out have not only increased the BEP performance while sacrificing the performance away from the BEP, which can often happen when only optimising around one test point, but have improved the performance across the whole range of test points resulting in much flatter efficiency curves.

The CFD model developed during the course of this research shows the most complete analysis of a Turgo runner carried out to date by producing the fully developed periodic torque curves on the inside and outside surfaces of the blades. This research also quantifies for the first time the effects of various design changes to the runner of a Turgo turbine on the efficiency. The numerical optimisations carried out are verified experimentally showing the ability of the numerical model to accurately predict the effects these changes have on the performance.

10.1.2 Impulse turbine injectors

Following a detailed literature review of the research carried out on impulse turbine injectors it became apparent that there were no studies looking at the basic geometric design parameters of impulse turbine injectors and the impact they have on the hydraulic performance. Focussing initially on a 2D axisymmetric straight pipe case with a generic injector design, a CFD model was developed using similar assumptions to the Turgo runner analysis. As only a simplified case was being looked at in steady state, a grid with much higher mesh independency could be used. After validation of the 2D axisymmetric model, a design of experiments study was carried out at a range of pressure heads from 150m-350m. The Nozzle Angle, Spear Angle and Spear Width were chosen as the primary geometric parameters for this study, having been identified as the most important design characteristics according to the current literature. The Nozzle Angles ranged from 70°-110° and the Spear Angles from 30°-70° as the tendency of modern designs are towards steeper angles. The DOE study found that the nozzle and spear angles have the biggest impact on the injector losses and suggested an optimum design with nozzle and spear angles of 110° and 70°, much larger than the original generic design with nozzle and spear angles of 90° and 50° . This optimisation of the nozzle and spear angles was applied to the Gilkes Turgo injector, d65/Standard (80/55) geometry with nozzle and spear angles of 80° and 55°. The optimised (d65mod-scaled/Novel (110/70)) injector was modelled as the 2D axisymmetric case as before and then extended to a 3D straight pipe case and finally a full 3D case including the branchpipe and spear holding vanes. The full 3D simulations reveal some important characteristics of the flow through the injector such as the creation of secondary cross-flow vortices after the pipe bend and their interaction with the spear holding vanes causing fragmentation into more vortices of various size and strength. They also reveal the role of the secondary velocities in the observed disturbances of the free jet surface. The increase of injector efficiency obtained by using steeper nozzle and spear valve angles can also be explained by the observed reduction of the non-symmetric jet structure characteristics which includes the secondary velocity magnitude. The Novel (110/70) injector design reduced the numerical injector losses by 0.24% in the 2D axisymmetric case, 0.20% in the 3D straight pipe case and 0.21% in the Full 3D case.

Both the Standard (80/55) and the Novel (110/70) injector designs were manufactured for testing on the Pelton and the Turgo test rigs at NTUA. In the Pelton injector tests, the Novel (110/70) design performed better than the Standard (80/55) design at all speeds, with the differences being more pronounced at lower flow rates where the losses through the injectors are greater. At the BEP flow $Q_{11k}=0.234$ and speed $n_{11}=39$, the Novel (110/70) design showed quite a substantial increase efficiency of 1% of the Standard (80/55) injector efficiency. The Turgo injector tests also showed the Novel (110/70) injector design to perform best overall, with a 0.80% increase in efficiency, at the BEP flow $Q_{11}=0.177\text{m}^3/\text{s}$ and $n_{11}=43\text{rpm}$, over the Standard (80/55) injector efficiency. The Turgo injector tests did however show slightly lower efficiencies for single jet operation at the lowest flow rates tested ($Q_{11}=0.03\text{m}^3/\text{s}$) and more disturbances on the outside of the jet at these lower flow rates for the steeper angled Novel (110/70) design. This very low flow rate (~10% of the rated flow) is outside of the normal operating conditions of this runner and for flows above this, the steeper angled Novel (110/70) performs best overall, showing improvements in efficiency in the order of 0.2-0.8%.

The results of the numerical injector studies are verified by combining the profiles produced by the full 3D Turgo injector simulations with the LE1 runner simulations. Combining the real jet profiles with the runner simulations showed that the non-uniform velocity and secondary velocities in the jet induced by the upstream geometry has a significant impact on the runner performance, reducing the normalised efficiency by over 2% compared to the ideal jet with uniform velocity profile. These full injector and runner simulations were used to calculate the difference in total numerical efficiency of the Standard (80/55) (d65) and Novel (110/70) (d65mod-scaled) injectors and runners combined which were compared to the experimental results. The normalised efficiencies (against the Standard (80/55) injector efficiency) showed a numerical increase in efficiency of 0.48% and an experimental increase of 0.87% between the Standard (80/55) and Novel designs at the BEP. There are several possible reasons for this 0.39% under-prediction in the numerical results with the most likely being the injector model only including the first bend in the pipework upstream of the injector and not the second two bends or the bifurcation. It has already been shown that the steeper angled Novel injector design reduces the average secondary velocities by over 35% and the secondary velocities resulting from the bends and bifurcation not included may be reduced further by the Novel design resulting in a bigger difference in efficiencies at the BEP. It is recommended that a CFD analysis of the injector including the full pipework is carried out combined with a runner simulation in order to investigate this.

The present results contradict the preferred historical designs found in all previous publications, which use much shallower nozzle and spear angles, and introduce new design guidelines for impulse turbine injectors.

10.1.3 Turgo full system model verification

As well as verifying the ability of the numerical models to predict the difference in performance between the injector and runner designs, verification of the full Turgo system was carried out looking at the differences in the absolute numerical and experimental efficiencies. This was done by estimating the mechanical losses of the Turgo test rig in order to calculate the experimental hydraulic efficiency, η_{eh} . The losses in the pipework upstream of the injector were then estimated using pipe flow equations which were combined with the losses through the full 3D injector and the runner simulation, using the real jet profile, giving the numerical hydraulic efficiency, η_{nh} . Comparing these two values showed the numerical models to be over predicting the efficiency by 1.26% which is inside of the total experimental uncertainty of 1.02% and the total numerical uncertainty of 0.62%. It is expected that this difference could be reduced by running a full periodic case (which has been shown to produce lower efficiencies than the 2 blade model) as well as modelling the full pipework and bifurcation. There are also some uncertainties not accounted for which could affect the absolute numerical efficiency such as the impact of using a RANS turbulence model over a DNS model or the effect of interactions with the casing.

Overall this research has shown how CFD can be used effectively in the detailed analysis and optimisation of Turgo impulse turbine runners and impulse turbine injectors. The optimised designs developed numerically were verified experimentally showing that the numerical runner model is able to predict improvements in experimental performance to within 0.1%. The injector models are less accurate in predicting these improvements as the analysis of the flow within the pipework is more complex requiring significantly higher computational resources however when combining the injector and runner simulations, the CFD is able to predict improvements to within 0.4%. It should be noted that these differences are based on the solver setup described and may vary using alternative controls.

The verification of the absolute efficiency of the full Turgo system model against the experimental efficiency showed a 1.26% over-prediction of the numerical model. Reasons for this over prediction are highlighted and recommendations for further research are given below to improve the full system model.

11 Recommendations for future work

11.1 Turgo runner optimisation

The optimisation of the design of Turgo runner could be extended by looking at design parameters not investigated during this research.

These include the axial inclination angle of the jet which may be dependent on the runner design and specific speed, since in existing turbines it ranges between about 20° and 30°. Such correlations should be investigated. The same may be valid for the optimum location of the jet impact point on the inlet plane of the runner in relation to the specific speed.

The blade number study showed that reducing the thickness of the blades as well as increasing the number of blades can improve the runner performance by allowing a wider flow passage between the blades and further reduction of the outflow energy losses. Reduction of the blade width to a minimum possible that can be manufactured and secure the required strength and lifetime of the runner will not only reduce the material and construction cost of the turbine, but will also improve its hydrodynamic behaviour.

11.2 Injector optimisation

The modelling of multiple injectors was not covered in this research and could provide a means for increasing the capacity of these turbines further as well as extending the range of flow rates they can accommodate without sacrificing the efficiency by operating at smaller spear openings. The axis orientation (vertical as opposed to horizontal) may improve the evacuation of the flow at the exit and allow the exit angles to be increased, reducing the outflow losses. The number of injectors and the power or flow rate values above which the use of multiple jets and vertical axis configuration becomes more advantageous, in terms of energy production and economic benefits should be investigated and correlated with the specific speed of the runner.

11.3 Casing design

Although Turgo turbines have the advantage of outflow from the opposite direction of the injectors, interference of water rebounding from the casing walls with the jets and the runner will affect the performance. Hence, the optimum design of the casing is an important issue, in order to minimize such interference and at the same time to reduce as much as possible the volume and cost of the casing. By reducing the size of the casing, the generator overhang and subsequent cost of the generator can also be reduced.

11.4 Manufacturing methods

The manufacture of Turgo turbines can be improved to reduce the construction cost and improve the accuracy of the runner and injectors fitting as well as facilitating the finishing of blade surfaces. The cost-effectiveness of alternative methods to casting or machining the full runner, like separate blades construction and assembly or machining, may be considered.

Investigation of the possible use of new materials to reduce the manufacturing cost and to enhance the performance of the runner should also be carried out. A large-scale runner made of composite materials is a challenging concept; not only for the Turgo but for other types of hydro turbines however using segmented blades may make the possibility of this more achievable. The use of special alloys or coatings to reduce the surface friction as well as erosion wear can improve the performance and prolong the lifetime of the runner in the case of higher silt concentrations in the water and should also be investigated.

11.5 Customised designs

Finally, some research may be targeted towards customising Turgo turbines for specific applications, such as multi-point design optimisation of runners operating at variable head, or the development of highly efficient, simple-design, low-cost runners that are being used for micro and pico hydropower production in developing countries and remote isolated regions.

References

- 1 Aggidis, G. A. and D. S. Benzon (2013). "Operational optimisation of a tidal barrage across the Mersey estuary using 0-D modelling." *Ocean Engineering* 66(0): 69-81.
- 2 Anagnostopoulos, J. (2011). Hydroaction: Development and laboratory testing of improved Action and Matrix hydro turbines designed by advanced analysis and optimization tools. Small Hydro Going Smart Conference. Brussels, European Small Hydropower Association.
- 3 Anagnostopoulos, J., P. Koukouvinis, et al. (2012). Optimal design and experimental validation of a Turgo model Hydro turbine. 11th Biennial Conference on Engineering Systems Design and Analysis. A. 2012: 157-166.
- 4 Anagnostopoulos, J. S., G. Aggidis, et al. (2015). Parametric Design and Optimization of Turgo Turbine Runners. HYDRO 2015 Conference. Bordeaux, France.
- 5 Anagnostopoulos, J. S. and D. E. Papantonis (2007). "Flow Modelling and Runner Design Optimization in Turgo Water Turbines." World Academy of Science, Engineering and Technology 2007 P206-211.
- 6 ANSYS, I. (2013a). ANSYS CFX Solver Modeling Guide. Release 15. Canonsburg, USA, ANSYS Inc.
- 7 ANSYS, I. (2013b). ANSYS CFX Solver Theory Guide. Release 15. Canonsburg, USA, ANSYS Inc.
- 8 Benzon, D. S. (2014). Using CFD in the analysis of Impulse turbines with a focus on the high capacity Turgo. 14th Annual Africa Utility Week/ Clean Power Africa. E. Africa. Cape Town.
- 9 Benzon, D. S., G. A. Aggidis, et al. (2016). "Development of the Turgo Impulse turbine: Past and present." *Applied Energy* 166: 1-18.
- 10 Benzon, D. S., G. A. Aggidis, et al. (2013). State of the art & current research on Turgo impulse turbines. 13th Annual Africa Utility Week/ Clean Power Africa. E. Africa. Cape Town.
- 11 Benzon, D. S., A. Židonis, et al. (2014). "Impulse turbine injector design improvement using Computational Fluid Dynamics." *ASME J. Fluids Eng.* 137(4): 041106.
- 12 Benzon, D. S., A. Židonis, et al. (2015). "Numerical Investigation of the Spear Valve Configuration on the Performance of Pelton and Turgo Turbine Injectors and Runners." *Journal of Fluids Engineering* 137(11): 111201-111201.
- 13 Bovet, T. (1957). Feuilles de Cours Illustrees A, 2ème édition. Institut de Machines Hydrauliques (Lausanne).
- 14 Catanase, A., M. Barglazan, et al. (2004). Numerical Simulation of a free jet in Pelton Turbine. The 6th International Conference on Hydraulic Machinery and Hydrodynamics. Timisoara, Romania, Scientific Bulletin of the Politehnica University of Timisoara
- 15 Cobb, B. R. and K. V. Sharp (2013). "Impulse (Turgo and Pelton) turbine performance characteristics and their impact on pico-hydro installations." *Renewable Energy* 50(0): 959-964.

- 16 Correa, J., J. D. Andrade, et al. (2012). A Preliminary Analysis of a Turgo Type
Turbine CFD Simulation Designed With an Integrated Dimensional Methodology.
24th Symposium on Fluid Machinery. Rio Grande, Puerto Rico, USA, July 8–12,
2012. Volume 1: Symposia, Parts A and B.
- 17 Correa, J., J. D. Andrade, et al. (2012). Design Procedure for a Turgo Type Turbine
Using a Three-Dimensional Potential Flow. ASME Turbo Expo 2012: Turbine
Technical Conference and Exposition. Copenhagen, Denmark, June 11–15, 2012,
ASME Proceedings | Turbomachinery. Volume 8: Turbomachinery, Parts A, B, and
C.
- 18 Crewdson, E. (1922). Design and Performance of a New Impulse Water-Turbine.
Minutes of Proceedings of the Institution of Civil Engineers, The Institution of Civil
Engineers.
- 19 Fiereder, R., S. Riemann, et al. (2010). Numerical and experimental investigation of
the 3D free surface flow in a model Pelton turbine. 25th IAHR Symposium on
Hydraulic Machinery and Systems.
- 20 Gaiser, K., P. Erickson, et al. (2016). "An experimental investigation of design
parameters for pico-hydro Turgo turbines using a response surface methodology."
Renewable Energy 85(0): 406-418.
- 21 Gass, M. and H. Water (2002). Modification Of Nozzles For The Improvement Of
Efficiency Of Pelton Type Turbines. Proceedings of the HydroVision Conference.
- 22 Gibson, A. H. (1908). Hydraulics And Its Applications, D. van Nostrand Company.
- 23 Gilbert Gilkes & Gordon Ltd. (1920). Improvements in water turbines. London Patent
Office. United Kingdom, Crewdson, E. 155175.
- 24 Gilbert Gilkes & Gordon Ltd. (1937). Improvements in water turbines. London Patent
Office. United Kingdom, Jackson, E. A. . 468557.
- 25 Gilbert Gilkes & Gordon Ltd. (1963). Improvements in water turbines. London Patent
Office. United Kingdom, Jackson, E. A. . 938967.
- 26 Gilbert Gilkes & Gordon Ltd. (2016). Gilkes Turgo Impulse Hydro Turbine.
http://www.gilkes.com/user_uploads/turgo%20paper2.pdf.
- 27 Hancock, E. (1982). "Comments by E. Hancock on the Russian paper 'Inclined jet
hydraulic turbine' by Shipulin."
- 28 Hartvigsen Hydro. (2015). "Turgo Runners, http://h-hydro.com/New_Site/turgo-runners/." Retrieved [13/08/15].
- 29 Harvey, A. (1993). Micro-Hydro design manual. Intermediate Technology
Publications. Warwickshire, UK,.
- 30 Jošt, D., A. Lipej, et al. (2008). Numerical Prediction of Efficiency, Cavitation and
Unsteady Phenomena in Water Turbines. ASME 2008 9th Biennial Conference on
Engineering Systems Design and Analysis. ASME: 157-166.
- 31 Jošt, D., P. Mežnar, et al. (2010). Numerical prediction of Pelton turbine efficiency.
25th IAHR Symposium on Hydraulic Machinery and Systems, IOP Conf. Series:
Earth and Environmental Science 12 (2010) 012080.

- 32 Khurana, S. and V. Goel (2014). " Effect of jet diameter on erosion of turgo impulse turbine runner." Journal of Mechanical Science and Technology 28(11): 4539-4546.
- 33 Khurana, S., V. Kumar, et al. (2012). "Effect of Nozzle Angle and Silt Parameters on Erosion and Performance of Turgo Impulse Turbine." International Journal of Thermal Technologies 2(4): 204-208.
- 34 Khurana, S., V. Kumar, et al. (2013). The effect of nozzle angle on erosion and the performance of turgo impulse turbines. . International Journal of Hydropower & Dams: 97–101.
- 35 Khurana, S., Varun, et al. (2013). "Effect of silt particles on erosion of Turgo impulse turbine blades." International Journal of Ambient Energy 35(3): 155-162.
- 36 Klemetsen, L. E. (2010). An experimental and numerical study of the free surface Pelton bucket flow. MSc, NTNU
- 37 Koukouvinis, P., J. S. Anagnostopoulos, et al. (2010). SPH modelling of a Turgo turbine. SPHERIC newsletter 11th issue – December 2010. SPH European Research Interest Community, <http://wiki.manchester.ac.uk/spheric/>.
- 38 Koukouvinis, P. K., J. S. Anagnostopoulos, et al. (2011). SPH Method used for Flow Predictions at aTurgo Impulse Turbine: Comparison with Fluent. World Academy of Science, Engineering and Technology 55 2011.
- 39 MacDuff, I. B. (1964). Report of Centrifugal Tests to establish a technique for measuring strain on a Turgo Impulse Wheel using Electrical Resistance Strain Gauges and a Slip Ring Unit. Glasgow, The Royal College of Science and Technology.
- 40 MacDuff, I. B. (1969). Stresses and Deformations in Impulse Water Turbines. Doctor of Philosophy, University of Glasgow.
- 41 Metro Pumps & Systems Inc (2016). Friction Losses in Pipe Fittings. <http://www.metropumps.com/ResourcesFrictionLossData.pdf>. accessed 02/02/16.
- 42 Muggli, F., Z. Zhang, et al. (2000). Numerical and experimental analysis of Pelton turbine flow. Part 2: the free surface jet flow. 20 th IAHR Symposium.
- 43 Nechleba, M. (1957). Hydraulic Turbines, Their Design and Equipment. Prague, ARTIA, Printed in Czechoslovakia.
- 44 Nesiadis, A. V., D. E. Papantonis, et al. (2011). Numerical study of the effect of spear valve design on the free jet flow characteristics in impulse hydroturbines. 7th GRACM International Congress on Computational Mechanics. Athens.
- 45 Patel, K., Patel, B., Yadav, M. and Foggia, T. (2010). Development of Pelton turbine using numerical simulation. 25th IAHR Symposium on Hydraulic Machinery and Systems, IOP Conf. Series: Earth and Environmental Science 12 (2010) 012048.
- 46 Peron, M., E. Parkinson, et al. (2008). Importance of jet quality on Pelton efficiency and cavitation. IGHEM2008. Milan, Italy.
- 47 Perrig, A. (2007). High Speed Flow Visualisation of an Impinging Jet on a Pelton Turbine Bucket. ASME/JSME 2007 5th Joint Fluids Engineering Conference, ASME: 165-168.

- 48 Perrig, A. (2007). Hydrodynamics of the free surface low in Pelton turbine buckets. ingénieur mécanicien diplômé EPF, ÉCOLE POLYTECHNIQUE FÉDÉRALE DE LAUSANNE.
- 49 Perrig, A., F. Avellan, et al. (2006). "Flow in a Pelton turbine bucket: numerical and experimental investigations." 128(2): 350-358.
- 50 Roache, P. J. (1994). "Perspective: A Method for Uniform Reporting of Grid Refinement Studies." ASME J. Fluids Eng. 116(405-413).
- 51 Santolin, A., G. Cavazzini, et al. (2009). "Numerical investigation of the interaction between jet and bucket in a Pelton turbine." Proceedings of the Institution of Mechanical Engineers, Part A: Journal of Power and Energy 223: 721 DOI: 10.1243/09576509JPE824.
- 52 Shipulin, I. F. (1956). The inclined-jet hydraulic turbine, Mashgiz, Moscow, Proceedings of the All-Union Scientific-Research Institute of Hydromachinery Construction.
- 53 SKF Group. (2016). "SKF Bearing Calculator." Retrieved (03/02/16).
- 54 Stat-Ease®. (2013). "Design-Expert® 9 Software." Retrieved 23/03/16.
- 55 Staubli, T. and H. P. Hauser (2004). Flow Visualization - a Diagnosis Tool for Pelton Turbines. IGHEM2004, Lucerne, Switzerland.
- 56 Staubli T., Abgottspion A., et al. (2009). Jet quality and Pelton efficiency. Hydro 2009, Lyon.
- 57 Vesley, J. and M. Varner (2001). A Case Study of Upgrading of 62.5MW Pelton Turbine. Proceedings of International Conference: IAHR 2001.
- 58 Webster, J. (1971). "Analysis of Jet Type Impulse Turbines." Water Power: P287-P292.
- 59 Webster, J. (1972). "Flow patterns related to jet-type impulse turbines." Water Power
- 60 Webster, J. (1973). "Hydraulic impulse turbines of high specific speed." Water Power: P250-260.
- 61 Williamson, S. J., B. H. Stark, et al. (2012). Experimental optimisation of a low-head pico hydro turgo turbine, on sustainable energy technologies. 3rd IEEE international conference. IEEE: 322-327.
- 62 Williamson, S. J., B. H. Stark, et al. (2013). "Performance of a low-head pico-hydro turgo turbine." Applied Energy 102: 1114–1126.
- 63 Williamson, S. J., B. H. Stark, et al. (2014). "Low head pico hydro turbine selection using a multi-criteria analysis." Renewable Energy 61: 43-50.
- 64 Wilson, P. N. (1967). "A High Speed Impulse Turbine."
- 65 Xiao, Y., Z. Wang, et al. (2014). Numerical and experimental analysis of the hydraulic performance of a prototype Pelton turbine. Institution of Mechanical Engineers, Part A: Journal of Power and Energy. 228: 46-55.
- 66 Youssef Aaraj, Sorina Mortanda, et al. (2014). Design Of A Turgo Two-Phase Turbine Runner. 15th International Refrigeration and Air Conditioning Conference. Purdue, Indiana.

- 67 Zhang, Z. and M. Casey (2009). "Experimental studies of the jet of a Pelton turbine." Proceedings of the Institution of Mechanical Engineers, Part A: Journal of Power and Energy 221(8): 1181-1192
- 68 Zidonis, A. (2015). Optimisation and efficiency improvement of pelton hydro turbine using computational fluid dynamics and experimental testing. PhD, Lancaster University.
- 69 Zidonis, A., D. Benzon, et al. (2015). "Development of hydro impulse turbines and new opportunities." Renewable and Sustainable Energy Reviews 51(RSER4610): 1624–1635.
- 70 Židoniš, A., A. Panagiotopoulos, et al. (2014). "Parametric Optimisation of Two Pelton Turbine Runner Designs Using Computational Fluid Dynamics." Journal of Hydrodynamics Ser. B.
- 71 Zoppe, B., C. Pellone, et al. (2006). "Flow analysis inside a Pelton turbine bucket." Journal of turbomachinery 128(3): 500-511.

Appendices

Appendix A: Runner mesh replay control

The replay control script used to define the element sizing, create the mesh density regions and generate the initial Octree and Delaunay meshes before manual editing of the elements and prism generation is given below:

1. ic_undo_group_begin
2. ic_set_meshing_params prism 0 law exponential layers 5 height 0 ratio 1.2 total_height 0
5. ic_set_meshing_params variable 0 tetra_batch 1
6. ic_set_meshing_params global 0 gfast 0 gedgec 0.1
9. ic_geo_new_family GEOM
10. ic_boco_set_part_color GEOM
11. ic_geo_project_curve_to_surface EDGE212 FACE264 crv.00 GEOM 0 0
18. ic_geo_create_density density.0 1.5 18 1.2
21. ic_geo_set_family_params R_BLADE1_IN no_crv_inf prism 1 emax 1.5 ehgt 0.0 hrat 0 nlay 5 erat 1.1 ewid 0 emin 0.0 edev 0.0 split_wall 0 internal_wall 0
22. ic_geo_set_family_params R_BLADE1_LE no_crv_inf prism 1 emax 0.5 ehgt 0.0 hrat 0 nlay 5 erat 0 ewid 0 emin 0.0 edev 0.0 split_wall 0 internal_wall 0
23. ic_geo_set_family_params R_BLADE1_OUT no_crv_inf prism 1 emax 1.5 ehgt 0.0 hrat 0 nlay 5 erat 0 ewid 0 emin 0.0 edev 0.0 split_wall 0 internal_wall 0
24. ic_geo_set_family_params R_BLADE1_RADSIN no_crv_inf prism 1 emax 1.0 ehgt 0.0 hrat 0 nlay 5 erat 0 ewid 0 emin 0.0 edev 0.0 split_wall 0 internal_wall 0
25. ic_geo_set_family_params R_BLADE1_RADSOUT no_crv_inf prism 1 emax 1.0 ehgt 0.0 hrat 0 nlay 5 erat 0 ewid 0 emin 0.0 edev 0.0 split_wall 0 internal_wall 0
26. ic_geo_set_family_params R_BLADE1_TE no_crv_inf prism 1 emax 0.5 ehgt 0.0 hrat 0 nlay 5 erat 0 ewid 0 emin 0.0 edev 0.0 split_wall 0 internal_wall 0
27. ic_geo_set_family_params R_BLADE2_IN no_crv_inf prism 1 emax 4.0 ehgt 0.0 hrat 0 nlay 5 erat 0 ewid 0 emin 0.0 edev 0.0 split_wall 0 internal_wall 0
28. ic_geo_set_family_params R_BLADE2_LE no_crv_inf prism 1 emax 0.5 ehgt 0.0 hrat 0 nlay 5 erat 0 ewid 0 emin 0.0 edev 0.0 split_wall 0 internal_wall 0
29. ic_geo_set_family_params R_BLADE2_OUT no_crv_inf prism 1 emax 1.5 ehgt 0.0 hrat 0 nlay 5 erat 1.1 ewid 0 emin 0.0 edev 0.0 split_wall 0 internal_wall 0
30. ic_geo_set_family_params R_BLADE2_RADSIN no_crv_inf prism 1 emax 2.0 ehgt 0.0 hrat 0 nlay 5 erat 0 ewid 0 emin 0.0 edev 0.0 split_wall 0 internal_wall 0

```

31. ic_geo_set_family_params R_BLADE2_RADSOUT no_crv_inf prism 1 emax 1.0 ehgt
0.0 hrat 0 nlay 5 erat 0 ewid 0 emin 0.0 edev 0.0 split_wall 0 internal_wall 0
32. ic_geo_set_family_params R_BLADE2_TE no_crv_inf prism 1 emax 0.5 ehgt 0.0 hrat 0
nlay 5 erat 0 ewid 0 emin 0.0 edev 0.0 split_wall 0 internal_wall 0
33. ic_geo_set_family_params R_HUB_MID no_crv_inf prism 1 emax 1.0 ehgt 0.0 hrat 0
nlay 5 erat 0 ewid 0 emin 0.0 edev 0.0 split_wall 0 internal_wall 0
34. ic_geo_set_family_params R_INTERFACE no_crv_inf prism 0 emax 4.0 ehgt 0.0 hrat 0
nlay 0 erat 0 ewid 0 emin 0.0 edev 0.0 split_wall 0 internal_wall 0
35. ic_geo_set_family_params R_OPENING no_crv_inf prism 0 emax 8.0 ehgt 0.0 hrat 0
nlay 0 erat 0 ewid 0 emin 0.0 edev 0.0 split_wall 0 internal_wall 0
36. ic_geo_set_family_params R_RING no_crv_inf prism 0 emax 4.0 ehgt 0.0 hrat 0 nlay 0
erat 0 ewid 0 emin 0.0 edev 0.0 split_wall 0 internal_wall 0
37. ic_geo_set_family_params R_RING_MID no_crv_inf prism 1 emax 1.5 ehgt 0.0 hrat 0
nlay 5 erat 0 ewid 0 emin 0.0 edev 0.0 split_wall 0 internal_wall 0
38. ic_geo_set_family_params R_RING_RADS no_crv_inf prism 0 emax 1.5 ehgt 0.0 hrat 0
nlay 0 erat 0 ewid 0 emin 0.0 edev 0.0 split_wall 0 internal_wall 0
40. ic_geo_params_blank_done part 1
42. ic_geo_set_family_params R_BLADE1_LE no_crv_inf prism 1 emax 0.25 ehgt 0.0 hrat 0
nlay 5 erat 0 ewid 0 emin 0.0 edev 0.0 split_wall 0 internal_wall 0
43. ic_geo_set_family_params R_BLADE2_LE no_crv_inf prism 1 emax 0.25 ehgt 0.0 hrat 0
nlay 5 erat 0 ewid 0 emin 0.0 edev 0.0 split_wall 0 internal_wall 0
44. ic_geo_set_family_params R_HUB no_crv_inf prism 1 emax 0.0 ehgt 0.0 hrat 0 nlay 5
erat 0 ewid 0 emin 0.0 edev 0.0 split_wall 0 internal_wall 0
45. ic_geo_set_family_params R_RING no_crv_inf prism 1 emax 4.0 ehgt 0.0 hrat 0 nlay 5
erat 0 ewid 0 emin 0.0 edev 0.0 split_wall 0 internal_wall 0
46. ic_geo_set_family_params R_RING_RADS no_crv_inf prism 1 emax 1.5 ehgt 0.0 hrat 0
nlay 5 erat 0 ewid 0 emin 0.0 edev 0.0 split_wall 0 internal_wall 0
48. ic_geo_params_blank_done part 1
50. ic_set_meshing_params prism 0 law exponential layers 3 height 0 ratio 1.2 total_height 0
53. ic_set_meshing_params global 0 gfast 0 gedgec 0.1
60. ic_geo_new_family FLUID
61. ic_boco_set_part_color FLUID
62. ic_geo_create_volume FLUID
69. ic_geo_set_family_params R_HUB no_crv_inf prism 1 emax 0.0 ehgt 0.3 hrat 0 nlay 5
erat 0 ewid 0 emin 0.0 edev 0.0 split_wall 0 internal_wall 0
70. ic_geo_set_family_params R_RING no_crv_inf prism 1 emax 4.0 ehgt 0.3 hrat 0 nlay 5
erat 0 ewid 0 emin 0.0 edev 0.0 split_wall 0 internal_wall 0

```

```

72. ic_geo_params_blank_done part 1
74. ic_save_tetin temp_tetra.tin
75. ic_run_tetra temp_tetra.tin ./tetra_mesh.uns run_cutter 1 delete_auto 1 run_smoothen 0
fix_holes 1 n_processors 1 show_progress 1 log ./tetra_cmd.log
76. ic_unload_mesh
77. ic_uns_load tetra_mesh.uns
78. ic_geo_set_modified 1
79. ic_uns_update_family_type visible {R_HUB R_RING R_BLADE1_OUT
R_BLADE2_IN R_RING_RADS R_BLADE1_RADSIN R_BLADE1_TE R_BLADE2_OUT
R_BLADE2_LE GEOM R_BLADE1_IN R_OPENING R_HUB_MID R_RING_MID
R_INTERFACE R_BLADE1_LE R_BLADE2_TE R_BLADE2_RADSIN
R_BLADE1_RADSOUT FLUID R_BLADE2_RADSOUT
80. ic_boco_solver
81. ic_uns_update_family_type visible {R_HUB R_RING R_BLADE1_OUT
R_BLADE2_IN R_RING_RADS R_BLADE1_RADSIN R_BLADE1_TE R_BLADE2_OUT
R_BLADE2_LE GEOM R_BLADE1_IN R_OPENING R_HUB_MID R_RING_MID
R_INTERFACE R_BLADE1_LE R_BLADE2_TE R_BLADE2_RADSIN
R_BLADE1_RADSOUT FLUID R_BLADE2_RADSOUT
82. ic_boco_clear_icons
83. ic_csystem_display all 0
84. ic_csystem_set_current global
85. ic_boco_nastran_csystem reset
86. ic_uns_subset_visible {added faces} 1
87. ic_uns_diagnostic diag_type single quiet 1
88. ic_smooth_elements map all upto 0.4 iterations 5 n_processors 1 smooth TRI_3 float
TETRA_4 laplace 1
89. ic_smooth_elements map all upto 0.4 iterations 5 prism_warp_weight 0.5 n_processors 1
smooth TETRA_4 float PENTA_6 freeze TRI_3
90. ic_smooth_elements map all upto 0.4 iterations 5 prism_warp_weight 0.5 metric Quality
n_processors 1 smooth TETRA_4 smooth TRI_3 float PENTA_6
91. ic_geo_set_modified 1
92. ic_uns_update_family_type visible {R_HUB R_RING R_BLADE1_OUT
R_BLADE2_IN R_RING_RADS R_BLADE1_RADSIN R_BLADE1_TE R_BLADE2_OUT
R_BLADE2_LE GEOM R_BLADE1_IN R_OPENING R_HUB_MID R_RING_MID
R_INTERFACE R_BLADE1_LE R_BLADE2_TE R_BLADE2_RADSIN
R_BLADE1_RADSOUT FLUID R_BLADE2_RADSOUT

```

```

93. ic_uns_update_family_type visible {R_HUB R_RING R_BLADE1_OUT
R_BLADE2_IN R_RING_RADS R_BLADE1_RADSIN R_BLADE1_TE R_BLADE2_OUT
R_BLADE2_LE GEOM R_BLADE1_IN R_OPENING R_HUB_MID R_RING_MID
R_INTERFACE R_BLADE1_LE R_BLADE2_TE R_BLADE2_RADSIN
R_BLADE1_RADSOUT FLUID R_BLADE2_RADSOUT

96. ic_uns_subset_delete tri2tet_errors

97. ic_save_unstruct tri2tet_temp0.uns 1

98. ic_run_tri2tet tri2tet_temp0.uns C:/ANSYSC~1/FEA/FEA_ME~1/dp0/ICM-
4/ICEMCFD/tri2tet_mesh.uns safety 1 use_tg_tri2tet 1 use_tg_tgrid_af 1 tetexpand 1 family
FLUID bgmesh 0 show_progress 1 errors tri2tet_errors verbose 0

99. ic_unload_mesh

100. ic_uns_diag_reset_degen_min_max

101. ic_uns_load {"C:/Ansys CFX/FEA/FEA_Meshes_files/dp0/ICM-
4/ICEMCFD/tri2tet_mesh.uns"} 3 1 0

102. ic_boco_solver

103. ic_uns_update_family_type visible {R_HUB R_RING R_BLADE1_OUT
R_BLADE2_IN R_RING_RADS R_BLADE1_RADSIN R_BLADE1_TE R_BLADE2_OUT
R_BLADE2_LE GEOM R_BLADE1_IN R_OPENING R_HUB_MID R_RING_MID
R_INTERFACE R_BLADE1_LE R_BLADE2_TE R_BLADE2_RADSIN
R_BLADE1_RADSOUT FLUID R_BLADE2_RADSOUT

104. ic_boco_clear_icons

105. ic_csystem_display all 0

106. ic_csystem_set_current global

107. ic_boco_nastran_csystem reset

108. ic_uns_list_material_families

109. ic_flood_fill_mesh 0 1

110. ic_uns_update_family_type visible {R_HUB R_RING R_BLADE1_OUT
R_BLADE2_IN R_RING_RADS R_BLADE1_RADSIN R_BLADE1_TE R_BLADE2_OUT
R_BLADE2_LE GEOM R_BLADE1_IN R_OPENING R_HUB_MID R_RING_MID
R_INTERFACE R_BLADE1_LE R_BLADE2_TE R_BLADE2_RADSIN
R_BLADE1_RADSOUT FLUID R_BLADE2_RADSOUT

111. ic_uns_update_family_type visible {R_HUB R_RING R_BLADE1_OUT
R_BLADE2_IN R_RING_RADS R_BLADE1_RADSIN R_BLADE1_TE R_BLADE2_OUT
R_BLADE2_LE GEOM R_BLADE1_IN R_OPENING R_HUB_MID R_RING_MID
R_INTERFACE R_BLADE1_LE R_BLADE2_TE R_BLADE2_RADSIN
R_BLADE1_RADSOUT FLUID R_BLADE2_RADSOUT

112. ic_uns_subset_create added

```

```

113. ic_uns_subset_add_number added faces 1 MIXED
114. ic_uns_create_selection_subset 0
115. ic_uns_subset_visible uns_sel_0 0
116. ic_uns_subset_copy uns_sel_0 all 0
117. ic_uns_uniqify uns_sel_0
118. ic_uns_subset_subtract_from added uns_sel_0
119. ic_uns_subset_delete uns_sel_0
120. ic_uns_create_selection_subset 0
121. ic_uns_subset_visible uns_sel_0 0
122. ic_uns_subset_copy uns_sel_0 all 1
123. ic_uns_uniqify uns_sel_0
124. ic_uns_subset_subtract_from added uns_sel_0
125. ic_uns_subset_delete uns_sel_0
126. ic_uns_create_selection_subset 0
127. ic_uns_subset_visible uns_sel_0 0
128. ic_uns_subset_copy uns_sel_0 all 2
129. ic_uns_uniqify uns_sel_0
130. ic_uns_subset_subtract_from added uns_sel_0
131. ic_uns_subset_delete uns_sel_0
132. ic_uns_create_selection_subset 0
133. ic_uns_subset_visible uns_sel_0 0
134. ic_uns_subset_copy uns_sel_0 all 3
135. ic_uns_uniqify uns_sel_0
136. ic_uns_subset_subtract_from added uns_sel_0
137. ic_uns_subset_delete uns_sel_0
138. ic_uns_subset_visible added 0
139. ic_uns_update_family_type visible {R_HUB R_RING R_BLADE1_OUT
R_BLADE2_IN R_RING_RADS R_BLADE1_RADSDIN R_BLADE1_TE R_BLADE2_OUT
R_BLADE2_LE GEOM R_BLADE1_IN R_OPENING R_HUB_MID R_RING_MID
R_INTERFACE R_BLADE1_LE R_BLADE2_TE R_BLADE2_RADSDIN
R_BLADE1_RADSDOUT FLUID R_BLADE2_RADSDOUT
141. ic_uns_subset_delete smooth_show_map
142. ic_uns_diag_reset_degen_min_max
143. ic_uns_subset_create smooth_do_map 0
144. ic_uns_subset_create smooth_show_map 10
145. ic_uns_subset_configure smooth_do_map -list_type 1

```

```

146. ic_uns_subset_configure smooth_show_map -shade flat_wire -color white -
dont_change_color_or_shade 1
147. ic_uns_update_family_type smooth_do_map {ORFN R_BLADE1_IN R_BLADE1_LE
R_BLADE1_OUT R_BLADE1_RADSIN R_BLADE1_RADSOUT R_BLADE1_TE
R_BLADE2_IN R_BLADE2_LE R_BLADE2_OUT R_BLADE2_RADSIN
R_BLADE2_RADSOUT R_BLADE2_TE R_HUB R_HUB_MID R_INTERFACE
R_OPENING R_RING R_RING_MID R_RING_RADS R_SHAFT
148. ic_uns_subset_delete smooth_show_map
149. ic_uns_diag_reset_degen_min_max
150. ic_uns_metric smooth_do_map Quality prism_warp_weight 0.5 eval_at_node_method 0
151. ic_uns_histogram smooth_do_map 0.073337 0.999986 20
153. ic_uns_update_family_type smooth_do_map {ORFN R_BLADE1_IN R_BLADE1_LE
R_BLADE1_OUT R_BLADE1_RADSIN R_BLADE1_RADSOUT R_BLADE1_TE
R_BLADE2_IN R_BLADE2_LE R_BLADE2_OUT R_BLADE2_RADSIN
R_BLADE2_RADSOUT R_BLADE2_TE R_HUB R_HUB_MID R_INTERFACE
R_OPENING R_RING R_RING_MID R_RING_RADS R_SHAFT
154. ic_smooth_elements map smooth_do_map upto 0.20 iterations 20 prism_warp_weight
0.5 fix_families metric Quality smooth TETRA_4 smooth TRI_3 n_processors 1
155. ic_uns_diag_reset_degen_min_max
156. ic_uns_metric smooth_do_map Quality prism_warp_weight 0.5 eval_at_node_method 0
157. ic_uns_histogram smooth_do_map 0.073337 0.999986 20
160. ic_uns_update_family_type smooth_do_map {ORFN R_BLADE1_IN R_BLADE1_LE
R_BLADE1_OUT R_BLADE1_RADSIN R_BLADE1_RADSOUT R_BLADE1_TE
R_BLADE2_IN R_BLADE2_LE R_BLADE2_OUT R_BLADE2_RADSIN
R_BLADE2_RADSOUT R_BLADE2_TE R_HUB R_HUB_MID R_INTERFACE
R_OPENING R_RING R_RING_MID R_RING_RADS R_SHAFT
161. ic_smooth_elements map smooth_do_map upto 0.4 iterations 20 prism_warp_weight 0.5
fix_families metric Quality smooth TETRA_4 smooth TRI_3 n_processors 1
162. ic_uns_diag_reset_degen_min_max
163. ic_uns_metric smooth_do_map Quality prism_warp_weight 0.5 eval_at_node_method 0
164. ic_uns_histogram smooth_do_map 0.073337 0.999986 20

```

Appendix B: CFX Command Language (CCL) for run

```
+-----+  
|  
|           CFX Command Language for Run  
|  
+-----+
```

LIBRARY:

CEL:

EXPRESSIONS:

```
Bladestep = (360/22)/Degperstep  
Degpersec = (Rotational Speed*360)/60  
Degperstep = 360/3300  
Rotational Speed = 1249  
Timestep = step((timestat-t)/1[s])*stepstat +step \  
((t-timestat)/1[s])*tstep)[s]  
Torque1f = -torque_y()@R_BLADE1_IN  
Torque2b = -torque_y()@R_BLADE2_OUT  
Torque2f = -torque_y()@REGION:R_BLADE2_IN  
Total Timestep = (Total Time-timestat)/tstep[s]+(timestat/stepstat)  
Total time = timestat+200[s]/Degpersec  
YPlus = maxVal(Yplus )@REGION:R_BLADE1_IN  
jetvel = 24.46790551 [m s^-1]  
jetvelu = -11.08830447 [m s^-1]  
jetvelv = 10.3400112 [m s^-1]  
jetvelw = -19.20448053 [m s^-1]  
jetvfair = step(((t-165[s]/Degpersec))/1[s])*1  
jetvfwater = step(((165[s]/Degpersec)-t)/1[s])*1  
massflowin = Water.massFlow()@S_JET_INLET  
massflowout = -massFlow()@R_OPENING  
maxpres = maxVal(Pressure)@REGION:ANSYS_Persist_Key_2  
maxvel = Water.maxVal(Water.Velocity )@REGION:ANSYS_Persist_Key_2  
meanjetvel = ave(Water.Velocity)@S_JET_INLET  
rpm = (-Rotational Speed*step((t-timestat)/1[s]))[rev min^-1]  
stepstat = 0.00005  
timestat = 0.008[s]  
tstep = Degperstep/Degpersec  
END  
END
```

MATERIAL: Air at 25 C

Material Description = Air at 25 C and 1 atm (dry)

Material Group = Air Data, Constant Property Gases

Option = Pure Substance

Thermodynamic State = Gas

PROPERTIES:

Option = General Material

EQUATION OF STATE:

Density = 1.185 [kg m⁻³]

Molar Mass = 28.96 [kg kmol⁻¹]

Option = Value

END

SPECIFIC HEAT CAPACITY:

Option = Value

Specific Heat Capacity = 1.0044E+03 [J kg⁻¹ K⁻¹]

Specific Heat Type = Constant Pressure

END

REFERENCE STATE:

Option = Specified Point

Reference Pressure = 1 [atm]

Reference Specific Enthalpy = 0. [J/kg]

Reference Specific Entropy = 0. [J/kg/K]

Reference Temperature = 25 [C]

END

DYNAMIC VISCOSITY:

Dynamic Viscosity = 1.831E-05 [kg m⁻¹ s⁻¹]

Option = Value

END

THERMAL CONDUCTIVITY:

Option = Value

Thermal Conductivity = 2.61E-02 [W m⁻¹ K⁻¹]

END

ABSORPTION COEFFICIENT:

Absorption Coefficient = 0.01 [m⁻¹]

Option = Value

END

SCATTERING COEFFICIENT:

Option = Value

Scattering Coefficient = 0.0 [m⁻¹]

END

REFRACTIVE INDEX:

Option = Value
Refractive Index = 1.0 [m m^-1]
END

THERMAL EXPANSIVITY:

Option = Value
Thermal Expansivity = 0.003356 [K^-1]
END
END

MATERIAL: Water

Material Description = Water (liquid)
Material Group = Water Data, Constant Property Liquids
Option = Pure Substance
Thermodynamic State = Liquid

PROPERTIES:

Option = General Material
EQUATION OF STATE:

Density = 997.0 [kg m^-3]
Molar Mass = 18.02 [kg kmol^-1]
Option = Value

END

SPECIFIC HEAT CAPACITY:

Option = Value
Specific Heat Capacity = 4181.7 [J kg^-1 K^-1]
Specific Heat Type = Constant Pressure
END

REFERENCE STATE:

Option = Specified Point
Reference Pressure = 1 [atm]
Reference Specific Enthalpy = 0.0 [J/kg]
Reference Specific Entropy = 0.0 [J/kg/K]
Reference Temperature = 25 [C]

END

DYNAMIC VISCOSITY:

Dynamic Viscosity = 8.899E-4 [kg m^-1 s^-1]
Option = Value

END

THERMAL CONDUCTIVITY:

Option = Value

```

    Thermal Conductivity = 0.6069 [W m^-1 K^-1]
END
ABSORPTION COEFFICIENT:
    Absorption Coefficient = 1.0 [m^-1]
    Option = Value
END
SCATTERING COEFFICIENT:
    Option = Value
    Scattering Coefficient = 0.0 [m^-1]
END
REFRACTIVE INDEX:
    Option = Value
    Refractive Index = 1.0 [m m^-1]
END
THERMAL EXPANSIVITY:
    Option = Value
    Thermal Expansivity = 2.57E-04 [K^-1]
END
END
FLOW: Flow Analysis 1
SOLUTION UNITS:
    Angle Units = [rad]
    Length Units = [m]
    Mass Units = [kg]
    Solid Angle Units = [sr]
    Temperature Units = [K]
    Time Units = [s]
END
ANALYSIS TYPE:
    Option = Transient
EXTERNAL SOLVER COUPLING:
    Option = None
END
INITIAL TIME:
    Option = Automatic with Value
    Time = 0 [s]
END
TIME DURATION:

```

```

Option = Total Time
Total Time = Total time
END
TIME STEPS:
Option = Timesteps
Timesteps = Timestep
END
END
DOMAIN: Rotating Domain
Coord Frame = Coord 0
Domain Type = Fluid
Location = Assembly
BOUNDARY: Fluid Interface Side 2
Boundary Type = INTERFACE
Location = R_INTERFACE
BOUNDARY CONDITIONS:
MASS AND MOMENTUM:
Option = Conservative Interface Flux
END
TURBULENCE:
Option = Conservative Interface Flux
END
END
END
BOUNDARY: R_blade1_in
Boundary Type = WALL
Frame Type = Rotating
Location = R_BLADE1_IN,R_BLADE1_LE,R_BLADE1_TE,R_BLADE1_RADSIN
BOUNDARY CONDITIONS:
MASS AND MOMENTUM:
Option = Free Slip Wall
END
END
END
BOUNDARY: R_blade1_out
Boundary Type = WALL
Frame Type = Rotating
Location = R_BLADE1_OUT,R_BLADE1_RADSOUT
BOUNDARY CONDITIONS:
MASS AND MOMENTUM:

```

```

    Option = Free Slip Wall
    END
    END
    END
    BOUNDARY: R_blade2_in
        Boundary Type = WALL
        Frame Type = Rotating
        Location = R_BLADE2_IN,R_BLADE2_LE,R_BLADE2_TE,R_BLADE2_RADSIN
    BOUNDARY CONDITIONS:
        MASS AND MOMENTUM:
            Option = Free Slip Wall
            END
            END
            END
        BOUNDARY: R_blade2_out
            Boundary Type = WALL
            Frame Type = Rotating
            Location = R_BLADE2_OUT,R_BLADE2_RADSOUT
    BOUNDARY CONDITIONS:
        MASS AND MOMENTUM:
            Option = Free Slip Wall
            END
            END
            END
        BOUNDARY: R_hub
            Boundary Type = WALL
            Frame Type = Rotating
            Location = R_HUB,R_HUB_MID,FAM7_5_HCTI3A_ROT_1_1 B
    BOUNDARY CONDITIONS:
        MASS AND MOMENTUM:
            Option = Free Slip Wall
            END
            END
            END
        BOUNDARY: R_opening
            Boundary Type = OPENING
            Frame Type = Rotating
            Location = R_OPENING
    BOUNDARY CONDITIONS:
        FLOW REGIME:

```

```

    Option = Subsonic
END
MASS AND MOMENTUM:
    Option = Entrainment
    Relative Pressure = 0 [Pa]
END
TURBULENCE:
    Option = Zero Gradient
END
END
FLUID: Air
BOUNDARY CONDITIONS:
    VOLUME FRACTION:
        Option = Value
        Volume Fraction = 1
    END
    END
    END
FLUID: Water
BOUNDARY CONDITIONS:
    VOLUME FRACTION:
        Option = Value
        Volume Fraction = 0
    END
    END
    END
    END
    BOUNDARY: R_ring
        Boundary Type = WALL
        Frame Type = Rotating
        Location = R_RING,R_RING_MID,R_RING_RADS,FAM7_5_HCTI3A_ROT_1_1 A
    BOUNDARY CONDITIONS:
        MASS AND MOMENTUM:
            Option = Free Slip Wall
        END
        END
    END
    DOMAIN MODELS:
        BUOYANCY MODEL:
            Option = Non Buoyant

```

```
END  
DOMAIN MOTION:  
    Angular Velocity = rpm  
    Option = Rotating  
AXIS DEFINITION:  
    Option = Coordinate Axis  
    Rotation Axis = Coord 0.2  
END  
END  
MESH DEFORMATION:  
    Option = None  
END  
REFERENCE PRESSURE:  
    Reference Pressure = 1 [atm]  
END  
END  
FLUID DEFINITION: Air  
    Material = Air at 25 C  
    Option = Material Library  
MORPHOLOGY:  
    Option = Continuous Fluid  
END  
END  
FLUID DEFINITION: Water  
    Material = Water  
    Option = Material Library  
MORPHOLOGY:  
    Option = Continuous Fluid  
END  
END  
FLUID MODELS:  
    COMBUSTION MODEL:  
        Option = None  
    END  
    HEAT TRANSFER MODEL:  
        Fluid Temperature = 25 [C]  
        Homogeneous Model = Off  
        Option = Isothermal  
    END  
    THERMAL RADIATION MODEL:
```

```
    Option = None
END
TURBULENCE MODEL:
    Option = SST
END
TURBULENT WALL FUNCTIONS:
    Option = Automatic
END
END
FLUID PAIR: Air | Water
INTERPHASE TRANSFER MODEL:
    Option = Free Surface
END
MASS TRANSFER:
    Option = None
END
SURFACE TENSION MODEL:
    Option = None
END
END
INITIALISATION:
    Frame Type = Rotating
    Option = Automatic
FLUID: Air
    INITIAL CONDITIONS:
        VOLUME FRACTION:
            Option = Automatic with Value
            Volume Fraction = 1
        END
    END
    END
FLUID: Water
    INITIAL CONDITIONS:
        VOLUME FRACTION:
            Option = Automatic with Value
            Volume Fraction = 0
        END
    END
    END
INITIAL CONDITIONS:
```

```

Velocity Type = Cartesian
CARTESIAN VELOCITY COMPONENTS:
    Option = Automatic with Value
    U = 0 [m s^-1]
    V = 0 [m s^-1]
    W = 0 [m s^-1]
END

STATIC PRESSURE:
    Option = Automatic with Value
    Relative Pressure = 0 [atm]
END

TURBULENCE INITIAL CONDITIONS:
    Option = Medium Intensity and Eddy Viscosity Ratio
END

MULTIPHASE MODELS:
    Homogeneous Model = On

FREE SURFACE MODEL:
    Option = Standard
END

DOMAIN: Stationary Domain
    Coord Frame = Coord 0
    Domain Type = Fluid
    Location = SHROUD,SOLID

BOUNDARY: Fluid Interface Side 1
    Boundary Type = INTERFACE
    Location = S_INTERFACE

BOUNDARY CONDITIONS:
    MASS AND MOMENTUM:
        Option = Conservative Interface Flux
    END

    TURBULENCE:
        Option = Conservative Interface Flux
    END

    END

    BOUNDARY: S_cyl_interface Side 1

```

```

Boundary Type = INTERFACE
Location = S_CYL_IF1_1
BOUNDARY CONDITIONS:
MASS AND MOMENTUM:
  Option = Conservative Interface Flux
END
TURBULENCE:
  Option = Conservative Interface Flux
END
END
END

BOUNDARY: S_cyl_interface Side 2
Boundary Type = INTERFACE
Location = S_CYL_IF1_2
BOUNDARY CONDITIONS:
MASS AND MOMENTUM:
  Option = Conservative Interface Flux
END
TURBULENCE:
  Option = Conservative Interface Flux
END
END
END

BOUNDARY: S_jet_inlet
Boundary Type = INLET
Location = S_JET_INLET
BOUNDARY CONDITIONS:
FLOW REGIME:
  Option = Subsonic
END
MASS AND MOMENTUM:
  Normal Speed = jetvel
  Option = Normal Speed
END
TURBULENCE:
  Option = Medium Intensity and Eddy Viscosity Ratio
END
END
FLUID: Air
BOUNDARY CONDITIONS:

```

```

VOLUME FRACTION:
  Option = Value
  Volume Fraction = jetvfair
END
END
END
FLUID: Water
BOUNDARY CONDITIONS:
VOLUME FRACTION:
  Option = Value
  Volume Fraction = jetvfwater
END
END
END
END
BOUNDARY: S_jet_wall
Boundary Type = WALL
Location = S_JET_WALL,S_CYL_INLET
BOUNDARY CONDITIONS:
MASS AND MOMENTUM:
  Option = Free Slip Wall
END
END
END
END
BOUNDARY: S_opening
Boundary Type = OPENING
Location = S_OPENING
BOUNDARY CONDITIONS:
FLOW REGIME:
  Option = Subsonic
END
MASS AND MOMENTUM:
  Option = Entrainment
  Relative Pressure = 0 [atm]
END
TURBULENCE:
  Option = Zero Gradient
END
END
FLUID: Air

```

BOUNDARY CONDITIONS:

VOLUME FRACTION:

Option = Value

Volume Fraction = 1

END

END

END

FLUID: Water

BOUNDARY CONDITIONS:

VOLUME FRACTION:

Option = Value

Volume Fraction = 0

END

END

END

END

DOMAIN MODELS:

BUOYANCY MODEL:

Option = Non Buoyant

END

DOMAIN MOTION:

Option = Stationary

END

MESH DEFORMATION:

Option = None

END

REFERENCE PRESSURE:

Reference Pressure = 1 [atm]

END

END

FLUID DEFINITION: Air

Material = Air at 25 C

Option = Material Library

MORPHOLOGY:

Option = Continuous Fluid

END

END

FLUID DEFINITION: Water

Material = Water

Option = Material Library

MORPHOLOGY:

Option = Continuous Fluid

END

END

FLUID MODELS:

COMBUSTION MODEL:

Option = None

END

HEAT TRANSFER MODEL:

Fluid Temperature = 25 [C]

Homogeneous Model = Off

Option = Isothermal

END

THERMAL RADIATION MODEL:

Option = None

END

TURBULENCE MODEL:

Option = SST

END

TURBULENT WALL FUNCTIONS:

Option = Automatic

END

END

FLUID PAIR: Air | Water

INTERPHASE TRANSFER MODEL:

Option = Free Surface

END

MASS TRANSFER:

Option = None

END

SURFACE TENSION MODEL:

Option = None

END

END

INITIALISATION:

Option = Automatic

FLUID: Air

INITIAL CONDITIONS:

VOLUME FRACTION:

Option = Automatic with Value

```

    Volume Fraction = 1
END
END
END
FLUID: Water
INITIAL CONDITIONS:
VOLUME FRACTION:
    Option = Automatic with Value
    Volume Fraction = 0
END
END
END
INITIAL CONDITIONS:
Velocity Type = Cartesian
CARTESIAN VELOCITY COMPONENTS:
    Option = Automatic with Value
    U = 0 [m s^-1]
    V = 0 [m s^-1]
    W = 0 [m s^-1]
END
STATIC PRESSURE:
    Option = Automatic with Value
    Relative Pressure = 0 [atm]
END
TURBULENCE INITIAL CONDITIONS:
    Option = Medium Intensity and Eddy Viscosity Ratio
END
END
END
MULTIPHASE MODELS:
Homogeneous Model = On
FREE SURFACE MODEL:
    Option = Standard
END
END
END
DOMAIN INTERFACE: Fluid Interface
Boundary List1 = Fluid Interface Side 1
Boundary List2 = Fluid Interface Side 2
Interface Type = Fluid Fluid

```

INTERFACE MODELS:

Option = General Connection

FRAME CHANGE:

Option = Transient Rotor Stator

END

MASS AND MOMENTUM:

Option = Conservative Interface Flux

MOMENTUM INTERFACE MODEL:

Option = None

END

END

PITCH CHANGE:

Option = Specified Pitch Angles

Pitch Angle Side1 = 360 [degree]

Pitch Angle Side2 = 360 [degree]

END

END

MESH CONNECTION:

Option = GGI

END

END

DOMAIN INTERFACE: S_cyl_interface

Boundary List1 = S_cyl_interface Side 1

Boundary List2 = S_cyl_interface Side 2

Interface Type = Fluid Fluid

INTERFACE MODELS:

Option = General Connection

FRAME CHANGE:

Option = None

END

MASS AND MOMENTUM:

Option = Conservative Interface Flux

MOMENTUM INTERFACE MODEL:

Option = None

END

END

PITCH CHANGE:

Option = None

END

END

MESH CONNECTION:

Option = GGI

END

END

OUTPUT CONTROL:

MONITOR OBJECTS:

MONITOR BALANCES:

Option = Full

END

MONITOR FORCES:

Option = Full

END

MONITOR PARTICLES:

Option = Full

END

MONITOR POINT: Jet Velocity

Coord Frame = Coord 0

Expression Value = meanjetvel

Option = Expression

END

MONITOR POINT: Massflowin

Coord Frame = Coord 0

Expression Value = massflowin

Option = Expression

END

MONITOR POINT: Massflowout

Coord Frame = Coord 0

Expression Value = massflowout

Option = Expression

END

MONITOR POINT: Rotational speed

Coord Frame = Coord 0

Expression Value = rpm

Option = Expression

END

MONITOR POINT: T1

Coord Frame = Coord 0

Expression Value = Torque1f

Option = Expression

END

```

MONITOR POINT: T2
  Coord Frame = Coord 0
  Expression Value = Torque2b
  Option = Expression
END

MONITOR POINT: YPLUS
  Coord Frame = Coord 0
  Expression Value = YPlus
  Option = Expression
END

MONITOR POINT: timestep
  Coord Frame = Coord 0
  Expression Value = Timestep
  Option = Expression
END

MONITOR RESIDUALS:
  Option = Full
END

MONITOR TOTALS:
  Option = Full
END

RESULTS:
  File Compression Level = Default
  Option = Standard
END

TRANSIENT RESULTS: Transient Results 1
  File Compression Level = Default
  Include Mesh = No
  Option = Selected Variables
  Output Variables List = Air.Volume Fraction,Water.Volume Fraction

OUTPUT FREQUENCY:
  Option = Timestep Interval
  Timestep Interval = 5
END

TRANSIENT RESULTS: Transient Results 2
  File Compression Level = Default
  Option = Standard
OUTPUT FREQUENCY:

```

```
    Option = Timestep Interval
    Timestep Interval = 20
    END
  END
END

SOLVER CONTROL:
Turbulence Numerics = High Resolution
ADVECTION SCHEME:
  Option = High Resolution
  END
CONVERGENCE CONTROL:
  Maximum Number of Coefficient Loops = 5
  Minimum Number of Coefficient Loops = 2
  Timescale Control = Coefficient Loops
  END
CONVERGENCE CRITERIA:
  Residual Target = 1e-04
  Residual Type = RMS
  END
TRANSIENT SCHEME:
  Option = Second Order Backward Euler
TIMESTEP INITIALISATION:
  Option = Automatic
  END
  END
  END
END

COMMAND FILE:
Version = 16.1
Results Version = 16.1
END

SIMULATION CONTROL:
EXECUTION CONTROL:
EXECUTABLE SELECTION:
  Double Precision = No
  END
INTERPOLATOR STEP CONTROL:
Runtime Priority = Standard
MEMORY CONTROL:
  Memory Allocation Factor = 1.0
```

```
END
END
PARALLEL HOST LIBRARY:
HOST DEFINITION: ngd030000019
    Host Architecture String = winnt-amd64
    Installation Root = C:\Program Files\ANSYS Inc\v%v\CFX
END
END
PARTITIONER STEP CONTROL:
    Multidomain Option = Automatic
    Runtime Priority = Standard
EXECUTABLE SELECTION:
    Use Large Problem Partitioner = Off
END
MEMORY CONTROL:
    Memory Allocation Factor = 1.0
END
PARTITION SMOOTHING:
    Maximum Partition Smoothing Sweeps = 100
    Option = Smooth
END
PARTITIONING TYPE:
    MeTiS Type = k-way
    Option = MeTiS
    Partition Size Rule = Automatic
END
END
RUN DEFINITION:
    Run Mode = Full
    Solver Input File = E:\PhD\Mesh Study and \
        Refinement\Pre\Stat1_96k_Rot1_1.76M_ts_1.46.def
    Solver Results File = E:\PhD\Mesh Study and \
        Refinement\Pre\Stat1_96k_Rot1_1.76M_ts_1.46_001.res
END
SOLVER STEP CONTROL:
    Runtime Priority = Standard
MEMORY CONTROL:
    Memory Allocation Factor = 1.0
END
PARALLEL ENVIRONMENT:
```

```
Number of Processes = 1
Start Method = Serial
END
END
END
END
```